CHEMICAL REVIEWS

Review

pubs.acs.org/CR

New Generation Cadmium-Free Quantum Dots for Biophotonics and Nanomedicine

Gaixia Xu,[†,⊥,▽] Shuwen Zeng,[‡,⊥,▽] Butian Zhang,[‡] Mark T. Swihart,[*,§] Ken-Tye Yong,[*,‡] and Paras N. Prasad[*,∥]

[†]Key Laboratory of Optoelectronics Devices and Systems of Ministry of Education/Guangdong Province, College of Optoelectronic Engineering, Shenzhen University, Shenzhen 518060, People's Republic of China

[‡]School of Electrical and Electronic Engineering, Nanyang Technological University, Singapore 639798, Singapore

[§]Department of Chemical and Biological Engineering and [∥]Institute for Lasers, Photonics, and Biophotonics and Department of Chemistry, University at Buffalo, The State University of New York, Buffalo, New York 14260, United States

[⊥]CINTRA CNRS/NTU/THALES, UMI 3288, Research Techno Plaza, 50 Nanyang Drive, Border X Block, Singapore 637553, Singapore

ABSTRACT: This review summarizes recent progress in the design and applications of cadmium-free quantum dots (Cd-free QDs), with an emphasis on their role in biophotonics and nanomedicine. We first present the features of Cd-free QDs and describe the physics and emergent optical properties of various types of Cd-free QDs whose applications are discussed in subsequent sections. Selected specific QD systems are introduced, followed by the preparation of these Cd-free QDs in a form useful for biological applications, including recent advances in achieving high photoluminescence quantum yield (PL QY) and tunability of emission color. Next, we summarize biophotonic applications of Cd-free QDs in optical imaging, photoacoustic imaging, sensing, optical tracking, and photothermal therapy. Research advances in the use of Cd-free QDs for nanomedicine applications are discussed, including drug/gene delivery, protein/peptide delivery, image-guided surgery, diagnostics, and medical devices. The review then considers the pharmacokinetics and biodistribution of Cd-free QDs and summarizes current studies on the in vitro and in vivo toxicity of Cd-free QDs. Finally, we provide perspectives on the overall current status, challenges, and future directions in this field.

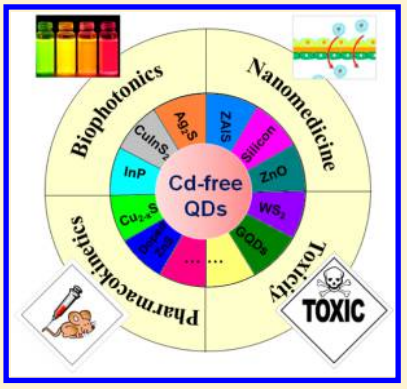

CONTENTS

Received: May 6, 2016
Published: September 22, 2016

DOI: 10.1021/acs.chemrev.6b00290
Chem. Rev. 2016, 116, 12234–12327

1. INTRODUCTION AND BACKGROUND

1.1. Introduction to Quantum Dots

Quantum dots (QDs) are semiconductor nanocrystals (typically 2−10 nm in diameter) that exhibit size-dependent optical properties, including absorbance and photoluminescence (PL). They have proven useful in many biophotonic and nanomedical applications including imaging and sensing.[1] A single QD typically contains hundreds to thousands of atoms of group II−VI elements (e.g., CdTe, CdSe, CdS, ZnS, ZnSe, or ZnTe), group III−V elements (e.g., InP or InAs), group I−III−VI_2 elements (e.g., $CuInS_2$ or $AgInS_2$), group IV−VI elements (e.g., PbSe, PbS, or PbTe), or group IV elements (e.g., Si, C, or Ge). QDs are large in comparison to conventional organic dyes, but can be comparable in size to fluorescent proteins and other large biomolecules. QDs have unique advantages relative to organic dyes as luminescent labels for biological applications.[2,3] Specifically, QDs of different sizes or compositions can all be excited by a single light source, to produce separate emission colors over a wide spectral range with minimal spectral overlap, making them particularly attractive for multiplex imaging.[4] Also, unlike organic dyes, most QDs are highly resistant to photobleaching, which allows them to be used for long-term in vitro and in vivo imaging.[5−7] More importantly, these nanocrystals can be engineered to emit at wavelengths ranging from 450 to 1500 nm by tailoring their size, shape, and composition.[8−11] QDs can be prepared as dispersions in either organic or aqueous media, depending on their intended application. The basic features of QDs are described in greater detail in section 2.

For biological applications, QDs must be water-dispersible. When QDs are initially synthesized as colloidal dispersions in nonpolar organic media, surface modification is required to render them dispersible in aqueous biological media. Ligand exchange and encapsulation of QDs using hydrophilic/amphiphilic molecules or polymers are common strategies for preparing water-dispersible QDs from hydrophobic QDs.[12−15] The QDs can then be functionalized with a variety of biomolecules (e.g., proteins, antibodies, peptides, DNA, and vitamins) through established conjugation techniques. The large surface area of each QD, relative to organic dyes and other small molecules, provides many surface attachment sites for conjugation.[16−18] This opens up possibilities for multivalent binding via multiple targeting moieties. Flexibility in surface chemistry as well as in emission wavelength of bioconjugated QDs enables their use as nanoprobes or traceable nanocarriers for broad applications in biophotonics and nanomedicine, including near-IR deep tissue imaging (e.g., 700−900 nm),[19,20] PL imaging in the second near-IR window (e.g., 1000−1400 nm),[21,22] single cell detection,[23] and controlled release of drugs.[24−26] However, to date, the majority of QD-related research in biology and medicine has employed Cd-based QDs including CdSe, CdTe, CdS, and CdTe/CdSe core/shell QDs, often with additional protective shells of ZnS and/or ZnSe.[27,28] The popularity of these Cd-based QDs is primarily due to their ease of synthesis using readily available precursors and straightforward solution phase synthesis methods. Protocols for preparing and using these QDs have been somewhat standardized. They are also readily available commercially in formats optimized for specific biological assays and applications.

With the rapidly developing biological applications of Cd-based QDs, their potential toxicity has become a subject of serious discussion and debate. Some studies have demonstrated that Cd-based QDs can degrade in a biological environment, releasing highly cytotoxic Cd^{2+} ions.[29,30] Other studies suggest that the observed degradation results from the poor quality (i.e., insufficient stability or encapsulation) of the QDs employed.[31,32] Researchers ranging from biomedical engineers to clinicians have raised doubts about the possible use of Cd-based QDs for clinical applications such as in vivo diagnostics and surgery, due to toxicity concerns associated with their Cd content. At present, two approaches are being pursued to address these concerns. The first approach involves the use of one or more biocompatible and long-lasting polymeric layers to encapsulate the QDs and prevent their breakdown in vivo.[33−35] The second approach, which is arguably more challenging and time-consuming as it requires advances in material science and nanochemistry, is to create Cd-free QDs with performance comparable to or even better than existing Cd-based QDs.[36−38] Currently, many research groups are developing and applying nanochemistry methods to design and fabricate Cd-free QDs

DOI: 10.1021/acs.chemrev.6b00290
Chem. Rev. 2016, 116, 12234−12327

with tunable emission color, and are testing them in applications ranging from diagnostics, to imaging, to traceable drug delivery. Nonetheless, matching the high brightness, narrow PL emission spectrum and high PL quantum yield of Cd-based QDs remains a challenge. Even when optical properties are comparable, Cd-based QDs have the benefits of longer history and the resulting better-developed encapsulation and surface functionalization strategies and better optimized protocols for specific applications.

With advances in solution phase synthesis methods over the past few years, a variety of Cd-free QDs have been prepared from materials including indium phosphide (InP),[39−42] copper indium sulfide ($CuInS_2$),[36,43,44] silver indium sulfide ($AgInS_2$),[45,46] silver sulfide (Ag_2S),[21,47] doped Zn chalcogenides,[48,49] graphene,[50−52] and silicon.[53,54] These QDs share many of the advantages of conventional Cd-based QDs with respect to their optical properties, colloidal stability, PL stability, and surface chemistry. The QD research community has begun to use these Cd-free QDs for biological applications and evaluate their potential in numerous in vitro and in vivo models such as cultured cells, tissues, and small animals. However, additional effort will be required to improve the performance of Cd-free QDs in biomedical applications and to optimize them for specific applications. This will facilitate their adoption by mainstream biomedical researchers and, ultimately, clinicians. The synthesis of QDs and their preparation for biological applications are addressed in sections 3 and 4.

1.2. Biophotonics Applications

Biophotonics is a multidisciplinary research frontier[2] that employs light for medical diagnostics,[55] bioimaging,[56] biosensing,[57] laser tissue engineering,[58] and light activated therapy.[59] It involves the study of light activated processes, from molecular, to cellular, to tissue levels. The unique optical properties of QDs make them useful as optical probes or optically trackable biomolecule carriers for in vitro and in vivo studies.[60,61] By conjugating appropriate functional biomolecules onto their surface, one can use QDs to target specific sites in vitro and in vivo.[62−64] For example, bioconjugated QDs have been applied in targeted cell labeling,[65,66] tissue imaging,[6,67] in vivo tumor detection,[36,68] photodynamic therapy,[69,70] sensing of biomolecules,[71] monitoring the biodistribution of drugs,[25] and drug delivery.[72] Moreover, bioconjugated QDs can be used with a wide variety of optical imaging techniques such as near field microscopy, confocal microscopy, multiphoton microscopy, and coherent anti-Stokes Raman scattering (CARS) microscopy, to study structure and dynamics from cellular to tissue levels.[6,73−76] QDs have also been used in multimodal imaging studies to derive fundamental molecular-level insights into biological processes such as cell replication, transcription, translation, and apoptosis.[31,77,78] To facilitate the use of QDs for multimodal imaging, QDs can be integrated with other contrast agents (e.g., gold nanoparticles, Raman tags, gadolinium chelates, or ^{125}I radioactive labels). These probes have been engineered and studied for imaging of cells and small animals using two or more imaging modalities.[79−83] In studies to date, in vitro and in vivo biophotonic imaging and sensing studies using QDs have aimed to create an understanding of cell localization and interaction, biomolecule and drug biodistribution, mechanism of drug action, and real time monitoring of disease progression or response to a therapy. The flexibility and versatility of QDs will surely provide keys to answer critical biological and medical questions and thereby improve diagnosis and treatment of human diseases. Applications of QDs in biophotonics provide unprecedented opportunities for resolving many current challenges in disease theranostics. Section 5 focuses on applications of Cd-free QDs in biophotonics.

1.3. Applications in Nanomedicine

Nanomedicine employs specifically designed nanoplatforms to achieve minimally or noninvasive diagnosis, targeted and controlled delivery of therapeutics, improved efficacy of an existing therapy, real-time monitoring of a treatment, or evaluation of in vivo pharmacokinetics.[3,84−88] QDs have been used as nanoplatforms for targeted delivery of pharmaceutical, therapeutic, and diagnostic nanoprobes. For example, identifying specific targets (e.g., endothelial cells, tumor cells, or tumor neovasculature) using an appropriate choice of QD-based nanoprobe can guide site-specific therapy.[89−92] In vivo diagnosis using biofunctionalized QDs also offers the benefit of combining different functions into a single nanoparticle (NP) platform. For example, conjugating or coencapsulating drugs and MRI or PET imaging contrast agents with QDs allows detailed disease profiling based on molecular, structural, and morphological changes as a disease evolves.[93−96] Specific targeting of QDs to the disease site allows use of a lower dose of QD probes for diagnosis, and thereby minimizes the potential toxicity of the designed nanocarrier. QDs are expected to contribute to development of nanomedicine via design of new therapeutic modalities and by increasing the effectiveness of existing therapies. For example, QD nanoformulations can be integrated with magnetic therapy using magnetic NPs, and with photothermal therapy using metallic NPs.[94,97,98] As an example of improving the efficacy of an existing therapy, QDs can be designed as nanocarriers to alter the biodistribution and circulation of a hydrophobic drug in order to localize a large concentration of the drug at the disease site. Additional benefits offered by QD nanocarriers include controlled and sustained release of a drug.[25,99,100] The controlled release of drugs from QD nanocarriers can be achieved via external stimulation using light, magnetic fields, heat, or radio frequency stimulation.

Theranostics is an emerging paradigm that combines diagnosis with therapy to enable a see, treat, and see therapeutic modality. This can enable a clinician to follow a medical treatment, surgery, or other procedure in real time, using the same material or device for both diagnosis and therapy. Nanoparticle technology allows creation of new theranostics in a single nanoformulation. QDs with their size tunable and compositionally tunable emission and ease of surface functionalization can provide a useful platform for nanotheranostics. The optical and electronic properties of QDs provide a basis for multiplexed imaging and sensing, while surface functionalization and encapsulation enable them to carry therapeutic payloads.

The Cd-free QDs covered in this review are particularly suitable for theranostics. First, without the toxicity concerns associated with Cd, they can more readily be considered for in vivo applications. Many of the materials covered in this review are ternary semiconductors in which compositional variation can provide wide spectral tuning of optical properties, providing emission in the near-IR range to enable deep tissue imaging and optical tracking of drug or gene delivery. In some cases, their optoelectronic properties can be exploited for biosensing and functional imaging. Magnetic impurities can be introduced to provide contrast for magnetic resonance imaging. Their

DOI: 10.1021/acs.chemrev.6b00290
Chem. Rev. 2016, 116, 12234−12327

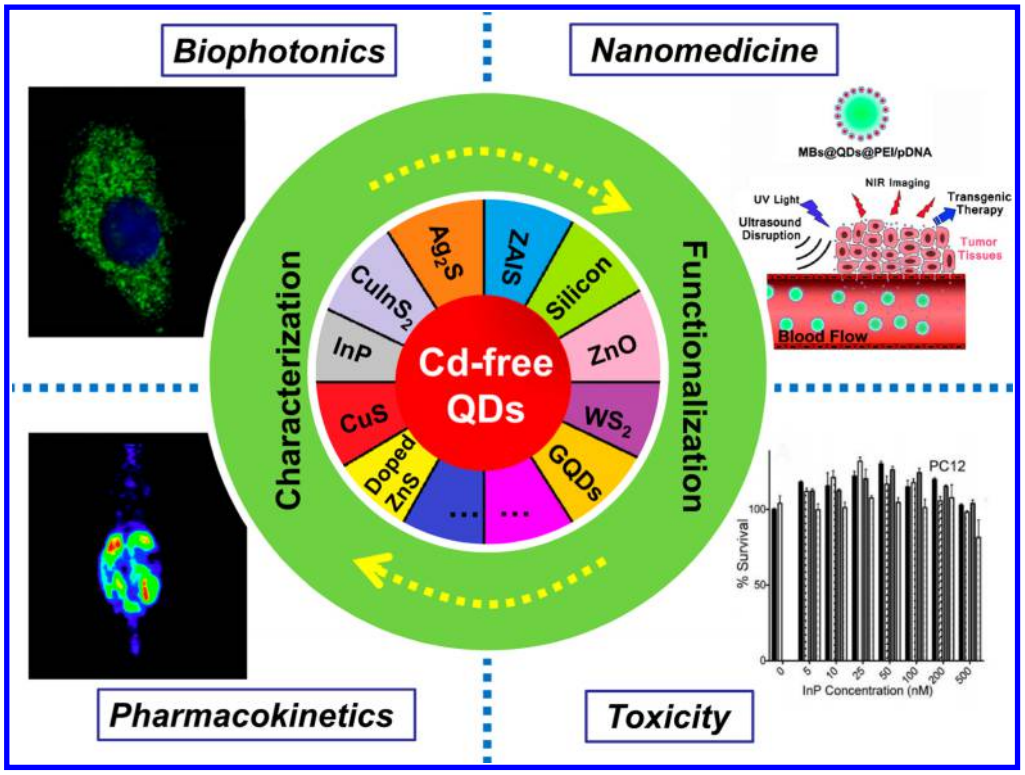

Figure 1. Cd-free QDs discussed in this review and representative applications in biophotonics and nanomedicine.

excitation dynamics can also be manipulated for use in light-induced therapies. Ease of surface functionalization enables conjugation with various therapeutic payloads such as drugs, genes, and RNA. In addition, a therapeutic agent can be coencapsulated with QDs in a biocompatible and biodegradable shell. Section 6 discusses nanomedical applications of Cd-free QDs in greater detail.

1.4. Pharmacokinetics and Biodistribution

The pattern of distribution among organs over time, i.e. the biodistribution, is a key characteristic of any nanoparticle or drug formulation. Biodistribution measurements provide key information on the accumulation of a NP formulation at the targeted site and in other sites where the accumulation may not be desirable. Several factors contribute to the specific localization of NPs in different organs, including the hydrodynamic size of NPs, plasma protein binding to NPs, hydrophobicity of the NPs, the ligands or polymers used to stabilize the NPs in the biological environment, and the types of biomolecules conjugated to the surface of NPs. Most often, biodistribution studies are carried out using radioactively or fluorescently labeled NPs that are injected into animals. Subsequently, the animals are sacrificed, and various organs are harvested and analyzed for the localization of the NPs by fluorescence, magnetic resonance, and/or nuclear imaging (e.g., PET and SPECT). Bioconjugation and size control of QDs provide the ability to create desired biodistribution patterns for specific applications using both active and passive targeting approaches. More importantly, in many cases the bright PL of QDs and the ability to combine them with other contrast agents can enable in vivo multimodal imaging in real time to monitor the biodistribution pattern. Such real-time monitoring allows rapid optimization of delivery and targeting strategies, compared to ex vivo measurements, and eliminates the animal-to-animal variability associated with sacrificing animals for ex vivo measurements at different time points. We discuss the details of biodistribution studies of Cd-free QDs in section 7.

1.5. In Vitro and in Vivo Toxicity

Toxicity of QDs is a function of many factors including not only their composition, but also their size, shape, encapsulation, and surface functionalization. Toxicity studies assess the response of specific cell types, tissues, organs, and organisms to varying doses of a given QD formulation. In the context of this review, we are concerned with the toxicity of QDs used in biophotonics and nanomedicine. Noting the importance of understanding the potential toxicity of QDs, many research teams worldwide have been devoting effort to elucidating underlying mechanisms of QD toxicity in vitro and in vivo, and many articles are being published on this subject.[31] In this review, we focus only on toxicity studies of Cd-free QDs. The toxicity of QDs is of two main types: (1) that directly associated with the intact QDs themselves and (2) toxicity associated with their chemical constituents. In the first case, the physical and surface properties of the QDs generate responses that can depend upon size, shape, surface charge, and surface coatings. Because the surface-to-volume ratio in NPs is very large, surface-initiated processes are significantly enhanced compared to larger structures. Their small size also alters immune-system response. Thus, size and shape play critical roles in determining the intact particle toxicity. In the second case, the toxicity is generated by the chemical constituents of the QDs. For example, the release of Cd^{2+} ions from CdSe or CdTe QDs can cause significant damage to cells and tissues. Because the toxicity of QDs can have multiple origins and mechanisms and depends on multiple physicochemical properties, and also because even within one formulation QDs are not all identical, assessing their toxicity can be much more complex than assessing the toxicity of a small molecule. Testing the toxicity for every possible combination of size, shape,

DOI: 10.1021/acs.chemrev.6b00290
Chem. Rev. 2016, 116, 12234−12327

composition, and surface modification of a given type of QD is generally not possible, and this can make guaranteeing the biocompatibility of a QD formulation difficult. Toxicity of Cd-free QDs is discussed in section 8.

1.6. Review Outline

This review summarizes recent progress in the design and applications of Cd-free QDs, with an emphasis on their role in biophotonics and nanomedicine (Figure 1). In addition, we discuss current challenges and opportunities faced in using these QDs for in vitro and in vivo applications. Section 2 presents features of Cd-free QDs, describing the physics and emergent optical properties of various types of Cd-free QDs whose applications are discussed in subsequent sections. Section 3 discusses specific QD systems, while section 4 covers preparation of these Cd-free QDs in a form useful for biological applications. It discusses recent advances in achieving high photoluminescence quantum yield (PL QY) and tunability of emission color, along with stable dispersion in biological media. Section 5 presents applications of Cd-free QDs for biophotonics, summarizing recent advances in biophotonic applications of Cd-free QDs, including optical imaging, photoacoustic imaging, sensing, optical tracking, photothermal therapy, and multimodal imaging. Section 6 discusses recent progress in the use of Cd-free QDs for nanomedicine applications such as drug delivery, gene delivery, protein and peptide delivery, cancer nanotechnology, image-guided surgery, diagnostics, medical devices, and drug screening. Section 7 focuses on the pharmacokinetics and biodistribution of Cd-free QDs. Section 8 summarizes recent studies on the in vitro and in vivo toxicity of Cd-free QDs. Finally, section 9 concludes by providing perspectives on the overall current status, challenges, and future directions in this field.

2. FEATURES OF CADMIUM-FREE QUANTUM DOTS

2.1. Quantum Confinement Effects

QDs are semiconductor nanocrystals whose size, in all three dimensions, is comparable to the exciton Bohr radius of the material from which they are prepared.[1] The exciton Bohr radius (a_B) is the average separation of the excited electron and hole that make up an exciton in a bulk semiconductor. In analogy to the Bohr model of the hydrogen atom, it can be written as

$$a_B = \frac{\hbar^2 \varepsilon}{e^2}\left(\frac{1}{m_e} + \frac{1}{m_h}\right) \quad (1)$$

where ε is the dielectric constant of the semiconductor, $\hbar$ is the reduced Planck constant, e is the charge of an electron, m_e is the effective mass of the electron, and m_h is the effective mass of the hole. Because the dielectric constant and effective masses of the hole and electron are material-dependent, the exciton Bohr radii for different semiconductors vary substantially (e.g., 2.3 nm for ZnO,[101] 4.1 nm for $CuInS_2$,[102] 18 nm for PbS,[103] and 46 nm for PbSe[104]). When the radius of a semiconductor nanocrystal approaches the exciton Bohr radius, the motions of the electron and hole are confined, within the particle, to dimensions smaller than in the bulk.[105] The electronic structure and optical properties of QDs differ significantly from their bulk counterparts due to this quantum confinement effect (Figure 2).[104,106−109]

The quasi-continuous states (energy bands) of the bulk semiconductor evolve into discrete levels in QDs, corresponding to hybridization of a finite number of atomic orbitals.[110] The energy gap between the bottom of the conduction band and the top of the valence band in QDs expands with decreasing size.[111] This increase in energy associated with exciton generation/recombination produces a blue shift of both absorbance and PL spectra with decreasing size. Because of the atom-like discrete structure of electronic states under strong quantum confinement, QDs are sometimes described as artificial atoms, with their discrete energy levels interpreted in a manner analogous to the discrete energy levels of an atom. The strongly size-tunable properties of QDs make them very useful for biomedical applications. Related properties of QDs, such as size-dependent Stokes shift, long lifetime of band-edge luminescence, and magnetic-field-induced lifetime shortening can also be exploited in some biophotonic and nanomedicine applications. Factors such as QD shape, lattice asymmetry, electron−hole exchange interaction, impurities, defects, and external fields affect these properties,[112−114] as well as the fine structure of their absorbance and PL spectra, especially in the strong confinement regime, in which the QD radius is significantly smaller than the exciton Bohr radius.

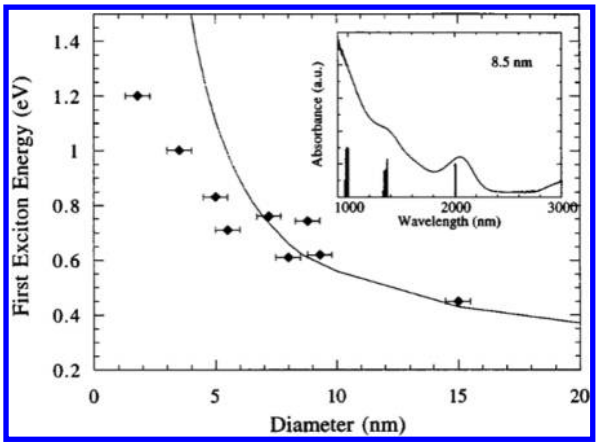

Figure 2. Measured (symbols) and calculated (line) energies of the lowest energy exciton for PbSe QDs of varying size. The inset shows the measured absorption spectrum (line) and calculated dipole transitions (bars) of 8.5 nm PbSe quantum dots. Reprinted with permission from Lipovskii et al.[104] Copyright 1997 AIP Publishing LLC.

Cadmium-free QDs typically range from 1 to 10 nm in diameter. The size dependence of optical and electronic properties is similar to that of Cd-based QDs, but varies in detail due to differences in bulk band structure, electron and hole effective masses, and other factors. The PL wavelength in Cd-free QDs can be tuned from the ultraviolet to mid-IR region by changing QD composition, size, and shape. Generally, the QD composition sets the range of wavelengths that are accessible, because quantum confinement can only produce a blue shift in the PL relative to the optical band gap energy of the bulk material. For a particular composition, the degree to which the PL emission can be tuned depends upon the Bohr radius of the material and the range of sizes that can be practically produced. Manipulating the composition and shape of the QDs requires control of the chemistry of QD synthesis and capping. For most Cd-free QDs, as for Cd-based QDs, the PL lifetimes and two-photon absorbance cross sections are much greater than those of traditional organic dyes.[115−117] These features make QDs very useful for two-photon imaging of deep tissues, with reduced autofluorescence

DOI: 10.1021/acs.chemrev.6b00290
Chem. Rev. 2016, 116, 12234−12327

background.[6,118,119] The PL lifetime and two-photon cross section, like the PL spectrum, vary with composition, size, and shape.

2.2. Core/Shell Architectures

Core/shell QD structures consist of a QD core of one semiconductor material coated by one or more shells of different composition. These have several advantages relative to single composition (core-only) QDs. Most importantly, surface-related quenching by surface defects and by solvent phonon-induced relaxation are minimized by reducing interaction between the exciton and the outer surface of the nanocrystal. In addition, the various possible relationships between energy levels in the core and shell provide control of the PL wavelength, lifetime, and QY that is not available in single-component QDs.

In general, core/shell QDs can be divided into three types based upon the band alignment of valence and conduction bands between their constituent materials (i.e., type I, type II, and quasi type II, Figure 3).[120,121] Type I (e.g., InP/ZnS and CdSe/ZnS) and type II core/shell QDs (e.g., CdTe/CdSe) are the most commonly prepared and have been widely used for biological applications. In conventional type I core/shell QDs, the conduction band of the shell is at higher energy than that of the core, whereas the valence band of the shell is at lower energy than that of the core (Figure 3a). As a result, both holes and electrons are confined within the QD core. This architecture has been widely applied in recently developed Cd-free QDs, e.g., InP/ZnS, $CuInS_2$/ZnS, $AgInS_2$/ZnS, and ZnSe/ZnS core/shell QDs. Encapsulation of a core QD in a higher band gap material to create a type I core/shell QD can greatly reduce nonradiative recombination, thereby dramatically increasing PL QY. For example, Kang et al. improved the QY of $AgInS_2$ QDs from 3.6−11.6% to 18.4−39.1% by adding a ZnS shell.[45] Similarly, Chen et al. observed a QY increase from 1.4 to 48% upon adding a ZnS shell to $CuInS_2$ QDs.[122] ZnS has been the most common shell material in type I core/shell QDs. A key advantage of this type I architecture is enhanced stability and prolonged shelf life due to the high chemical stability of ZnS. In type II QDs, both the conduction and valence bands are at higher energy in one material than in the other (Figure 3b). Thus, one carrier type (electron or hole) is mainly confined to the core while the other is mainly confined to the shell. This spatial separation of carriers can produce properties that are quite different from those of type I QDs. Type II QDs can be prepared to emit at near-IR wavelengths using materials with band gaps that are too wide to provide near-IR emission in a type I QD structure. Typical Cd-based type II QDs include CdSe/CdTe and CdSe/ZnTe core/shell QDs, which exhibit near-IR (NIR) emission due to electron−hole recombination across the core/shell interface.[123]

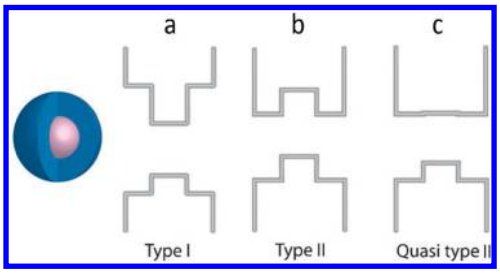

Figure 3. Schematic band diagrams of representative core−shell QDs: type I (a); type II (b); quasi type II (c). Adapted with permission from Deutsch et al.[120] Copyright 2011 Royal Society of Chemistry.

Recently, a handful of studies have explored preparation of Cd-free type II QDs.[124,125] Bang et al. prepared ZnTe/ZnSe QDs with PL colors from blue to amber by simply varying the shell thickness (Figure 4).[124] This sensitivity of PL emission wavelength to shell thickness is a characteristic of type II core/shell QDs. Another distinguishing feature of type II QDs is their extended exciton lifetime. However, compared to type I

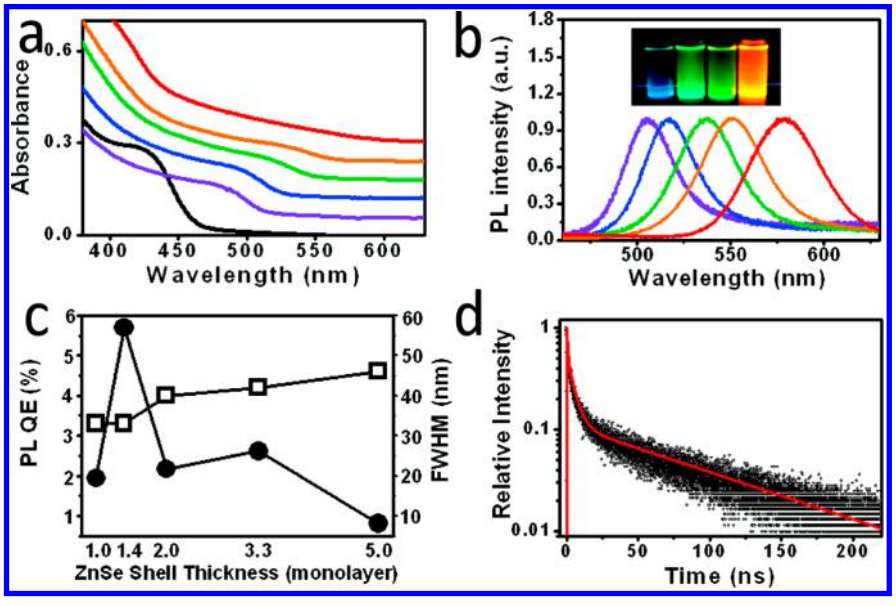

Figure 4. (a) Absorption and (b) emission spectra of ZnTe cores (black), ZnTe/ZnSe core/shell QDs that have the same ZnTe cores and 1.0 (violet), 1.4 (blue), 2.0 (green), 3.3 (orange), and 5.0 (red) monolayers of ZnSe shells. The inset in (b) shows various ZnTe/ZnSe (core/shell) QD samples under UV illumination. (c) Photoluminescence quantum efficiencies (PL QEs, closed circles) and full widths at half-maximum (fwhm's, open squares) for ZnTe/ZnSe QDs. (d) Room-temperature normalized photoluminescence decay of ZnTe/ZnSe QDs dispersed in hexanes. Reprinted from Bang et al.[124] Copyright 2010 American Chemical Society.

DOI: 10.1021/acs.chemrev.6b00290
Chem. Rev. 2016, 116, 12234−12327

QDs, most type II QDs exhibit lower QY. Carrier separation slows radiative recombination due to reduced overlap of the hole and electron wave functions, extending the lifetime of the exciton. However, this longer radiative lifetime inherently increases the time during which nonradiative recombination can occur, lowering QY.

In an exception to the general rule of low QY from type II core−shell QDs, Tyrakowski et al. achieved bright type II QDs with 61% QY based on a novel ZnSe/CdS/ZnS structure. In this case the intermediate CdS shell has a type II alignment with the ZnSe inner core and a type I alignment with the ZnS outer shell.[126] Interestingly, the high QY was found to be a result of increased radiative recombination rate, rather than suppression of defect-related nonradiative recombination. In another study, Soni et al. synthesized CdSe/CdS/ZnSe QDs that could achieve both type I and type II emission simultaneously.[127] Investigation of their optical properties demonstrated that the intermediate CdS layer formed a type I structure with the inner CdSe core while it also formed a type II structure with the outermost ZnSe shell. While these two examples are for Cd-containing structures, the principles demonstrated in them are applicable to Cd-free core−shell QDs as well.

In addition to band alignment, several other factors should be considered when designing and synthesizing core/shell QDs. In general, reaction conditions during shell growth, including the reaction temperature, precursor concentration, ligand identities and concentrations, and shell precursor injection rate must be optimized and controlled to obtain core/shell QDs without nucleation of separate NPs of the shell material, formation of "dumbbell"-like heterodimers, or undesired alloying of the core and shell materials. The core and shell materials must have commensurate crystalline structures and tolerable lattice mismatch. Large lattice mismatch induces strain at the core/shell interface, which can be relieved by defect formation, or can even cause a strain-induced transition between the type I and type II band alignment.[128] Lattice mismatch is an important parameter for evaluating the feasibility of shell growth on a given core material. Large lattice mismatch (>12%) typically makes epitaxial growth of a shell difficult and leads to the formation of many interface defects that degrade the optical properties of the QDs,[129,130] or even to the formation of separate NPs of the shell material. Effects of lattice mismatch can be partially ameliorated by growth of an intermediate layer between the core and shell to form multishell QDs, e.g. CdSe/CdS/ZnS QDs and CdSe/ZnSe/ZnS QDs. In analogy to these multishell Cd-based QDs, Ippen et al. developed Cd-free InP/ZnSe/ZnS QDs with 50%−70% QY.[131] ZnSe has a lattice constant between those of InP and ZnS, making it useful as a buffer material or "lattice adapter" in that study. The multishell, or "sandwiched" InP/ZnSe/ZnS QDs showed improved PL intensity compared with InP/ZnS QDs.

2.3. Tunability in the Biological Transparency Window

A major limitation in the application of UV and visible light based biotechnology is the very limited penetration of light of these wavelengths through most tissues. Effects limiting light propagation through biological media include both absorption by its constituent materials and scattering by the many heterogeneous structures present in tissues. Both effects are strongly wavelength-dependent. Figure 5 shows the attenuation coefficient vs wavelength for typical biological media. There are two optical transmission windows in the IR region where the attenuation is minimized. Transmission window I is from 650 to 950 nm, and transmission window II is from 1000 to 1350 nm.[132]

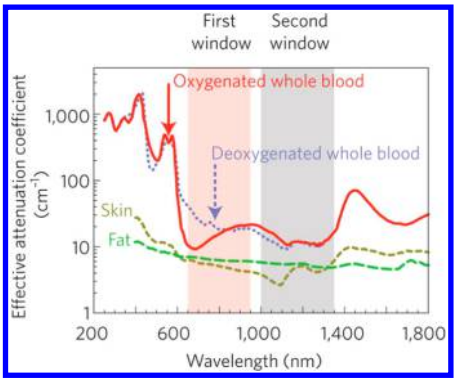

Figure 5. Effective attenuation coefficient (on a logarithmic scale) versus wavelength in a typical biological medium. Absorption and scattering from oxygenated blood, deoxygenated blood, skin and fatty tissue is lowest in either the first (pink) or second (gray) near-IR window. Reprinted with permission from Smith et al.[132] Copyright 2009 Nature Publishing Group.

Many Cd-free QDs are based on narrow band gap semiconductors. Their band gaps can be tuned by varying composition and size so that the QDs both absorb and emit at near-IR wavelengths where attenuation in tissues is minimized. Chalcopyrite $AgInS_2$, with 1.87 eV band gap, and $CuInS_2$, with 1.55 eV band gap, can emit in the first NIR transmission window. Recently, Dai and co-workers prepared $AgInS_2$ QDs with PL emission peak tunable from 650 to 850 nm by varying the Ag:In precursor ratio. The blue shift of the absorbance and PL spectra upon decreasing the Ag content was attributed to lowering of the valence band maximum.[133] Several studies of $CuInS_2$ QDs found similar effects of composition on absorbance and emission wavelengths, while other studies reported the size dependence of their optical properties. Chen et al. observed a blue shift of the PL peak of $CuInS_2$ QDs from 760 to 650 nm upon decreasing the Cu:In ratio from 1.6 to 0.3.[134] In another study on $CuInS_2$ QDs, Li et al. obtained bright $CuInS_2$ QDs with PL emission tunable from 630 to 780 nm by controlling the size while fixing the Cu:In ratio close to 1:1.[135] The emission wavelengths of $CuInS_2$ and $AgInS_2$ can be further tuned to longer wavelengths through substitution of S by Se. In both materials, Se substitution narrows the band gap, producing a red shift of the PL. Allen et al. obtained Cu−In−Se QDs with PL emission peaks from 650 to 975 nm.[173] They also achieved similar tunable PL by optimizing the synthesis of Ag−In−Se QDs. Cassette et al. fabricated Cu−In−Se/ZnS QDs with PL from 700 to 1030 nm by varying the synthesis temperature.[136] Another strategy for tuning emission of these ternary I−III−VI QDs is to incorporate Zn to generate quaternary QDs. For example, Deng et al. tuned the emission of Zn−Ag−In−Se QDs from 660 to 800 nm by varying the Zn:Ag precursor ratio from 5:0.5 to 0.5:2.[137]

Compared to the NIR-I transmission window, the NIR-II window can provide improved signal-to-noise ratio in bioimaging due to minimal biological autofluorescence as well as reduced scattering.[132] Ag_2S and Ag_2Se QDs are promising optical probes for use in the NIR-II window. Jiang et al. fabricated Ag_2S QDs with tunable PL from 690 to 820 nm. To extend the emission to longer wavelengths, they used their NIR-I emitting Ag_2S QDs as seeds for a second growth process

DOI: 10.1021/acs.chemrev.6b00290
Chem. Rev. 2016, 116, 12234−12327

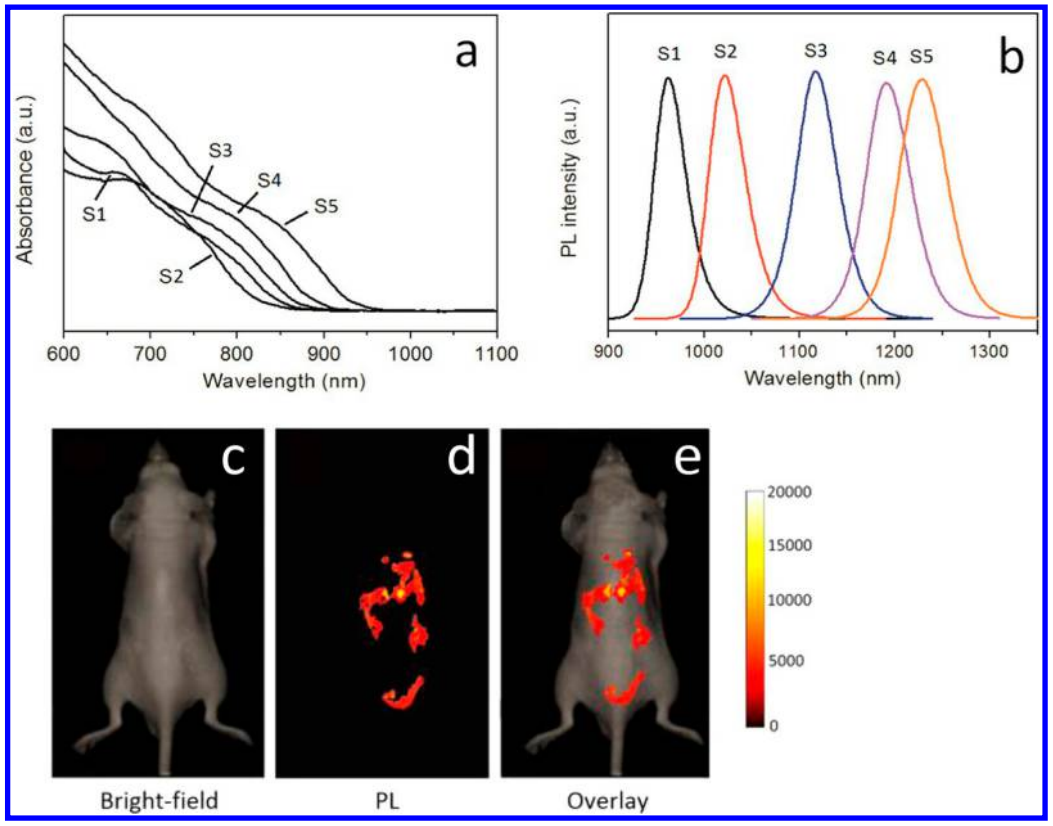

Figure 6. (a) Visible−NIR absorption and (b) emission spectra of multidentate polymer capped Ag_2Se QDs produced at different reaction times (S1−S5: 0.5, 1, 1.5, 2, and 3 h). (c) Bright-field image, (d) in vivo PL image, and (e) overlaid images of a nude mouse 12 h after tail vein injection of Ag_2Se QDs. Reprinted from Tan et al.[22] Copyright 2014 American Chemical Society.

that produced larger Ag_2S QDs with PL in the NIR-II range (1227 nm).[138] Tan and co-workers produced Ag_2Se QDs with visible-NIR absorption (Figure 6a) and 966−1228 nm PL with a narrow spectral width (Figure 6b).[22] The multidentate polymer capped Ag_2Se QDs were administered to nude mice and provided good in vivo image contrast in the NIR-II range (Figure 6c−e). Using Ag_2Se QDs with emission centered at 1300 nm, Dong et al. performed an in vivo imaging study in mice and achieved high-resolution imaging of both the vascular structure and organs at a depth of ∼100 μm, demonstrating the potential of these NIR Ag_2Se QDs for use in deep imaging applications.[139]

2.4. Opportunity To Introduce Tunable Plasmonic Features

Some of the QDs discussed here can be prepared with a nonstoichiometric ratio of constituents (i.e., can be vacancy-doped) or can be doped with impurity atoms to produce a high concentration ($>10^{21}$ cm^{-3}) of free charge carriers, either holes or electrons. Such degenerately doped semiconductor nanocrystals can exhibit localized surface plasmon resonance (LSPR), derived from oscillations of free charge carriers, at near-IR wavelengths. LSPR absorbance and scattering in these nanocrystals can be used in many biological applications. Moreover, when they are sufficiently small, quantum confinement effects can produce quantized excitonic states, in addition to LSPR, in these degenerately doped QDs. In one of the first examples of such materials, free carrier-doped Cd-free QDs exhibiting LSPR were fabricated by Luther et al.[140,141] This discovery enabled the generation of LSPR at wavelengths up to 1800 nm in Cd-free QDs with an average size smaller than 5 nm. In comparison to noble metal nanostructures with near-IR LSPR (>50 nm in at least one dimension) that have been employed for in vivo photothermal therapy and photoacoustic imaging, these smaller QDs can allow rapid excretion and better circulation/biodistribution profiles, while providing similar optical performance. Moreover, these plasmonic QDs maintain their excitonic absorbance, which is also subject to quantum confinement. Kriegel et al. studied the plasmonic and excitonic properties of copper chalcogenide QDs, showing the coupling between the excitonic and plasmonic modes.[142] Doping of the Cu_2E (E = S, Se, or Te) QDs, by oxidizing them to generate oxygen vacancies and free holes, creates $Cu_{2-x}E$ QDs that exhibit LSPR. However, the PL of the stoichiometric Cu_2E QDs decreases in intensity and ultimately disappears as the doping level increases. The high hole concentration in the QDs enables Auger-like nonradiative recombination of excitons. Thus, while having both PL and LSPR from the same QDs is unlikely, one can imagine QDs that initially exhibit efficient PL but, upon oxidation, show PL quenching and the appearance of LSPR absorbance. This could enable interesting combinations of short-term optical and longer-term photoacoustic imaging methods.

2.5. Doping To Achieve Enhanced Emission from Dopant States

The finite dimensions of QDs lead to relaxation of the *k*-selection rule in indirect band gap semiconductors as well as significant enhancement of oscillator strength due to the overlap of the electron and hole wave functions. This can produce efficient PL from materials that are not ordinarily considered good light emitters. Confinement of excitons also produces more efficient photosensitization of impurity bands,

DOI: 10.1021/acs.chemrev.6b00290
Chem. Rev. 2016, 116, 12234−12327

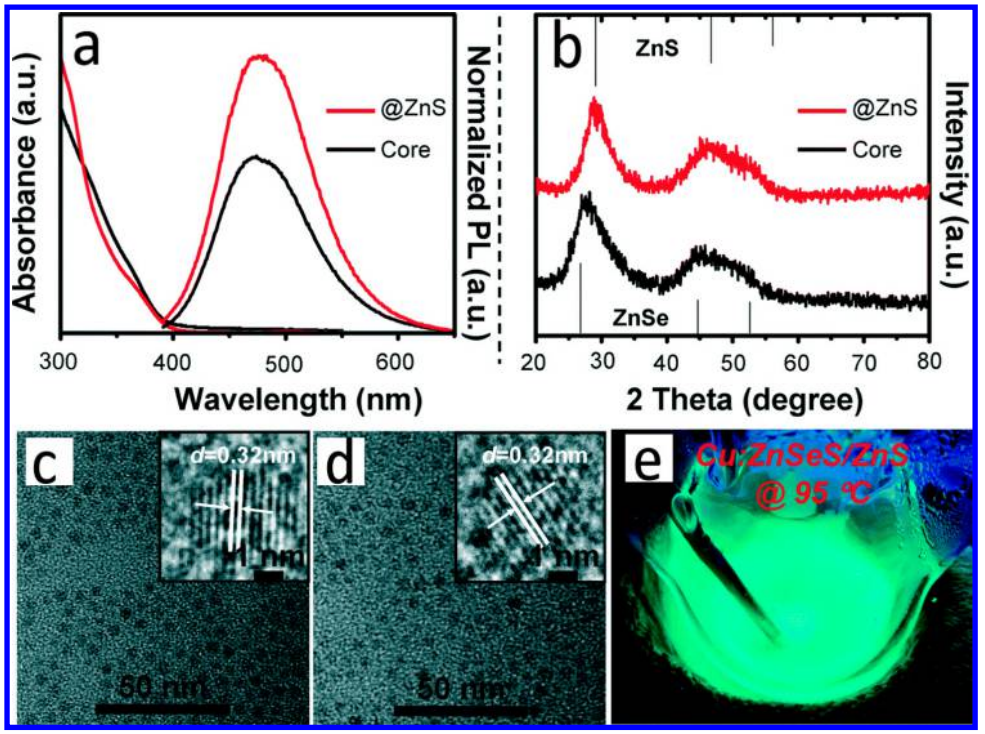

Figure 7. (a) Absorbance and emission spectra and (b) XRD patterns of Cu:ZnSeS and Cu:ZnSeS/ZnS QDs. TEM images of (c) Cu:ZnSeS and (d) Cu:ZnSeS/ZnS QDs, and (e) a photograph of Cu:ZnSeS/ZnS QDs under a 365 nm UV lamp at 95 °C. Reprinted with permission from Zeng et al.[144] Copyright 2014 Royal Society of Chemistry.

allowing for high QY emission from impurity states introduced by dopant atoms. Such doped QDs can also produce multiple emission peaks, which can be useful for multichannel bioimaging. For instance, zinc chalcogenides (i.e., ZnS and ZnSe) doped with Cu, Mn, Eu, or Ga have attracted attention for biophotonic applications due to their large Stokes shifts, which minimize reabsorbance of emitted photons. Cooper and co-workers[143] prepared codoped core/shell ZnSe/ZnS QDs using Cu^{+} as a primary dopant with trivalent codopants including Al^{3+}, Ga^{3+}, and In^{3+}. The peak emission wavelengths ranged from 430 to 570 nm with a narrow full width at half-maximum (fwhm) of ~80 nm. The codopant strategy combined with a novel bidentate thiol ligand led to a significant improvement of both the PL intensity and the shelf life of the QDs. The authors explained that the tunability of the emission arises from changes in donor and acceptor energy levels. Specifically, the trivalent codopant provided donor states within the band gap while acceptor states were provided by the Cu dopant. Emission arose from recombination of donor−acceptor pairs (DAPs), whose energy varied with codopant identity. Note that, in general, quantum confinement effects change both the band energies of the host semiconductor and the energies of donor and acceptor states relative to the band edges and to one another.

Zeng et al. reported aqueous synthesis of Cu-doped ZnSeS/ZnS core/shell QDs with a high PL QY of 40% (Figure 7).[144] The QDs showed good stability, retaining 90% of their initial PL intensity after 30 days of continuous air exposure. The outer ZnS shell not only helped to confine excitons to the core, but also served as a passivation layer to prevent photodegradation. PL saturation at higher Cu content was attributed to defect formation and increased Cu−Cu interactions. The emission also red-shifted with increasing Cu doping. Doping of QDs with Mn^{2+} can similarly produce dopant-related PL. Song et al.[125] found that the QY of Mn^{2+}-doped core/shell ZnTe/ZnSe QDs improved from 5.3% for undoped QDs to 7% for Mn^{2+}-doped QDs. The PL emission from the doped QDs was dominated by the dopant-related emission, peaking at 593 nm, rather than the host emission near 450 nm.

2.6. Magnetic Doping To Introduce Magnetic Imaging Capability

QDs can be endowed with magnetic functionality to provide contrast in magnetic resonance imaging (MRI), thereby achieving multimodal imaging with a single nanostructure. Magnetic functionality generally originates from paramagnetic ions or magnetic nanoparticles that are incorporated within or linked to the QDs. MRI plays a critical role in clinical diagnostics, because it allows monitoring of morphological changes of soft tissues at the whole organism level.[145,146] MRI is commonly employed for profiling the state of a disease or injury.

MRI relies on the nuclear magnetic resonance of spin states of hydrogen protons present in water. When a paramagnetic contrast agent is introduced and accumulates in the tissue of interest, it produces changes in the spin−lattice relaxation (T_1 contrast) and/or the spin−spin relaxation (T_2 contrast) dynamics of protons in nearby water molecules.[147,148] This change allows one to differentiate the tissue of interest from others. Contrast agents are called either T_1 or T_2 agents, depending on whether the relative change in relaxation times is greater for T_1 or T_2. The performance of the contrast agent is described by its relaxivity (r_1 or r_2), which is the change in $1/T_1$ or $1/T_2$ of protons per unit concentration of the contrast agent.[149] Typical paramagnetic ions used as contrast agents include manganese (Mn^{2+}) and gadolinium (Gd^{3+}).[150,151] A QD formulation containing such ions can have advantages including targeted delivery to the tissue of interest for

DOI: 10.1021/acs.chemrev.6b00290
Chem. Rev. 2016, 116, 12234−12327

improving MRI contrast and reduced toxicity of the paramagnetic ions, when they are embedded within the QDs. Note that caution must be exercised in comparing relaxivity values between studies, because they are reported using different definitions and measurements of concentration. Some studies report relaxivity in terms of the concentration of paramagnetic ions, while others use the concentration of QDs. The relaxivity per QD is larger than the relaxivity per ion simply because each QD can host many ions.

An example of a QD formulation containing Mn is Mn-doped ZnS in which the manganese ions within the QDs influence the relaxation times of protons in the water surrounding them.[152] Another type of formulation prepared by our group utilizes Mn:ZnSe/ZnS/ZnMnS sandwiched QDs for combined MRI and optical imaging (Figure 8).[153] In this

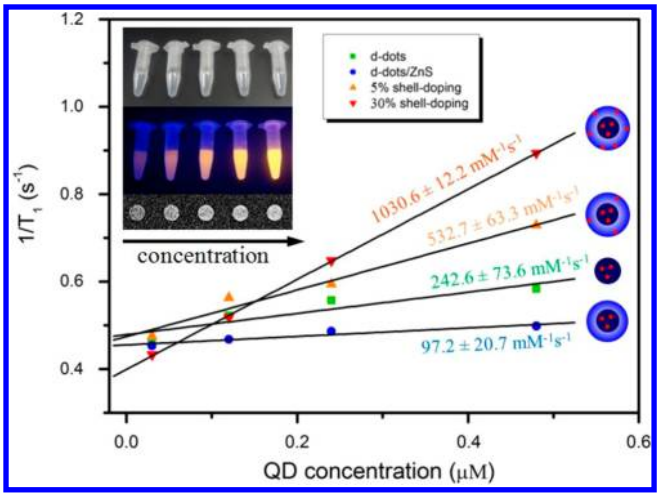

Figure 8. T_1 relaxation rate ($R_1 = 1/T_1$) plotted against Mn:ZnSe/ZnS/ZnMnS QD concentration. Insets are MR images and photographs of the QD samples under room light and UV excitation. Adapted from Wang et al.[153] Copyright 2016 John Wiley and Sons.

core/shell codoped system, paramagnetic Mn^{2+} ions are employed in the core to produce Mn photoluminescence while those in the shell provide the MRI contrast. The T_1 relaxivity of the nanocrystals can be enhanced by raising the shell doping level. Under optimized conditions, a T_1 relaxivity of r_1 = 1030.6 mM^{-1} s^{-1} can be produced by these Mn-doped nanocrystals. By packaging these QDs within liposomes and conjugating them with folic acid, our group was able to use these sandwiched QDs for MR imaging of Panc-1 tumor cells, capturing excellent MR signals from the treated tumor cells.

Mn-doped ZnS QDs, designed and prepared by Jahanbin et al. for MR imaging,[154] generated T_1 contrast enhancement that could be manipulated by changing the Mn dopant content, at concentrations below 0.1 mM. $CuInS_2$–$Zn_{1-x}Mn_xS$ core/shell QDs[155] displayed a T_1 relaxivity of r_1 = 7.2 mM^{-1} s^{-1}. MR imaging of BXPC-3 cells showed that the Mn concentration in the nanocrystals was sufficient to generate MR contrast from QDs taken up by the cells. Similarly, $CuInS_2$@ZnS:Mn QDs[156] with a gradient of Zn concentration in the core showed reduced Mn-based quenching of PL. This architecture optimized both the optical and magnetic functionalities of the QDs.

Another type of copper-based QD formulation for MR imaging is Gd-doped CuInS/ZnS.[157] Gd doped into the QD matrix produced MR relaxivity. The QDs were packaged within PEGylated dextran–stearic acid polymeric lipid vesicles for in vivo imaging experiments. The QDs possessed excellent near-IR PL and relatively high T_1 relaxivity in water. In vivo experiments demonstrated application of these QDs for targeted MR imaging of tumors. Based on a similar concept, Zheng et al. reported water-dispersible Gd-doped $CuInS_2$ QDs.[158] Their QDs had a reasonable T_1 relaxivity of 12.84 mM^{-1} s^{-1}, and further engineering these particles to incorporate targeting ligands and drugs may allow their use as dual optical and MR probes.

ZnO is another promising QD host for incorporation of Gd ions. Gd-doped ZnO QDs have been engineered for MR imaging.[94] The size of these nanoparticles ranged from 4 to 6 nm, implying that they may be cleared from the body through renal filtration. In MRI studies, these particles exhibited a large T_1 relaxivity of 16 mM^{-1} s^{-1}. Subsequently, these particles were used for MR imaging of HeLa cells. The T_1-weighted MR image of HeLa cells treated with QDs was much brighter than that of untreated ones, demonstrating that the QDs were indeed being taken up by the HeLa cells.

Zn–Cu–In–(S,Se)/$Zn_{1-x}Mn_xS$ core–shell QDs are another type of nanocrystals with magnetic functionality that can be used for MR imaging.[159] The incorporation of Mn ions into the QDs makes them paramagnetic. These QDs have T_1 relaxivities[159] up to 1400 mM^{-1} [QD] s^{-1} at 7 T and 300 K. They were applied for MR imaging of regional lymph nodes in mice.

2.7. Relationship of Quantum Dot Physics, Properties, and Applications

Before moving on, we briefly summarize the relationship between the QD physics described in the preceding subsections, the resulting properties, and the applications that depend on those properties, as illustrated schematically in Figure 9. The defining feature of QDs, whether Cd-based or Cd-free, is their size-dependent electronic band structure, which allows them to exhibit narrow, tunable PL emission spectra combined with broad PL excitation spectra. Core–shell structures are often employed to enhance this feature, by tuning the confinement and providing a high-quality (defect free) interface between the QD core and its immediate surroundings.

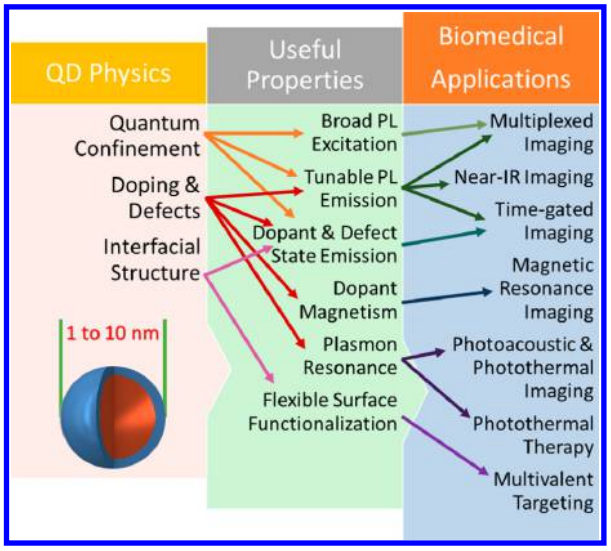

Figure 9. Schematic illustration of the relationships between the physics associated with quantum dot structures, the resulting QD properties, and biomedical applications enabled by these properties.

DOI: 10.1021/acs.chemrev.6b00290
Chem. Rev. 2016, 116, 12234–12327

When the semiconductor from which the QDs are prepared has a narrow band gap, the PL emission can be tuned to match the NIR windows in which tissue absorbance and scattering are minimized. Together, these properties allow multiplexed and NIR optical imaging by a variety of imaging modalities in contexts from single cells to live animals. One can also employ QDs as hosts for dopants. Dopants or defects can lead to emissive states that provide another means of accessing NIR emission, or can introduce magnetic features that provide MRI contrast for multimodal imaging. Very high dopant concentrations can produce NIR LSPR absorbance, opening up an additional range of applications including photoacoustic and photothermal imaging and photothermal therapy. Finally, the size range of QDs allows their surface to accommodate multiple targeting groups, which can be identical or different, to enable multivalent targeting of particular biomolecules, cells, and tissues that is not possible with smaller structures, such as molecular dyes.

3. SELECTED QUANTUM DOT SYSTEMS

This section describes the different types of Cd-free QDs that have been studied for biological applications (discussed in sections 5 and 6) in recent years. Table 1 summarizes the various materials, material properties, and key references discussed in the subsequent sections.

3.1. InP and InP/ZnS Quantum Dots

QDs of group III−V semiconductors, particularly InP QDs, are generally more robust and stable than QDs of II−VI materials such as CdSe, because the bonding in III−V materials is less ionic and more covalent than in II−VI QDs.[37,186−190] However, the PL intensity and the QY of InP QDs have generally been lower than those of CdSe and other II−VI QDs, due to less effective passivation of dangling bonds and surface defects.[191−194] To overcome this challenge, the InP core QDs can be coated with a shell of a wider band gap semiconductor like ZnS or ZnSe. Tessier et al.[161] produced InP/ZnSe and InP/ZnS core/shell QDs with emission peaks tunable from 510 to 630 nm and narrow full widths at half-maximum (fwhm's) ranging from 46 to 63 nm (Figure 10). The bare core InP QDs, 3.2 nm in diameter, showed negligible PL. However, their absorbance spectra showed two excitonic features separated by 0.3 eV. The first excitonic absorbance peak of InP core QDs was at 570 nm. The two excitonic features correspond to the two transitions from the highest occupied state (h1, HOMO) to the first and second unoccupied states (e1 and e2, LUMO and LUMO + 1). After coating the InP QDs with a 1.5 nm ZnS shell, the first exciton transition was red-shifted by 60 meV, and the PL QY increased to 60%. The emission line width was 56 nm. The size of the resulting InP/ZnSe QDs with the same precursor concentration was larger than that of InP/ZnS QDs due to a smaller lattice mismatch of 3.2% between InP and ZnSe. The smaller band gap of 2.7 eV for ZnSe compared to 3.6 eV for ZnS led to a larger red shift of the first exciton transition, by 120 meV, due to weaker confinement by the ZnSe shell. The resulting InP/ZnSe had a narrower emission fwhm of 48 nm and a slightly lower QY of 50%. The authors attributed the narrower emission to the lower lattice mismatch between InP and ZnSe (3.2%) than that between InP and ZnS (7.7%). Moreover, a broadened fwhm up to 70 nm and increased QY up to 80% were observed in the InP/ZnS QDs upon further increasing the shell thickness. Increasing the shell thickness of InP/ZnSe QDs only increased the QY. These results revealed the advantage of a ZnSe shell relative to a ZnS shell for maintaining narrow emission spectra.

The temperature dependence of PL emission from InP/ZnS QDs was studied by Narayanaswamy and co-workers.[195] They focused on the band gap change, i.e., the energy change of the e1−h1 (HOMO−LUMO) transition over a temperature range from 300 to 525 K. They showed that the energy decreased as the temperature increased, due to coupling between the e1−h1 exciton and acoustic phonon modes. The experimental results were fit with an empirical function from which the average phonon energy and Huang−Rhys factor were derived. The fwhm of the QD PL spectra broadened with increasing temperature, and this broadening was analyzed with an equation that described the temperature dependence of the energy of the lowest-lying exciton. For a fixed temperature of 300 K, the absorption and PL peaks red-shifted with increasing QD size. The Stokes shift, defined as the energy difference between the first absorbance and PL peaks, increased with decreasing QD diameter as 101.3, 133.6, and 191.2 meV for InP/ZnS with diameters of 3.2, 2.8, and 2.3 nm (Figure 11).

Copper-doped InP/ZnS core/shell QDs were fabricated by Zhang et al. to achieve broadband emission from visible to near-IR wavelengths under a single excitation wavelength.[196] Their Cu-doped InP/ZnS/InP/ZnS core/barrier/quantum well/shell QDs had two PL peaks that respectively resulted from the Cu-doped InP core and the InP quantum well layer. The dual emission peaks were tuned by changing the core size and the thickness of the quantum well. The ZnS layer inside the QDs was placed between the InP core and the InP quantum well and worked as a barrier to decouple the QD core and the quantum well. The outer layer of ZnS at the QD surface enhanced the QY and photostability of emission from the quantum well. The PL peak of the Cu-doped InP core (1.8 nm) at 690 nm was unchanged upon coating with 3 monolayers of ZnS (to 3.8 nm diameter) and then 1.5 layers of InP (to 4.9 nm diameter) to form Cu:InP/ZnS/InP. The new PL peak at 530 nm was obtained only upon surface passivation of the InP quantum well layer by growth of the outer ZnS shell, which increased the overall QD diameter to 6.2 nm. The lifetime of the first PL peak was measured to be 499 ns, which is much longer than that of the second PL peak of 46 ns. The large lifetime difference confirmed the role of the ZnS barrier in decoupling of the dual emission channels in the particle. By changing the thickness of the InP quantum well layer from 0.35 to 1.2 nm, the second PL peak could be tuned from 480 to 600 nm. In addition, the first PL peak could be tuned from 600 to 800 nm by only changing the diameter of the core InP QD from 1.5 to 2.6 nm. This illustrates the effect of quantum confinement on the energy of the Cu dopant states in the QD.

Recently, Thomas and co-workers[197] systematically studied the Förster resonance energy transfer (FRET) from InP QDs to different fluorescent dyes including rhodamine 101 (Rh101), Texas red cadavarine C5 (TxRed), and lissamine rhodamine B ethylene diamine (LiRh). The efficient energy transfer observed in that study illustrates the potential of InP QDs for harvesting energy in biophotonics and photovoltaics. Chemical groups like the amine groups on TxRed and LiRh and the carboxyl group on Rh101 can coordinate directly to the QD surface. From the steady-state and time-resolved emission spectra, large quenching constants of 10^{13}−10^{14} M^{-1} s^{-1} were observed upon anchoring of the dyes to InP/ZnS core/shell QDs. A rapid PL decay followed by increased acceptor emission with a rise time of 200 ps was observed under 405 nm excitation. Thus, the

DOI: 10.1021/acs.chemrev.6b00290
Chem. Rev. 2016, 116, 12234−12327

Table 1. Summary Cd-Free QD Types, Properties, and Synthesis Methods

QD type[a]	exciton Bohr radius[b] (nm)	bulk band gap (eV)	synthesis method	size[c] (nm)	emission wavelength (nm)	quantum yield	ref
InP	20	1.35	hot colloidal	2.8	480−750	1−30%	160
			hot colloidal	2.8−3.2	_	not luminescent	161
InP/ZnS	_	1.35	hot colloidal	4.5	480−735	up to 60%	160
			hot colloidal	6	510−630	up to 80%	161
$CuInS_2$	4.1	1.5	hot colloidal	2−4	630−780	5−10%	135
			hot colloidal	2.5	620−870	up to 18%	36
			hydrothermal	2.2	660	3.3%	162
$CuInS_2$/ZnS and ZnS−$CuInS_2$	_	1.5−3.7	hot colloidal	7	550−815	up to 60%	163
			hot colloidal	4	550−800	20−80%	36
			continuous flow	3.0	432−615	up to 40%	164
			hydrothermal	3.8 ± 0.3	543−625	20−38%	165
			microwave	3.3	540−680	up to 24%	166
$AgInS_2$	5.5	1.87	hot colloidal	2.5−4.3	770−855	36−63%	167, 168
$AgInS_2$/ZnS and ZnS−$AgInS_2$	_	1.87−3.7	hot colloidal	1.4−5.2	620−815	1.5 ± 0.1%	169
			thermal decomposition	4.1−4.4	540−720	up to 24%	170
			sonochemical	12 ± 1.3	480−700	57.6−336% relative to CdSe/ZnS	171
Cu_2S	3−5	1.2	sonoelectrochemical	12.1−18.1	NIR Abs peak >1100 nm		172
			hot colloidal	2.5−6	NIR Abs peak >1796 nm		140
$CuInSe_2$	10.6	1.04	hot colloidal	2−3.5	650−975	up to 25%	173
Ag_2S	2.2	0.9−1.1	hot colloidal	5.6	1200	16%	174
			hot colloidal	1.5−4.6	690−1227	0.18%	138
			hydrothermal	2.6−3.7	687−1096	14.2−16.4%	73
			hydrothermal	1.5−6.3	510−1221	up to 2.1%	8
Ag_2Se	2.9	0.15	aqueous at room temperature	3.4−5.9	966−1228	11.1−12.2%	22
			hot colloidal	3.4	1300	29.4% after phase transfer	139
ZnS−$AgInSe_2$	_	1.2−3.7	hot colloidal	5	660−800	up to 50%	137
Mn:ZnSe	4.5	2.7	hydrothermal	3.8	410, 480, 570	2.4%	175
			hydrothermal	7.0	400, 480, 590	up to 17%	153
Mn:ZnS	2.5	3.7	hot colloidal	3.8 ± 0.2	585	51.3%	176
Cu:ZnS	2.5	3.7	hydrothermal	_	482	4.2%	48
ZnSe/InP/ZnS	_	2.7	hot colloidal	5.4	430−610 (for ZnSe/InP)	60%	177
silicon	4	1.1	pulsed laser ablation	4	450	0.4%	178
			microemulsion	3.5−4.3	420−280	5.2%	179
			gas phase	2.8−5.2	700−1000	0.3−10.2%	180
ZnO	2.3	3.3	sol−gel	2.85−12.16	450−550	23−61%	181
			sol−gel	3−4	520−550	20−50%	182
WS_2	_	1.35	chemical exfoliation	8−15 (lateral)	369−461	4%	183
graphene	infinite	0	hydrothermal	5−25	377−493 (Exc: 300−400)	28%	184
			pyrolysis	4.66 ± 1.24	415−580 and 800−850 (Exc: 320−540)	up to 54.5%	185

[a]For simplicity, ideal chemical formulas are provided to represent the QDs even when the actual QDs are not stoichiometric; e.g., Cu_2S can represent Cu_xS and $CuInS_2$ can represent Cu_xIn_yS. [b]For doped QDs, the Bohr radii of the host materials are provided. [c]Sizes from TEM imaging or calculated from absorption spectra are given here. Hydrodynamic diameters in solution are inevitably larger.

DOI: 10.1021/acs.chemrev.6b00290
Chem. Rev. 2016, 116, 12234−12327

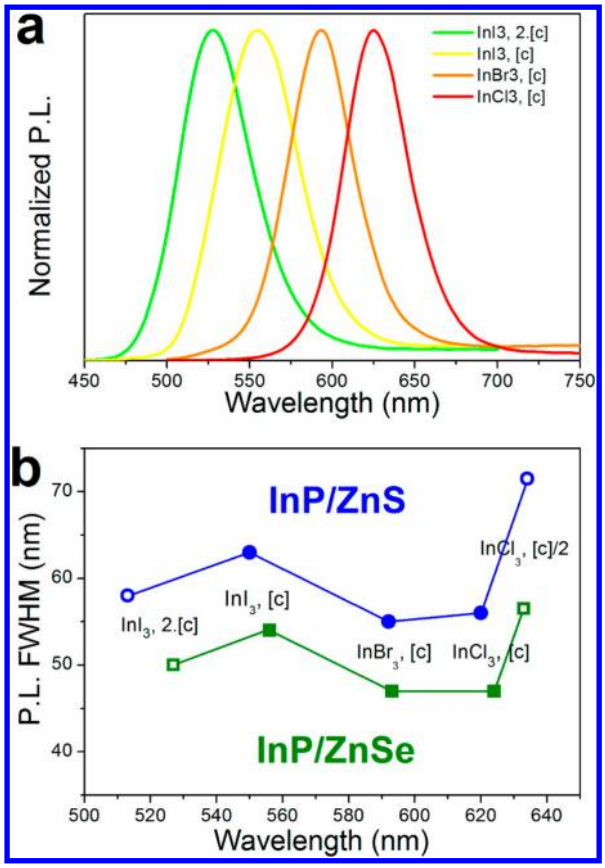

Figure 10. (a) PL emission spectra of InP/ZnSe QDs. (b) Full width at half-maximum (fwhm) of InP/ZnS and InP/ZnSe using different indium halides and different precursor concentrations ([c] corresponds to 0.09 M In precursor). Reprinted from Tessier et al.[161] Copyright 2015 American Chemical Society.

mechanism of energy transfer was nonradiative. The excitation energy of the InP/ZnS QDs was transferred to the fluorescent dyes via FRET. The authors demonstrated that the energy transfer rate varied with the QD size. For example, the InP/ZnS QDs with maximum PL at 530 nm showed a higher energy transfer rate than those whose PL spectrum peaked at 500 nm, due to better overlap between QD emission and dye absorbance for the 530 nm emitting QDs.

3.2. $CuInS_2$ and $CuInS_2$/ZnS Quantum Dots

$CuInS_2$ (CIS) QDs have a Bohr exciton radius of 4.1 nm, and thus quantum confinement effects can be observed when their diameter falls below 8 nm.[166,198−200] The molar absorptivity of CIS is relatively high across the entire visible spectral range (e.g., 10^5 cm^{-1} at 500 nm). However, bare CIS QDs are not stable in air or water and show a low PL QY.[201−203] Chen et al.[122] demonstrated that the PL intensity of the CIS QDs could be improved dramatically by coating with a ZnS shell. The signal enhancement was attributed to passivation of defects at the core QD surface. The PL QYs for the core and core/shell QDs were 1.4 and 48%, respectively, under 460 nm excitation. The large band gap difference between ZnS (3.2 eV) and CIS (1.5 eV) leads to strong confinement of excitons within the CIS core, and thus significant QY enhancement. A 100 nm blue shift of the emission peak was observed after the ZnS shell coating due reduction in size of the CIS core during the ZnS shell growth reaction. Encapsulation of the QDs with *O*-carboxymethyl chitosan (OCMCS) made the CIS/ZnS QDs water-dispersible, with a hydrodynamic diameter of ∼200 nm. Many QDs were enclosed within each OCMCS spheroid. After encapsulation, the PL emission peak shifted to the near-IR biological window (∼700 nm), which is favorable for in vivo imaging. Rao et al.[204] showed that doping the ZnS shell with aluminum could significantly improve the photostability and QY of the $CuInS_2$/ZnS core/shell QDs (Figure 12). The active Al introduced at the surface of the ZnS shell was oxidized to an Al_2O_3 layer that protected the QDs from degradation under long-term irradiation. The optimum molar ratio between Al and Zn was found to be 0.5. Addition of too much Al may reduce the stability of the ZnS/Al shell due to the formation of less stable Al−S bonds. A red shift of the PL peak of the CIS/ZnS QDs without aluminum doping after 30 min of light excitation was attributed to corrosion of ZnS. The PL peak of the CIS/ZnS−Al QDs remained unchanged under the same conditions.

The QY of hydrophobic CIS/ZnS QDs synthesized in organic solvents has reached 80% in some studies, and their PL emission wavelength is widely tunable across the visible to NIR spectral region (Figure 13).[205] However, in most cases the QY dropped dramatically after the hydrophobic to hydrophilic ligand exchange process required to make the QDs water-dispersible. Recently, Jiang et al.[206] reported Cu-doped Zn−In−S/ZnS core/shell QDs (CZIS/ZnS QDs) fabricated directly in water, with a QY up to 35%. In this study, the absorbance and PL peaks of the QDs showed a red shift with

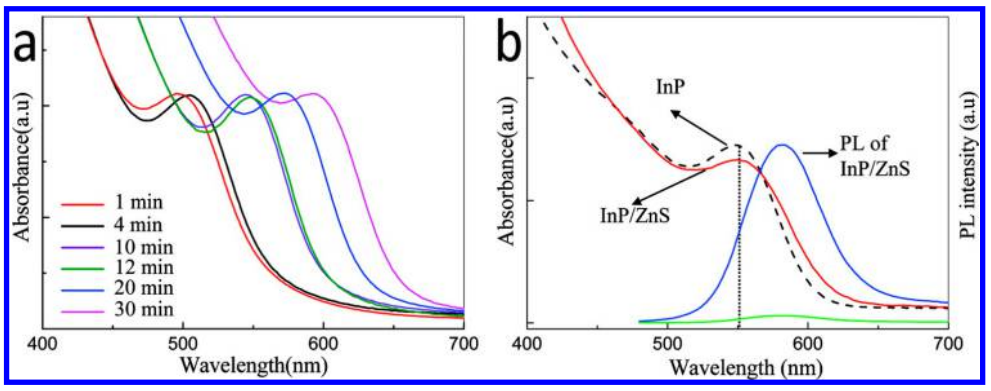

Figure 11. (a) Temporal evolution of the UV−vis absorption spectra of InP QDs with synthesis time in ODE. (b) UV−vis absorption and PL spectra of InP (black dashed line and green solid line) and InP/ZnS QDs (red solid line and blue solid line). Reprinted from Narayanaswamy et al.[195] Copyright 2008 American Chemical Society.

DOI: 10.1021/acs.chemrev.6b00290
Chem. Rev. 2016, 116, 12234−12327

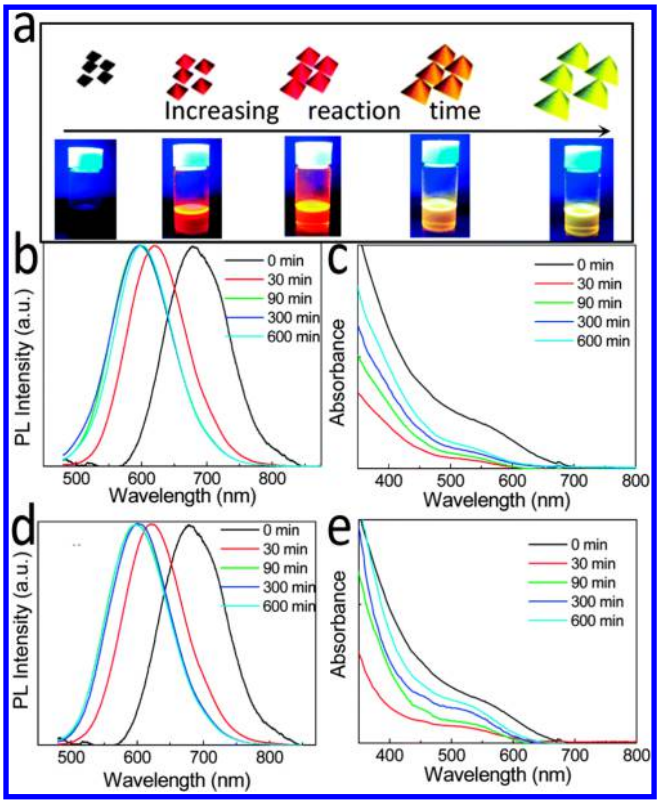

Figure 12. (a) Crystal growth process and color change of CIS@ZnS:Al QDs. (b) PL and (c) UV−vis absorbance spectra of CIS@ZnS QDs. (d) PL and (e) UV−vis absorbance spectra and CIS@ZnS:Al QDs with an Al/Zn molar ratio of 0.5. Reprinted with permission from Rao et al.[204] Copyright 2015 Royal Society of Chemistry.

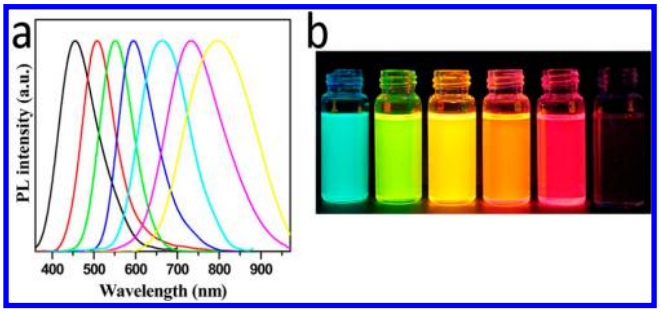

Figure 13. (a) Normalized PL emission spectra (λ_{ex} = 350 nm) of Zn−Cu−In−S/ZnS QDs synthesized in organic solvents. (b) Photograph of samples under UV illumination. Reprinted from Zhang et al.[205] Copyright 2014 American Chemical Society.

decreasing Zn and In precursor concentrations and increasing Cu precursor concentration. The QD PL emission wavelength was tunable from 465 to 700 nm. Changes in the Zn^{2+} precursor concentration induced a larger shift in the emission peak wavelength of QDs than changes in the In^{3+} precursor concentration. Before coating with ZnS shells, a shoulder PL peak was observed at 700 nm and attributed to recombination of trapped electrons with holes in the acceptor level of zinc vacancies. The ZnS shell suppressed this shoulder peak, suggesting that electron traps and zinc vacancies were eliminated.

The optical properties of $CuInS_2$/ZnS quantum rods (QRs) can also be tuned by changing the precursor ratios during synthesis. Li et al.[207] found that the absorbance spectra and PL peaks of $CuInS_2$/ZnS QRs were strongly dependent on the zinc precursor concentration in the seed growth process rather than the final diameter and length of the QRs. In comparison to pure CIS QRs, the absorbance spectra of $CuInS_2$/ZnS QRs were shifted to shorter wavelengths. The optical band gap of the QRs increased from 1.82 to 2.27 eV with increasing ZnS:CIS ratio from 1:2 to 2:1, while the PL peaks of $CuInS_2$/ZnS QRs were blue-shifted from 760 to 520 nm under 450 nm excitation. Currently, quaternary CuInZnS/ZnS QDs with reproducible size and QY can be obtained even at large scale (gram scale). Li et al.[164] designed a continuous-flow synthesis method using a stainless steel cannula (1.6 mm diameter × 400 mm long needle) as the reaction chamber, a geometry similar to the narrow channels in microfluidic chips.[208] For the QD synthesis, the Cu, In, and Zn precursors were mixed with oleylamine (OAm) and pumped into a commercial stainless steel cannula. The CuInZnS/ZnS core/shell QDs were formed with a high yield of 82−85%. The emission wavelengths of the QDs could be tuned from 432 to 615 nm by varying the fraction of each precursor during synthesis. The maximum PL QY of the CuInZnS/ZnS QDs from the continuous-flow reaction was ∼40%.

3.3. Ag_2S and Ag_2Se Quantum Dots

Ag_2S and Ag_2Se QDs are based on I−VI semiconductors with narrow band gaps of 0.85 and 0.15 eV.[209−213] They are known as NIR-II emitting probes (950−1400 nm) which are often more suitable for deep tissue imaging than NIR-I emitters (650−950 nm). Reduced autofluorescence and other background in the NIR-II window allow larger penetration depths and higher imaging fidelity.[214−216] Also, the optical absorbance and scattering by biological tissues are significantly reduced in the NIR-II window. Silver ions were ultraslowly released into the biological environment, ensuring high biocompatibility of the Ag_2S and Ag_2Se QDs. Recently, the exciton Bohr radius of Ag_2S QDs was determined to be 2.2 nm from both experimental and theoretical results.[217] Thus, Ag_2S QDs below 4.4 nm diameter are in the quantum confinement regime and show size-dependent PL emission and excitation spectra. Sun and co-workers[218] studied multiple-exciton generation in Ag_2S QDs and found that their lifetimes were 1−2 orders of magnitude longer than those of PbS QDs.

Li et al.[174] reported that PEGylated Ag_2S QDs with an average size of 5.6 nm showed a PL peak at 1200 nm and QY of 16% (Figure 14). Compared to indocyanine green (ICG), an organic dye with NIR-I emission, the Ag_2S QDs with NIR-II emission showed a narrower feature width in a tissue phantom study when immersed in high concentration of intralipid solution. A spatial resolution of 40 μm was achieved by using these QDs for in vivo angiogenesis imaging of blood vessels (43 μm) in a small tumor (2−3 mm). The QDs retained 70% of their peak PL intensity after 2 h irradiation at 808 nm by a laser diode at a flux of 123.8 mW/cm^2. Using these QDs, a penetration depth of 1.1 cm was achieved in a phantom model, with an injection concentration of 0.1 mg/mL.

Gui et al.[219] fabricated thiol-multidentate polymer functionalized Ag_2S QDs with sizes ranging from 2.6 to 3.7 nm and QY of 14.2−16.4%. Their PL emission was tuned across a wide range from deep red to NIR-II (687−1096 nm), making the Ag_2S QDs an ideal candidate for multicolor targeted imaging. Tan et al.[22] demonstrated the tunability of PL multidentate polymer (MDP) functionalized Ag_2Se QDs from 966 to 1228 nm by changing the reaction time from 0.5 to 3 h. Upon

DOI: 10.1021/acs.chemrev.6b00290
Chem. Rev. 2016, 116, 12234−12327

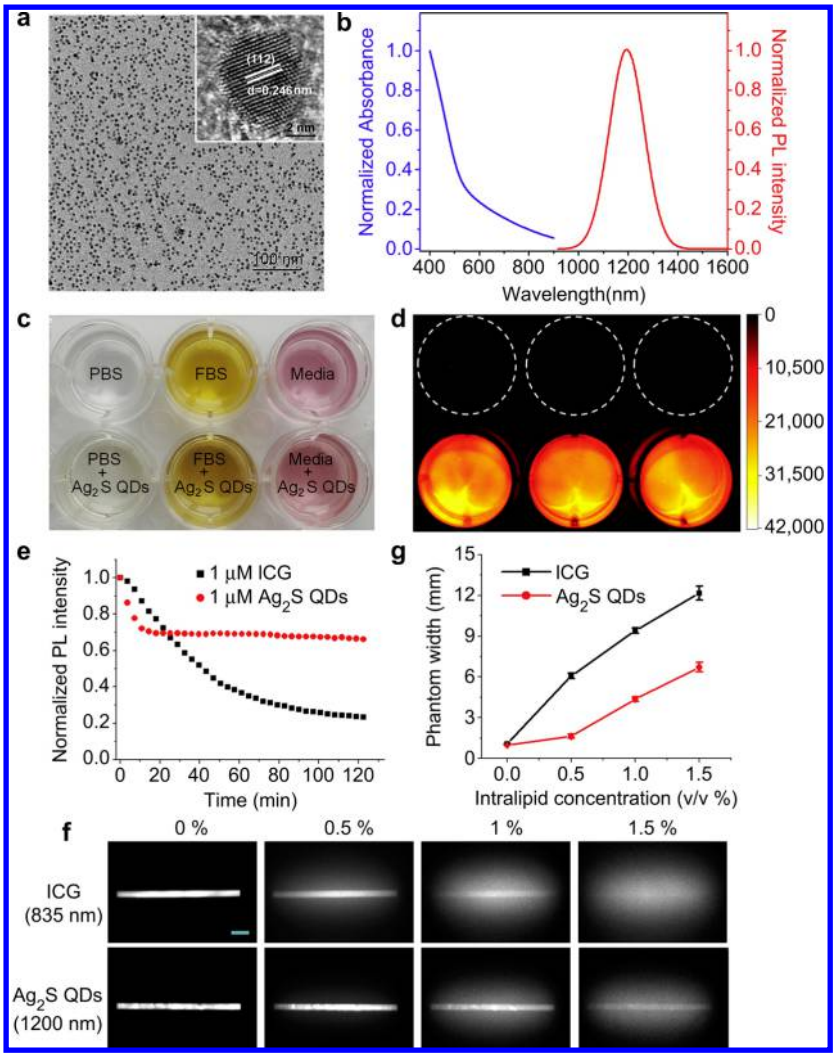

Figure 14. Characterization of PEGylated Ag_2S QDs. (a) TEM and HRTEM (inset) image; (b) absorbance and PL spectra of PEGylated Ag_2S QDs. (c and d) Dispersion (0.1 mg/mL) of PEGylated Ag_2S QDs in PBS, FBS, and cell culture media and their NIR-II PL images. (e) Photostability of PEGylated Ag_2S QDs and ICG under irradiation of an 808 nm laser. (f) Fluorescent images of ICG at 835 nm and Ag_2S QDs at 1200 nm immersed in different concentrations of intralipid solutions. Scale bar: 0.5 cm. (g) Phantom width of Ag_2S QDs and ICG capillary images corresponding to (f), showing a narrower feature width of NIR-II emitting Ag_2S QDs in comparison with the NIR-I emitting ICG. Reprinted with permission from Li et al.[174] Copyright 2014 Elsevier.

increasing the growth time, the absorbance and emission spectra were red-shifted. As a result, the PL emission of the QDs could be excited within the NIR-I window, which is preferable for in vivo imaging. The longer reaction time also led to broadening of the size distribution and the PL emission spectrum. The Ag_2Se QDs synthesized in water had a relatively high QY of 12.2% and a long PL lifetime of 135.3 ns. The photostability of the MDP-functionalized Ag_2Se QDs was compared with that of ICG. The fluorescence intensity of the ICG was fully bleached after 3 h of excitation, while the QDs suffered only a 20% decrease in PL intensity under the same conditions. The effects of different capping ligands including 1-octanethiol, oleylamine (OAm), and tetradecylphosphonic acid (TDPA) on formation of Ag_2Se QDs were demonstrated by Zhu et al.[220] They found that, among the three ligands, 1-octanethiol was most effective for producing highly monodisperse and photostable Ag_2Se QDs. This is attributed to differences in interaction between the ligands and the Ag precursor. The Ag(I) precursor is a soft Lewis acid and 1-octanethiol is a soft Lewis base ligand, while OAm and TDPA are hard Lewis base ligands. In this case, the Ag(I) precursors could be effectively stabilized at a higher reaction temperature during the nucleation and growth process. The Ag_2Se QDs exhibited NIR-II PL emission wavelengths from 1080 to 1330 nm.

3.4. ZnS–$AgInS_2$ (ZAIS) Quantum Dots

$AgInS_2$ QDs are ternary I–III–VI_2 QDs that are similar to $CuInS_2$ QDs.[221−223] $AgInS_2$ can exist in two crystal phases: chalcopyrite and orthorhombic. The chalcopyrite phase has a tetragonal unit cell and in the bulk is thermodynamically stable below 620 °C, while the orthorhombic phase is more stable at higher temperatures. Thus, $AgInS_2$ QDs are mainly produced in the chalcopyrite phase, which has a direct band gap of 1.87 eV (663 nm), with a high absorption coefficient. The band gap of $AgInS_2$ QDs was tuned from 1.87 to 2.03 eV by changing the Ag:In precursor ratio during synthesis.[221] Water-dispersible $AgInS_2$/ZnS core/shell QDs with a long PL lifetime of 170 ns and a high QY of 20% were recently fabricated by Regulacio and co-workers.[224] To achieve water dispersibility, they modified the QD surface with mercaptoacetic acid (MAA)

DOI: 10.1021/acs.chemrev.6b00290
Chem. Rev. 2016, 116, 12234−12327

and poly(acrylic acid) (PAA). Hamanaka et al.[168] investigated the effect of $AgInS_2$ QD size on the PL QY and radiative recombination rate. They found that the QY of $AgInS_2$ QDs increased with decreasing size from 4.3 to 2.5 nm, reaching 60% for 2.5 nm QDs. The authors concluded that the low reaction temperature used in preparing the smaller QDs might increase the number of donor−acceptor recombinations trapped by defect sites, leading to a higher QY. Using a low reaction temperature of 165 °C and a small amount of zinc precursor (8 atom %) in the reaction system, the NIR emission peak of $AgInS_2$/ZnS core/shell QDs was tuned to 815 nm. Zinc can not only prevent aggregation of the QDs at higher reaction temperature, but can also reduce the number of defects formed on the QD surface through cation exchange by zinc ions and ZnS shell growth. The optimum Ag/In/Zn precursor ratio reported by Mao et al.[169] was 1:0.68:0.08 for preparing ZAIS QDs with an average diameter of 2.5 nm and high QY.

3.5. Silicon Quantum Dots

In contrast to the Cd-free QDs discussed in the previous subsections, Si QDs have an indirect bulk band gap that leads to reduced radiative recombination of electrons and holes in the bulk state due to mismatch between the wave vectors at the valence band maximum and conduction band minimum. Matching is required by the *k*-selection rule for an optical transition between them. However, finite size effects in the quantum confinement regime[225−228] relax the wave vector matching requirement, as the valence and conduction bands become discrete states. If the QD surface is well passivated so that no other recombination routes are available, SiQDs can exhibit efficient size-tunable PL emission, when their radius is below the exciton Bohr radius of 4.2 nm.[226,229−236] Because of strong covalent bonding in Si, fabrication at temperatures accessible in solution-phase synthesis is difficult, and high-temperature gas-phase and solid-phase synthesis methods have been developed.[233,235,237,238] The PL QY of Si QDs produced in the gas phase, and then surface passivated by covalent attachment of organic ligands and dispersed in organic solvents, can exceed 60%.[236] Two-photon and three-photon excited PL have also been demonstrated using Si QDs produced in the gas phase followed by solution-phase etching and surface functionalization.[239] This opens up the possibility of multi-photon imaging using Si QDs. Solution-phase synthesized Si QDs often exhibit blue PL associated with oxide defects at the QD surface, and blue PL can also be produced by oxidation of gas-phase synthesized QDs.[240,241] Our group introduced a combination of bottom-up gas-phase synthesis of Si nanoparticles from silane gas with solution phase (top-down) etching and surface passivation which allowed production of high quality, high quantum yield Si QDs with relatively narrow emission spanning the visible and near-IR spectral ranges.[65,231−233,242] The band gap and emission wavelengths of Si QDs can be tuned by functionalizing the NP surface with different ligands. For example, Zhou and co-workers[243] successfully produced a 70 nm red shift of the PL peak of Si QDs by conjugating the particle surface with organic moieties such as 4-ethynyl-*N*,*N*-bis(4-methoxyphenyl)aniline (MeOT-PA). Due to the indirect band structure of Si QDs, their absorption efficiency in the visible wavelength region is relatively low in comparison with that in the UV region, where silicon has direct transitions.[244] Sugimoto et al.[180] demonstrated that codoping Si QDs with boron (p-type dopant) and phosphorus (n-type dopant) enhanced radiative transitions by producing donor−acceptor states associated with the B and P atoms. The diameter of the codoped Si QDs was tuned from 2.8 to 5.2 nm by changing the annealing temperature from 1050 to 1150 °C during Si QD preparation. The peak of the PL spectra red-shifted from 760 to 1000 nm and the PL lifetime of QDs was wavelength dependent (Figure 15). The PL spectra of the codoped Si QDs were not affected

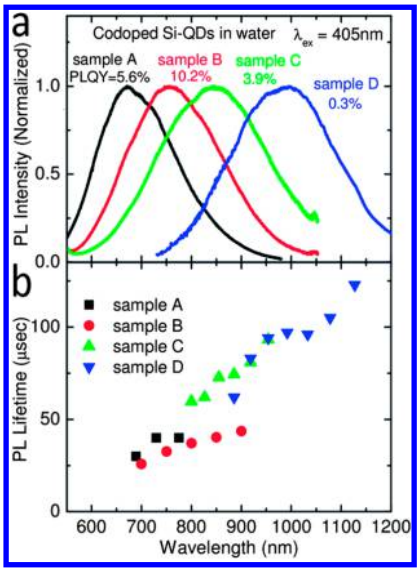

Figure 15. (a) PL spectra of Si QDs prepared under annealing temperature 1050−1150 °C. (b) PL lifetimes of Si QDs as a function of detection wavelength. Reprinted with permission from Sugimoto et al.[180] Copyright 2014 Royal Society of Chemistry.

by the solvent polarity or pH (from 2 to 10), when dispersed in water or methanol solutions or in acidic or alkaline media. A QY of 10.2% and a long lifetime of 30 μs were obtained for the Si QDs with an average size of 2.8 nm and emission peak of 760 nm.

3.6. Graphene Quantum Dots

Pristine graphene consists of a single layer of carbon atoms arranged in a hexagonal lattice.[245] The band gap of graphene is zero and its exciton Bohr radius is infinite due to its linear dispersion relation with conduction and valence bands that meet at Dirac points.[245,246] Nonetheless, quantum confinement effects emerge in graphene layers of nanometer lateral dimensions, which have finite band gaps. In such graphene QDs (GQDs) PL emission can be tuned by varying the size in the two lateral dimensions. The emission peaks of GQDs shift to longer wavelengths with increasing size. For example, the PL peak wavelengths of zigzag-edged GQDs can be tuned to cover the entire visible spectrum by changing their diameter from 0.89 to 1.80 nm.[247] GQDs exhibit broad absorption in the UV−visible region (from 400 to 700 nm). Ge et al.[70] reported that the Stokes shift of GQDs was up to 205 nm, which minimizes self-absorbance of their PL emission. The PL QY and lifetime measured in air or nitrogen were higher than those measured in oxygen.

According to density functional theory (DFT) calculations, the emission peak of pristine GQD with an average diameter of 2 nm should be in the red region.[247] However, exfoliation-based preparation of graphene from bulk graphite can disrupt the sp^2-hybridized carbon network and introduce defects and functional groups that result in blue and green emission.

DOI: 10.1021/acs.chemrev.6b00290
Chem. Rev. 2016, 116, 12234−12327

Sandeep Kumar and co-workers demonstrated that the PL spectra of 5−7 nm GQDs that were edge-functionalized with amino groups depended strongly on excitation wavelength (Figure 16a).[248] They further studied the mechanism of the

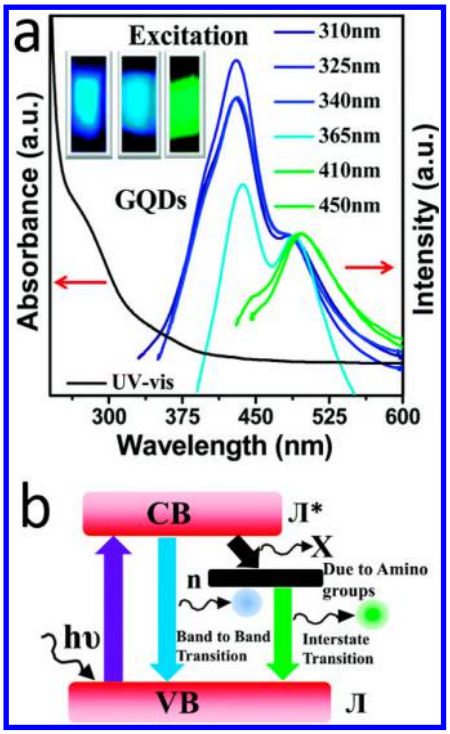

Figure 16. (a) UV−vis absorption and excitation dependent PL spectra of amino-functionalized GQDs. (b) Schematic representation of the energy band diagram model to explain $\pi^*-\pi$ and $n-\pi$ transitions. Reprinted with permission from Sandeep Kumar et al.[248] Copyright 2014 Royal Society of Chemistry.

excitation-dependent PL emission in terms of the GQD energy band variation using first-principles calculations. The amino functionalization at the GQD surface edges led to (i) a zigzag effect (i.e., band-to-band $\pi^*-\pi$ transition at 429 nm) and (ii) interstate to band transitions ($n-\pi$ transitions at 497 nm) (Figure 16b). This edge-functionality-induced PL was also observed when the size of the GQD increased to a dimension larger than 20 nm.

Recently, Huang et al.[99] demonstrated shifts in absorbance and PL of GQDs due to surface functionalization with folic acid. After conjugation with folate groups, the absorbance peak of the GQDs shifted from 290 to 370 nm. The peak at 290 nm was attributed to the $\pi^*-\pi$ transition of aromatic carbon−carbon bonds, while the red-shifted absorption peak at 370 was due to the $\pi^*-\pi$ transition and $n-\pi$ transitions involving the folate molecules. The PL emission peak for the folate-conjugated GQDs was at 517 nm under 350 nm excitation. Two other factors that influence the PL spectra of GQDs are the pH of their environment and heteroatom doping (e.g., with N).[249] The PL intensity of the GQDs was greater under alkaline conditions (pH 10) than under acidic conditions (pH 3), because the emissive triplet carbene state was disrupted by protonation of the free zigzag sites at the GQD surface in acid, but was restored at high pH. Sun et al.[250] reported that nitrogen doping in the aromatic rings of GQDs can significantly enhance their PL intensity and result in a high QY of 74% through the $n-\pi^*$ transition between the doped nitrogen atom and the graphene structure.

3.7. Doped ZnS/ZnSe Quantum Dots

Doped semiconductor QDs with low intrinsic toxicity are mostly based on zinc chalcogenides doped with Mn^{2+}, Eu^{2+}, Cu^{2+}, or Ga^{2+}.[251−254] The Stokes shift of these doped QDs is much larger than in conventional QDs, because the QD host absorbs the excitation light, but emission is from the dopant atom. This reduces self-absorbance and PL self-quenching. The PL emission peaks of these doped QDs can be tuned by changing the dopant concentration. Doping Mn^{2+} into ZnS QDs produces a strong dopant emission centered around 575 nm, by transitions between the Mn^{2+} $^4T_1$ first excited state and its $^6A_1$ ground state.[255,256] Recently, Yu et al.[257] demonstrated that Mn^{2+} doped ZnS QDs had a large three-photon cross section ($1.3\ (\pm 0.5) \times 10^{-79}$ $cm^6\ s^2$) that enabled imaging with spatial resolution exceeding the single-photon diffraction limit (Figure 17). The Mn^{2+} concentration in their study was 1.1%, and the QD diameter was 5.5 nm. The three-photon (3P) excited PL with Mn emission at 580 nm was excited at 920 nm using a Ti:sapphire pulsed laser. The 3P PL was attributed to

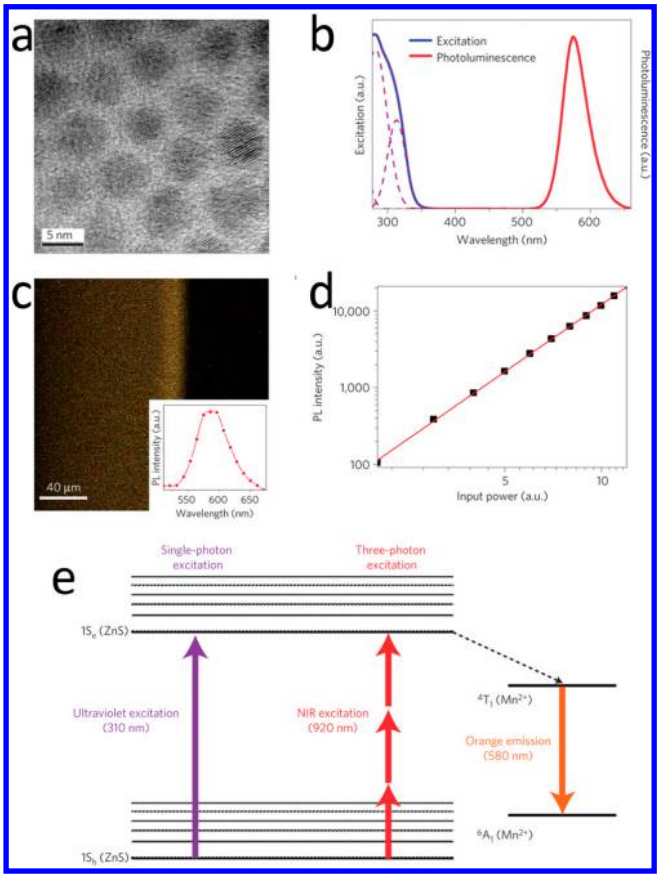

Figure 17. (a) TEM image of 5.5 nm ZnS:Mn QDs. (b) Normalized one-photon PLE (blue) and PL (red) spectra of ZnS:Mn QDs. The Gaussian fit to the PLE spectrum (purple dashed line) matches the $1S_e-1S_h$ transition peaked at 314 nm. (c) Multiphoton PL image of the ZnS:Mn QD thin film under 920 nm laser excitation. Inset: luminescence spectrum extracted from the image. (d) Log−log plot of the power dependence of PL intensity. (e) Jablonski diagram of one-photon and three-photon excited luminescence in ZnS:Mn QDs. Reprinted with permission from Yu et al.[257] Copyright 2013 Nature Publishing Group.

DOI: 10.1021/acs.chemrev.6b00290
Chem. Rev. 2016, 116, 12234−12327

absorbance via the $1S_e-1S_h$ exciton transition of the ZnS QDs followed by energy transfer to Mn^{2+}. The 3P cross section was 10 000 times that of conventional UV dyes, which allowed the use of much lower excitation power than would be possible using dyes. This reduces phototoxicity during long-term imaging studies.

PL quenching of Mn-doped ZnS QDs by an anticancer drug molecule called idarubicin (IDA) was demonstrated by Ertas and co-workers.[258] The Mn-doped ZnS QDs had an average diameter of 3.5 nm and two absorbance peaks at 209 and 290 nm. Their PL peak under 290 nm excitation was ~590 nm. The hybrid IDA/Mn-doped QDs were sensitive to the presence of target double stranded DNA (dsDNA), because the IDA drug preferentially adsorbs to the dsDNA. The desorption of IDA from the QD restored the QD PL. In this manner, double stranded DNA was detected at concentrations ranging from 1.2 to 6.0 mM. Song et al. prepared Mn-doped type II core/shell ZnTe/ZnSe QDs with emission wavelengths from blue to orange.[125] The QY of ZnTe/ZnSe core/shell QDs improved from 5.3 to 7% upon doping with Mn^{2+} ions. Aqueous Cu-doped ZnSeS/ZnS QDs with a QY of 40% and impressive photostability were also fabricated by Zeng et al.[144] These QDs retained 90% of their PL intensity after 30 days of exposure to air and light. The maximum QY was obtained with a 0.43% Cu^+ cation fraction (Cu/(Cu + Zn) atomic ratio). Further increasing the dopant concentration decreased the QY due to nonradiative decay via interaction between Cu^+ ions. Emission from the doped QDs red-shifted with increasing Cu^+ dopant concentration. Doping an element such as Cu^+ into ZnSe and ZnS QDs could generate charge imbalance because the preferred oxidation state differs from that of the cation of the host lattice.[259] The charge imbalance can produce compensating effects like lattice distortion and vacancies that can reduce PL QY. To overcome this challenge, trivalent cations have been used as codopants in Cu^+ doped ZnSe/ZnS QDs to form a neutral lattice. Cooper et al.[143] fabricated codoped core/shell ZnSe/ZnS QDs with Cu^+ as the primary dopant and In^{3+}, Ga^{3+}, and Al^{3+} as codopants. The resulting QDs showed tunable PL emission from 430 to 570 nm with an average PL fwhm of 80 nm (Figure 18). The PL from the core 8 nm diameter ZnSe QDs was weak, but improved after coating with a 2 nm ZnS shell. The PL intensity of the doped QDs was enhanced 10-fold after surface functionalization with bidentate thiol-based ligands. This may indicate that the ligands could further passivate defects at the QD surface. The undoped core/shell ZnSe/ZnS had a PL peak at 437 nm. The emission peak intensity decreased after doping with Cu^+, but increased with further addition of Al^{3+}. A green PL peak at 509 nm and a yellow peak at 550 nm were obtained for Cu^+-Al^{3+} codoped QDs and Cu^+-Ga^{3+} codoped QDs. The largest red shift in the PL peak, to 570 nm, was achieved with Cu^+-In^{3+} codoped QDs. The PL lifetime for undoped ZnSe was 9.3 ns, but significantly increased lifetimes of 480, 710, and 940 ns were observed for the Cu^+-Al^{3+}, Cu^+-Ga^{3+}, and Cu^+-In^{3+} codoped QDs. The longer lifetime demonstrated that elimination of compensation effects by codoping could effectively stabilize the photogenerated carriers.

3.8. Plasmonic Copper Chalcogenide Quantum Dots

Degenerately doped semiconductor QDs, especially copper chalcogenide QDs (i.e., $Cu_{2-x}S$, $Cu_{2-x}Se$, $Cu_{2-x}Te$, etc.), have recently emerged as a new type of plasmonic nanomaterial for biomedical applications.[140,141,260,261] The localized surface

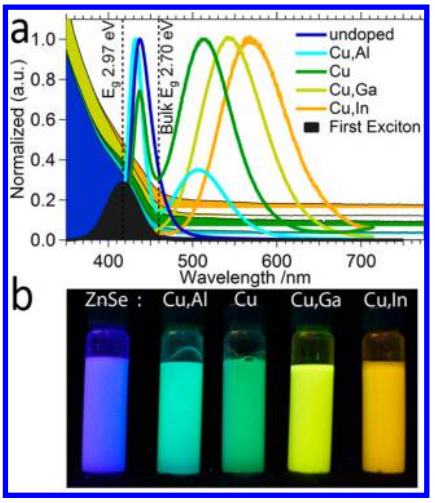

Figure 18. (a) Normalized absorbance and PL spectra of ZnSe/ZnS (undoped), Cu- and Al-doped ZnSe/ZnS (Cu, Al), Cu-doped ZnSe/ZnS (Cu), Cu- and Ga-doped ZnSe/ZnS (Cu, Ga), Cu- and In-doped ZnSe/ZnS (Cu, In) QDs. E_g and bulk E_g represent the absorbance onset of the ZnSe/ZnS QDs and band gap of bulk ZnSe, respectively. (b) Photograph of the codoped ZnSe/ZnS QD dispersions under UV excitation. Reprinted from Cooper et al.[143] Copyright 2015 American Chemical Society.

plasmon resonance (LSPR) of noble metal NPs has been well studied.[262−264] LSPR arises from collective oscillations of free charge carriers confined in subwavelength structures. Based on this principle, metallic NPs such as gold nanorods have been studied for photothermal cancer therapy, photoacoustic imaging, and related applications where strong absorbers are needed. More recently, LSPR in doped copper chalcogenide QDs with free carrier concentrations about an order of magnitude lower than those of noble metals has been investigated.[140,172,265−268] In these QDs, free holes oscillate in resonance with incoming light to produce LSPR. Wang et al.[269] studied the plasmonic properties of $Cu_{2-x}S$ QDs prepared from Cu_3N NPs through a one-pot approach. $Cu_{2-x}S$ QDs of different sizes were synthesized by changing the precursor ratios. The highly monodisperse as-synthesized QDs exhibited very weak LSPR, but slow oxidation by dissolved oxygen over hundreds to thousands of hours produced strong LSPR that was "pinned" at different wavelengths for QDs of different sizes (Figure 19). The pinned LSPR peak energy increased from 1.09 to 1.23 eV, as the QD diameter increased from 5.4 to 11.1 nm. This shift was attributed to reduced carrier scattering in larger QDs. The authors also investigated ternary $Cu_{2-x}S_ySe_{1-y}$ QDs, which exhibited similar behavior. The pinned LSPR energy after long-term oxidation increased from 0.9 to 1 eV as the Se anion fraction increased from 11 to 66%. This was attributed to a change in the effective mass of free holes as reported earlier by Liu et al.[270]

$Cu_{2-x}S$ QDs with a broad LSPR absorbance band in the near-IR region (700−1100 nm) were also described by Liu and co-workers (Figure 20).[271] They first obtained oleylamine (OAm)-functionalized $Cu_{2-x}S$ QDs in a nonpolar solvent by a thermal decomposition process. The QDs were later transferred to water through ligand exchange reactions. The OAm molecules on the QD surface were replaced by 6-aminocaproic acid. The diameter of the hydrophilic $Cu_{2-x}S$ QDs dispersed in water ranged from 12 to 20 nm. The photothermal characteristics of the QDs were investigated under NIR laser

DOI: 10.1021/acs.chemrev.6b00290
Chem. Rev. 2016, 116, 12234−12327

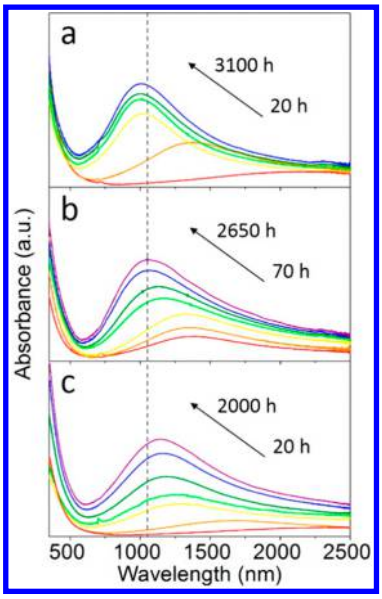

Figure 19. Time evolution of LSPR absorbance spectra of $Cu_{2-x}S$ QDs due to oxidation by dissolved O_2 in CCl_4. The $Cu_{2-x}S$ QD diameters are (a) 11.0 ± 0.3, (b) 9.2 ± 0.4, and (c) 5.4 ± 0.3 nm. All samples show pinning of the LSPR band at long time. Reprinted from Wang et al.[269] Copyright 2015 American Chemical Society.

illumination (980 nm), showing that the temperature of a 0.2 mg/mL dispersion of QDs in water increased by 15 °C after 5 min illumination (1.5 W/cm^2). The temperature increase was much greater than the 5 °C change for control samples without QDs. Photoinduced generation of reactive oxygen species from the $Cu_{2-x}S$ QDs was also observed. The Cu^{2+} ions could be reduced to Cu^+ ions by glutathione or ascorbic acid in biological media. Reactive oxygen species (ROS) were then produced by the Cu^+ ions. Generation of ROS only occurred under NIR illumination. ROS production was quantified using oxidation-responsive dichlorofluorescein diacetate, which is oxidized by ROS to fluorescent 2,7-dichlorofluorescein. In addition to $Cu_{2-x}S$, copper tin sulfide (Cu_2SnS_3) QDs also exhibit tunable LSPR.[272] The crystal phase and the size of the Cu_2SnS_3 QDs were strongly dependent on the Cu and Sn precursor ratios and the reactivity of the chalcogenide source. Different Cu:Sn elemental ratios correspond to different doping levels (i.e., different cation vacancy concentrations) in the QDs. The LSPR peak was red-shifted and damped with increasing Sn content, disappearing completely at a Cu−Sn ratio of 1:3.

As discussed in section 2.4, the PL and LSPR intensity of copper chalcogenide ($Cu_{2-x}S$, $Cu_{2-x}Se$, or $Cu_{2-x}Te$) QDs during oxidation and reduction are inversely correlated.[142] A high concentration of free charge carriers in these QDs is necessary to observe LSPR. However, transfer of energy from photogenerated excitons to the LSPR modes quenches PL. Thus, although these plasmonic QDs can exhibit both excitonic and plasmonic absorbance features, those with strong LSPR absorbance typically do not exhibit significant PL.

The LSPR absorbance spectrum of plasmonic semiconductors can be tuned not only by changing their composition and crystal structure, which in turn changes the free carrier concentration and effective mass, but also by changing the shape of the nanostructures.[261] Liu et al. demonstrated room-temperature synthesis of covellite CuS nanoplatelets with a fixed thickness of about 4 nm and diameters ranging from ∼4 to ∼33 nm.[273] Such nanoplatelets exhibit in-plane and out-of-plane plasmon resonances, but the in-plane resonance dominates. With increasing aspect ratio of the nanoplatelets, the LSPR peak wavelength shifted from below 1000 nm to above 1600 nm, all at a fixed composition, crystal phase, and free carrier concentration. The aspect-ratio dependence of the LSPR peak wavelength was quantitatively modeled, reproducing the experimental results (Figure 21). This aspect-ratio-

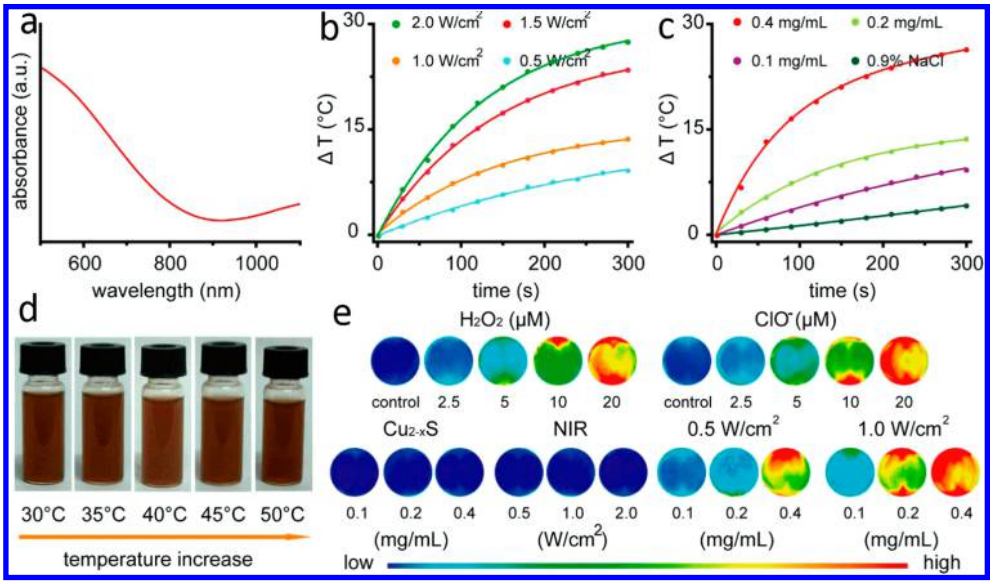

Figure 20. Photothermal characteristics of plasmonic $Cu_{2-x}S$ QDs. (a) UV−vis−NIR absorbance spectra of $Cu_{2-x}S$ QDs in water. Temperature change of (b) $Cu_{2-x}S$ QDs at 0.2 mg/mL irradiated by a NIR laser (980 nm) with different power intensities and (c) $Cu_{2-x}S$ QDs at different concentrations irradiated at 1.5 W/cm^2. (d) Photos of $Cu_{2-x}S$ NCs in a 0.9% NaCl solution incubated at various temperatures. (e) Fluorescence imaging of ROS generation detected by 2′,7′-dichlorodihydrofluorescein diacetate (DCFH-DA) assay. (upper) Standard H_2O_2 and NaClO solutions with different concentrations treated with DCFH-DA. (lower) Experimental samples under different intensities of NIR power intensities and with various concentrations treated with DCFH-DA. Reprinted from Liu et al.[271] Copyright 2015 American Chemical Society.

DOI: 10.1021/acs.chemrev.6b00290
Chem. Rev. 2016, 116, 12234−12327

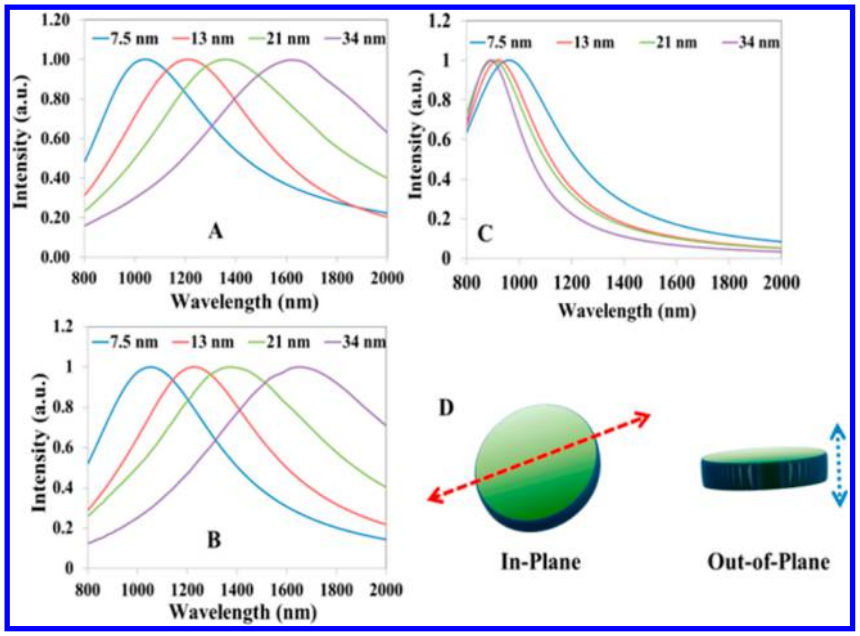

Figure 21. Comparison of smoothed experimental (A) and simulated (in-plane (B) and out-of-plane (C)) spectra for CuS nanoplatelets of four different diameters, at fixed thickness of ~4 nm. (D) Illustration of in-plane and out-of-plane modes. Reproduced from Liu et al.[273] Copyright 2015 American Chemical Society.

based tuning of the plasmon resonance is entirely analogous to that observed in gold nanorods.[274] The key difference is that, in plasmonic semiconductors, this shape-based LSPR tuning can be combined with composition- and phase-based tuning, providing greater flexibility in the combinations of size, shape, and LSPR energy that can be achieved.

4. PREPARATION OF BIOCOMPATIBLE CADMIUM-FREE QUANTUM DOTS

Developments in the synthesis and surface functionalization of Cd-free QDs provide the basis for their eventual adoption as efficient nanotags for in vitro and in vivo applications. Currently, many research groups are developing new techniques for preparing biologically applicable Cd-free QDs. By changing the precursor ratios, reaction temperatures, and shell compositions, one can optimize the QD size, quantum yield, and emission wavelength. Moreover, the wide variety of capping molecules that can be used on the surfaces of QDs allows creation of multifunctional nanoprobes that simultaneously serve as drug carriers and imaging probes. In this section, we review recent progress on the synthesis of Cd-free QDs for in vitro and in vivo applications. This builds on the discussion in section 3, but focuses on the development of synthetic methods for preparing these Cd-free QDs in forms useful for biological applications.

4.1. InP and InP/ZnS Quantum Dots

Indium phosphide (InP) QDs are III−V semiconductor nanocrystals with PL properties similar to Cd-based II−VI QDs, but with better stability in biological environments due to their more covalent bonding.[275] In part because of their similarity to CdSe QDs, InP QDs have been among the first Cd-free QDs to become commercially available for biological research applications. The intrinsic lower cytotoxicity and long-term in vivo biocompatibility of InP QDs have been demonstrated by Brunetti et al. and our group.[276,277] The first synthesis of colloidal InP QDs was reported by Micic and co-workers in 1994.[278] Indium precursors were first prepared by reacting $InCl_3$ with $Na_2C_2O_4$ in CH_3CN at a 1:1 molar ratio. The In precursors were added to tris(trimethylsilyl)phosphine ($P(SiMe_3)_3$ or $P(TMS)_3$) in trioctylphosphine oxide (TOPO), which served as a stabilizing agent. The diameter of the nearly monodisperse InP QDs was 2.5 ± 0.19 nm. Later, Battaglia et al.[279] demonstrated a more facile and "greener" synthesis method for InP QDs that required only 3−4 h and used a less toxic solvent (octadecene, ODE) in place of TOPO, with fatty acids (e.g., palmitic acid and myristic acid) as surface ligands to cap the QDs. Briefly, the In precursors were obtained by heating indium acetate ($In(Ac)_3$) in solutions of fatty acid ligands in ODE at 100−120 °C until the solution became clear. Phosphorus precursors containing $P(TMS)_3$ in ODE were added to the In precursors at a molar ratio of 2:1. The resulting InP QDs were 3.1 ± 0.15 nm in diameter. They were dispersible in nonpolar solvents and showed clear PL. To reduce the toxicity of InP QDs for in vitro and in vivo applications, our group developed a one-pot approach for preparing InP/ZnS core/shell QDs with a particle size of 15−20 nm.[42,277] The ZnS shell coating protected the InP core QD from degradation in biological systems, minimizing the release of In^{3+} ions. The InP core QDs were prepared by heating $In(Ac)_3$, myristic acid, and ODE, followed by injection of $P(TMS)_3$ in ODE. Subsequently, zinc 2-ethylhexanoate and sulfur dissolved in oleylamine were added to the InP cores. The InP/ZnS core/shell QDs solutions were purified by centrifugation and redispersion. Ligand exchange using mercaptosuccinic acid made the QDs water dispersible. The emission peak of the QDs was centered at 650 nm with a QY of 25−30%. More recently, Brunetti et al.[160,276] synthesized InP/ZnS core/shell QDs with a QY of 60% by using zinc carboxylate as both the Zn shell precursor and stabilizing agent. In that study, zinc undecylenate, hexadecylamine, stearic acid, and indium chloride were first dissolved in ODE under nitrogen at room temperature. Injection of $P(TMS)_3$ into the heated Zn precursor solution produced the InP core QDs. For ZnS shell growth, zinc diethyldithiocarbamate was added into the core

DOI: 10.1021/acs.chemrev.6b00290
Chem. Rev. 2016, 116, 12234−12327

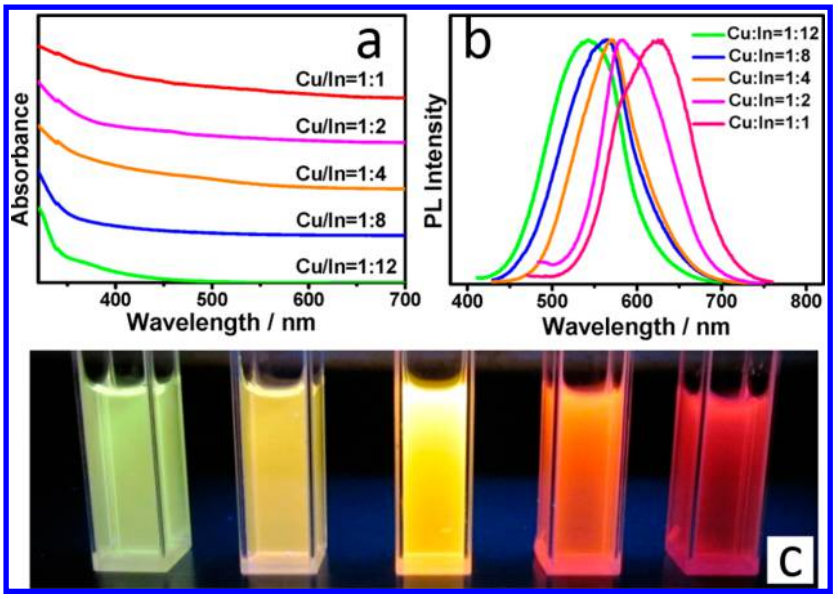

Figure 22. (a) UV−vis absorbance and (b) PL spectra of Cu−In−S/ZnS QDs with varying Cu:In ratios. (c) Digital photograph of Cu−In−S/ZnS QDs under UV illumination. Reprinted from Chen et al.[165] Copyright 2013 American Chemical Society.

QD solution. The hydrodynamic diameter of the dispersed InP/ZnS core/shell QDs was 11.3 ± 0.6 nm.

4.2. $CuInS_2$, $CuInS_2$/ZnS, and CuInZnS/ZnS Quantum Dots

Ternary $CuInS_2$ QDs are Cd- and Pb-free alternatives to intrinsically toxic II−VI and IV−VI QDs as PL labels. The $CuInS_2$ direct band gap of ∼1.5 eV allows these QDs to have tunable emission across visible and near-IR wavelengths combined with large molar extinction coefficients.[122,280] Liu et al.[162] demonstrated a facile one-pot hydrothermal preparation method for aqueous $CuInS_2$ QDs with an average size of 2.2 nm and PL at 660 nm, using mercaptopropionic acid (MPA) as a capping ligand. Briefly, copper chloride ($CuCl_2$) and indium chloride ($InCl_3$) were mixed with MPA in water at pH 11.3 and room temperature. Thiourea ($CS(NH_2)_2$) was added and the mixture was heated in an autoclave for 21 h to form the $CuInS_2$ QDs. Molar ratios of Cu:In:S and Cu:MPA were 1:1:2 and 1:12. Although these QDs initially had a maximum QY of only ∼3%, after adding a ZnS shell the QY increased to 40−60%. The ZnS shell has a large band gap of 3.7 eV that forms a type I band alignment with the $CuInS_2$ cores.[28,281,282] In addition, the lattice mismatch between the ZnS shell and the $CuInS_2$ cores is only ∼2.2%, allowing formation of defect-free shells and core/shell interfaces. Li et al.[163] prepared $CuInS_2$/ZnS QDs with PL peaks ranging from 550 to 815 nm and QY of 60% through a two-step approach. They used 1-dodecanethiol (DDT) as both the sulfur precursor and the stabilizing agent during the core QD formation. The $CuInS_2$ core QDs were prepared by mixing indium acetate and copper iodide with dodecanethiol and octadecene under argon. QD emission wavelengths red-shifted with increasing reaction time. To form the ZnS shell, zinc stearate and zinc ethylxanthate were added to the core QD solutions at the same temperature. The authors transferred the QDs to water for in vivo imaging by ligand exchange using dihydrolipoic acid (DHLA). The PL lifetimes of the core/shell QDs reached hundreds of nanoseconds. $CuInS_2$/ZnS QDs with tunable emission from yellow to red and a maximum QY of 65% were prepared by Nam and co-workers.[283] In their method, copper(I) iodide, indium acetate, 1-dodecanethiol, and 1-octadecene were heated in a sealed autoclave to produce $CuInS_2$ core QDs with a PL QY up to 8.8%. Zinc ethylxanthate, dimethylformamide (DMF), and toluene were then added to the core QD dispersion and autoclaved. Along with dramatically increased QY, blue shifts of the emission peaks were observed for the core/shell QDs due to the decrease of the core QD size during the shell growth. Later, Chen et al.[165] demonstrated a green aqueous-phase synthesis of $CuInS_2$/ZnS QDs with a QY of 38% using sodium citrate and L-glutathione as costabilizers. Briefly, $CuInS_2$ core QDs were prepared by mixing $CuCl_2$ and $InCl_3$ at a molar ratio of 1:4 with sodium citrate (4:1 to In^{3+}) and L-glutathione, followed by injection of Na_2S. An aqueous mixture of zinc acetate, thiourea, and L-glutathione was added to the core QD dispersions. The emission peaks of the QDs could be tuned from 543 to 625 nm by changing the Cu:In precursor ratio (Figure 22).

More recently, Xiong et al. reported a microwave-assisted synthesis method for preparing water-dispersible $CuInS_2$/ZnS QDs in which glutathione (GSH) was used as a stabilizing agent (ligand).[166] $CuInS_2$ core QDs were prepared by mixing aqueous $Cu(NO_3)_2$, $InCl_3$, and GSH with aqueous Na_2S at pH 8.5, and then heating in a Discover (CEM) microwave system. Zinc acetate and Na_2S were added to the core QD solution to form the core/shell QDs. The QDs had an average diameter of 3.3 nm and PL tunable from 540 to 680 nm by varying the Cu:In precursor ratio. The QD PL showed a long lifetime of 690 ns. Guo et al.[91] demonstrated that adding zinc ions in the $CuInS_2$ core synthesis before shell coating could reduce the blue shift of the PL during ZnS shell growth. This is attributed to ion accumulation and inhibition of cation exchange. ZnCuInS core QDs were prepared by mixing zinc stearate ($Zn(SA)_2$), copper iodide (CuI), indium acetate ($In(Ac)_3$), and oleic acid (OA) with 1-dodecanethiol (DDT) and 1-octadecene (ODE) under argon. The emission wavelength of the $ZnCuInS_2$ core QDs was tuned from 600 to 815 nm by varying the Cu:Zn precursor ratio from 2:1 to 1:5. For the ZnS shell coating, the core QDs were reacted with sulfur powder dissolved in ODE/oleylamine (10:1) and $Zn(SA)_2$. The ZnCuInS/ZnS (ZCIS/ZnS) core/shell QDs were transferred

DOI: 10.1021/acs.chemrev.6b00290
Chem. Rev. 2016, 116, 12234−12327

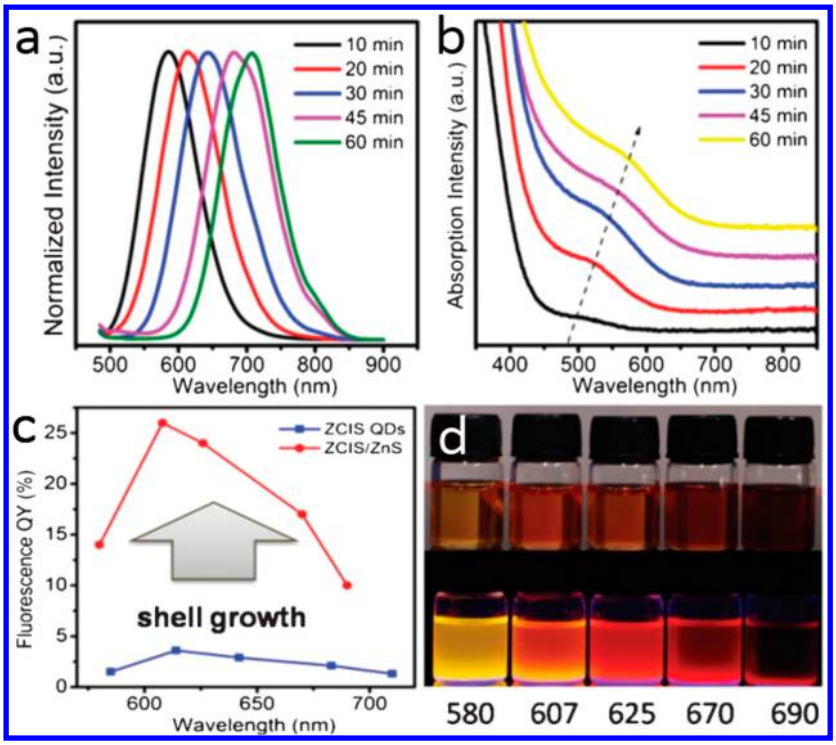

Figure 23. Temporal evolution of (a) PL emission spectra and (b) UV−vis absorbance spectra of ZCIS QDs dispersed in water. (c) PL QY and emission peak wavelength of QDs before and after ZnS shell growth. (d) Digital photograph of ZCIS/ZnS QDs dispersed in ethanol, taken under a 365 nm UV lamp. Reprinted with permission from Guo et al.[284] Copyright 2013 Royal Society of Chemistry.

to water using poly(maleic anhydride-*alt*-1-octadecene) (PMAO) molecules.

Later, the same group[284] developed a direct colloidal preparation method for water-dispersible ZnCuInS/ZnS QDs without the phase transfer steps that were required in the previous report. Briefly, hydrophilic ZnCuInS QDs were synthesized by mixing copper iodide (CuI), indium acetate ($In(Ac)_3$), zinc stearate, and 6-sulfanyl-1-hexanol (MPH) with poly(ethylene glycol) (PEG, 400 Da). ZnS shells were added by injection of zinc stearate dissolved in low molecular mass PEG. Here, the hydrophilic MPH ligands with mercapto and hydroxyl groups served as both sulfur precursor and stabilizing agent. The emission wavelength of the ZnCuInS core/shell QDs was tuned from 580 to 710 nm by changing the reaction time from 10 to 60 min (Figure 23). With the ZnS shell coating, the QY of the QDs increased from less than 5 to 26%. In another study, Han et al. employed a lipophilic silane to encapsulate hydrophobic $CuInS_2$/ZnS QDs in silica beads.[199] The $CuInS_2$/ZnS@SiO_2 nanocomplexes maintained a reasonably small diameter of 17−25 nm. Holo-transferrins (Tf) were then conjugated to these QDs as targeting molecules. Bright red PL was observed from HeLa cells incubated with $CuInS_2$/ZnS@SiO_2@Tf NPs.

4.3. Ag_2S and Ag_2Se Quantum Dots

Ag_2S and Ag_2Se QDs are promising NIR-II nanoprobes for in vivo imaging and detection with tunable emission wavelengths ranging from 1000 to 1400 nm.[208,285,286] Imaging in the NIR-II window allows one to obtain a maximum penetration depth up to 5 mm with high fidelity and signal-to-noise ratio because tissue autofluorescence and scattering signals are minimized in this wavelength range. The first synthesis of Ag_2S QDs with emission in the NIR-II region was demonstrated by Du and coworkers.[287] In a typical reaction, silver diethyldithiocarbamate (Ag(DDTC)) was mixed with oleic acid (OA), 1-octadecane (ODE), and octadecylamine (ODA). The mixture was heated to 100 °C to remove dissolved oxygen, and then reacted at 200 °C for 30 min under nitrogen. The QDs had an average diameter of 10 nm with high monodispersity and peak PL emission at 1058 nm under 785 nm excitation. Later, Jiang et al.[138] reported a two-step seed-mediated growth method for Ag_2S QDs (1.5−4.6 nm) with PL emission tunable from 690 to 1227 nm. The PL emission wavelength was tuned by changing the reaction temperature. Here, Ag_2S QD seeds were first prepared by mixing silver acetate (AgAc) solutions with 1-octylamine (OA), 1-octadecene, and myristic acid (MA), followed by rapid injection of hexamethyldisilathiane ($(TMS)_2S$) at a fixed reaction temperature to initiate QD nucleation. During the seed-mediated growth process, another Ag precursor (silver nitrate and OA in toluene) and sulfur precursor (S powder dissolved in toluene) were added to the Ag_2S QD seed solution to grow the QDs to the desired size (Figure 24).

Hocaoglu et al.[288] demonstrated a one-step aqueous synthesis of Ag_2S QDs with emission wavelengths from 780 to 950 nm and used them as biocompatible PL labels for in vitro imaging. The QDs had a QY of 7−39% and showed low cytotoxicity to mouse embryo fibroblast NIH/3T3 cells even at concentrations as high as 600 μg/mL. The emission peak of the QDs was tuned by changing the Ag to S precursor ratio or the MPA to Ag ratio (Figure 25).

A similar one-step method was reported by Jiang et al.[8] using 3-mercaptopropionic acid (3-MPA) and ethylene glycol (EG) rather than 2-MPA. In this case, the QD surface was terminated with carboxyl groups. The QD PL emission wavelength was broadly tunable, from 510 to 1221 nm, by varying the growth time. Typically, the precursor solutions of $AgNO_3$, MPA, and EG were first reacted at 110 °C under argon, and then heated

DOI: 10.1021/acs.chemrev.6b00290
Chem. Rev. 2016, 116, 12234−12327

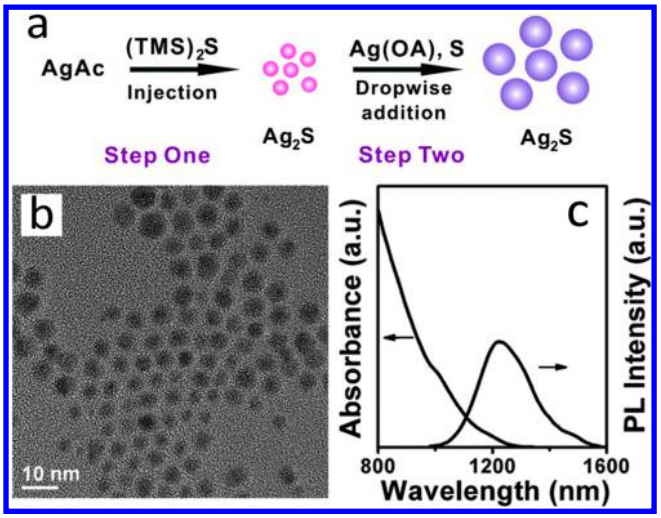

Figure 24. (a) Scheme of two-step synthesis of NIR Ag_2S QDs. (b) TEM image and (c) absorbance and PL spectra of Ag_2S QDs synthesized in step two. Reprinted from Jiang et al.[138] Copyright 2012 American Chemical Society.

to 145 °C for several minutes. During reaction, the white solution became yellowish and then dark brown. Ag_2S QDs were collected by centrifugation and redispersed in deionized (DI) water for further use, including in vivo small animal imaging.

Zhang et al.[289] synthesized PEGylated-Ag_2S QDs with strong NIR-II luminescence at 1200 nm through a facile thermal decomposition approach based on a single-source precursor.[21,290] They also evaluated the long-term in vivo biodistribution and toxicity of these QDs in mice. They prepared a single-source precursor, $(C_2H_5)_2NCS_2Ag$, by mixing $AgNO_3$ with $(C_2H_5)_2NCS_2Na{\cdot}3H_2O$ (Na(DDTC)) and then adding 1-dodecanethiol (DDT). A ligand exchange process was used to replace the DDT with dihydrolipoic acid (DHLA), thereby making the QDs hydrophilic. The PEG-conjugated Ag_2S QDs were obtained after 30 min sonication of the DHLA-capped QDs with a solution of six-armed PEG and EDC/NHS.

Wang et al.[290] demonstrated that the emission wavelength of the Ag_2S QDs prepared by this method was independent of the particle size. However, the PL intensity decreased with increasing QD diameter from 5.4 to 10 nm. Hong et al.[21] studied the photostability of PEGylated-Ag_2S QDs under 808 nm excitation at 0.14 W/cm^2. The PL intensity remained stable for 200 s and was reduced by only 50% after 30 min continuous irradiation, which was much longer than the typical illumination time of 2 min for in vivo imaging. A one-pot synthesis method for preparing bovine serum albumin (BSA)-functionalized Ag_2S QDs with near IR PL was developed by Wang and co-workers.[291] They further conjugated these QDs with vascular endothelial growth factor antibodies (antiVEGF) for targeted in vivo imaging of VEGF positive U-87 MG human glioblastoma tumors in mice. The Ag_2S QDs were synthesized by first mixing $AgNO_3$ and BSA solutions. A Na_2S solution was quickly injected into the BSA−Ag^+ mixture with intense agitation. The mixture was then incubated at 37 °C for 12 h. The color of the mixture changed from light yellow to colorless and finally reddish brown. For VEGF bioconjugation, antiVEGF was first processed at room temperature with *N*-(3-(dimethylamino)-propyl)-*N*′-ethylcarbodiimide hydrochloride (EDC) and *N*-hydroxysulfosuccinimide sodium salt (sulfo-NHS) in PBS for 15 min. The antiVEGF mixtures were then added to the BSA−Ag_2S QD dispersions and reacted at 4 °C for 12 h to obtain antiVEGF-Ag_2S QDs for biological labeling.

To obtain both UV/blue (380−450 nm) and near-IR (1155−1175 nm) PL from a single nanostructure, Shen et al.[292] designed Ag_2S−ZnS heteronanostructures having a matchstick shape with Ag_2S QDs as the heads and ZnS quantum rods as the stems. These hybrid quantum rods were synthesized by a one-pot thermal decomposition method, and their size could be tuned by changing the ratio between the silver diethyldithiocarbamate (Ag(DDTC)) and zinc diethyldithiocarbamate ($Zn(DDTC)_2$) precursors. Ag(DDTC) and $Zn(DDTC)_2$ precursors were first prepared by mixing silver nitrate/zinc acetate and sodium diethyldithiocarbamate (Na(DDTC)) for 3 h. Then, Ag(DDTC) and $Zn(DDTC)_2$ precursors were mixed with oleylamine and 1-dodecanethiol

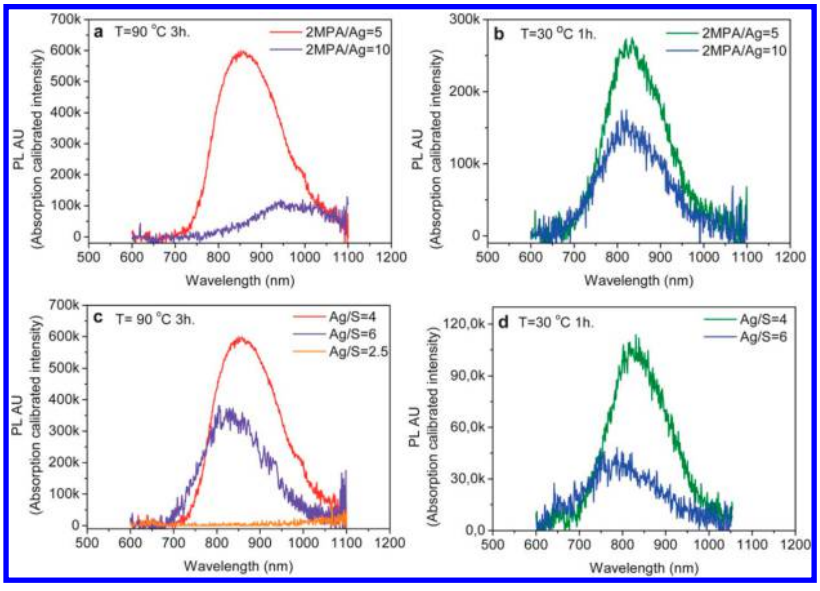

Figure 25. PL spectra of Ag_2S QDs prepared at different 2MPA/Ag ratios at (a) 90 and (b) 30 °C, and at different Ag/S ratios at (c) 90 and (d) 30 °C. Reprinted with permission from Hocaoglu et al.[288] Copyright 2012 Royal Society of Chemistry.

DOI: 10.1021/acs.chemrev.6b00290
Chem. Rev. 2016, 116, 12234−12327

and heated to 70 °C for 20 min and then to 160 °C for 30 min. The diameter of the Ag_2S head in the heterostructures was around 8.5 nm and the stem size was ~7.8 × 35 nm when a 1:2 Ag(DDTC):$Zn(DDTC)_2$ molar ratio was used in the synthesis. With an increased molar ratio of 2:1, the diameter of the Ag_2S head in the heterostructures was around 4.5 nm and the stem size was ~4 × 48 nm. Both the UV/blue and NIR emission peaks were red-shifted with increasing diameter of the Ag_2S–ZnS heteronanostructures. Later, the same group[293] modified the synthesis approach to demonstrate one-pot fabrication of manganese (Mn)-doped Ag_2S–ZnS quantum rods with multicolor PL in three wavelength regions including blue, orange, and NIR (Figure 26). The orange emission (580–590 nm) of the heteronanostructures was due to the $^4T_1$–$^6A_1$ transition of Mn ions in the ZnS lattice. Blue emission resulted from the ZnS stems while the NIR emission was attributed to the band gap emission of Ag_2S QDs (match heads).

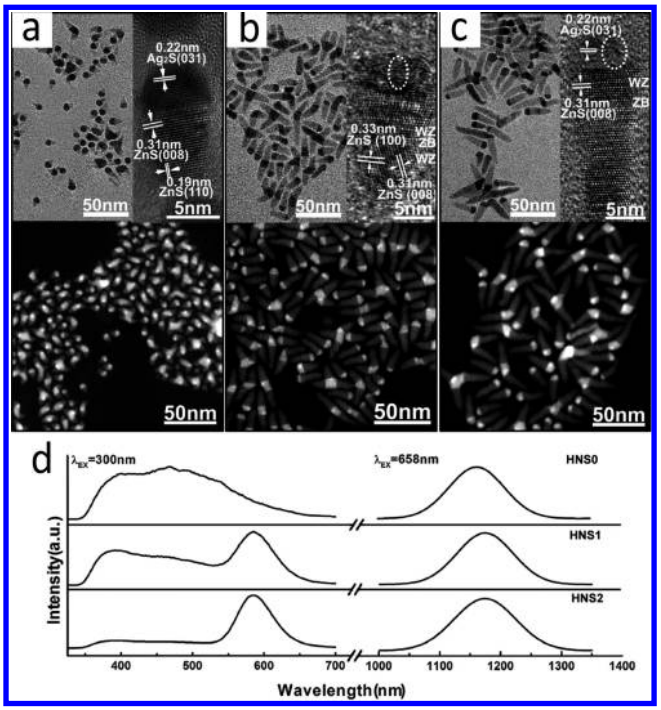

Figure 26. TEM, HRTEM, and STEM images of Ag_2S–ZnS heteronanostructures doped with (a) 0, (b) 2.1, and (c) 5.9% Mn^{2+}. (d) Normalized PL and NIR PL spectra of Ag_2S–ZnS heteronanostructures with (upper) 0, (middle) 2.1, and (lower) 5.9% Mn^{2+} dopants. Reproduced from Shen et al.[293] Copyright 2012 American Chemical Society.

A biomimetic green synthesis approach was developed by Gu and co-workers[294] for preparing water-dispersible ultrasmall Ag_2Se QDs ranging from 1.5 ± 0.4 to 2.4 ± 0.5 nm diameter, with corresponding PL peaks from 700 to 820 nm (Figure 27). The Ag and Se precursors were prepared by processes that mimicked binding of Ag^+ with alanine and reduction of selenite from SeO_3^{2-} to GSSeH in yeast cells. Ag_2Se QDs were generated by injecting the Se precursor into the Ag^+–Ala precursor and reacting at 90 °C for 10 min under nitrogen. The size of the Ag_2Se QDs was tuned by changing the Ag:Se precursor ratio.

Dong et al. developed a solvothermal approach to fabricate luminescent Ag_2Se QDs with bright emission at 1300 nm.[139] Silver nitrate was heated in oleylamine (OAm) and toluene until it became transparent. The Ag–OAm solution was then reacted with dodecanethiol (DDT) and NaHSe at 180 °C for 1 h, followed by ethanol precipitation and collection by centrifugation. The QY of these QDs reached 70%. Their size and PL were tuned by changing the Ag to Se precursor ratio. A PEG grafted amphiphilic polymer, poly(maleic anhydride-*alt*-1-octadecene)–methoxy poly(ethylene glycol) (C18-PMH-PEG), was used to transfer the QDs into water for biological applications (Figure 28). They used these QDs as PL labels in the first demonstration of in vivo imaging using NIR-II emission of Ag_2Se QDs.

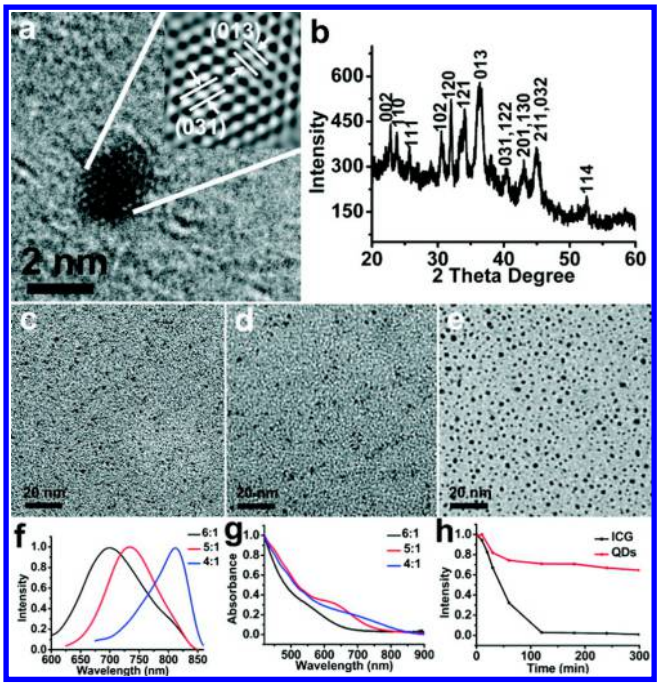

Figure 27. Characterization of Ag_2Se QDs synthesized in water. (a) HRTEM image; (b) XRD pattern; (c–e) TEM images of Ag_2Se QDs synthesized at 6:1 (c), 5:1 (d), and 4:1 (e) Ag:Se precursor ratios; (f) PL emission spectra; (g) absorbance spectra; and (h) photostability curve of Ag_2Se QDs. Reprinted from Gu et al.[294] Copyright 2012 American Chemical Society.

4.4. ZnS–$AgInS_2$ (ZAIS) Quantum Dots

Ternary I–III–VI $AgInS_2$ QDs with a band gap of 1.8 eV are promising nanoprobes for in vivo imaging because their emission wavelength can fall in the red to NIR range.[295] However, biological applications of these QDs have been limited due to their low PL QY and relatively broad emission spectra. Torimoto et al.[170] demonstrated a thermal decomposition synthesis of ZnS–$AgInS_2$ (ZAIS) QDs with a QY of 24% and PL emission peak tunable from 540 to 720 nm. PL tunability arises from the energy gap change with varying ZnS content in the ZnS–$AgInS_2$ alloy QDs (Figure 29). In this study, precursor solutions containing $(AgIn)_xZn_{2(1-x)}(S_2CN(C_2H_5)_2)_4$ were first prepared by mixing sodium diethyldithiocarbamate with $AgNO_3$, $In(NO_3)_3$, and $Zn(NO_3)_2$ in a molar ration of x:x:2(1 − x), followed by 30 min heating at 180 °C. After purification and drying, the brown precursor powder was dissolved in oleylamine and then reacted at 180 °C for 3 min under nitrogen. The highest QY of 24% was obtained with an x value of 0.86. The emission wavelengths of ZAIS QDs red-shifted with increasing x.

DOI: 10.1021/acs.chemrev.6b00290
Chem. Rev. 2016, 116, 12234–12327

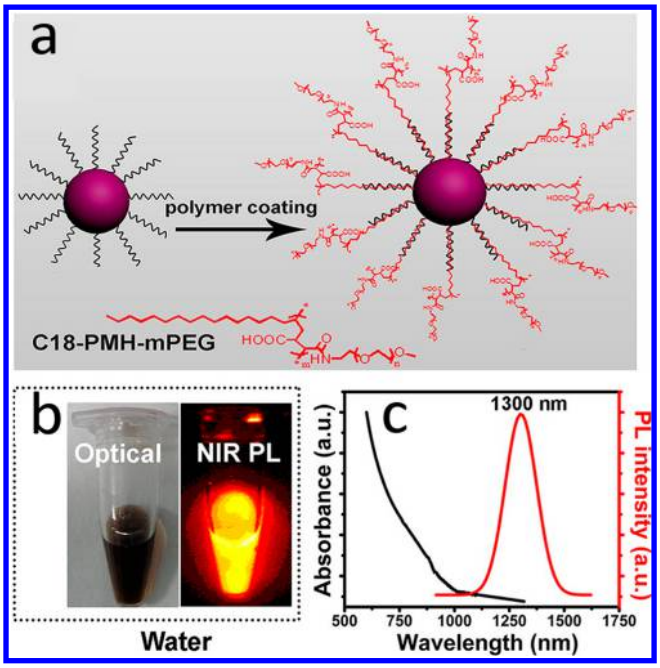

Figure 28. Optical properties of Ag_2Se QDs coated with C18-PMH-PEG polymer. (a) Scheme for C18-PMH-PEG polymer coating on the surface of organic synthesized Ag_2Se QDs. (b) White light optical image and PL image of C18-PMH-PEG-Ag_2Se QDs dispersed in water. (c) Absorbance and PL spectra of C18-PMH-PEG-Ag_2Se QDs in water. Reprinted from Dong et al.[139] Copyright 2013 American Chemical Society.

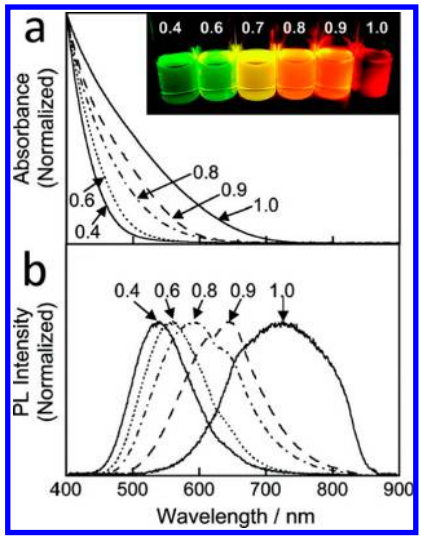

Figure 29. (a) Absorbance and (b) PL spectra of ZnS−$AgInS_2$ (ZAIS) QDs. The value of x in the $(AgIn)_xZn_{2(1-x)}(S_2CN(C_2H_5)_2)_4$ precursor is indicated in the figure. The inset in panel a shows a photograph of ZAIS QDs under UV illumination. Reprinted from Torimoto et al.[170] Copyright 2007 American Chemical Society.

Subramaniam et al.[171] demonstrated a facile room-temperature sonochemical approach for rapid synthesis of a series of $Zn_xS-Ag_yIn_{1-y}S_2$ (ZAIS) QDs of varied composition. The QD PL was tuned from blue to red (480−700 nm) by changing the cation composition (x and y). The PL of these QDs showed less size dependence than that of CdSe or CdTe QDs. Precursor solutions prepared by mixing sodium diethyldithiocarbamate ($NaS_2CN(C_2H_5)_2$) with solutions of $AgNO_3$, $In(NO_3)_3{\cdot}xH_2O$, and $Zn(NO_3)_2{\cdot}6H_2O$ were reacted with dodecylamine by sonication for 5 min at an optimum frequency of 20 kHz and output power of 200 W. 3-Mercaptopropionic acid (MPA) was used to modify the dodecylamine-coated ZAIS QDs to make them water dispersible. The QDs were used for both brain tumor cell and stem cell imaging, and also served as siRNA nanocarriers for targeting cancer cells. Recently, Hsu's group reported a two-step, one-pot synthesis of highly luminescent $AgInS_2$/ZnS QDs by directly injecting Zn and S precursors into a dispersion of as-prepared $AgInS_2$ cores without purification, resulting in a dramatic increase of QY from 22 to 60%.[46] The core/shell QDs were coated with PMAO polymers and then conjugated with folic acid (FA) to label HepG2 cells.

Gu's group reported the aqueous synthesis of quaternary Zn−Ag−In−S (ZAIS) QDs with PL emission tunable from 525 to 625 nm and a QY of 15−30%.[296] Then QDs were modified using DHLA-PEG functionalized with folic acid and RGD peptide. FA receptor-negative and positive cells, A549 and BEL-7402 cells, were coincubated with the QD-PEG2000-FA probes. This study demonstrated enhanced cell penetration and nuclear binding by the folate modified QDs. In addition, the QD-PEG2000-RGD probes were coincubated with $\alpha_v\beta_3$-positive MDA-MB-231 cells and $\alpha_v\beta_3$-negative MCF-7 cells to investigate their targeting ability. QDs incubated with MDA-MB-231 cells were internalized through phagocytosis and mainly accumulated in the cytoplasm.

4.5. ZnSe/InP/ZnS Quantum Dots

Kim et al.[177] reported the synthesis of type II QDs with a ZnSe/InP/ZnS core/shell/shell structure with PL emission tuned from blue to red by tuning the thickness of the inner InP shell layer. The QY was improved by addition of the outer ZnS shell. In the first step, ZnSe cores were prepared from diethyl zinc (Et_2Zn) and tri-*n*-octylphosphine selenide (TOP-Se) by first heating hexadecylamine (HDA) and tri-*n*-octylphosphine oxide (TOPO) under nitrogen at 125 °C for 2.5 h and then increasing the temperature to 320 °C, followed by injection of a solution containing Et_2Zn and TOP-Se. The mixture was held at 270 °C for 1 h. After cooling to room temperature, zinc acetate powder was added, and the mixture was heated to 230 °C for 3 h to obtain the ZnSe QDs. The use of zinc acetate eliminated surface traps and improved the QY from 20 to 43%. InP shells were coated on the ZnSe cores by adding solutions of tris(trimethylsilyl)phosphine and tributylphosphine-indium followed by reaction at 210 °C. The outer ZnS shells were coated onto the ZnSe/InP by adding zinc acetate at room temperature followed by reaction at 230 °C for 4 h and another 1 h reaction with 1-dodecanethiol. The ZnSe/InP/ZnS core/shell/shell QDs had an average size of 5.4 nm and a QY of 60%.

4.6. InAs/InP/ZnSe Quantum Dots

InAs/InP/ZnSe core/shell/shell QDs with NIR emission at 800 nm were also prepared by Gao et al.[297] They functionalized these QDs with mercaptopropionic acid (MPA) and human serum albumin (HSA) for in vivo tumor imaging. Briefly, InAs core QDs were first synthesized, as described by Xie et al.,[298] by heating indium stearate, trioctylphosphine (TOP), and octadecene (ODE) to 150 °C under argon, followed by addition of $As(Si(CH_3)_3)_3$. The InAs QDs were obtained after 75 min reaction at 300 °C. The InAs core QDs were cooled to 110 °C, and then stearic acid in ODE and tris(trimethylsilyl)-phosphine ($(TMS)_3P$) in octylamine were added. The reaction mixture was heated to 178 °C for 45 min to form the InAs/InP core/shell QDs. Finally, Se dissolved in TOP was injected,

DOI: 10.1021/acs.chemrev.6b00290
Chem. Rev. 2016, 116, 12234−12327

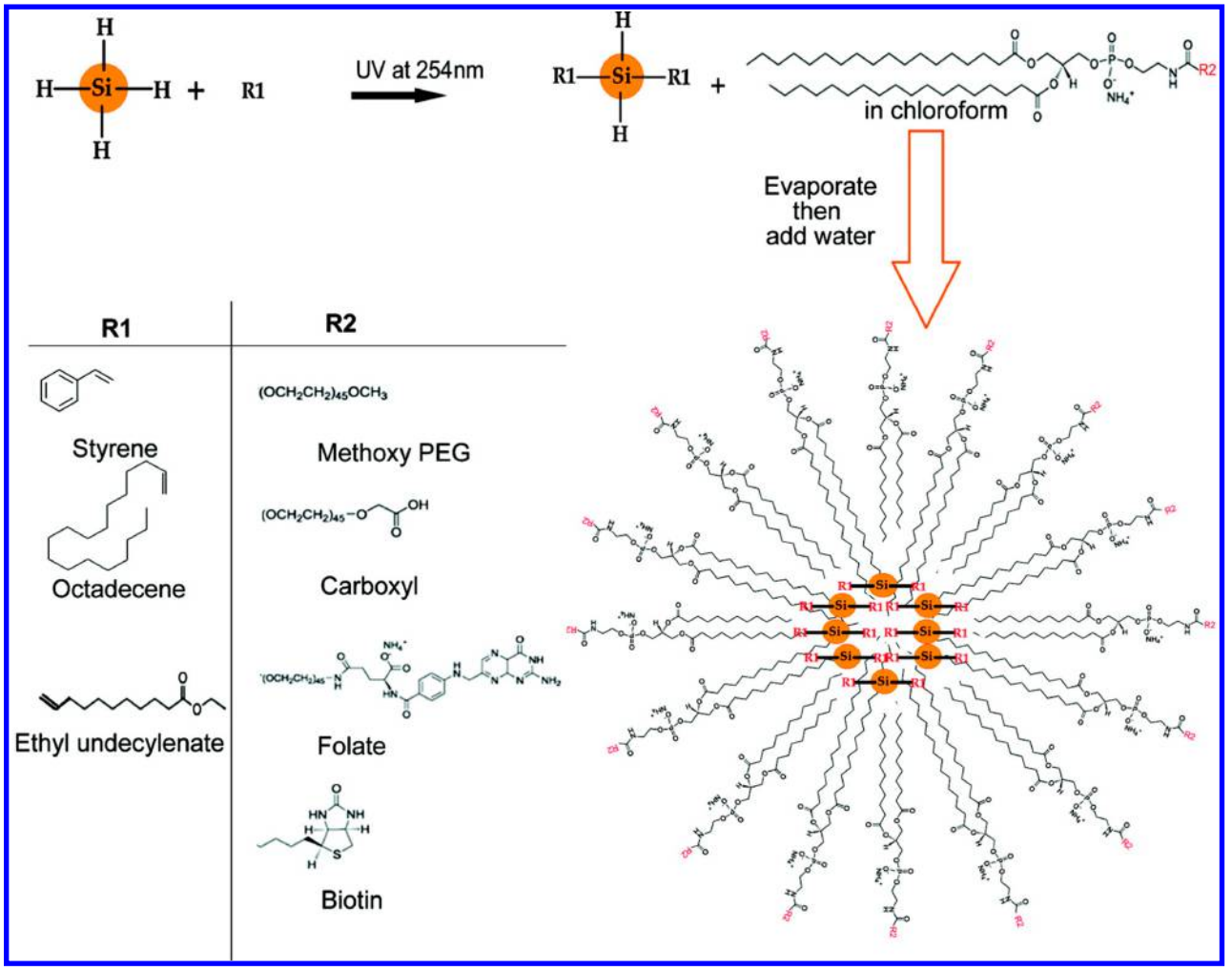

Figure 30. Scheme of surface functionalization of Si QDs using organic compounds (R1) followed by micellar encapsulation using phospholipids with different functional groups (R2). Reprinted from Erogbogbo et al.[65] Copyright 2008 American Chemical Society.

followed by zinc undecylenate solution. A 30 min reaction at 220 °C produced the outer ZnSe shell on the InAs/InP QDs.[299] The QDs were then transferred to water using MPA. Finally, human serum albumin (HSA) was attached to the QDs through electrostatic interactions.

4.7. Silicon Quantum Dots

In this section, we highlight the recent developments on the synthesis of silicon QDs (Si QDs) for biological applications.[300] Erogbogbo et al.[38] prepared RGD peptide-conjugated Si QDs and used them for in vivo multichannel bioimaging and sentinel lymph node (SLN) mapping. In that study, nonluminescent Si QDs with diameters of 5−10 nm were first obtained through high-temperature CO_2 laser pyrolysis of SiH_4. These QDs were dispersed in methanol and etched with hydrofluoric acid and nitric acid for 2−4 min to form hydrogen-terminated Si QDs that exhibited bright PL.[65] Organic molecules were covalently attached to the QD surface via hydrosilylation, yielding stable colloidal dispersions in organic solvents (Figure 30). For biological applications, the QDs were encapsulated in PEGylated phospholipid micelles using DSPE-PEG(2000). The mixture was sonicated and evaporated before conjugating with thiolated RGD peptide. Later, the same group[242] demonstrated the preparation of F127 block copolymer-encapsulated Si QDs and showed that the nanoformulation did not show any adverse impact to monkeys injected with 200 mg/kg QDs. In this study, the QDs exhibited near-IR emission peaking at 800 nm, and could be imaged using NIR excitation and emission wavelengths.

Water-dispersible Si QDs (20−40 nm) with ultrahigh stability against UV light irradiation were synthesized by Shen et al.[301] using a two-step approach. The Si QDs were first prepared by 13.56 MHz radio frequency (rf) plasma-assisted decomposition of $SiBr_4$. The QDs were then dispersed in toluene via sonication and treated with HF to remove surface oxides. Then, a solution containing a block copolymer (Pluronic F127) was added into the Si−toluene dispersion. After 10 h reaction, F127-coated Si QDs were formed and showed a higher PL stability in live cells (>30 min) compared to endoplasmic reticulum (ER)−tracker red (<90 s).

Shiohara et al.[302] prepared Si QDs of varying size using a microemulsion technique. The particle size was tuned by changing the hydride reducing agents used in synthesis. The stronger the hydride reducing agent used, the smaller the size and narrower the size distribution of the QDs. Typically, hydrogen-terminated Si QDs were first prepared by dissolving $SiCl_4$ in anhydrous hexane and pentaethylene glycol monododecyl ether ($C_{12}E_5$) and then reacting it with allylamine under 4 h UV-irradiation. The surface-passivated Si QDs were further purified through size-exclusion chromatography (SEC).

DOI: 10.1021/acs.chemrev.6b00290
Chem. Rev. 2016, 116, 12234−12327

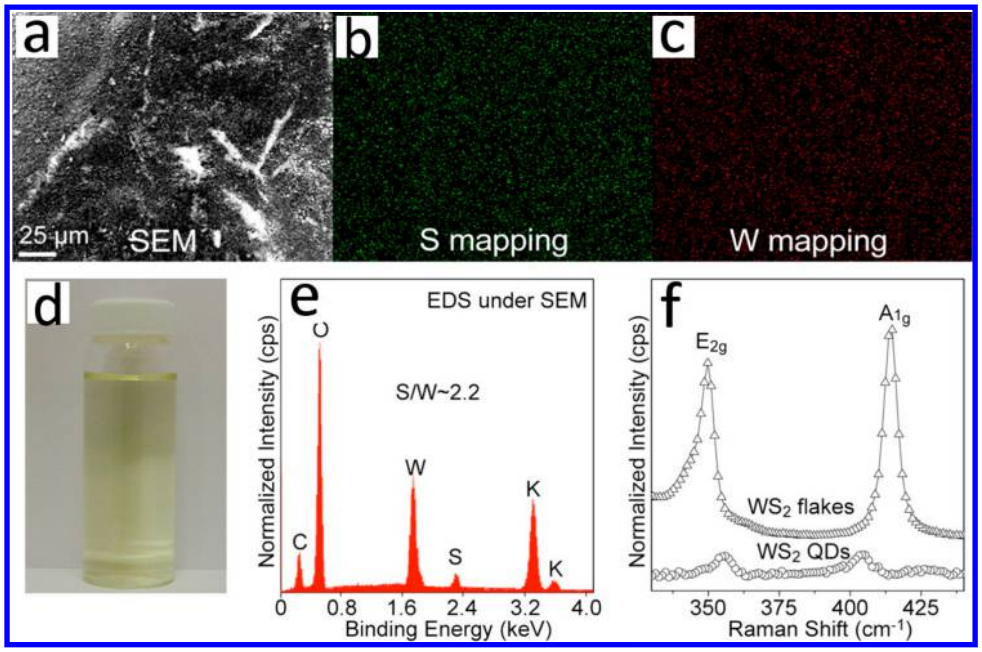

Figure 31. Characterization of exfoliated and disintegrated WS_2 QDs. (a) SEM image and (b and c) EDS elemental mapping of the dried suspension; (d) photograph of the WS_2 QD suspension; (e) EDS analysis and (f) Raman analysis of the dried suspension. Reprinted from Lin et al.[183] Copyright 2013 American Chemical Society.

A one-step method of producing ssDNA conjugated Si QDs (4 nm) using pulsed laser ablation in liquid (PLAL) was demonstrated by Intartaglia et al.[178] Single stranded DNA was added to DI water in which bulk Si was then ablated by femtosecond laser pulses. The attached DNA molecules were not denatured during the ablation process, and these bioconjugates could be applied for labeling.

Cheng et al.[179] reported a novel colloidal solution method for the synthesis and functionalization of Si QDs with PL QY of ~5.2% and used them for imaging of HeLa cancer cells. Si QDs were prepared through a microemulsion process by reducing halogenated silane precursors. To make the QDs dispersible in both polar and nonpolar solvents, the hydrogen-terminated QDs were functionalized with 1,8-nonadiyne molecules by UV-promoted hydrosilylation and then purified by size-exclusion chromatography, followed by modifying their surface with azide molecules through a copper(I)-catalyzed azide alkyne cycloaddition (CuAAC) "click" reaction. In a typical click reaction, 10 mg of nonadiyne–Si QDs were first dispersed in 3 mL of DI water and 3 mL of dimethylformamide (DMF). Then $CuSO_4$, L-sodium ascorbate, and azides (molar ratio of 1:20:100) were added. The mixture was stirred overnight at room temperature to produce the biocompatible Si QDs. The authors showed that this multistep functionalization approach enabled a higher efficiency of attachment of the desired groups than a conventional single-step method.

4.8. ZnO Quantum Dots

A facile sol–gel preparation of biocompatible polymer-coated ZnO QDs with emission wavelengths in the green (520 nm) and yellow regions (550 nm) was reported by Xiong and coworkers.[182] They mixed zinc methacrylate in ethanol with poly(ethylene glycol) methyl ether methacrylate (PEGMEMA) and 2,2′-azobis(isobutyronitrile) (AIBN) molecules. The mixtures were reacted at 80 °C for 2 min, followed by the addition of LiOH and AIBN solutions and refluxing for 1 h. ZnO QDs with green emission and a QY of 50% were obtained after dialysis in DI water for 3 days. The synthesis protocols for ZnO QDs with yellow emission were similar except that the LiOH was replaced by NaOH. The QDs were nontoxic and were used for cytoplasm imaging at concentrations up to 0.2 mg/mL. More recently, Asok et al.[181] demonstrated a room-temperature synthesis method for ZnO QDs based on ethanolic precipitation. Solutions containing Zn^{2+} precursors and LiOH were degassed in an ultrasonic bath, and the reaction vessel was purged with nitrogen. The ZnO QD surface exhibited a high concentration of oxygen due to the oxygen deficient conditions, leading to bright PL from these defects, with a QY of 60%. QDs with average diameters from 2.9 to 12.2 nm were produced by varying the [Zn]/[LiOH] precursor ratio from 0.25 to 2. This was attributed to counterion capping on the hydroxylated QD surface. The emission peak of the ZnO QDs was found to be size-dependent and could be tuned from ~450 to 550 nm.

4.9. WS_2 Quantum Dots

Two-dimensional transition metal dichalcogenide (TMDC) nanomaterials such as tungsten disulfide (WS_2) and molybdenum disulfide (MoS_2) have a structure similar to that of graphene, with atomically thin layers held together only by van der Waals interactions.[303,304] Recently, Lin et al.[183] fabricated luminescent WS_2 QDs by chemical exfoliation, similar to the approach used to exfoliate and cut graphite into graphene QDs. In general, there were three main steps: (i) WS_2 was intercalated by potassium atoms, exploiting the weak van der Waals force between the WS_2 layers; (ii) air exposure at room temperature produced deintercalation of the K–WS_2 mixtures; and (iii) first EtOH and then H_2O were added, and the solution was ultrasonicated for 2 h. After filtration, a WS_2 QD dispersion with yellow color was collected (Figure 31). Because the intercalation in the first step expanded the interlayer distance, exfoliation to single layers with reduced sizes was easily achieved by the ultrasonication process. The WS_2 QDs were characterized as monolayer structures with lateral sizes from 8

DOI: 10.1021/acs.chemrev.6b00290
Chem. Rev. 2016, 116, 12234–12327

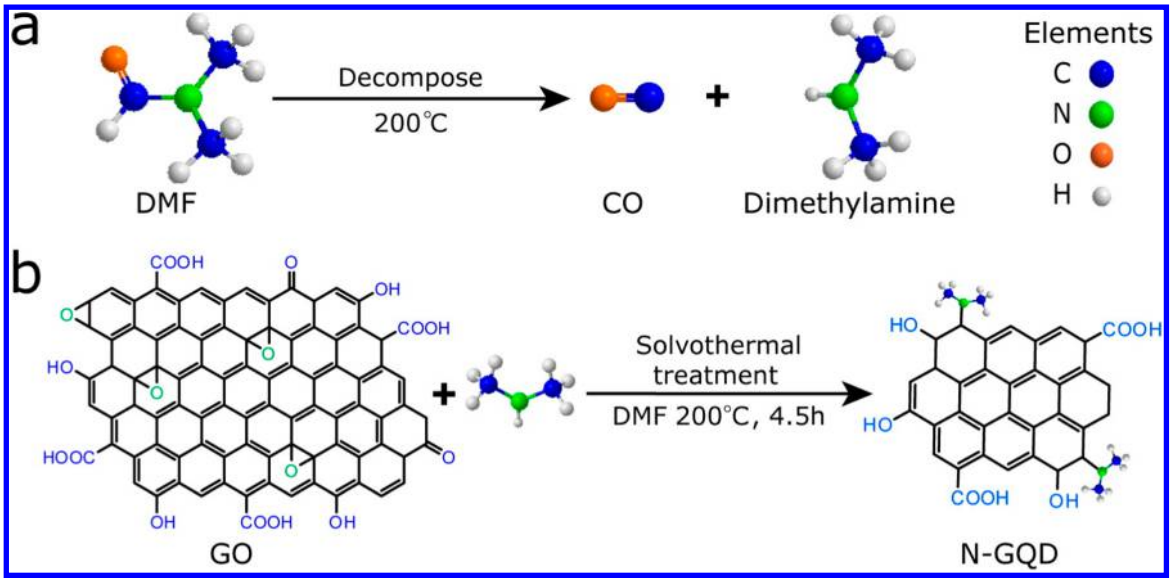

Figure 32. Scheme for preparation of nitrogen-doped graphene QDs (N-GQDs). (a) Decomposition of DMF at a high temperature. (b) Reduction of GOs to N-GQDs in the presence of DMF. Reprinted from Liu et al.[6] Copyright 2013 American Chemical Society.

to 15 nm. UV−vis absorbance spectroscopy showed that the transition energy of WS_2 QDs (3.16 eV) was much larger than that of the pristine WS_2 sheets (2.1 eV), leading to a bright green-blue PL that could not be observed in the WS_2 flakes. WS_2 QDs were used for in vitro imaging at a concentration of 50 μg/mL.

4.10. Graphene Quantum Dots

In general, there are two types of luminescent carbon-based QDs, i.e., carbon nanodots and graphene QDs.[305] Carbon nanodots are quasi-spherical carbon NPs with an average diameter less than 10 nm. Structurally, they are either amorphous or crystalline carbon with sp^2-bonded clusters. Graphene QDs are similar in size to carbon nanodots but clearly possess the crystalline structure of single or multiple graphene layers (usually three or fewer layers). In this review, we only consider graphene QDs as they exhibit features similar to other QDs.

Luminescent graphene QDs were prepared by Pan et al.[306] in 2009 by cutting micrometer-scale reduced graphene oxide (rGO) into 9.6 nm graphene QDs via a hydrothermal treatment. The graphene QDs showed strong blue PL. Such PL is not observed from pristine graphene sheets or graphene nanoribbons with larger lateral dimensions. The authors attributed the luminescence to edge effects in the graphene QDs. TEM imaging showed that the (002) interlayer spacings were 3.64 and 3.34 Å for reduced GO and bulk graphite, respectively. The first step of the graphene QD synthesis involves the oxidation of rGOs with strong acid mixtures of HNO_3 and H_2SO_4. The size of the rGOs decreased from several micrometers to 50 nm to 2 μm, while their (002) interlayer spacing increased to 3.85 Å. After hydrothermal treatment at 200 °C, their size was reduced below 10 nm and the (002) interlayer spacing decreased to 3.43 Å, close to that of bulk graphite. The interlayer spacing change confirms the deoxidization of the graphene sheets.

Later, a one-pot hydrothermal preparation method for poly(ethylene glycol) (PEG)-functionalized graphene QDs was reported by Shen et al.[184] They first prepared GO via the Hummers method and then oxidized the GO with concentrated HNO_3 at 70 °C for 24 h. The resulting suspensions were ultrasonicated mildly after cooling to room temperature. In the next step, PEG10000 was added, and the mixtures were autoclaved at 200 °C for 24 h, followed by dialysis for 7 days. The emission wavelength of the graphene QDs-PEG was 360 nm and their QY was ∼28%, which was double that of graphene QDs without the PEG surface passivation.

Deviating from previous preparation methods for graphene QDs, Peng et al.[307] developed a much simpler approach using low-cost and commercially available carbon fibers. Pitch-based carbon fibers are resin-rich materials. Graphene QDs were obtained by chemically exfoliating the carbon fibers (CFs) with strong acids (H_2SO_4 and HNO_3 in a volume ratio of 3:1). The mixture of CFs and acids was first sonicated for 2 h and then stirred for 24 h at a fixed reaction temperature. The submicrometer-scale stacked graphitic planar structures of the carbon fibers were easily broken down to produce graphene QDs with diameters from 1 to 4 nm. The as-prepared graphene QDs showed good dispersibility in water and polar solvents such as dimethyl sulfoxide (DMSO) and dimethylformamide (DMF). Their thicknesses ranged from one to three layers. Their emission wavelength was size dependent and was tuned by changing the reaction temperature from 80 to 120 °C. Dong et al.[308] demonstrated a one-step synthesis method for simultaneous production of single layer and multilayer graphene QDs. They used CX-72 carbon black as a precursor to produce large batches of QDs at low cost. The CX-72 carbon black was chemically oxidized by concentrated HNO_3. After refluxing for 24 h, the mixture was centrifuged at 2770*g* for 10 min. The supernatant was heated at 200 °C to evaporate water and residual acids. The graphene QDs from the supernatant were single-layer structures. The precipitates were purified by hydrochloric acid treatment, dried in vacuum, dispersed in DI water, and filtered through a 100-kDa membrane. The filtrates were multilayer graphene QDs. The authors suggested that the monolayer graphene QDs are potential candidates for bioimaging, and multilayer GQDs may serve as building blocks for optical or electronic devices.

Protein-functionalized graphene QDs for immunosensing applications were produced by Zhao et al.[309] Briefly, graphene

DOI: 10.1021/acs.chemrev.6b00290
Chem. Rev. 2016, 116, 12234−12327

QDs were prepared from powders containing GO sheets by reaction with *N*,*N*-dimethylformamide and dichlorosulfoxide at 80 °C for 72 h. The mixture was then centrifuged and collected as the precipitate, followed by washing with anhydrous tetrahydrofuran. After evaporation, the product was mixed with *n*-butylamine and heated at 60 °C for 96 h to form a yellow solution containing graphene QDs. To functionalize the graphene QD surface with carboxyl groups, the solution was mixed with sodium hydroxide and chloroacetic acid and sonicated for 3 h to convert hydroxyl groups to carboxyl groups. Protein molecules like mouse IgG could then be covalently bound to carboxyl groups on the surface of graphene QDs by a *N*-(3-(dimethylamino)propyl)-*N*′-ethylcarbodiimide hydrochloride (EDC)/*N*-hydroxysuccinimide (NHS) reaction. The antibody-conjugated graphene QDs were further used in immunoassays for specific biomolecule detection.

Zhu et al.[310] investigated the luminescence mechanism of graphene QDs with different surface functionalizations, showing that the structure of the graphene QDs varied when the nonradiative recombination of electron−hole pairs was suppressed by functionalization. Graphene QDs with green PL emission were synthesized by a two-step solvothermal approach (Figure 32). GO was first reacted with DMF by 30 min ultrasonication and then autoclaved at 200 °C for 8 h, followed by purification using column chromatography. The epoxy and carboxyl groups on the surface of the graphene QDs could be reduced to hydroxyl groups using alkylamine coupling or reduction by sodium borohydride. The luminescence of the graphene QDs was tuned from green to blue using this surface modification technique. The authors asserted that the intrinsic state emission, and not defect state emission, is the dominant source of graphene QD luminescence. Up-converted luminescence from graphene QDs was also successfully demonstrated by exciting them with a pulsed NIR laser. Nitrogen-doped graphene QDs (N-GQDs) have recently shown promise as fluorescent labels for two-photon in vitro/in vivo imaging due to their large two-photon absorption cross section of up to 48 000 Göppert-Mayer (GM) units, which is much larger than either traditional organic dyes or Cd-based QDs. Liu and co-workers[6] demonstrated a one-pot synthesis method for making N-GQDs using GO in combination with dimethylformamide (DMF) as the nitrogen source. The GO precursors were first synthesized by the Hummers method and then dispersed into DMF. Heating decomposed the DMF into dimethylamine and CO. Doping of GO occurred via ring-opening reactions between dimethylamine and epoxy groups on the GO. The two-photon luminescence of the N-GQDs was excited by a femtosecond laser in the near-IR region. Imaging depths of up to 1800 μm were demonstrated in scattering tissue phantoms.

Wu and co-workers demonstrated a one-step thermolysis method for preparing luminescent graphene QDs (GQDs) with a QY of 54.5%.[185] In that study, L-glutamic acid was pyrolyzed at 210 °C. The color of the L-glutamic acid changed from transparent to brown after 45 s, indicating formation of the graphene QDs, which were recovered by centrifugation. These graphene QDs showed excitation-wavelength-dependent PL from blue to NIR wavelengths. Their NIR luminescence showed a large 455 nm Stokes shift. This unique property could be used to improve the sensitivity of QDs for distinguishing specific biotargets.

4.11. Doped ZnS/ZnSe Quantum Dots

Doped zinc chalcogenide QDs (e.g., ZnS and ZnSe QDs) are another type of Cd-free QDs that show great potential in bioimaging and bioanalysis.[311−313] Currently, doped QDs for biological applications are mainly based on doping with transition metal ions such as Mn^{2+} and Cu^{2+}. The emission lifetimes from these dopants are longer than that of the host QDs and that of typical tissue autofluorescence. The intrinsic toxicities of doped ZnS/ZnSe QDs containing nontoxic metals are significantly lower than those of CdSe and CdTe QDs. Manzoor et al.[314] reported a facile synthesis method for producing doped ZnS QDs with different dopants including Mn^{2+}, Cu^{2+}−Al^{3+}, Cu^{+}−F^{-}, and Cu^{+}−Al^{3+}−Mn^{2+} that exhibited PL ranging from 480 to 622 nm. Mn^{2+}-doped ZnS QDs with orange-red PL were prepared by mixing aqueous $ZnSO_4$ and $MnSO_4$ in a nitrogen atmosphere, and then injecting Na_2S at pH 6.5. Cu^{2+}−Al^{3+} codoped ZnS QDs were prepared by mixing $ZnSO_4$ and copper acetate under nitrogen, adding Na_2SO_3 to reduce Cu(II) ions to Cu(I), then adding aluminum chloride, and finally precipitation by Na_2S addition. Cu^{+}−Al^{3+}−Mn^{2+}-doped ZnS QDs were produced by the same process with manganese sulfate added along with the $AlCl_3$. The doped ZnS QDs were directly functionalized with folic acid (FA) through zinc(II)−carboxylate coordination. The FA-QDs were used to image human nasopharyngeal epidermoid carcinoma (KB) cells with folate receptors.

In addition to FA, mercaptopropionic acid (MPA) was also used as a stabilizing agent for doped ZnS QDs. MPA-functionalized Mn^{2+}-doped ZnS QDs were synthesized by Wu and co-workers[253,315,316] and used for phosphorescent sensing after further conjugation with glucose oxidase (GOD). Aqueous $ZnSO_4$ and manganese(II) acetate ($Mn(Ac)_2$) were mixed with MPA and reacted for 30 min under argon. The pH was adjusted to 11 using NaOH. Na_2S was then injected and reacted for 20 min at room temperature and then at 50 °C for 2 h. The MPA-functionalized Mn^{2+}-doped ZnS QDs were collected by precipitation and centrifugation, then redispersed in DI water. GODs were conjugated to the QD surface by an EDC/NHS procedure. The QY of the MPA-functionalized Mn^{2+}-doped ZnS QDs was ∼8.2%.[316] Later, Geszke et al.[119] improved the QY of MPA-functionalized Mn^{2+}-doped ZnS QDs to 22% by coating a ZnS shell onto the doped ZnS core. They used zinc acetate ($Zn(OAc)_2{\cdot}2H_2O$) and MPA as the ZnS shell precursors. The Zn^{2+}−MPA mixtures were reacted at pH 10.3 for 30 min under a nitrogen atmosphere, and then injected into dispersions of the MPA-functionalized Mn^{2+}-doped ZnS QDs. ZnS shells were formed on the core QD surface by decomposing the Zn^{2+}−MPA precursors at 100 °C for 7 h. The ZnS:Mn/ZnS core/shell QDs were coupled with 2,2′-(ethylenedioxy)-bis-ethylamine and then conjugated with FA through EDC/NHS chemistry.

More recently, Zhou et al.[317] demonstrated that deposition of nano fluorine-doped hydroxyapatite (nanoFAp) onto Mn^{2+}-doped ZnSe/ZnS core/shell QDs could further reduce their cytotoxicity. In this study, Mn^{2+}-doped ZnSe core QDs were prepared by a nucleation doping method.[316] Zn and Mn precursors were produced by mixing manganese chloride and zinc stearate with stearic acid. For the core QD synthesis, selenium powder was first reacted with oleylamine and octadecene at 100 °C for 30 min and then at 280 °C under argon, followed by the addition of Mn precursors. MnSe QDs were formed after 2 min reaction at 260 °C. Zinc precursors were then injected and reacted at 250 °C for 15 min.

DOI: 10.1021/acs.chemrev.6b00290
Chem. Rev. 2016, 116, 12234−12327

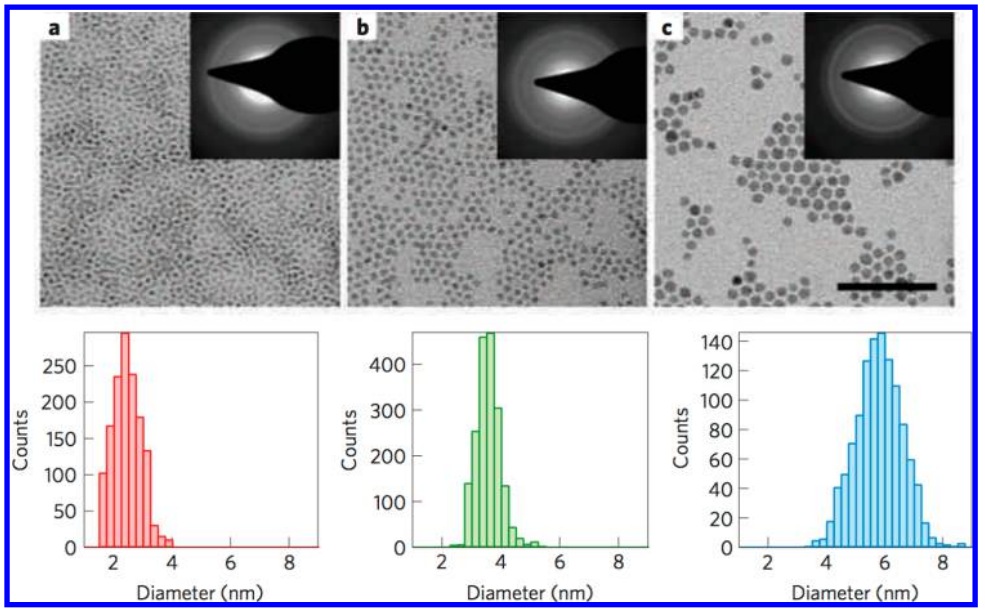

Figure 33. TEM images, (inset) SAED patterns, and size distribution histograms of three $Cu_{2-x}S$ QDs with average size of (a) 2.4 ± 0.5, (b) 3.6 ± 0.5, and (c) 5.8 ± 0.8 nm. Scale bar represents 50 nm. Reprinted with permission from Luther et al.[140] Copyright 2011 Nature Publishing Group.

Subsequently, mixtures containing the second Zn precursor and oleylamine were added and reacted at 240 °C for another 15 min. The Mn^{2+}-doped ZnSe core QDs were functionalized with MPA and reacted with Na_2S and zinc acetate, first at 50 °C and then at 70 °C for 40 min. To form the nanoFAp-QDs, the Mn^{2+}-doped ZnSe/ZnS core/shell QDs were conjugated with *O*-phosphoethanolamine (PEA)-modified nanoFAp in an optimum weight ratio of 1:2 through covalent binding.

4.12. Plasmonic Copper Chalcogenide Quantum Dots

Plasmonic copper chalcogenide QDs have only recently been introduced into the biomedical field.[141,260,261] These QDs exhibit localized surface plasmon resonance (LSPR) properties like those observed in noble metal NPs. Because they have a much lower free charge carrier density than metallic NPs, their LSPR absorption peak is at much longer wavelength, typically in the NIR region that is optimal for biological applications like photothermal therapy and photoacoustic imaging. Zhao et al.[172] synthesized $Cu_{2-x}S$ (x = 1, 0.2, 0.03) QDs with stoichiometry-dependent NIR absorbance by three different approaches, including sonoelectrochemical, hydrothermal, and solventless thermolysis methods. $Cu_{1.97}S$ QDs exhibited better stability in air than did Cu_2S QDs. With the sonoelectrochemical approach, the composition of the QDs could be changed from covellite (CuS) to djurleite ($Cu_{1.97}S$) by varying the reduction potential. More specifically, 33 mM cupric sulfate solution was reacted with 16.5 mM sodium thiosulfate and 87 mM citric acid by ultrasonication at 20 kHz for 1 h and electrodeposition with a fixed potential of 0.0, −0.6, or −1.2 V to produce CuS, $Cu_{1.8}S$, or $Cu_{1.97}S$ QDs, respectively. The average diameters of CuS QDs, $Cu_{1.8}S$ QDs, and $Cu_{1.97}S$ QDs were 14.9 ± 7.1, 18.1 ± 7.9, and 12.1 ± 4.6 nm, respectively. Absorbance spectra of $Cu_{1.8}S$ QDs and $Cu_{1.97}S$ QDs had a peak near 400 nm and a valley around 800 nm with increased intensity at longer wavelengths, while that of CuS QDs showed a broad absorbance peak around 450 nm and a valley at 650 nm with a stronger rise at longer wavelengths. For the hydrothermal approach and solventless thermolysis, QDs of different compositions were produced by tuning the pH during the preparation and the precursor pretreatment. In the hydrothermal approach, copper precursors ($CuSO_4·5H_2O$) were first reacted with mercaptopropionic acid (MPA) to form a Cu−MPA complex. The pH was tuned by adding 1 M sodium hydroxide (pH 2 for CuS QDs and pH 5 for $Cu_{1.97}S$ QDs), followed by 7 h reflux with 0.2 M $Na_2S_2O_3$ at 100 °C. Both types of QDs exhibited an absorbance minimum around 600 nm and increased absorbance from 800 nm to longer wavelengths. In the solventless thermolysis approach, the Cu−MPA precipitates were (i) dried in air at room temperature and heated under nitrogen at 200 °C for 1 h to obtain $Cu_{1.8}S$ QD powder, or (ii) dried as a wax-like gel in nitrogen for 30 min before the heating process to form $Cu_{1.97}S$ QD powder. The $Cu_{1.8}S$ QDs (D = 50 nm) and $Cu_{1.97}S$ QDs (D = 70 nm) both showed a broad absorbance peak from 400 to 650 nm, which was respectively 70 and 50 nm red-shifted in comparison to those prepared by sonoelectrochemical and hydrothermal approaches.

Luther and co-workers[140] prepared highly monodisperse $Cu_{2-x}S$ QDs with precise control of QD size, from 2.5 to 6 nm (Figure 33). The Cu^{2+} precursors were obtained by heating cupric acetylacetonate ($Cu(acac)_2$) in oleic acid at 110 °C. The sulfur precursors were prepared by heating 1-dodecanethiol, oleic acid, and ammonium diethyldithiocarbamate at 180 °C under nitrogen. $Cu_{2-x}S$ QDs were synthesized by injecting 3 mL of Cu^{2+} precursors into sulfur precursors dissolved in oleic acid, followed by 3−12 min reaction. The total reaction volume was fixed at 20 mL by tuning the amount of the oleic acid. Size control of the $Cu_{2-x}S$ QDs was achieved by changing the Cu:S precursor ratios and the reaction time. For instance, the 2.5 and 6 nm QDs were prepared using Cu:S ratios of 3:0.63 and 1:1.25 with reaction times of 3 and 12 min, respectively. The NIR absorbance peaks of the $Cu_{2-x}S$ QDs were red-shifted and broadened with decreasing QD size due to surface scattering of free carriers.

Liu et al.[273] reported a room temperature synthesis approach for CuS nanoplates with a fixed thickness of 4 nm and tunable diameter from 4 nm to over 30 nm. The peak LSPR absorbance of the CuS nanoplates was tuned by up to 600 nm by changing

DOI: 10.1021/acs.chemrev.6b00290
Chem. Rev. 2016, 116, 12234−12327

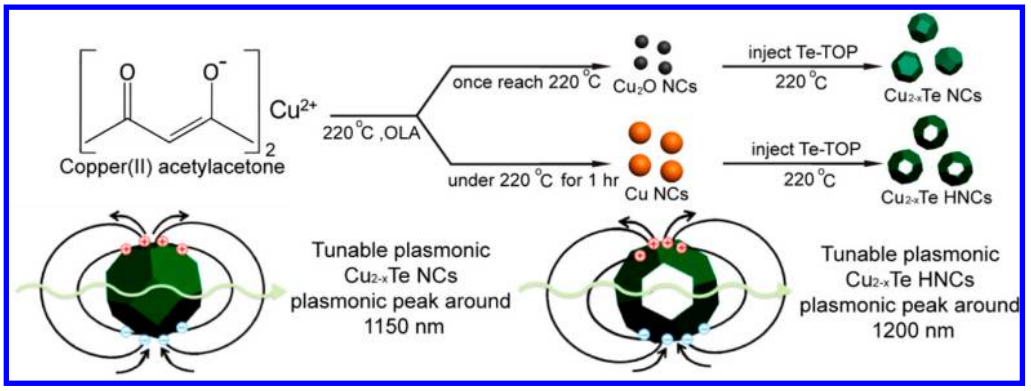

Figure 34. Scheme for formation of solid $Cu_{2-x}Te$ QDs and hollow $Cu_{2-x}Te$ nanostructures by injecting TOP-Te at different reaction times. Reprinted from Yang et al.[318] Copyright 2013 American Chemical Society.

the aspect ratio (i.e., the ratio between the lateral dimension and the thickness). The reaction precursors for Cu and sulfur were oleylamine−Cu (OAm−Cu) and ammonium sulfide (AS) dissolved in toluene.

Hollow and solid $Cu_{2-x}Te$ QDs with high NIR extinction coefficients of 8.1×10^7 M^{-1} cm^{-1} at 1200 nm for the hollow structure and 2.6×10^7 M^{-1} cm^{-1} at 1150 nm for the solid structure were recently synthesized by Yang and co-workers.[318] The difference in the preparation of solid and hollow $Cu_{2-x}Te$ QDs was the injection time of trioctylphosphine-Te (TOP-Te) into the Cu^{2+} precursors (Figure 34). TOP-Te precursors were prepared by dissolving 0.025 g of Te powder in 2 mL of TOP by heating at 150 °C for 1 h. In a typical synthesis, 6 mL of oleylamine (OAm) was mixed with 0.078 g of $Cu(acac)_2$ under argon and then heated to 120 °C for 1 h, followed by heating to 220 °C. At this time, 1.5 mL of TOP-Te with a concentration of 0.1 M was injected into the Cu^{2+} precursors and reacted for 1 h at 220 °C. For the synthesis of hollow $Cu_{2-x}Te$ QDs, the Cu precursors were kept at 220 °C for another 1 h after the 1 h at 120 °C. Then, the Te-TOP precursors were added and reacted for only 30 min rather than 1 h. The color of the mixture changed from dark red to dark green. The average diameters of the solid and hollow $Cu_{2-x}Te$ QDs were 8.8 ± 1.8 and 16.5 ± 2.7 nm, respectively. The NIR absorbance peaks of the solid and hollow $Cu_{2-x}Te$ QDs could be tuned by adding a reducing agent (diisobutylaluminum hydride) that resulted in a decrease of free carrier concentration (i.e., the number of copper deficiencies). It is also worth noting that the LSPR response to the refractive index change of the surrounding media was more pronounced for the hollow $Cu_{2-x}Te$ QDs than for the solid ones.

5. BIOPHOTONIC APPLICATIONS

QD technology is having a tremendous positive impact on biophotonic sensing and imaging. New nanoemitters such as copper indium sulfide ($CuInS_2$), silver indium sulfide ($AgInS_2$), indium phosphide (InP), doped Zn chalcogenides, silver sulfide (Ag_2S), silver selenide (Ag_2Se), silicon (Si), and graphene QDs have been synthesized and used for these applications. The manipulation of QD optical properties can be used to selectively image and monitor a specific biological site as well as to understand local macromolecular interactions such as protein−protein interactions.[319,320] By combining QDs with other contrast agents, one can achieve multimodal imaging of biological structures and processes in vivo.[95,321] Such information can be used to study molecular events that are early indicators of an emerging disease state, or to monitor response to a particular stimulus.[322,323] Multiple targeting ligands can be attached to QDs of different emission colors to identify multiple biomarkers of a specific disease through multiplexed imaging.[324,325] Integrating QDs into various optical imaging techniques coupled with localized microspectrosopy can provide detailed molecular imaging with high spatial resolution. More importantly, QD nanoprobes and nanocarriers that are sensitive to pH, temperature, activity of a specific ion, or activity of biomolecules in cells can enable functional imaging.[326−329] Cd-free QDs can be used for both optical and photoacoustic imaging as well as sensing in vitro, ex vivo, and in vivo to create a highly integrated approach for diagnostics.[20,57,330] Section 5 of this review presents a detailed description of the use of QDs in biophotonic applications including optical imaging, photoacoustic imaging, sensing, optical tracking, photothermal therapy, and multimodal imaging (Figure 35).

The typical biophotonic applications of Cd-free QDs are summarized in Table 2.

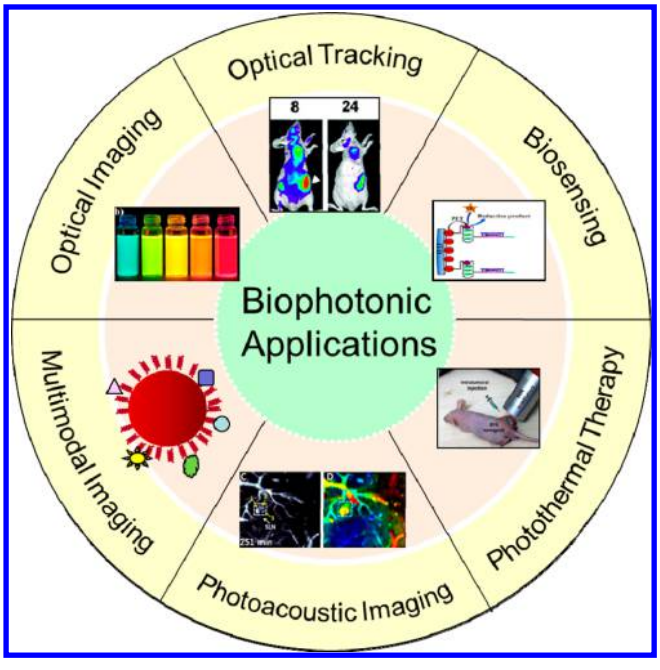

Figure 35. Schematic illustration of the biophotonic applications of Cd-free QDs.

DOI: 10.1021/acs.chemrev.6b00290
Chem. Rev. 2016, 116, 12234−12327

Table 2. Typical Biophotonic Applications of Cd-Free QDs

biophotonic application	QD type	functional group/ molecule	feature of technique	model used	ref
optical imaging					
in vitro imaging	$AgInS_2$	Pluronic F127 triblock copolymer micelles	NIR imaging at 800 nm	human peripheral blood monocyte-derived macrophages	331
	$AgInSe_2$/ZnS core/ shell	RGD-PAA	PL QYs 40%, emission peak 700−820 nm	MDA-MB-231	332
	$CuInS_2$/ZnS core/ shell	ε-PL-*g*-LA/DMA	positive surface charge at low pH	HeLa cell	333
	CIZS/ZnS	AFP	PL QYs 25−35%, emission peak 465−700 nm	HepG2 cell	206
	InP/ZnS core/shell	anticlaudin 4 or anti-PSCA	cell-targeted imaging	pancreatic cancer cells	42, 76
	GQDs	polydopamine	stable PL intensity	KB cells	334
	Si QDs	IgG	PL QYs 25%, emission peak 470−560 nm	HeLa cells	335
	Mn-doped ZnSe	AMACR	cell-targeted imaging	LNCaP	336
	ZnS:Mn/ZnS core/ shell	folic acid	cell-targeted imaging	HeLa cells	337
	ZAIS	PEG2000-FA-RGD	emission peak 525−625 nm	MDA-MB-231	296
	(Zn)$CuInS_2$	anti-Her2 Abs	time-gated imaging	human breast cancer cells	338
in vivo imaging	$AgInS_2$	multidentate polymer	imaged with 630 nm laser	nude mice	223
	$CuInS_2$/ZnS core/ shell	FA-SOC micelles	emission peak 720−800 nm	Bel 7402 tumor mice	36
	Cu_xInyS_2/ZnS	PMMA microspheres	emission peak of 726 nm	nude mice	280
	$CuInSe_2$/ZnS core/ shell	−	emission peak 700−1000 nm	lymph node in nude mice	136
	GQDs	−	multicolor cell imaging	BALB/c mice	339
photoacoustic imaging					
in vivo imaging	$Cu_{2-x}Se$	−	1.7 pmol/L for PA LOD	SLN in nude mice	340
	CuS	−	800 μm resolution at 0.7 nmol	SLN in nude mice	341
optical sensing					
in vitro detection	Ag_2S	silica NPs and anti-oocysts McAb	LOD of 10 oocysts/mL	*C. parvum*	342
	Ag_2Se QDs	PEI	LOD of 2 mM	dopamine	343
	Ag_2Se QDs	TGA	LOD of 0.08 μg/mL	ConA	344
	$CuInS_2$	3-APBA	LOD of 0.2 μmol/L	dopamine	345
	GQD	c-ssDNA	LOD of 0.4 nM	ssDNA	346
optical tracking					
in vivo tracking	InAs/InP/ZnSe	MPA-HAS	large fluorescence contrast	LS174t and 22B tumor mice	297
	PbS	SOC	PL intensity increased from 24 to 48 h	Bel-7402 tumor mice	347
	Ag_2S	Tat peptide	1000 stem cells with 100 ms resolution	thMSCs in nude mice	47
photothermal therapy					
in vitro therapy	$Cu_{2-x}Se$	amphiphilic poly(maleic anhydride)	22% transduction rate	HCT-116	348
in vivo therapy	CuS	cysteine	38% transduction rate	K7M2 tumor mice	349
multimodal imaging					
MRI/ fluorescent	InP/ZnS	80 Gd(III)	900 mM^{-1} s^{-1} relaxivity	rat brain and ovarian cells	193
	$AgInS_2$/ZnS core/shell	folic acid and $MnFe_2O_4$ NPs	bright yellow fluorescence	HeLa cells	350
	$CuInS_2$@ZnS:Mn	DHLA-PEG	multitarget imaging	LS180 tumor mice	156

5.1. Optical Imaging

Optical imaging is an extremely useful tool for biological research because it can provide high-resolution in vitro and in vivo information.[351,352] Key advantages of optical imaging include high sensitivity, low cost, high frame rate, easy portability, and powerful potential for multiplex imaging. The real-time capability of optical imaging allows one to employ this technique during surgery and endoscopic procedures. Optical imaging is useful for early cancer detection and for image-guided surgical resection of tumors. For both in vitro and in vivo optical imaging, cells or tissues are often labeled with organic dyes, and fluorescence from these dyes is collected using appropriate imaging tools.[174,353,354] Optical probes for these applications should have high QY and resistance to photobleaching for long-term imaging. QDs combine high QY

DOI: 10.1021/acs.chemrev.6b00290
Chem. Rev. 2016, 116, 12234−12327

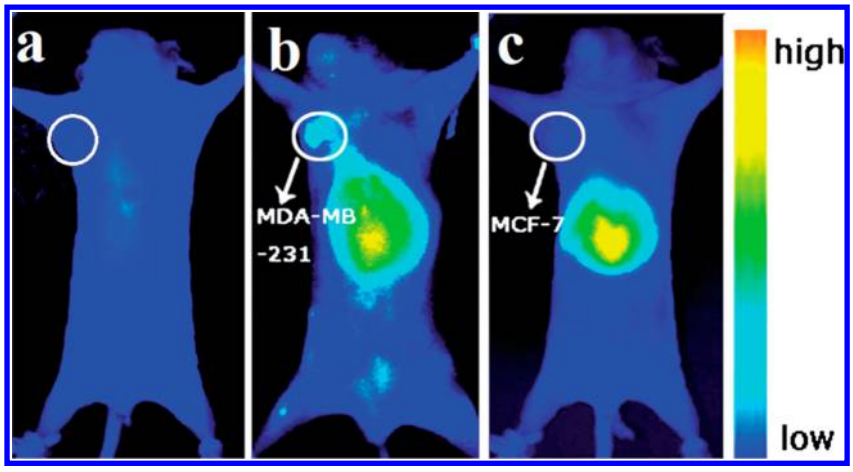

Figure 36. NIR PL images of tumor-bearing mice before tail-vein injection (a) and 6 h after intravenous injection with 775 nm emitting RGD-PAA-QDs: (b) $\alpha_v\beta_3$-positive MDA-MB-231 tumor and (c) $\alpha_v\beta_3$-negative MCF-7 tumor. Reprinted with permission from Deng et al.[332] Copyright 2014 Royal Society of Chemistry.

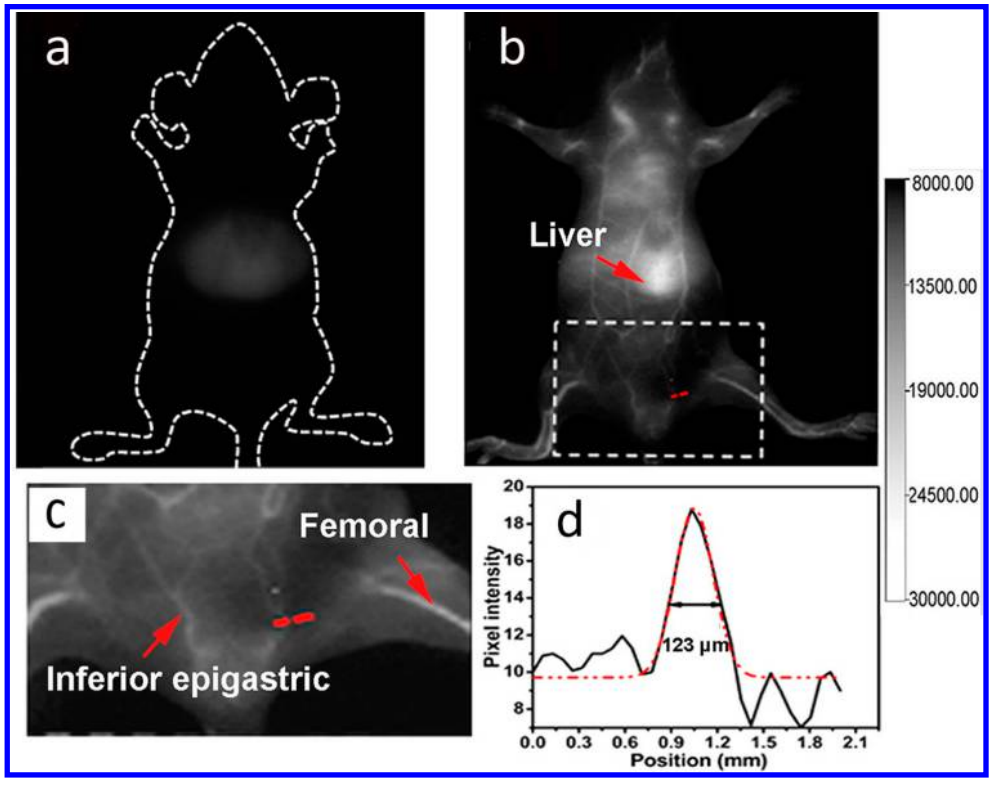

Figure 37. In vivo imaging using ICG and C18-PMH-PEG-Ag_2Se QDs. In vivo imaging of a live mouse in supine position after tail vein injection of (a) ICG or (b) C18-PMH-PEG-Ag_2Se QDs. (c) Magnified view of the zone indicated in (b). (d) Cross-sectional intensity profile measured along the red-dashed line in (c) with its peak fitted to a Gaussian function. Reprinted from Dong et al.[139] Copyright 2013 American Chemical Society.

and excellent photostability with other attractive features, and can outperform organic dyes in many imaging applications. In addition, the large surface area and rich surface chemistry of QDs allows them to be conjugated with biomolecules for targeted imaging. In contrast to most dyes, QDs with different emission wavelengths can be excited with a single light source, which facilitates multiplex imaging of QD-labeled samples.[36,38,66,219] In comparison to QDs, organic fluorophores typically have broader emission spectra and smaller Stokes shifts. The overlap of emission and absorbance spectra complicates imaging. Here, we survey the use of Cd-free QDs in optical imaging methods including fluorescence/photoluminescence (PL) imaging, multicolor imaging, confocal imaging and multiphoton imaging.

Liu et al. prepared NIR-emitting $AgInS_2$ QDs (emission peak at ~800 nm) and encapsulated them within Pluronic F127 triblock copolymer micelles to make them water-dispersible.[331] The $AgInS_2$ QDs served as luminescent probes for in vitro and in vivo tumor-targeted imaging. The in vitro study showed that the Pluronic F127 encapsulated $AgInS_2$ QDs were taken up by human peripheral blood monocyte-derived macrophages. For the in vivo study, fibrosarcoma cells were implanted on the shoulder of mice to establish a tumor model. Accumulation of micelle-encapsulated QDs at the tumor site was observed as

DOI: 10.1021/acs.chemrev.6b00290
Chem. Rev. 2016, 116, 12234−12327

early as 15 min after tail vein injection. After 80 min, the $AgInS_2$ NCs had accumulated in the liver and spleen, and signal from the tumor site decreased significantly. These results suggest that tumor tissue accumulation was a passive process driven by the enhanced permeability and retention (EPR) effect. Compared with $AgInS_2$ QDs, $AgInS_2$/ZnS core/shell QDs exhibit higher optical stability and better biocompatibility. More recently, our group has synthesized $AgInS_2$/ZnS and $CuInS_2$/ZnS QDs and encapsulated them in F127 micelles.[355] Both $AgInS_2$/ZnS and $CuInS_2$/ZnS QD−micelles were taken up by macrophages in vitro, and the cells showed no morphological changes or signs of damage. In vivo imaging showed that the $AgInS_2$/ZnS QD−micelles accumulated at the tumor site after tail vein injection, via the EPR effect. PL from intra-abdominally injected $CuInS_2$/ZnS QD−micelles was easily differentiated from the background autofluorescence.

Tan et al. used a multidentate polymer (MDP) to encapsulate NIR-emitting $AgInS_2$ QDs for in vivo optical imaging.[223] The effects of administration route were demonstrated using two groups of nude mice. One group received QDs via subcutaneous injection and were then imaged under 630 nm laser excitation at successive time points. PL intensity decreased little over time, suggesting localized accumulation of the QDs at the injection site and reflecting the high PL stability of the QDs in vivo. In the other group, QDs were injected via the tail vein and images were collected 4, 12, and 24 h after injection. Four hours after injection, the QDs were distributed throughout the bodies of the mice. At later times, the QD PL signal gradually decreased, reflecting the slow degradation and clearance of QDs (with a half-life of 20.1 ± 3.4 h). The excellent contrast of the images suggested that such QDs were suitable for deep tissue imaging in vivo. Gu's group prepared $AgInSe_2$/ZnS QDs functionalized with an RGD peptide for targeted in vivo imaging.[332] Both $\alpha_v\beta_3$-positive MDA-MB-231 cells and $\alpha_v\beta_3$-negative MCF-7 cells were injected subcutaneously into nude mice, followed by intravenous administration of the RGD-PAA-QDs. Six hours after administration of QDs, stronger QD PL was observed in the $\alpha_v\beta_3$-positive tumor-bearing nude mice compared to that in the $\alpha_v\beta_3$-negative tumor-bearing ones (Figure 36), demonstrating targeting of the RGD-PAA-QDs to tumor cells that overexpress $\alpha_v\beta_3$ integrin receptors.

NIR imaging of Ag_2Se QDs with PL at 1300 nm was also demonstrated in small animals.[139] The Ag_2Se QDs were functionalized with C18-PMH-PEG to obtain a stable aqueous dispersion with bright PL and good photostability. The hydrodynamic diameter of the QDs was ∼43 nm. The imaging performance of Ag_2Se QDs was compared to ICG. A dose of 37 mg/kg ICG provided a weak signal and fuzzy images of the vasculature due to scattering and absorbance by tissues. On the other hand, C18-PMH-PEG-Ag_2Se QDs at a dose of 6 mg/kg produced clear images of the liver, spleen, and vasculature, under 808 nm laser excitation, within a few minutes following injection (Figure 37).

$CuInS_2$ QDs also exhibit strong near-IR PL and show promise in biomedical optical imaging. In the research works from our group mentioned above, the $CuInS_2$/ZnS QDs were encapsulated in F127 micelles to make them water-dispersible.[281] They were then conjugated with folic acid (FA) to construct QD-FA probes that target cells which overexpress FA receptors. Pancreatic cancer cells (CRL-1469) that overexpress FA receptors were used to create a tumor model in nude mice. The QD-FA formulation was systemically administered by intravenous injection followed by whole-animal PL imaging. Strong QD PL was observed from tumors of mice treated with FA-conjugated QDs while mice treated with unconjugated QDs exhibited little PL from the tumor site, demonstrating the tumor specificity of the QD-FA probes. In addition, $CuInS_2$ QDs with two different emission colors were injected subcutaneously at different sites to demonstrate the potential of these NIR QDs for in vivo multiplex imaging. The luminescence from the two different QDs was easily distinguished. In a separate study, $CuInS_2$/ZnS QDs were packaged in biodegradable folic acid modified chitosan micelles for cancer imaging.[36] The ability of the QD-loaded micelles to target tumor cells was evaluated in vitro and in vivo. FA-receptor-positive Bel-7402 cells showed a much higher uptake of the QD-loaded folate-modified *N*-succinyl-*N*′-octyl chitosan (FA-SOC) micelles than did FA-receptor-negative A549 cells. For in vivo studies, A549 and Bel-7402 cells were injected into nude mice to generate tumors, and QD-loaded micelles were administered by tail vein injection. The results confirmed the high targeting efficacy of QD-loaded FA-SOC micelles to FA-receptor-positive tumors. Multiplex NIR PL imaging was performed by administering two types of QD-loaded micelles (QD720 and QD800) subcutaneously. Again, signals of different QDs were well separated.

Yu et al. developed a low-temperature approach for producing $CuInS_2$/ZnS QDs with bright PL and applied them for in vitro and in vivo imaging.[356] Mercaptoundecanoic acid (MUA) and dihydrolipoic acid (DHLA) were each used for phase transfer of the QDs into water. Two single-domain antibodies (sd Abs), 2A3 and EG2, were used to functionalize QDs for tumor cell targeting in vitro and in vivo. The in vitro result showed that the 2A3-conjugated $CuInS_2$/ZnS QDs were efficiently taken up by BxPC3 pancreatic cancer cells, yielding images with good contrast. However, the signal from cells treated with unconjugated $CuInS_2$/ZnS QDs was barely detectable. The in vivo result showed PL signals from EG2-conjugated $CuInS_2$/ZnS QDs in a brain tumor 4 h after intravenous injection.

Because the extracellular microenvironment in a tumor is typically more acidic (pH ∼6.5−6.8) than normal tissue, targeting strategies exploiting this pH difference have been studied as a route to smart and programmable delivery systems. Dong et al. designed a charge-reversible pH-sensitive NIR luminescent nanoprobe that showed enhanced cellular uptake at low extracellular pH.[333] The $CuInS_2$/ZnS QDs were encapsulated within a lauric acid and 2,3-dimethyl maleic anhydride modified ε-polylysine (ε-PL-*g*-LA/DMA) shell, which provided a dense protective layer for the QDs and enhanced charge-mediated endocytosis at low pH. When the negatively charged QDs were exposed to low pH, the β-carboxyl amide bond in the polymer shell was broken, creating positive surface charge on the QDs. In vitro experiments showed higher QD uptake by tumor cells at pH 6.8 than at pH 7.4. The pH-responsive nature of these QDs may prolong circulation time and enhance QD accumulation in tumor tissue. Such nanoprobes avoid the limitation of receptor targeting probes associated with the heterogeneity of different cancer cells and thus provide an attractive general tumor targeting strategy. Using $Cu_xIn_yS_2$/ZnS QDs with bright NIR PL at 726 nm, Choi et al. achieved a detection depth of 9 mm and acquired strong signals from 2 mm beneath the skin of nude mice.[280] In comparison, $Cu_xIn_yS_2$/ZnS QDs with 589 nm

DOI: 10.1021/acs.chemrev.6b00290
Chem. Rev. 2016, 116, 12234−12327

emission showed negligible signal at the same conditions (Figure 38).

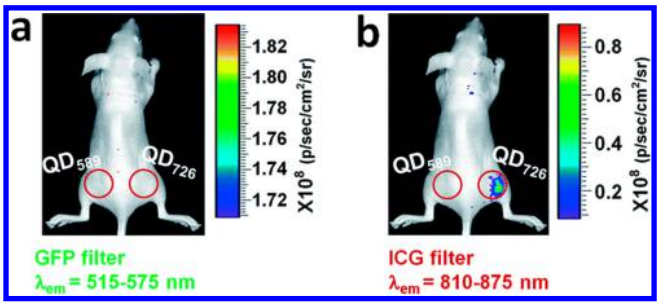

Figure 38. PL images of QD-loaded PMMA microspheres implanted into thigh muscles by intramuscular injection. Images taken using a GFP excitation filter (445−490 nm) with a GFP emission filter (515−575 nm) (a) and an ICG emission filter (810−875) (b). Reprinted with permission from Choi et al.[280] Copyright 2015 Royal Society of Chemistry.

Cassette et al. also prepared NIR (700−1000 nm) Cu−In−Se/ZnS QDs for small animal imaging.[136] The QD formulation was injected subcutaneously in the right anterior paw of healthy mice. PL from the regional lymph node was observed after a few minutes, and the QDs accumulated in the right axillary lymph node after 4 h, as confirmed by inductively coupled plasma mass spectrometry (ICP-MS) measurements. Lymph node imaging can provide useful information for diagnosis and therapy of potentially metastatic tumors. Use of QDs as luminescent contrast agents for imaging lymph nodes in vivo can therefore have rapid clinical impact. Similarly, Jiang et al. synthesized Cu-doped In−Zn−S QDs (CIZS QDs) by a hydrothermal method and achieved tunable PL emission from 465 to 700 nm.[206] Adding a ZnS shell to the CZIS core improved the PL QY to 25−35%. For imaging, rabbit anti-α-fetoprotein (AFP) was covalently conjugated to the QDs, and the CIZS/ZnS QD-AFP were incubated with HepG2 cancer cells. Bright yellow PL was observed in the cytoplasm along with weak PL in the nucleus. The same group synthesized Zn-doped $AgIn_5S_8$ (ZAIS) QDs, and performed similar cell-targeted imaging.[295] Again, QDs coated with AFP antibodies bound specifically to the antigen receptor in the cytoplasm of HepG2 cells.

Fahmi and Chang prepared double-layer-encapsulated $AgInS_2$/ZnS QDs (DL-QDs) using alkyl-capping ligands that interact with the hydrophobic ligands on the QD surface.[357] The alkyl-capping ligands included carbon chains of varied length with different terminal functional groups (e.g., thiol, amine, carboxyl, and hydroxyl), which can serve as reactive sites for coupling with biomolecules (e.g., antibodies, DNA/RNA, enzymes). Specifically, DL-QD-COOH were functionalized with folate to target HeLa cells. Confocal imaging demonstrated that the folate-conjugated DL-QDs specifically and effectively targeted HeLa cells through a folate receptor mediated pathway and showed minimal uptake by breast cancer (MCF-7) cells and liver carcinoma (HepG2) cells.

Generally, the PL lifetimes of QDs are long relative to autofluorescence and typical fluorescence lifetimes of dyes. Heyes's group reported biocompatible (Zn)$CuInS_2$ QDs with long PL lifetime and used them as probes in time-gated imaging.[338] Suppression of autofluorescence by time-gating produced an order-of-magnitude improvement in signal-to-noise ratio. The PL lifetime of these (Zn)$CuInS_2$ QDs was 21 ns, significantly longer than the 8 ns lifetime of Cd-based QDs, which enabled better suppression of cell autofluorescence through time-gated detection. The (Zn)$CuInS_2$/ZnS QDs were used to specifically detect the Her2 receptor on human breast cancer cells (Figure 39). The sensitivity was comparable to, or

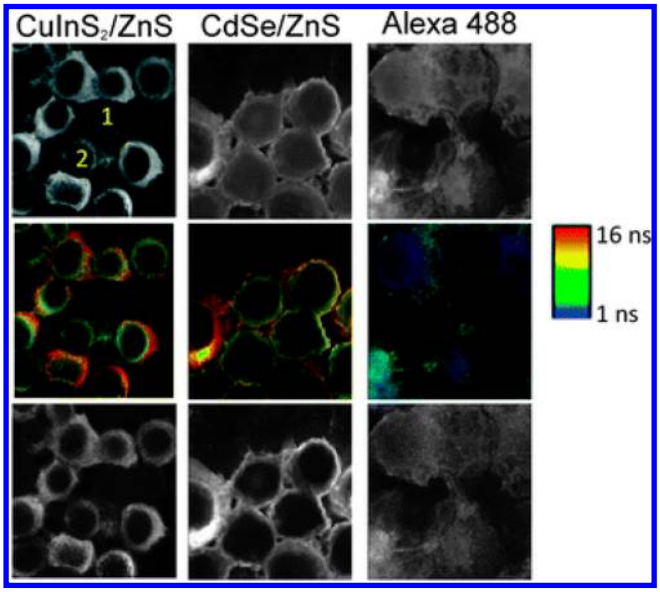

Figure 39. Time-gated bioimaging of human breast cancer cell labeled by QDs-anti-Her2. Upper row: PL intensity images of the cancer cells; the cells labeled "1" and "2" are two cancer cells expressing Her2 receptors at different levels. Middle row: FLIM images, ranging from 1 (blue) to 16 ns (red). Bottom row: image after time-gating the first 10 ns of photons, which significantly improves contrast, and removes unlabeled cells from the images. Reprinted with permission from Mandal et al.[338] Copyright 2013 Royal Society of Chemistry.

even superior to, Cd-based QDs and much higher than molecular probes. The authors asserted that this was the first report of using Cd-free QDs for labeling breast cancer cells by time-gated imaging.

Bouccara et al. developed Zn−Cu−In−Se/ZnS QDs for cell labeling via time-gated imaging.[358] The PL lifetime of their QDs was much longer (150−200 ns) than that of (Zn)$CuInS_2$/ZnS QDs, which further facilitates separation of PL from autofluorescence (5−10 ns). To prolong the observation time, they stained the cells with a high concentration of NIR QDs via electroporation. The internalized NIR QDs were homogeneously distributed in the cell cytoplasm, and the time-gated imaging effectively eliminated contributions from autofluorescence.

InP and InP/ZnS QDs are also promising optical probes due to their excellent optical features and strong resistance to corrosion in biological systems. Our group has modified water-dispersible InP/ZnS core/shell QDs with mercaptosuccinic acid and functionalized them with two antibodies (anticlaudin 4 and anti-PSCA) as targeting molecules.[42,76] Receptors for these antibodies are overexpressed on pancreatic cancer cells. Confocal microscopy revealed that the QDs were transported into the cytoplasm by a receptor-mediated pathway.

In addition to Cu- and In-based QDs, Mn-doped ZnSe QDs were also demonstrated as nontoxic and effective optical probes for tumor targeting. Su et al. conjugated Mn-doped ZnSe QDs with the anti-α-methylacyl-CoA racemase (AMACR) for specific imaging of prostate cancer cells.[336] The targeting

DOI: 10.1021/acs.chemrev.6b00290
Chem. Rev. 2016, 116, 12234−12327

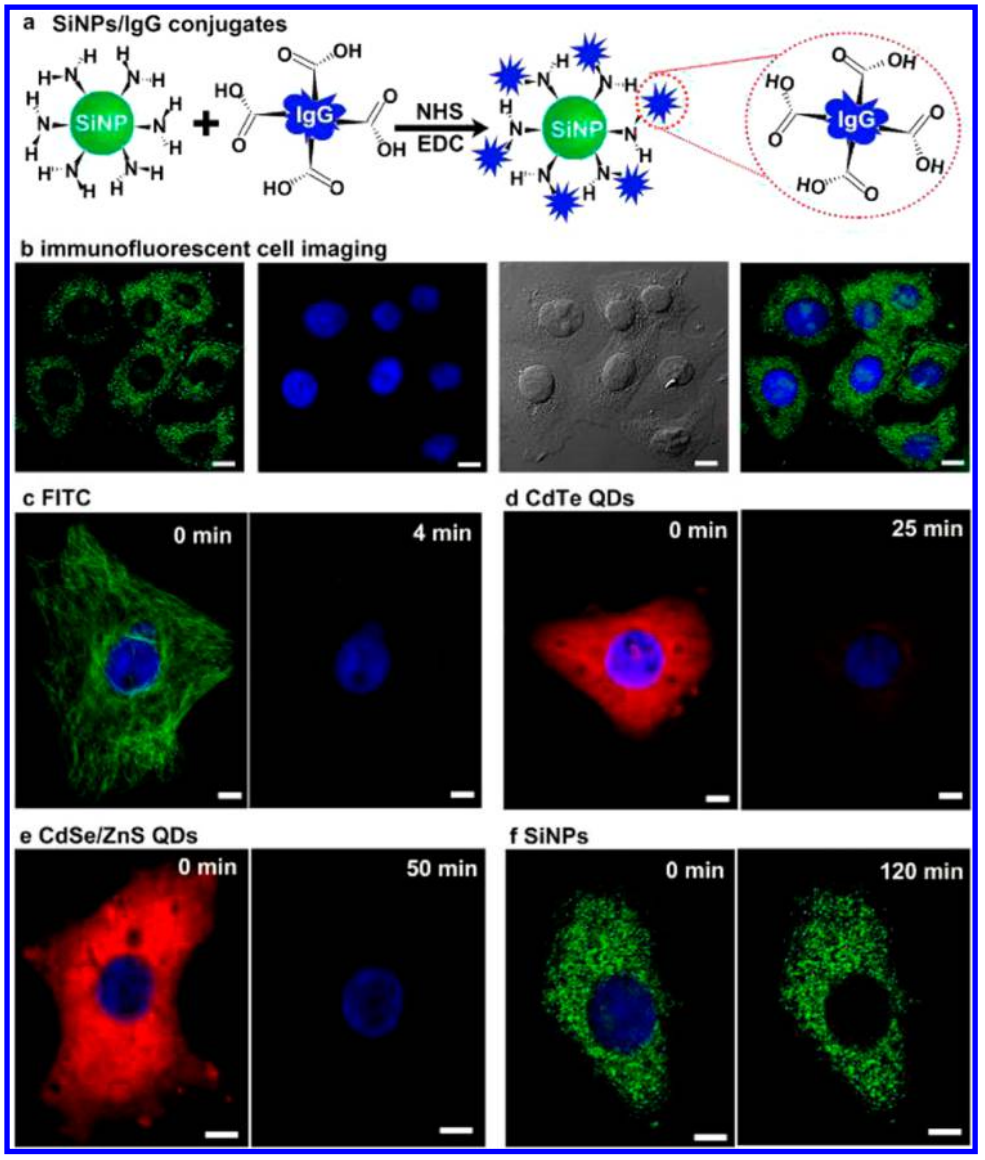

Figure 40. Fluorescence images of cells labeled by different probes and their photobleaching rates. (a) Schematic illustration of conjugation of SiNPs with goat-antimouse IgG. (b) (left) Microtubules are labeled by IgG-conjugated SiNPs; (middle) cellular nuclei are imaged by Hoechst; (right) overlay of the two fluorescence images. (c–f) Photobleaching of FITC, CdTe QDs, CdSe/ZnS QDs, Hoechst, and SiNPs after the indicated times. Scale bars: 10 μm. Reprinted from Zhong et al.[335] Copyright 2015 American Chemical Society.

ability of the QDs was confirmed by comparing their internalization in AMACR-negative PC3M cancer cells and AMACR-positive LNCaP cancer cells. ZnS:Mn/ZnS core/shell QDs have also been used for bioimaging.[337] Yu et al. synthesized ZnS:Mn/ZnS QDs using MPA as a stabilizer. The QDs were then functionalized with FA to form nanocomplexes that specifically bound to FA receptors. The QDs targeted HeLa cells in vitro and accumulated at the HeLa cell tumor site in vivo, demonstrating that the Mn-doped QDs could provide another alternative to Cd-based QDs in biomedical optical imaging.

Cellular uptake of NPs generally depends on their size and surface functionalization.[359] However, Soenen et al. suggested that the QD core composition may also affect the cell uptake. They prepared ZnSe/ZnS QDs and InP/ZnS QDs with the same size and surface ligands and used them for cellular bioimaging. Confocal microscopy showed highly colocalized QD PL from endosomal compartments, revealing the intra-endosomal accumulation of QDs. Moreover, they estimated the QD concentration from PL intensity observed in cells and found that ZnSe/ZnS QDs were internalized by cells slightly more efficiently than the InP/ZnS QDs. This result suggests that QD core composition may affect cellular uptake, but further evaluation of this possibility is needed.

Silicon QDs (Si QDs) are potential optical probes for in vivo imaging due to their nontoxic properties, small size, high brightness, and resistance to photobleaching.[360] Porous silicon NPs have been shown to degrade in physiological environments and to thereby be eliminated in mice via renal clearance, further reducing toxicity concerns. All these advantages have motivated the investigation of Si QDs for in vitro and in vivo bioimaging, biosensing, and cancer theranostics. Gooding et al. prepared photostable Si QDs and functionalized their surface using a versatile click-chemistry approach.[53] To demonstrate the biomedical potential of the functionalized Si QDs, amine-functionalized Si QDs were used as in vitro PL probes for HeLa cells under continuous laser excitation. After 45 s of irradiation, the cell autofluorescence was bleached while the PL of Si QDs

DOI: 10.1021/acs.chemrev.6b00290
Chem. Rev. 2016, 116, 12234–12327

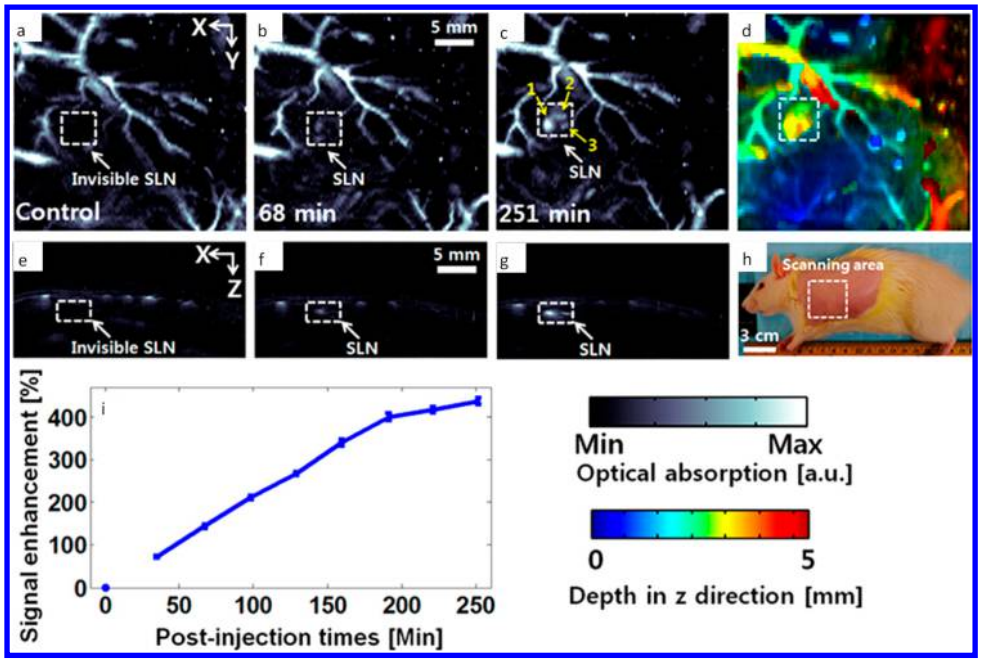

Figure 41. In vivo photoacoustic (PA) coronal maximum amplitude projection (MAP) images. PA images were acquired before (a) and after (b, c) Au−Cu_{2-x}Se injection. (d) Depth-encoded PA coronal MAP image of (c). (e−g) Depth-resolved cross-sectional PA B-scan images of a−c. (h) Photograph of the experimental rat. (i) Enhancement of PA signal from a sentinel lymph node (SLN) over time. Reprinted from Liu et al.[369] Copyright 2013 American Chemical Society.

remained. Such photostable and biocompatible Si QDs have great potential for long-term cellular imaging. Zhong et al. presented a facile and low-cost photochemical method to obtain highly photoluminescent (QY 25%) Si QDs with PL tunable from 470 to 560 nm.[335] After conjugating with IgG using carbodiimide chemistry, the Si QD-IgG conjugates served as bioprobes for cellular immunofluorescent imaging. To compare photobleaching rates, the Si QDs, FITC dye, CdTe QDs, and CdSe/ZnS QDs were all employed for cellular imaging by laser-scanning confocal luminescence microscopy. All the QDs showed less photobleaching than the dye, which stopped emitting within 4 min. Long-time UV irradiation lead to severe PL bleaching of II−VI Cd-based QDs (absolute bleaching within 25 min for CdTe and within 50 min for CdSe/ZnS). Impressively, the Si QDs exhibited the best resistance to photobleaching, remaining bright and stable after 2 h of continuous irradiation (Figure 40). The results suggested that the Si QDs are suitable PL probes for long-term bioimaging and tracking. In that study, the Si QDs were capped with covalently bound hydrophobic ligands. For bioimaging, they were encapsulated in phospholipid−PEG polymer micelles that were further functionalized with a cyclic RGD peptide for in vivo targeting of the tumor vasculature.

More recently, Cheng et al.[361] employed Si QDs for both one- and two-photon cellular imaging using fluorescence lifetime imaging microscopy (FLIM). The use of FLIM minimized signal from the biological background, while the two-photon near-IR light excitation avoided the phototoxicity associated with UV excitation of Si QDs. The authors functionalized the Si QDs with amine groups and used HeLa cells as target label examples. The PL lifetime of the Si QDs, >4 ns, was much longer than that of the cell autofluorescence (<2.5 ns). Thus, the cellular autofluorescence could be separated from Si QD PL through deconvolution of the FLIM. Two excitation wavelengths of 740 and 800 nm were tested for the two-photon FLIM imaging,and 800 nm excitation was found to be more effective. Most of the detected PL was distributed throughout the cytoplasm rather than the nucleus. Förster resonance energy transfer (FRET) from SiQDs to DY485, a dye that serves as an acceptor, was also demonstrated and allowed tuning of the emission from blue to yellow. The dye emission was enhanced by 200% after coupling with the Si QDs.

Recently, graphene QDs have emerged as novel optical probes with advantages including small size, superior stability, and good biocompatibility. Zhu et al. used the top-down "nano-cutting" method to create photoluminescent GQDs of ∼4 nm diameter.[339] The GQDs were incubated with rat Schwann cells, and their uptake over time was observed by confocal microscopy and fluorescence activated cell sorting (FACS). GQDs were distributed in the cytoplasm and in lysosomes. Multicolor cellular imaging was demonstrated using different excitation wavelengths. In addition, the GQDs were injected subcutaneously into BALB/c mice. The Ex/Em = 465/620 nm wavelength pair provided the best bioimaging result with minimal autofluorescence and increased signal-to-noise ratio. Similarly, Lee's group synthesized low-toxicity GQDs by a facile exfoliation/oxidation approach and then functionalized them with polydopamine (pDA) for improved colloidal stability.[334] When dispersed in PBS buffer, the uncoated GQDs showed a 45% decrease in PL intensity after 14 days, while PL from pDA-coated GQDs remained stable. In vitro imaging showed that GQDs with and without the pDA coating were taken up by KB cells. However, the biodistribution and clearance profiles observed by in vivo imaging differed between coated and uncoated GQDs.

Peng et al. reported that different sizes of graphene QDs were produced by acid treatment and chemical exfoliation of traditional pitch-based carbon fibers.[307] The QDs had diameters of 1−4 nm, and thicknesses of 1−3 atomic layers

DOI: 10.1021/acs.chemrev.6b00290
Chem. Rev. 2016, 116, 12234−12327

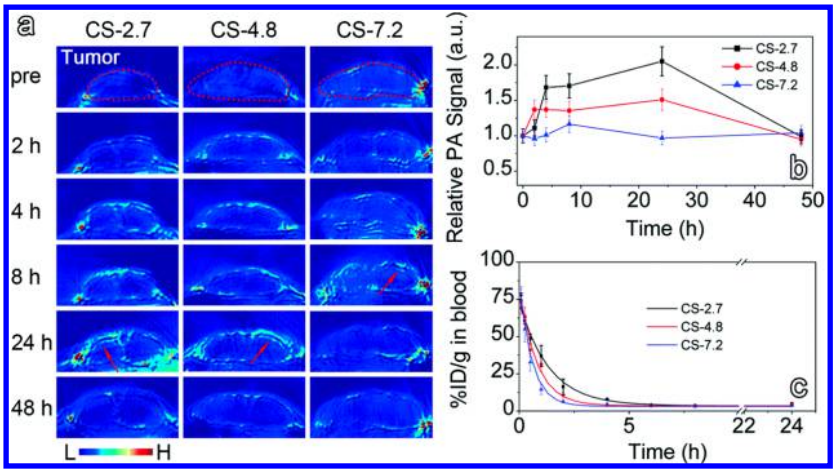

Figure 42. In vivo photoacoustic images acquired before and at different time points after intravenous injection of CuS QDs of three different sizes into tumor-bearing mice (a), temporal photoacoustic signals recorded from the tumor region (b), and blood clearance profiles of differently sized CuS QDs in rats (n = 4) (c). Reprinted with permission from Ding et al.[370] Copyright 2015 Royal Society of Chemistry.

(0.4−2 nm). The QD PL color was tuned by varying the synthesis parameters to produce QDs of varying size. Green-emitting graphene QDs were used to stain T47D cancer cells, and the nucleus of the cells was stained with DAPI (blue color) for comparison. PL imaging clearly showed the high contrast PL signal of green GQDs near the nucleus. These images suggest that graphene QDs can be used for bioimaging, but their QY remains relatively low compared to Cd-based QDs. Thus, further engineering is needed to improve brightness and QY for ultrasensitive imaging of cells.

Two-photon PL contrast agents can enable increased imaging depth while reducing autofluorescence and photodamage, because they are excited in the near IR. One of the earliest demonstrations of two-photon imaging using Cd-free QDs was presented by Bharali et al. in 2005[76] using InP/ZnS core−shell QDs. The large Bohr radius of InP makes these QDs more polarizable, enhancing nonlinear optical properties. Liu et al. employed nitrogen-doped graphene QDs as two-photon PL contrast agents.[6] The two-photon absorbance cross section of the QDs reached 48 000 Göppert-Mayer units, exceeding that of conventional chromophores and comparable to that of Cd-based QDs. The authors achieved imaging depths of 1800 μm in a tissue phantom. Moreover, they found that the QDs are biocompatible and possess excellent photostability. This combination of imaging depth, high two-photon absorption cross section, and outstanding photostability of the QDs can make them valuable two-photon PL probes for long-term two-photon imaging in vivo. He et al. demonstrated two- and three-photon excited upconverted emission from Si QDs,[239] but did not present bioimaging results in that study. Geszke-Moritz et al. demonstrated two-photon excited PL imaging using Mn-doped ZnS QDs.[256]

5.2. Photoacoustic Imaging

Recently, photoacoustic (PA) imaging has emerged as a valuable noninvasive biomedical imaging method combining key advantages of optical imaging and ultrasound imaging. It acquires images based upon optical absorbance contrast, with a combination of high spatial resolution and deep imaging depth that cannot be achieved by either optical or ultrasound imaging alone (Figure 41).[78,340,362−366] The use of NIR optical excitation in PA imaging significantly increases the penetration depth of imaging.[366−368] Our recent work reported the use of $Cu_{2-x}Se$ QDs, a new type of QDs with NIR LSPR absorbance, for lymph node mapping by PA imaging.[369] The $Cu_{2-x}Se$ QDs were used for volumetric in vivo mapping of SLNs by injection into the paw pad of rats, followed by PA imaging of the corresponding axillary region. Results showed strong NIR LSPR absorbance from the SLN. The PA detection limit of the 7.6 nm $Cu_{2-x}Se$ QDs was 1.7 pmol/L. If compared on the basis of particle volume, rather than number concentration of particles, this matches the performance of gold nanocages and other top-performing PA contrast agents. Building on this study, our group presented a heterodimer nanostructure composed of a semiconductor domain ($Cu_{2-x}Se$) and a metal domain (Au).[369] This nanostructure exhibits broad LSPR absorbance spanning visible and NIR wavelengths, arising from interactions between the $Cu_{2-x}Se$ and Au domains. A clinically relevant imaging depth of up to 17 mm was achieved in this study.

In addition to $Cu_{2-x}Se$ QDs, 11 nm CuS NPs with absorbance peaking at 990 nm have been engineered as a PA contrast agent for deep tissue imaging using 1064 Nd:YAG laser excitation.[341] The CuS NPs were clearly visualized in the mouse brain 24 h after intracranial injection. Following interstitial injection into the front paw pad, images of lymph nodes located 12 mm beneath the skin were acquired. To further probe the application potential of these CuS NPs, an agarose gel containing CuS NPs was embedded in chicken breast at depth of ∼5 cm. Imaging resolution of ∼800 μm was achieved with a detection limit of ∼0.7 nmol per imaging voxel. Similarly, Ding et al. employed PEGylated CuS NPs as PA contrast agents.[370] In their in vitro studies, the contrast enhancement effect of the CuS NPs was proportional to particle size, with higher signal intensity from larger NPs. However, in in vivo studies CuS NPs smaller than 5 nm achieved better performance in tumor imaging, especially at the tumor boundary (Figure 42). These results provide useful information to support development of precision-engineered PA probes for imaging guided tumor therapy.

Yang et al. designed an activatable CuS-based PA imaging nanoprobe to label matrix metalloproteinases (MMPs) in vivo.[371] The MMPs play an important role in tumor angiogenesis and are overexpressed in the tumor microenvironment. CuS NPs with NIR absorbance were conjugated with black hole quencher 3 (BHQ3) via an MMP-sensitive peptide

DOI: 10.1021/acs.chemrev.6b00290
Chem. Rev. 2016, 116, 12234−12327

linker. After conjugation, the absorbance spectra of the CuS−peptide−BHQ3 complexes showed two distinctive peaks at 630 and 930 nm. When exposed to the tumor microenvironment, the MMP-sensitive peptide was cleaved by the overexpressed MMP and the BHQ3 was released from the CuS NPs. The BHQ3, which is a small molecule, was rapidly cleared out of the tumor while CuS NPs were retained. The ratio of PA signal at 680 nm to that at 930 nm provided a sensitive indicator of MMP activity in the tumor. This simple and straightforward strategy allows researchers to use PA imaging to monitor specific enzyme activity in deep tissues.

Dai's group developed multifunctional CuS nanoparticles (NPs) capped with doxorubicin (DOX)-conjugated gelatin, CuS@Gel-DOX, and demonstrated their use for photoacoustic imaging and photothermal therapy.[372] Moreover, the gelatin−DOX was degraded by gelatinase to provide enzyme-responsive drug release. The potential of CuS@Gel-DOX NPs as PA contrast agents was investigated both in vitro and in vivo. The in vitro study employed a phantom containing an agar gel loaded with CuS@Gel-DOX NPs, which was embedded beneath chicken breast tissue. At a depth of 3.2 cm, five agar objects embedded with CuS NPs were clearly distinguished from the agar gel background. As an in vivo demonstration, the cerebral cortex of a mouse was imaged using PA imaging before and after the injection of the functionalized CuS NPs. The brain vasculature began to be clarified 5 min after injection of CuS@Gel-DOX NPs and the PA signal increased gradually. The analysis of drug release profile revealed a 3-fold increase in drug release during the 6 h following gelatinase addition, relative to the release without adding gelatinase. Such CuS@Gel-DOX NPs could potentially be used for imaging cancer tissues and killing cancer cells by combining PA imaging, photothermal therapy, and chemotherapy. Using CuS NPs as a PA imaging platform, the same group also constructed a nanoplatform functionalized with manganese(II) chelate and poly(ethylene glycol) (PEG) for PA/MR dual-modal imaging and imaging-guided photothermal therapy.[373] The CuS NPs exhibited uniform small size (~9 nm), excellent NIR absorbance, and minimal cytotoxicity. The NPs were injected into tumor-bearing mice, and PA images were collected. The PA signal from the tumor site gradually increased after intravenous injection, and peaked 5 h after injection. Enhanced PA signal from the tumor site persisted after 24 h, indicating the CuS NPs remained at the tumor site. PA results were further confirmed by MR imaging. Finally, photothermal therapy was performed on MDA-MB-231 xenograft tumor-bearing mice. The tumor treated with the laser and CuS NPs disappeared within the first week. Tumor growth was unaffected in mice treated with the laser or CuS NPs alone. The authors suggested that CuS NPs functionalized with Mn(II) chelate hold great potential as a theranostic for PA/MR imaging-guided photothermal therapy. However, the use of a chelator on the NP surface may limit the ability to conjugate other targeting or therapeutic agents.

Gao et al. developed a doping method for constructing a Ni-integrated CuS nanostructure as a new PA/MRI contrast agent.[368] The Ni:CuS NPs exhibited small and uniform size along with good crystallinity. Their absorbance spectra covered the 700−900 nm range over which tissues are relatively transparent. Moreover, compared to Ni ions, the doped NPs exhibited a dramatically enhanced T_1 relaxivity, indicative of promise as MRI contrast agents. To demonstrate sentinel lymph node mapping, mice were administered Ni:CuS NPs subcutaneously at the distal part of the right anterior paw. Increased PA signal from the Ni:CuS NPs at the sentinel lymph node was observed 30 min postinjection. MR imaging demonstrated the same accumulation, suggesting that the Ni:CuS NPs are promising PA/MRI dual-modal nanoprobes.

Song et al. constructed a novel nanovesicle based on reduced graphene oxide (rGO) for PA imaging and chemo/photothermal therapy and tested it in vitro and in vivo.[374] They designed and synthesized a new type of carbon−metal hybrid nanostructure, rGO-doxorubicin (DOX)-loaded plasmonic gold nanorod vesicles (rGO-AuNRVe-DOX). The encapsulation of rGO-DOX in the gold nanorod vesicle protected the rGO-DOX from degradation or damage during circulation and cellular internalization. The PA signal, photothermal effect, and drug release profiles were measured and evaluated systematically. The rGO-AuNRVe nanocomplexes exhibited better photothermal effect and higher PA signal compared with AuNR alone or the mixture of rGO and AuNRVe. This enhancement was attributed to the plasmonic coupling between the encapsulated rGO and AuNR in the vesicular shell. In vivo, the PA signal in the tumor region increased gradually after injection of rGO-AuNRVe. The maximum PA signal, at 24 h postinjection, was 4 times that obtained using AuNRVe alone. The in vivo evaluation on the chem/photothermal therapeutic effect of rGO-AuNRVe-DOX demonstrated that such nanovesicles had a dual photoresponsive and acid-responsive DOX release pattern and synergistic chemo/photothermal effects. Their combination of properties makes the nanovesicles useful for visualization of the shape and size of a tumor by PA imaging, elimination of the cancer cells through chemo/photothermal effects, and minimization of side effects to the surrounding tissue.

Overall, advances in plasmonic nanotechnology are allowing rapid development of NP-based PA contrast agents with exceptionally strong absorbance in the NIR spectral range. Several of these recently developed materials incorporate QDs, although the absorbance used for PA contrast is usually associated with plasmonic, rather than excitonic, properties of the QDs. Rapidly developing PA technology is expected to significantly enhance both preclinical and clinical targeted imaging of tumors and other tissues.

5.3. Biosensing

Specific biomarker detection is valuable for early diagnosis and therapy of diseases, as well as for probing complex physiological processes. In the past decade, the unique optical properties of QDs and the ability to specifically functionalize their surfaces have been widely applied to the detection of various chemical and biological species.[83,211,375,376] In this section, we discuss some important examples of the use of Cd-free QDs for optical sensing applications in biophotonics.

Dinakaran et al. developed an immunosensor for detection of *Cryptosporidium parvum* using NIR-emitting Ag_2S@silica nanospheres.[342] In a sandwich assay, anti-oocyst McAb were immobilized on functionalized quartz glass, incubated with *C. parvum*, and treated with anti-oocyst McAb immobilized Ag_2S@silica nanospheres. The PL spectra of the washed glass plates were recorded and used to determine the concentration of *C. parvum*. The PL intensity increased as oocyst number increased, and the detection limit was 10 oocysts/mL. They also studied the specificity of binding using five other pathogens, and found that the PL intensity only changed dramatically when the pathogen *C. parvum* was added.

DOI: 10.1021/acs.chemrev.6b00290
Chem. Rev. 2016, 116, 12234−12327

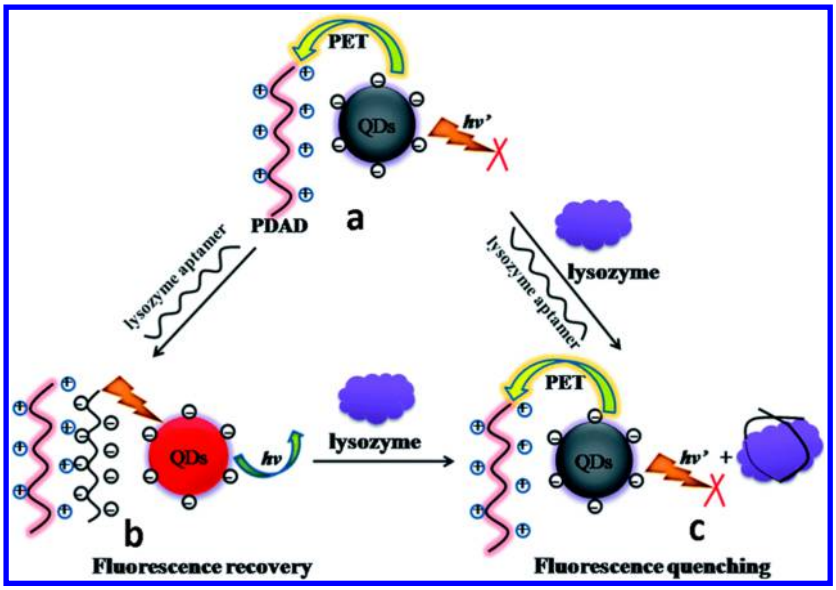

Figure 43. Schematic design for lysozyme sensing. (a) Coexistence of the MPA-capped $CuInS_2$ QDs and cationic polyelectrolyte PDAD. (b) Electrostatic bonding of the lysozyme aptamer and PDAD. (c) Bonding of the lysozyme aptamer and lysozyme. Reprinted with permission from Liu et al.[378] Copyright 2014 Royal Society of Chemistry.

Dopamine (DA) is an important neurotransmitter in the central nervous, renal, and hormonal systems. Cui et al. reported the use of near-IR electrogenerated chemiluminescence (ECL) of Ag_2Se QDs for detection of dopamine in a pharmaceutical drug formulation (dopamine hydrochloride injection) that contains other chemicals such as sodium bisulfite, edetate disodium, and sodium chloride.[343] Immobilized on a glassy carbon electrode, the Ag_2Se QDs displayed a cathodic ECL signal in the presence of $K_2S_2O_8$ as a coreactant. A peak at 695 nm was observed in the ECL spectrum, and this is consistent with the PL emission peak of the Ag_2Se QDs. Dopamine, with an energy level between the lowest unoccupied molecular orbital (LUMO) and the highest occupied molecular orbital (HOMO) of Ag_2Se QDs, was selected as an analyte model for evaluating the potential of this system as an ECL sensor. Upon increasing the concentration of dopamine, the ECL signal intensity decreased linearly due to energy transfer between Ag_2Se QDs and dopamine. The authors reported that, even after 10000-fold dilution, dopamine was still detected in the drug formulation at the level of 0.055 ± 0.002 M using ECL sensing. This obtained value was consistent with the reference value of 0.054 M.

The interactions between sugar chains and proteins play an important role in biological processes. Shinchi et al. developed sugar-chain-functionalized photoluminescent NPs (SFNPs) based upon Zn−Ag−In−S (ZAIS) QDs and applied them to probe lectin−sugar interactions.[222] Cellular imaging and flow cytometry analysis were performed to detect binding between SFNPs and lectins. Binding profiles differed between cell types, reflecting differing expression levels of sugar chain binding receptor proteins in cells. These functionalized NPs can be applied for cell profiling based on sugar chain−protein interactions.

Concanavalin A (ConA) is a legume lectin harvested from jack bean which can bind to the glucose moiety of cell membrane glycoproteins. This binding can initiate cell mitogenesis, agglutination, T-cell activation, and apoptosis. Various detection methods have been engineered to sense ConA because this biomolecule is a useful probe for studying carbohydrate−protein interactions. Thus, development of a simple approach for detecting ConA would be quite valuable. Yan et al. prepared ultrasmall water-dispersible Ag_2Se QDs by reduction of selenium powder along with binding of thioglycolic acid (TGA) and silver ions.[344] Glycine was used to passivate the QD surface. This method does not require the use of high temperature, high pressure, or organic solvents. Conjugating ConA to TGA-modified Ag_2Se QDs produced structures whose aggregation was detectable by resonance Rayleigh scattering (RRS). The RRS signals from the QDs were used to detect ConA with a detection limit of 0.08 μg/mL. This method provides a relatively low limit of detection and can be adapted for sensing other complex biomolecules in blood samples.

Water-dispersible $AgInS_2$/ZnS QDs prepared by a microwave-assisted method were used to determine intracellular copper(II) levels.[377] Briefly, HeLa cells were incubated with $AgInS_2$/ZnS QDs, and then $Cu(NO_3)_2$ was used to manipulate the intracellular copper(II) level. In this experiment, the PL intensity was found to decrease due to quenching by intracellular Cu^{2+} ions. The introduced Cu^{+} could displace Zn^{2+} on the QD surface and form a CuS shell, thereby facilitating nonradiative recombination of excitons. In addition, confocal laser scanning microscopy (CLSM) was employed to investigate the PL quenching process in HeLa cells. The authors highlighted that $AgInS_2$/ZnS QDs can be used as intracellular Cu^{2+} imaging probes for imaging the dynamic interaction between copper ions and cell components.

Liu et al. created a PL detection system for sensing lysozyme using $CuInS_2$ QDs as optical probes.[378] Poly(dimethyl diallyl ammonium chloride) (PDAD), a cationic polyelectrolyte, was applied to quench the PL of $CuInS_2$ QDs via electrostatic interactions and subsequent electron transfer between PDAD and the QDs. When a negatively charged lysozyme aptamer was added, it bound PDAD and disrupted the interaction between QDs and PDAD, producing PL recovery. When lysozyme was also introduced into the system, it bound its aptamer and released the PDAD which then quenched the QD PL (Figure

DOI: 10.1021/acs.chemrev.6b00290
Chem. Rev. 2016, 116, 12234−12327

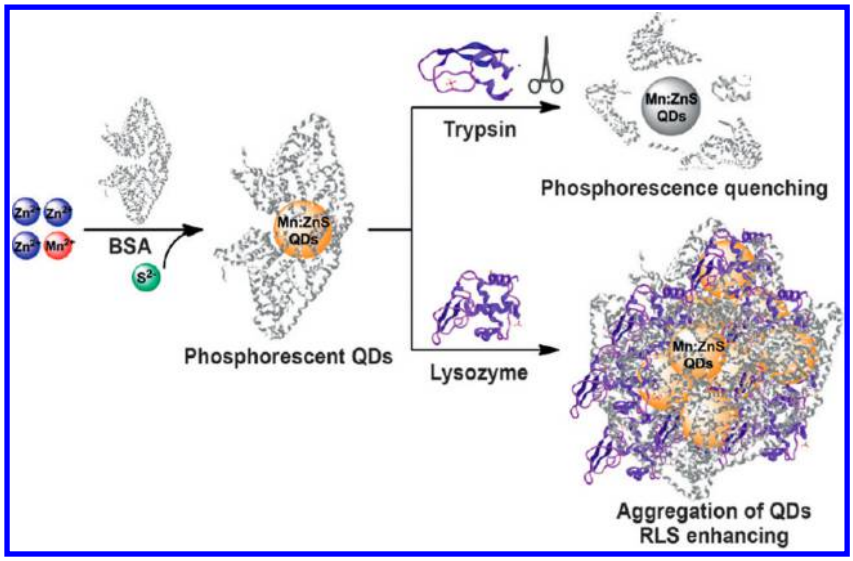

Figure 44. Schematic diagram of Mn-doped ZnS QDs for dual-functional sensing: phosphorescent sensing for trypsin and RLS sensing for lysozyme. Reprinted with permission from Wu et al.[380] Copyright 2013 John Wiley and Sons.

43). The concentration of lysozyme was determined by measurement of PL intensity changes.

$CuInS_2$ QDs have been modified with 3-aminophenylboronic acid and used as PL probes for the detection of benzene-based organic compounds.[345] The bioconjugated $CuInS_2$ QDs displayed PL peaking at 736 nm. The boronic acid functional groups were reactive toward vicinal diols. Their reaction formed five- or six-member cyclic esters in an alkaline buffer and caused PL quenching of the QDs. Thus, one can use these QDs for monitoring of dopamine and vicinal diols such as catechol, pyrogallol, and gallate. This assay is unaffected by other phenolic compounds such as phenol, resorcinol, and hydroquinone. The QDs were also used to detect dopamine in human serum samples with reasonable accuracy. Using the same strategy, the same group reported a method for sensing dicyandiamide based on PL quenching of surface-modified $CuInS_2$ QDs.[379] Based on cyclization of the guanidine group of dicyandiamide with 2,3-butanedione and 3-aminophenylboronic acids, the PL of the 3-aminophenylboronic acid functionalized $CuInS_2$ QDs was quenched by dicyandiamide in the presence of 2,3-butanedione. This approach can be used to differentiate dicyandiamide from other amino acids and nitrogen pollutants such as melamine in milk samples. A linear correlation between the luminescence intensity of surface modified QDs and the dicyandiamide concentration, from 2.0 $\times 10^{-6}$ to 2.0 $\times 10^{-3}$ mol L^{-1}, was reported for this detection scheme. A sensitivity of 0.6 μmol L^{-1} was achieved in this system. Later, they demonstrated a urea-biosensing system using dopamine-modified $CuInS_2$ QDs as the luminescence probe.[376] When the pH of the dopamine-capped $CuInS_2$ QD dispersion was changed from neutral to basic, the dopamine on the QD surface was converted to quinone, which quenched the PL of the bioconjugated QDs. This was mainly due to charge transfer interactions between QDs and the proximal quinone molecules. Because the hydrolysis of urea in the presence of urease will release OH^- and raise the pH, the fluorescence intensity of dopamine-capped QDs can be used to evaluate the enzymatic degradation of urea. The proposed urea-biosensing scheme can be used to determine urea concentrations ranging from 0.2 to 6 mM.

Many proteins have both nanosize dimensions and sites that bind inorganic ions. These features allow them to be used for the synthesis of NP−protein hybrids with specific functionality and excellent water dispersibility. Wu et al. reported protein-templated fabrication of Mn-doped ZnS QDs using bovine serum albumin (BSA) as a template.[380] The QDs exhibited phosphorescence at 590 nm with a decay lifetime of 1.9 ms. Two sensing approaches for the detection of trypsin and lysozyme with dBSA-templated Mn-doped ZnS QDs were developed. Phosphorescence quenching was used to detect trypsin molecules, while enhancement of resonant light scattering (RLS) and phosphorescence were applied for sensing lysozyme. Trypsin could digest the BSA on the QD surface and quenched the phosphorescence, while lysozyme was hypothesized to assemble with the BSA and induce aggregation of QDs, leading to an enhanced RLS signal (Figure 44). The detection limits for trypsin and lysozyme were 40 and 3 nM, respectively.

The ability to sense intracellular Zn^{2+} is important due to its significance in various biological processes. Ren et al. reported the synthesis of silica-coated S^{2-}-enriched Mn-doped ZnS QDs for imaging of intracellular Zn^{2+} ions.[381] The excited states in S^{2-}-enriched QDs are prone to nonradiative recombination because of the abundant S^{2-} dangling bonds. As a result, the S^{2-}-enriched QDs exhibited weak PL. Exposure to Zn^{2+} ions could eliminate the S^{2-} dangling bonds and suppress nonradiative recombination, thereby enhancing the PL of the QDs. The probes provided a good linear correlation between the recovered PL intensity of the QDs and the concentration of Zn^{2+} from 0.3 to 15.0 μM, good reproducibility, and a detection limit of 80 nM Zn^{2+}. Furthermore, the QDs displayed low cytotoxicity.

Wen et al. reported a phosphorescence nanosensing system based on L-cysteine-capped Mn-doped ZnS QDs.[382] Sanguinarine was attached to the QD surface to form nanoconjugates with quenched phosphorescence. When G-quadruplex sequences combined with the sanguinarine of the nanoconjugates, the QD phosphorescence was recovered. The interactions between sanguinarine and six G-quadruplex DNAs with various sequences (tel24-1, tel24-2, tel22, k-ras, HIF-1α, and c-kit1) were examined using this method and were found to depend on the number of bases and conformation of the DNA. The

DOI: 10.1021/acs.chemrev.6b00290
Chem. Rev. 2016, 116, 12234−12327

developed method is simple, rapid, and insensitive to fluorescence interferences of the system. These features can make it a valuable tool for studying the interaction of drugs with different G-quadruplexes.

QDs are commonly employed for PL sensing. However, their use in time-resolved fluorometry could be more effective if they had longer-lived emission. Zhu et al. prepared aqueous Mn-doped ZnSe QDs using a microwave synthesis approach.[383] The PL lifetime of the QDs was 400 μs, roughly 10 000 times that of CdS, CdSe, and CdTe QDs. The QDs displayed good photostability over 35 h under continuous irradiation at 260 nm. The Mn-doped mercaptopropionic acid capped ZnSe QDs were used for time-resolved PL sensing of 5-fluorouracil (5-FU), and provided a detection limit of 128 nM. These results suggest that the Mn-doped ZnSe QDs can be used for highly sensitive time-resolved fluorometry in the detection of other drugs.

Graphene QDs (GQDs) are of interest for biomedical imaging and sensing owing to their distinct optical properties, resistance to photobleaching, and excellent biocompatibility. Qian et al. designed a DNA nanosensor that combined GQDs with carbon nanotubes (CNTs).[346] Single-stranded DNA probes, ssDNA−rGQDs, were obtained by linking DNA with reduced GQDs. Multiwalled CNTs were modified to be water dispersible by oxidation in nitric and sulfuric acids. The ssDNA−rGQDs were then adsorbed on the oxidized CNTs through $\pi-\pi$ stacking and electrostatic interactions to form ssDNA−rGQD/CNT complexes. The PL of the ssDNA−rGQD was almost completely quenched when assembled with CNTs, due to energy transfer to the CNTs. When complementary DNA was added, it bound to ssDNA−rGQDs with a high affinity and separated the ssDNA−rGQDs from the CNTs, producing PL recovery. With a detection limit of 0.4 nM, this method shows promise for distinguishing complementary and mismatched DNA sequences with high sensitivity and good reproducibility. In a subsequent study, CNTs were replaced with graphene oxide (GO) to construct a dual-color GQD/GO sensor.[384] GO, 1,2-ethylenediamine functionalized graphene QDs (eGQDs), and different-colored reduced graphene QDs, rGQDs were prepared separately. ssDNA was connected to the eGQDs and a thrombin aptamer was linked with the rGQDs. The ssDNA−eGQDs and TA−rGQDs were mixed with GO to form an assembly, and fast electron transfer between them caused PL quenching of the GQDs. Addition of complementary DNA or thrombin could recover the PL due to comparatively stronger affinity to ssDNA and TA, respectively. The result demonstrated that, as dual-color probes, the developed GQD/GO assemblies allow the simultaneous detection of DNA and thrombin.

Zhao et al. reported a GQD/graphene probe for sensing human immunoglobulin G (IgG).[309] In their work, the FRET pair was fabricated using mouse antihuman immunoglobulin G (mIgG)-conjugated GQDs as donor and graphene as an acceptor. In the graphene dispersion, the functionalized GQDs had their PL quenched as a combined result of the $\pi-\pi$ stacking interaction between graphene and GQDs and nonspecific binding of the mIgG to the graphene surface. When human IgG, which binds mIgG through a specific antibody−antigen interaction, was added, the mIgG-GQDs separated from the graphene surface, leading to recovery of the GQD PL.

Zhang et al. developed another graphene-based nanosensor for selective glucose detection.[385] They produced boron-doped graphene QDs (BGQDs) by hydrothermal cutting of boron-doped graphene (BG). Boronic acid groups on the BGQD surface allowed them to serve as optical probes for label-free glucose sensing. In the sensing process, the reaction between the boronic acid groups on the BGQD surfaces and the *cis*-diol units in glucose formed BGQD−glucose aggregates, which surprisingly resulted in greatly enhanced PL. The authors suggested that the aggregation of the BGQDs could stiffen their structure, limiting interactions of neighboring luminescence centers, which reduced nonradiative recombination and therefore enhanced the PL.

5.4. Optical Tracking

Scattering, absorbance, and endogenous autofluorescence of living tissues produce significant challenges to improving tissue penetration depth and three-dimensional (3D) spatial resolution of fluorescence- and PL-based imaging using exogenous optical nanoprobes. Near-IR-emitting Cd-free QDs open up new capabilities for in vivo imaging to achieve precise optical tracking.[47,174,386] Li et al. synthesized $CuInS_2$/ZnS QDs with PL QY up to 60% and used them for an in vivo biodistribution study.[163] QDs with emission wavelengths from 650 to 750 nm were transferred into water by ligand exchange using DHLA. The biodistribution of the QDs was visualized by PL imaging after tail vein injection in nude mice. Fifteen minutes after injection, the QDs had accumulated mainly in the spleen, lungs, and liver. Twenty-four hours after injection, the mice were dissected and their organs were analyzed, confirming the noninvasive in vivo observations. The lungs are among the blood first-pass organs and functioned as a filter immediately after QD injection. The liver and spleen take up QDs in their functional roles as part of the reticuloendothelial system (RES). Aggregation of QDs within the organs was attributed to opsonin binding. The biodistribution of these nontargeted QDs in nontumor-bearing mice provides general information on the fate of such QDs upon tail vein injection.

NIR InAs/InP/ZnSe QDs coated with MPA, with hydrodynamic diameter below 10 nm and PL near 800 nm (QD800-MPA), were also used for in vivo imaging.[297] Two murine tumor models, 22B and LS174T, were employed. One hour after tail-vein injection, PL from QD800-MPA was observed in both tumor models. PL from other organs was much lower. After 4 h, the tumors were easily distinguished from other tissues by PL, indicating high uptake efficiency. The PL intensity of QD800-MPA in the tumor gradually increased from 0.5 to 4 h after injection, then decreased slowly after 6 h due to renal clearance, and finally remained low after 18 h. To assess the dependence of uptake by enhanced permeation and retention (EPR) effects on size, they conducted a parallel experiment using QD800-COOH with hydrodynamic diameter of 25 nm as a control sample to target 22B tumors. In contrast to the results with smaller QDs, there was no obvious PL from QD800-COOH at the tumor site, and the PL intensity from the liver, spleen, and bone marrow became brighter from 30 min to 6 h after injection. Human serum albumin (HSA) protein, a major soluble protein of the circulatory system, was used to modify QD800-MPA to reduce uptake in the RES system. The results showed increased QD800-MPA-HSA uptake by the tumor, compared with QD800-MPA, accompanied by reduced uptake by the RES organs. Later, the same group coupled QD800-PEG with arginylglycylaspartic acid (RGD) and

DOI: 10.1021/acs.chemrev.6b00290
Chem. Rev. 2016, 116, 12234−12327

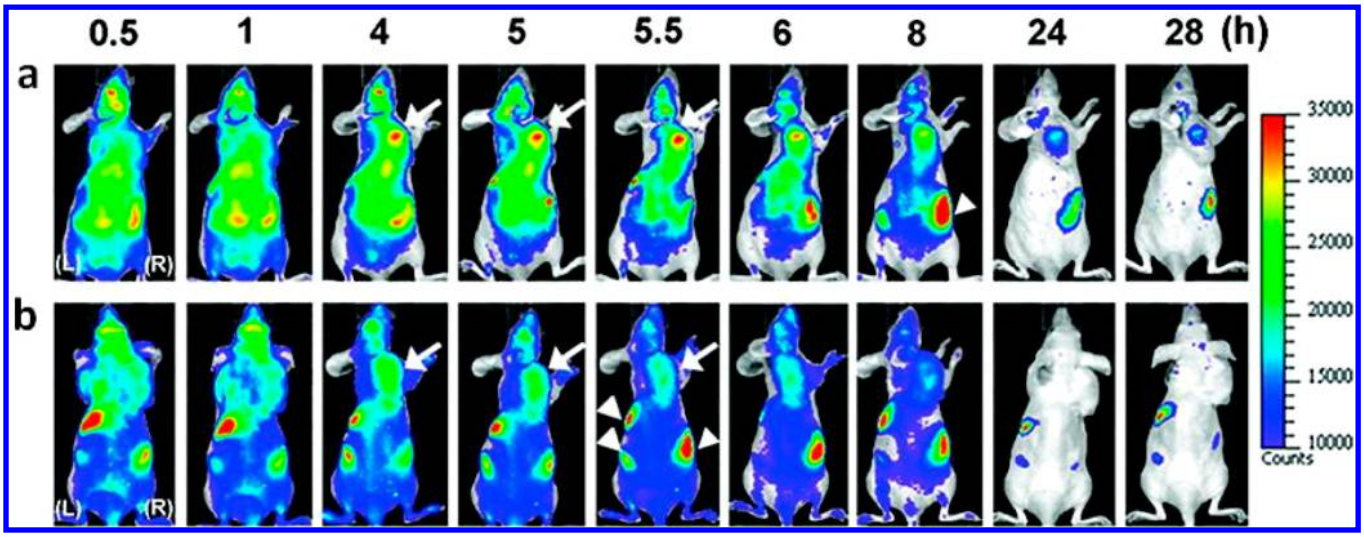

Figure 45. In vivo NIR PL images of tumor-bearing mice, at different time points, postinjection with QD710-dendron-RGD_2 (a) and QD710-dendron (b) (arrows, tumor; L, left side; R, right side). Reprinted from Gao et al.[389] Copyright 2012 American Chemical Society.

arginine-alanine-aspartic acid (RAD) peptides to visualize tumors.[387] Due to the PEG coating, these QDs had larger hydrodynamic diameter than QD800-MPA. Size measurements by dynamic light scattering (DLS) gave hydrodynamic diameters of 16.5, 20.1, and 19.6 nm for QD800-PEG, QD800-RAD, and QD800-RGD, respectively. The three types of QDs were administered intravenously into nude mice with subcutaneous human glioma (U87MG) tumors. PL from the tumors of mice injected with either QD800-RAD or QD800-RGD was detected at 30 min postinjection. After 1 h, the tumors of mice treated with QD800-RGD showed bright PL, while the PL signal from tumors of mice treated with QD800-RAD had decreased. This indicated that the QD800-RGD had higher specificity for U87MG tumor. No significant PL contrast was observed in tumors of mice treated with QD800-PEG. Moreover, PL contrast remained pronounced even after 24 h in the mice treated with QD800-RGD. All these results confirmed that specific tumor targeting by QD800-RGD led to longer retention of QDs in the tumor.

In another study, the same group used anti-HER2 antibodies with a cysteine added at their N-terminus to functionalize maleimide-terminated QD800-PEG.[388] Two tumor models with varied HER2 expression levels, SKOV3 (high HER2 level) from human ovarian cancer and PC-3 (low HER2 level) from human prostate carcinoma, were used to study HER2 based targeting. PL images were collected at multiple time points from 30 min to 24 h after injection into tumor-bearing mice. Already at 30 min postinjection, PL from the QD800-affibody was observed in the SKOV3 tumor models. Within 4 h, the PL intensity of the tumor provided high contrast with other tissues in SKOV3 tumor-bearing mice, while no tumor contrast was observed in the control groups of PC-3 tumor-bearing mice or SKOV3 tumor-bearing mice treated with QD800-PEG. In the SKOV3 tumor-bearing mice treated with the QD800-HER2, tumor PL contrast remained distinguishable even after 24 h, due to the enhanced tumor retention of the QDs induced by the high targeting efficiency of HER2. This study showed that the QD800-HER2 could serve as excellent labels for imaging and tracking of HER2 expressing tumors.

Gao et al. prepared dendron-functionalized InP/ZnS core/shell QDs for molecular tracking, with PL emission peaking at 710 nm.[389] The QDs were conjugated with RGD peptide dimers (RGD2) to form QD710-dendron-RGD2. In vivo PL images were collected at successive time points, while ICP-MS was used to quantify the QD content of urine and feces. Acute tumor uptake of QD710-dendron provided high contrast between the tumor and surrounding tissues, suggesting that passive targeting by the EPR effect was significant. However, the specific interaction of QD710-dendron-RGD2 with integrin $\alpha_v\beta_3$-positive tumor cells (SKOV3) led to greater tumor uptake and longer retention (>24 h) of the QDs at tumor sites (Figure 45). ICP measurements demonstrated that the QD710-dendron was cleared renally, with 60% of the initial dose cleared after 1 day, nearly all cleared after 1 week, and reaching undetectable levels 10 weeks after the injection.

Lymph nodes (LNs) play an essential role in immune response to exogenous substances. Dubertret et al. prepared $CuInS_2$/ZnS core/shell QDs with PL near 800 nm and high QY and stability in both organic and aqueous media.[390] They administered $CuInS_2$/ZnS QD-loaded phospholipid micelle dispersions subcutaneously in the right anterior paw of mice. Two regional lymph nodes, i.e., right axillary LNs (RALNs), could be clearly visualized a few minutes after injection. No obvious inflammation was found 7 days after injection. Later, the same group used these $CuInS_2$/ZnS QDs to visualize the sentinel lymph node (SLN) in a murine metastatic breast tumor model using a NIR imaging system.[391] Indium content of selected organs was then analyzed by ICP-MS. Metastasis was assessed through molecular techniques and immunohistology. SLN metastasis is an important predictor of recurrence/survival and guides the therapy modality for tumor patients. Thus, real-time localization and evaluation of the SLN plays a key role in the clinic. Imaging showed that QD PL appeared in the SLN 5 min after injection and increased up to 8 h after subcutaneous injection. ICP-MS analysis showed that the QD levels significantly decreased at the administration point and increased in the LNs within 1 h after injection. In addition, 3.5% of the injected indium content was excreted through feces after 96 h. The immunoassay revealed a maximum of 36% metastatic invasion to the SLN.

$CuInSe_xS_{2-x}$/ZnS core/shell QDs have also been used as probes for tracking the fate of oral vaccines administered to mice.[392] The QDs were loaded into poly(lactic-*co*-glycolic acid) to form microparticles 500 nm−2 μm in diameter. QDs

DOI: 10.1021/acs.chemrev.6b00290
Chem. Rev. 2016, 116, 12234−12327

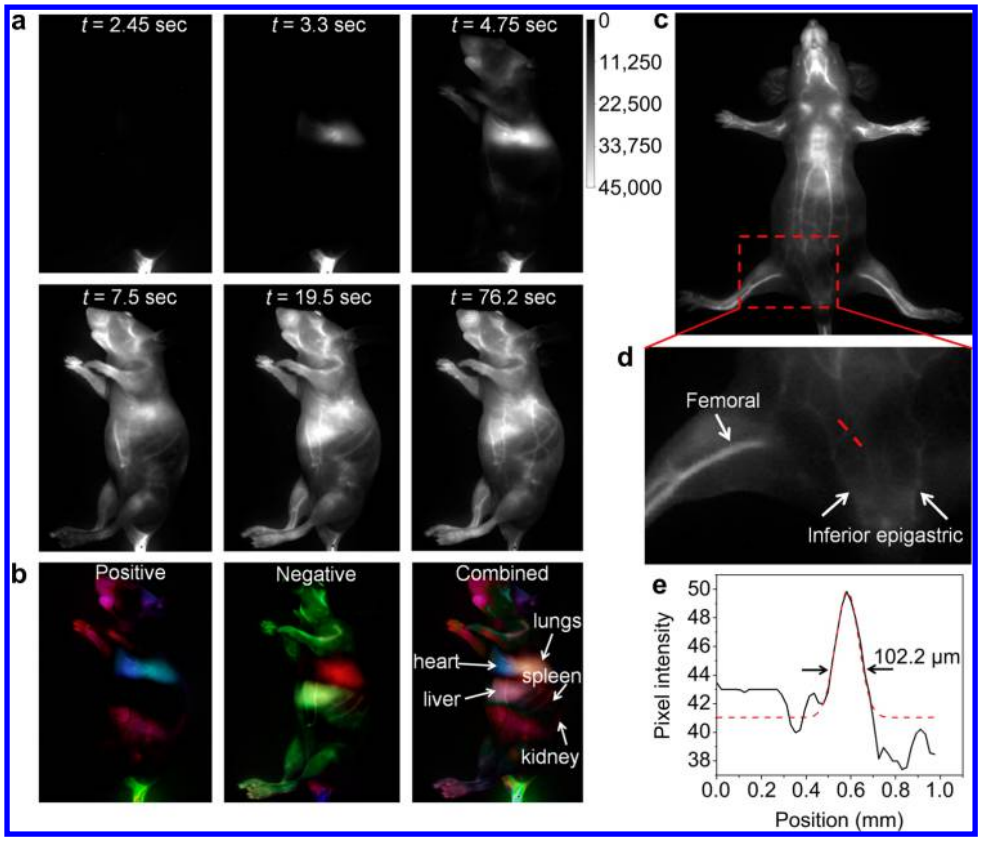

Figure 46. Blood pool PL imaging of a nude mouse. (a) Time-lapse images of blood flow in the nude mouse after injection of PEGylated Ag_2S QDs. (b) Dynamic contrast-enhanced images with PEGylated Ag_2S QDs based on PCA analysis. Deep organs such as heart, lungs, liver, spleen, and kidney were observed. (c) Intravital image of the nude mouse in supine position. (d) Amplified fluorescent image of vasculature in the nude mouse. (e) Cross-sectional intensity profile measured along the red-dashed line in (d) with its peak fitted to a Gaussian function. Reprinted with permission from Li et al.[174] Copyright 2014 Elsevier.

conjugated with nonbinding variant D911A or wild-type invasin were used as control. The QD-PLGA-invasin microparticles were orally gavaged to mice. A noninvasive Caliper Life Sciences IVIS Spectrum System was employed for in vivo tracking of PL retention in the gastrointestinal tract from 15 min to 45 h. After 15 min, the QD PL appeared in the stomach. After 18 and 45 h, QD PL was only visible in the cecums and the colons of the mice treated with QDs-PLGA-invasin. In mice treated with QDs-PLGA-D911A, no PL was observed after 18 and 45 h.

For in vivo imaging, probes with emission in the second near-IR region (NIR-II, 1000−1350 nm) are often more desirable than visible or even NIR-I probes (700−950 nm). Both tissue autofluorescence and noise associated with absorbance and scattering from tissues are significantly reduced in the NIR-II window. Li et al. prepared PEGylated Ag_2S QDs with PL emission peaking at 1200 nm.[174] They explored in vivo dynamic imaging using Ag_2S QDs as labels for monitoring lymph flow, blood flow, and angiogenesis in mice with subcutaneous xenograft tumors (Figure 46). Upon subcutaneous injection, the Ag_2S QDs were first located in the lymphatics and transferred to the popliteal and lumbar lymph nodes within 2 min. Lymphatic vessels with an average diameter of 100 μm were unambiguously visualized. The video-rate PL images showed that the QDs returned to the heart after intravenous injection and then entered the pulmonary circulation before being distributed throughout the mouse body. Real-time visualization of tumor-induced angiogenesis showed that vascular structures were recruited to feed the tumor, with PL clearly observed on the 15th day after tumor xenografting. The NIR-II QD labels could improve diagnostic efficiency through tracking pathological and physiological processes in the lymphatic and circulatory systems.

Recently, stem-cell-based therapies have shown increasing potential for applications including liver disease treatment, bone regeneration, and even cardiac repair. However, development of this field is impeded by a lack of precise data on aspects such as the in vivo engraftment efficiency of transplanted stem cells, and consistent interpretation of therapeutic effects and migration behaviors. High-resolution imaging labels and techniques to visualize the fate of the stem cells in living animal models remain urgently needed.[393] Tamaki et al. employed NIR QDs to label bone marrow stromal cells and visualize cell delivery in mice with cerebral infarct over a 4 week period after transplantation.[394] This work demonstrated a novel strategy to observe stem cell function for therapy, showing that NIR QDs could be an excellent probe to track the migration and transport of stem cells. Using a similar strategy, Chen et al. developed Cd-free NIR QDs for stem cell tracking. They conjugated Ag_2S QDs (NIR-II, 1.0−1.4 μm) with Tat peptide.[47] The peptide-functionalized QDs were then used as probes to label and track transplanted human mesenchymal stem cells (thMSCs) in mice. In vivo imaging of organ-specific accumulation and translocation of QD-labeled thMSCs in mice with liver failure tracked 1000 Ag_2S QD-labeled thMSCs. The

DOI: 10.1021/acs.chemrev.6b00290
Chem. Rev. 2016, 116, 12234−12327

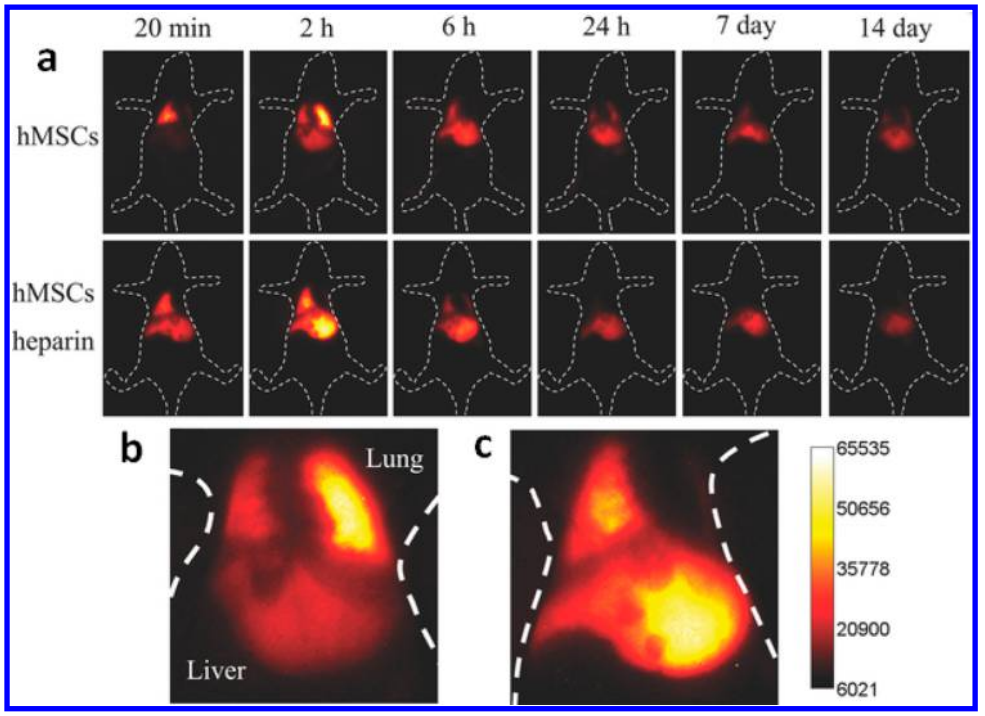

Figure 47. In vivo tracking of intravenously injected Ag_2S QD-labeled hMSCs in mice. (a) Time-lapse in vivo NIR PL images of a healthy mouse after transplantation of Ag_2S QD-labeled hMSCs (upper) and a mouse with acute liver failure after transplantation of QD-labeled hMSCs (lower) in combination with heparin at different times (20 min−14 days). (b) Higher magnification PL image of a mouse transplanted with hMSCs after 2 h. (c) Higher magnification PL image of a mouse with liver failure transplanted with hMSCs in combination with heparin after 2 h. Reprinted with permission from Chen et al.[47] Copyright 2014 John Wiley and Sons.

distribution of thMSCs in the liver and lung was tracked for 14 days, showing heparin-facilitated transfer of thMSCs from lung to liver and the long retention of thMSCs in the liver (Figure 47). The NIR-II Ag_2S QDs provided the ability to track stem cells in living animals with high temporal and spatial resolution, which can potentially accelerate clinical application of stem cell therapies.

5.5. Photothermal Therapy

Photothermal therapy (PTT) of tumors combines nanomaterial delivery with optically driven heat generation at the tumor site. PTT can significantly reduce tumor size with minimal damage to surrounding healthy tissues. NPs for PTT are usually designed to generate heat upon absorbance of near-IR light from 650 to 900 nm.[395−398] In vivo PTT effectiveness is determined by accumulation of NPs, light intensity, and the efficiency of conversion of light to heat.[399−402] For example, Hu et al. prepared hydrophilic plate-shaped Cu_9S_5 NPs with an average size of 13 nm × 70 nm and used them as photothermal agents.[403] These NPs showed strong NIR LSPR absorbance with an extinction coefficient of 1.2×10^9 M^{-1} cm^{-1} at 980 nm. Their light-to-heat conversion efficiency was up to 25.7%. Ex vivo tumors were exposed to 980 nm light for 10 min. Subsequent histological results indicated that most of the cancer cells were killed due to photothermal heating mediated by the Cu_9S_5 NPs.

Gold nanoshells have been used as PTT agents in research laboratories since 1990, and were commercialized by AuroShell (Nanospectra Biosciences, Houston, TX, USA) in 2008.[404] However, their therapeutic efficacy can still be improved to treat deeper tumors, and their relatively large size may be an impediment to achieving desirable biodistribution. Thus, additional PTT agents are still of interest. In 2011, Korgel's group synthesized ligand-functionalized $Cu_{2-x}Se$ NPs with an average diameter of 16 nm and used them in PTT experiments.[348] The NPs were obtained through a hot injection technique followed by coating with amphiphilic polymer layers. They showed strong NIR absorbance with an extinction coefficient up to 7.7×10^7 M^{-1} cm^{-1} at 980 nm. Even under 800 nm light, the $Cu_{2-x}Se$ nanocrystals showed a photothermal transduction efficiency of 22%, which was higher than that of gold nanorods and gold nanoshells under the same conditions. In vitro photothermal heating of cancer cells (HCT-116) loaded with the $Cu_{2-x}Se$ QDs resulted in cell destruction after 5 min irradiation at a power density of 33 W/cm^2. Likewise, Liu et al. synthesized cysteine-functionalized CuS QDs (Cys-CuS QDs) as PTT agents with high therapeutic efficacy.[349] The QDs exhibited high stability in the biological environment due to the biocompatible cysteine coating. They also showed strong absorbance in the NIR with a high photothermal conversion efficiency of 38%. This value is higher than that of the recently reported Cu_9S_5 and even $Cu_{2-x}Se$ nanocrystals. In vivo experiments demonstrated that such QDs could efficiently inhibit tumor growth with an 18.5 °C temperature increase in 300 s under 0.72 W cm^{-2} excitation at 980 nm for solutions with a concentration of 50 ppm (Figure 48). The high conversion efficiency, photostability, and biocompatibility of these NPs show great promise for use in PTT.

Surface functionalization of NPs with therapeutic drugs can create bimodal chemotherapy−PTT agents. For example, Hu et al. designed and prepared $Cu_{2-x}Se@mSiO_2$-PEG core/shell QDs. The core of the $Cu_{2-x}Se$ QDs served as a PTT agent, while the $mSiO_2$ nanoshells were loaded with doxorubicin, an anticancer drug. Drug release from the QD conjugates could be triggered by pH changes and/or illumination. Both chemotherapy and photothermal therapy were triggered by irradiation

DOI: 10.1021/acs.chemrev.6b00290
Chem. Rev. 2016, 116, 12234−12327

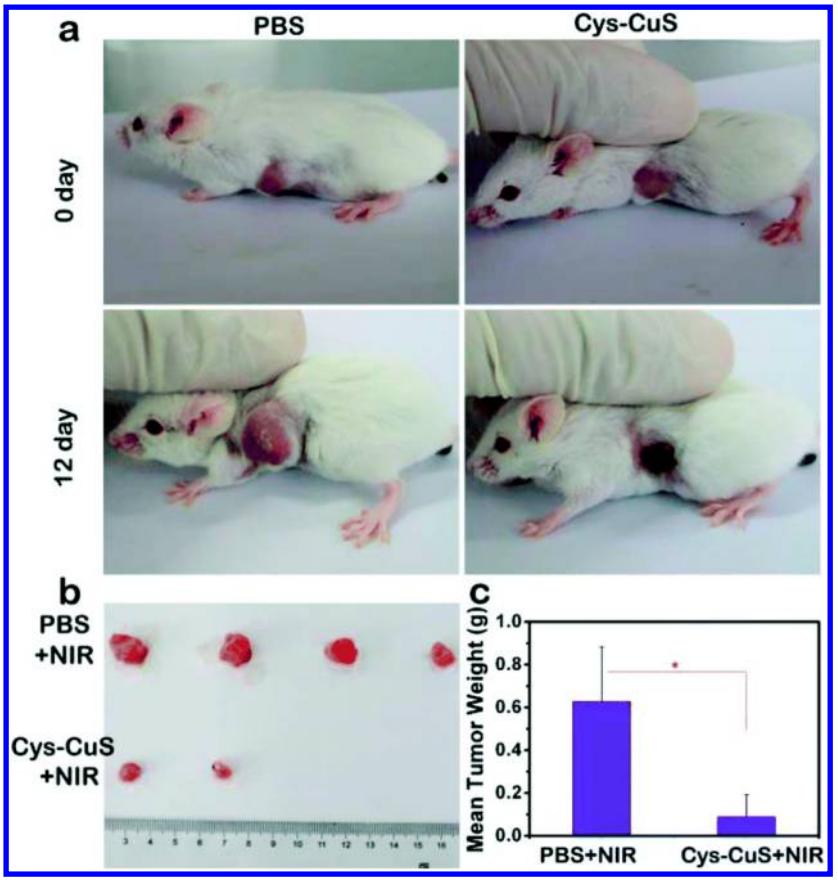

Figure 48. Inhibitory effect of Cys-CuS QDs on tumor growth. (a) Representative photos of mice bearing osteosarcoma tumors before and after treatment with PBS or Cys-CuS. (b) Photos of the tumors collected from the mice at the end of treatment (day 12). (c) Mean weights of tumors in (c). Reprinted with permission from Liu et al.[349] Copyright 2014 Royal Society of Chemistry.

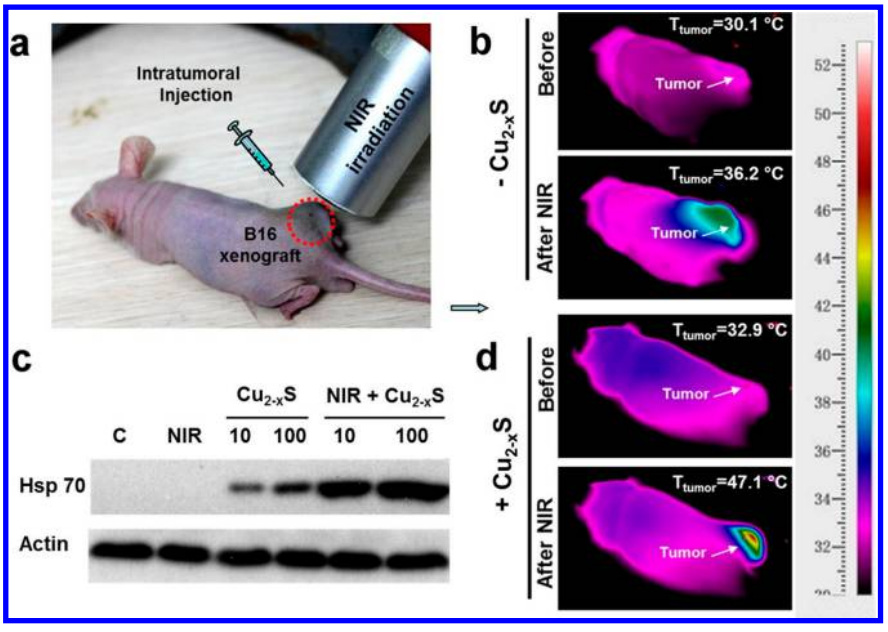

Figure 49. IR thermal images of BALB/c mice bearing B16 tumors after 100 s NIR laser irradiation and in vitro results for heat shock protein (hsp) expression. (a) B16 tumor-bearing BALB/c nude mouse. The NCs were injected intratumorally, followed by NIR irradiation. (b) IR thermal images taken in the nontreated mice before and after NIR irradiation. (c) Hsp70 expression of B16 cells after treatment with $Cu_{2-x}S$ NCs and NIR irradiation. NIR alone was used as a control. (d) IR thermal images of the tumor site postinjection of $Cu_{2-x}S$ NCs before and after NIR laser irradiation. Reprinted from Wang et al.[406] Copyright 2015 American Chemical Society.

at a safe power density. This significantly improved the therapeutic efficacy compared to single modality therapy. The same group also demonstrated similar CuS@mSiO_2-PEG NPs as an NIR-light-dependent drug release system.[405]

DOI: 10.1021/acs.chemrev.6b00290
Chem. Rev. 2016, 116, 12234−12327

Mou et al. produced monodisperse and ultrasmall (<5 nm) $Cu_{2-x}S$ QDs (u-$Cu_{2-x}S$ QDs) with high NIR absorbance and conversion efficiency for PA imaging-guided in vivo photothermal therapy.[366] Such QDs provide long circulation time and good passive tumor targeting via the EPR effect. Advantages of these QDs include not only their small diameter but also their water dispersibility and long-term stability. In vivo experiments showed a significant decrease in tumor volume after 48 h for the groups injected with QDs and exposed to laser illumination. Tumors were eliminated in 48 h and had not reoccurred after 16 days. No obvious side effects or toxicity of QDs to blood or normal tissue were found after 3 months. Metabolic pathway studies showed that the QDs could be thoroughly cleared through feces and urine within 5 days. This efficient excretion bodes well for future clinical translation.

Wang et al. also examined PTT effectiveness of $Cu_{2-x}S$ QDs.[406] B16 tumor bearing BALB/c nude mice were intratumorally injected with $Cu_{2-x}S$ QDs in PBS, and photothermal conversion efficiency was measured. After 100 s exposure to laser irradiation, the temperature of the experimental group increased from 32.9 to 47.1 °C (Figure 49). This temperature was high enough to kill the tumor cells in tumor-bearing mice. Interestingly, they also found that these QDs generated high levels of reactive oxygen species. Thus, the $Cu_{2-x}S$ QDs could be used for dual mode therapy, i.e., NIR PTT and photodynamic therapy.

Zhu et al. developed a facile one-pot synthesis of PEGylated functionalized mesoporous silica coated CuS QDs (CuS@$mSiO_2$-PEG) for chemo/photothermal cotherapy.[407] The QDs were colloidally stable and highly monodisperse. The antitumor drug, doxorubicin, was loaded in the mesoporous silica shell of the QDs to provide both pH-dependent drug release and high photothermal efficiency. In vitro experiments showed obvious cell death under 980 nm laser diode illumination. However, negligible cell death was observed in control groups treated with either laser exposure or QDs alone. Compared to gold NPs, these Cd-free CuS@$mSiO_2$-PEG QDs have two key advantages. First, fabrication costs are reduced because all the elements are earth-abundant and the preparation procedures are relatively simple, using a one-step reaction. Second, the absorbance peak of the obtained QD composites was around 980 nm. The penetration depth is much deeper at 980 nm than at 808 nm, the wavelength often used with metallic NPs. The safe power density is also higher at 980 nm than at 808 nm.

To improve therapeutic efficiency and minimize toxicity to healthy organs, localized treatment is preferred over systemic chemotherapy. Liu et al. designed an anticancer drug carrier nanoplatform, in which doxorubicin was encapsulated within core/shell Cu_9S_5@$mSiO_2$ QDs.[408] These QD composites were further integrated with gelatin and poly(ε-caprolactone) to form nanofibrous fabrics through electrospinning. The fabric pieces were then directly attached at the surface of the exposed tumor site of mice. The pieces loaded with QDs showed a high light−heat transfer rate and could ablate tumor cells under 980 nm illumination. At the same time, DOX was released from the spun pieces and diffused to the tumor site. The results showed that the synergistic therapy of DOX loaded Cu_9S_5@$mSiO_2$ composite fibers under 980 nm laser irradiation provided better tumor inhibition, compared with pure photothermal treatment using Cu_9S_5@$mSiO_2$ composite fibers.

Jiang et al. designed a dual plasmonic Au−Cu_9S_5 nanostructure for photothermal therapy in the second near-IR window (NIR-II: 1000−1350 nm).[81] Larger penetration depth and higher maximum permissible exposure are possible in this window. A 50% enhanced absorbance at 1064 nm was observed for QD conjugates compared to pure Cu_9S_5 QDs prepared under similar conditions. This enhanced absorbance improved the photothermal performance. Moreover, Au−Cu_9S_5 QDs exhibited excellent colloidal stability and photostability. The NPs had a high photothermal transduction efficiency of 37% and a tissue penetration depth up to 5 mm at 1064 nm.

To ensure a safe and efficient PTT process, precise determination of the tumor size, location, and morphology together with the PTT agent distribution are essential. These aspects could be enhanced through contrast-enhanced imaging combined with PTT to achieve imaging-guided PTT. PTT and its integration with traditional chemotherapy are another promising research area, since most QDs and their nanocomposites that are explored as PTT agents can also function as PA imaging agents and can exhibit the above-mentioned synergistic effects for thermoradiotherapy and thermochemotherapy.

5.6. Multimodal Imaging

Over the past few decades, cancer has become an increasingly important cause of human mortality and morbidity worldwide. New diagnostic and imaging technologies are continuously being developed for early diagnosis and for monitoring of therapies. However, to date, no single imaging modality can provide both precise and comprehensive information about complex tumor systems. Multimodal-imaging strategies have attracted attention from the research community for their potential to address these challenges.[409−411] Currently, MRI is widely used for cancer diagnosis, based upon its ability to achieve high contrast in soft tissues. However, MRI has key limitations, such as relatively slow imaging speed, high cost, and limited compatibility with intraoperative use. Other imaging modalities such as IR thermal imaging and newly developed PA imaging techniques have been combined with MRI to complement its weaknesses. The integration of MR/IR-thermal/PA/PL multimodal imaging provides new opportunities for cancer detection and monitoring.[81,321]

Stasiuk et al. developed photoluminescent/magnetic dual-mode QDs via covalent binding of Gd(III) chelates to InP/ZnS QDs.[193] The conjugated QDs exhibited a large relaxivity up to 900 mM^{-1} s^{-1} (13 mM^{-1} s^{-1} per Gd ion) at 298 K and 35 MHz (0.81 T). Bright PL from the InP/ZnS QDs was also demonstrated. Tb(III) and Eu(III) chelates were also successfully conjugated to the surface of InP/ZnS QDs. There was no energy transfer between the lanthanide ions and the QDs. Thus, multicolor composites could be formed. Different target-specific ligands were used to functionalize the QD surface through a direct graft method. For instance, peptides that could permeate through cell membranes were grafted in a facile one-pot synthesis reaction. QD PL was used to locate the cells. The QDs also showed longer tissue retention compared to traditional contrast agents.

To obtain both strong MRI signal enhancement and NIR optical absorbance, Mou et al. prepared a novel contrast agent based on $Cu_{2-x}S$ nanoprobes for T_1-weighted MRI/IR thermal/PA multimodal imaging.[411] These $Cu_{2-x}S$ NPs were prepared through thermal decomposition, followed by biomimetic phospholipid modification. The QDs exhibited high stability in the physiological environment, prolonged circulation, and effective passive accumulation within tumors

DOI: 10.1021/acs.chemrev.6b00290
Chem. Rev. 2016, 116, 12234−12327

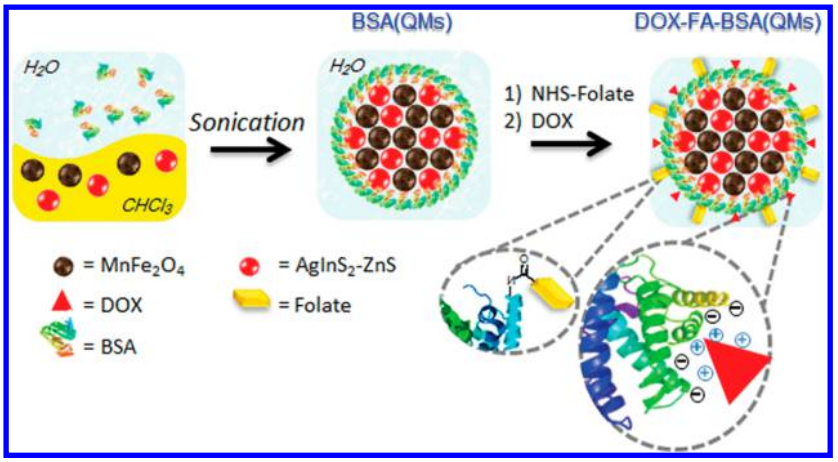

Figure 50. Schematic diagram for preparing multifunctional nanoparticles. Reprinted with permission from Fahmi et al.[350] Copyright 2014 Royal Society of Chemistry.

through the EPR effect. Their low cost and one-step synthesis increase their potential for mass production and future clinical translation. More importantly, the $Cu_{2-x}S$ QDs were found to enhance MRI contrast both in vitro and in vivo. In addition, the $Cu_{2-x}S$ NPs exhibit strong NIR optical absorbance due to their LSPR properties. This enables them to serve as an excellent candidate contrast agent for IR thermal/PA imaging. The use of pure single component $Cu_{2-x}S$ NPs for enhanced MR/IR thermal/PA multimodal imaging may bring new possibilities for better diagnosis and therapy of cancer.

Recently, $AgInS_2$−ZnS QDs aggregated with $MnFe_2O_4$ magnetic NPs (MNPs) through ultrasonication were prepared and employed for multimodal imaging (Figure 50).[350] Bovine serum albumin (BSA) molecules were used as functional groups for phase transfer into water and clustering of the QDs. The QD composites worked as both MRI and PL imaging agents. After further functionalizing them with folic acid and DOX, the hybrid nanostructures could also deliver DOX to HeLa cells. Yellow PL indicated the localization of $AgInS_2$−ZnS QDs in the cell cytoplasm and red fluorescence showed the release of DOX in the cell nucleus. The QD−MNP composite NPs showed strong MRI contrast in in vitro T_2-weighted analyses, demonstrating their potential as contrast agents for PL/MR dual-mode imaging.

Our group has also developed InP/ZnS QDs for multimodal MRI imaging and chemotherapy applications.[412] The InP/ZnS QDs and DOX were coencapsulated in PEGylated phospholipid micelles. The micelles were further conjugated with chelated Gd^{3+}. Conjugation with transferrin or anti-claudin-4 was used to enhance the specificity of the multimodal probes. These functional molecules could bind with claudin-4 and transferrin receptors overexpressed by cancer cells. The Gd-conjugated InP/ZnS QDs provided both PL and MRI contrast simultaneously. T_1-weighted and T_2-weighted MR imaging showed that the QDs with different formulation ratios exhibited increased or decreased MRI signal. The in vivo optical imaging of mice bearing pancreatic cancer xenograft tumors showed that the QD probes could specifically target the tumors to provide high contrast.

QD-based probes can also be prepared with both NIR PL and ultrasound contrast.[413] To do so, $CuInS_2$/ZnS (ZCIS) QDs were modified with plasmid DNA and polyethylenimine (PEI). PEI is commonly employed to decorate NPs for electrostatic binding of negatively charged DNA. The QDs were then adsorbed onto the surface of microbubbles to form MB@QD@PEI/pDNA conjugates that provided contrast in both PL and ultrasound imaging. In vitro cell viability experiments demonstrated that pDNA molecules were controllably released from the QD conjugates and could be internalized by cancer cells (HeLa) upon destruction of the microbubbles. The assays showed a high transfection efficiency and low toxicity to the cells.

Ding et al. engineered magnetic $CuInS_2$@ZnS:Mn QDs as bimodal nanoprobes for in vivo MRI and PL tumor imaging.[81] The $CuInS_2$@ZnS:Mn QDs were transferred into water via ligand exchange to be used for in vivo imaging. Dodecanethiol ligands on the QD surface were replaced by hydrophilic dihydrolipoic acid−poly(ethylene glycol). PL and MRI images were collected at successive time points after injection of PEGylated $CuInS_2$@ZnS:Mn QDs into tumor-bearing mice. PL signals appeared in the tumor region by 10 min postinjection and rapidly increased, reaching maximum intensity after 6 h. Meanwhile, in T_1-weighted MRI, the T_1 value of the tumor decreased and reached a minimum at 8 h postinjection. The kidneys showed a similar variation in T_1, suggesting that these QD probes were being cleared via a renal pathway, consistent with their small size.

Bismuth-based nanomaterials have a high X-ray attenuation coefficient and have been used as X-ray computed tomography (CT) contrast agents. Yang et al. synthesized Cu_3BiS_3 NPs coated with amphiphilic polyvinylpyrrolidone (PVP) for multimodal imaging and therapy of cancer.[414] The NPs showed strong NIR absorbance, high photostability, and photothermal conversion efficiency. Their cytotoxicity was evaluated, followed by CT imaging and both in vitro and in vivo experiments on photothermal ablation of cancer cells. The results demonstrated that the CT value at the tumor site after the NP administration significantly increased from 151.1 ± 10 to 741.8 ± 10 HU. Moreover, tumors targeted by the NPs were effectively inhibited under NIR laser irradiation. Thus, these nanoprobes are good candidates as multifunctional agents for CT imaging, photothermal imaging, and photothermal therapy.

Poulose et al. developed multifunctional theranostic QDs that can be used as trimodal contrast agents for PL, PA, and X-ray micro CT imaging.[415] They prepared Cu_2S QDs by a hot injection colloidal approach and then functionalized them with 1,2-distearoyl-*sn*-glycero-3-phosphoethanolamine-*N*-[folate-(poly(ethylene glycol))-2000] (DSPE-PEG-Fol). The func-

DOI: 10.1021/acs.chemrev.6b00290
Chem. Rev. 2016, 116, 12234−12327

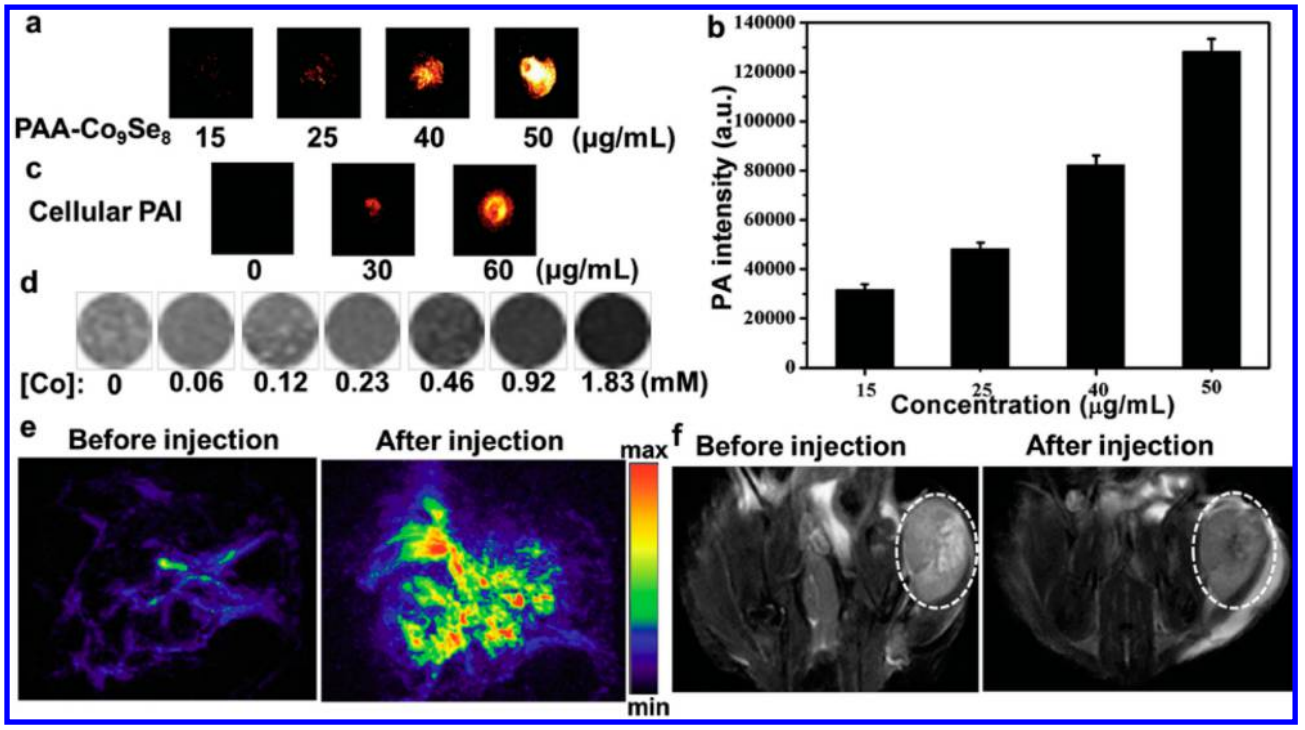

Figure 51. Multimodal imaging using PAA-Co_9Se_8 nanoplates. (a) PA images and (b) PA intensity of PAA-Co_9Se_8 nanoplates at different concentrations. (c) PA images of HepG2 cells incubated with PAA-Co_9Se_8 nanoplates. (d) T_2-weighted MR images of the PAA-Co_9Se_8 nanoplates in aqueous solution at different Co concentrations. (e) PA images of a tumor before and after injection with PAA-Co_9Se_8 nanoplates. (f) T_2-weighted MRI scans of mice before and after injection with PAA-Co_9Se_8 nanoplates (white circle, tumor). Reprinted with permission from Song et al.[417] Copyright 2015 John Wiley and Sons.

tional molecules were used here both to make the QDs water-dispersible and to provide targeting of tumors that overexpress folate receptors. The resulting QDs exhibited a blue-green emission centered at 420 nm under 365 nm light excitation and also broad NIR absorbance due to the localized surface plasmon resonance from minority carriers, leading to a high absorbance coefficient as PL and PA contrast agents. In addition, the attenuation coefficient of Cu for the QDs was demonstrated to be high enough to allow them to serve as contrast agents for X-ray imaging. The QD surface was further conjugated with DOX. The resulting multimodal PEG-Cu_2S-Fol-DOX QDs exhibited excellent biocompatibility and show promise for use in personalized cancer treatment.

Although numerous QD-based strategies have been proposed for cancer treatment, specific targeting remains a challenge in the design of biocompatible and efficient theranostic QDs. Chen et al. recently reported QD nanoprobes with high specificity for the vasculature in targeted in vivo imaging.[416] The QDs could be used for both photothermal imaging and positron emission tomography (PET) imaging. Photothermally responsive copper sulfide (CuS) NPs were loaded into biocompatible mesoporous silica nanoshells (CuS@MSN). The surface of the QD conjugates was then further modified with TRC105 antibodies for targeting and with ^{64}Cu positron emitters. In vitro targeting, a long-term (60 day) toxicity study, in vivo vasculature-targeted photothermal imaging, and PET imaging were performed systematically. The NPs exhibited low in vivo toxicity even at high doses. The TRC105 antibody on the QD surface could specifically target both human and murine CD105 in the tumor neovasculature. This significantly enhanced the tumor vasculature targeting of ^{64}Cu-CuS@MSN-TRC105 during the in vivo photothermal imaging and PET imaging.

Song et al. reported the synthesis of biocompatible poly(acrylic acid) functionalized Co_9Se_8 nanoplates (PAA-Co_9Se_8) and investigated their theranostic properties through both in vitro and in vivo experiments.[417] The PAA-Co_9Se_8 NPs exhibited strong absorbance in the NIR and low cytotoxicity without light excitation. An 808 nm laser diode was used to excite the NPs for targeted PA and photothermal therapy. The PAA-Co_9Se_8 NPs could also serve as T_2-MRI contrast agents (Figure 51). After encapsulation of DOX drugs, pH-dependent chemotherapy was observed for the DOX-PAA-Co_9Se_8 QDs. Thus, this theranostic nanoplatform is promising for PA/MR dual-modal-imaging and chemo-photothermal cotherapy.

6. NANOMEDICINE APPLICATIONS

Nanomedicine is the application of nanotechnology to disease prevention, detection, diagnosis, imaging, and therapy.[3,84,418−421] A key aim of this field is to engineer targetable diagnostic and therapeutic probes at the nanoscale. These probes can be engineered to respond to stimuli such as light, heat, pH, and magnetic fields, and can combine diagnostic and therapeutic effects, to create theranostics.[422−424] Nanomedicine approaches can overcome challenges faced by existing molecular imaging and delivery methods. For instance, using a nanomedicine approach, one can design formulations for enhanced drug protection to prevent degradation in vivo, prolong blood circulation time, reduce side effects, and improve targeting specificity to label and treat diseased cells or tissues.[425,426] Over the past two decades, numerous inorganic nanomaterials have been engineered with unique physiochemical properties for nanomedicine applications.[427−431] This

DOI: 10.1021/acs.chemrev.6b00290
Chem. Rev. 2016, 116, 12234−12327

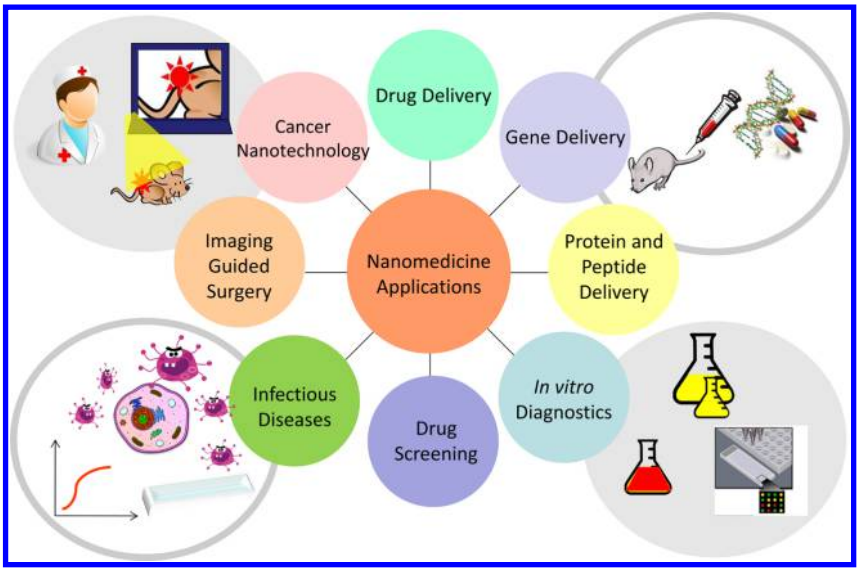

Figure 52. Visual summary of nanomedicine applications of Cd-free QDs.

section provides a description of nanomedicine applications of Cd-free QDs, including drug delivery, gene delivery, protein and peptide delivery, cancer nanotechnology, imaging guided surgery, in vitro diagnostics, drug screening, and infectious disease studies (Figure 52). Nanomedical applications discussed in this section are listed in Table 3.

The versatility of using bioconjugated QDs for targeted delivery in vitro and in vivo has led researchers to employ them in many new nanodrug and nanoprobe designs.[448,449] Much current research on applications of QDs in nanomedicine is concentrated in two areas. The first is creation of QDs with multiple functionalities for disease detection and therapy.[203,291,337] A single QD can be linked with multiple biomolecules on its surface to produce multivalent binding and thereby improve specificity in the targeted delivery of the nanoprobes to the disease site. Bioconjugated QDs can be applied to detect and quantify biomarkers on cells and tissues with high sensitivity and specificity. The second key application area of QDs in nanomedicine is in imaging-guided drug and gene delivery.[90,305,450] With sensitive multimodal imaging methods engineered into a cross-evaluation platform for biomolecule screening and investigation, we may soon achieve real-time monitoring of distribution, transport, drug release, and pharmacodynamics of QD nanoprobes in vivo.

The mechanism of delivering a formulation containing both QDs and drugs to a targeted site such as a tumor is dictated by the overall formulation. Several key principles must be carefully implemented in QD/drug formulations for targeted delivery:[451−453] (i) the nanoprobe surface must be conjugated with biomolecules for targeted delivery; (ii) the nanoprobes should degrade into components below 6 nm in diameter, after performing their function, for rapid renal clearance; (iii) drugs must be tightly linked to the nanoprobes to minimize off-target effects, but must be released or activated at target sites in response to external triggers or local microenvironmental factors; (iv) QDs must be coated with a biocompatible polymer to avoid aggregation and premature breakdown of the nanoprobes in biological fluids.

Two general approaches are used to create nanoprobes that contain both QDs and drugs:[354,454−456] (i) conjugating drugs to the QDs for delivery to target sites, with release of the drugs triggered by a change of pH or the presence of enzymes; or (ii) coencapsulating the drug molecules and QDs in a biocompatible polymer, delivering these nanocapsules to the specific sites, and releasing drugs by simple diffusion out of the encapsulating polymer or when the polymer NP is broken down at a lower pH or in the presence of enzymes. Some groups are employing the second method for drug delivery, because the preparation process does not require conjugating the drug to the QD surface and purifying the conjugates. Additional stimuli-response characteristics, such as light- or field-induced drug release are also possible. Specific examples are given in subsequent sections of this section. In addition to traditional small molecule drugs, QDs can be employed for delivery of short interfering RNA (siRNA),[151,457] to inhibit the expression of disease-causing genes. Free siRNA is negatively charged and rapidly degrades in a physiological environment, which impedes its application for in vivo and in vitro biomedical studies and applications. Therefore, siRNA is usually modified with or electrostatically bound to cationic moieties to provide physiological stability and target specificity.

6.1. Drug Delivery

Over the past two decades, significant efforts have been made to prepare drugs in nanoparticulate forms to alter their pharmacokinetics and biodistribution. Nanodrugs can be fabricated with the drugs loaded into or onto nanosize carriers such as liposomes, micelles, biodegradable polymer NPs, and inorganic NPs (e.g., QDs, gold NPs, iron oxide, etc.).[419,458−462] Nanocrystals loaded with a drug formulation can provide pharmacokinetic advantages such as targeted delivery, improved uptake by cells, and long circulation lifetime. The physicochemical properties of QD−drug formulations can be controlled by tuning the size, surface charge, and hydrophobicity of the QDs to enhance cellular uptake. Generally, QDs can enter cells through endocytotic processes such as clathrin-mediated endocytosis, potocytosis, pinocytosis, and patocytosis.[463−465] Larger particles, >200−300 nm in diameter, are opsonized and removed from the bloodstream via the reticuloendothelial (RES) system. In designing QDs functionalized with drug molecules, one must reduce opsonization to extend the blood circulation time. This is most often achieved by coating the QDs with biocompatible polymers such as

DOI: 10.1021/acs.chemrev.6b00290
Chem. Rev. 2016, 116, 12234−12327

Table 3. Nanomedicine Applications of Cd-Free QDs

nanomedicine application	QD type	functional group/ molecule	feature of technique	model used	ref
drug delivery					
in vitro	InP/ZnS QDs	DOX-PEGylated micelles	80% inhibition rate at a dose of 80 μg/mL	Panc-1 cancer cells	412
	Ag_2S QDs	DOX-cyclic RGD peptide	50% inhibition rate at a dose of 2.5 μg/mL	U87 tumor cells	209
	$AgInSe_2$/ZnS core/ shell	MTX-PMAO	75% inhibition rate at a dose of 200 μg/mL	HeLa cell	432
	Mn-doped ZnS	IBU-glycopolypeptide	50% inhibition rate at a dose of 85 μg/mL	HEK293T	433
	Si QDs	Quercetin-PEG-PLA	drug loading (4%)	HepG2	225
in vivo	Ag_2S QDs	DOX-cyclic RGD peptide	100% survival rate after 16 days	tumor-bearing mice models MDA-MB-2311	209
gene delivery					
in vitro	$CuInS_2$/ZnS core/ shell	PEI-pDNA	7.85% transfection rate at a dose <300 μM	HeLa cell	413
	Mn-doped ZnS	chitosan-pCD-UPRT	DNA binding up to 5.2 μg	–	434
	Si QDs	2-vinylpyridine siRNA	50% transfection rate at a dose of 75 μg/mL	Caco-2 cells	435
protein and peptide delivery					
in vitro	InP/ZnS QDs	CPPs and DSPE-PEG2000	2% transduction rate at a dose of 150 nM	A549 cells	41
	$CuInS_2$	BSA	monitor catalyzed reaction	lactate dehydrogenase	436
	Si QDs	anti-IgG	monitor antibodies-conjugation	HRP	437
cancer nanotechnology					
in vitro	$CuInS_2$	silica NPs and anti-PSCA Abs	as a NIR PL tracer	PC-3M	203
	InP/ZnS	chlorin e6	photosensitizer of PDT	MDA-MB-231	438
	Mn-doped ZnS	folic acid and thioglycerol	two-photon target imaging	T47D	256
imaging-guided surgery					
in vivo	$InAs_xP_{1-x}$QDs	oligomeric phosphines	SLN mapping	nude mice	439
	Si QDs	phospholipid–PEG micelle	tumor vasculature and SLN imaging	Panc-1 tumor mice	38
in vitro diagnostics					
in vitro	Ag_2S QDs	3-APBA	LOD of 3.2×10^{-5} M and 98 cells/mL	glucose and MCF-7 cell	211
	$CuInS_2$	fibrinogen	LOD of 8.7×10^{-12} mol/L	thrombin	440
	$CuInZn_xS_{2+x}$/ZnS	anti-CRP	LOD of 1 ng/mL	CRP	441
	Mn-doped ZnS	cysteine-anti-EGFR	86% specificity and 88% accuracy	A431 cells	442
infectious diseases					
in vitro	ZnS	oligonucleotides	pulse anodic stripping voltammetry	H5N1, H1N1, and H3N2 influenza	443
	PbS	12 (+5 adenine) bp	target efficiency >60%	H5N1 chains	444
	GQDs	–	induction of oxidative stress	*E. coli* and *S. aureus*	445
	Mn-doped ZnS	chitosan	emission peak at 590 nm	*E. coli*	446
	Si QDs	FGK45	enhance immune activation	CD40 Abs in B cells	447

poly(ethylene glycol) (PEG).[466,467] In addition, functionalizing the drug-loaded QDs with targeting ligands can significantly improve drug delivery to disease sites.[468,469] Oral delivery, transdermal delivery, intravenous or subcutaneous injection, and pulmonary administration can be used to introduce QD–drug formulations. Overall, using QDs as drug carriers can enhance the therapeutic potential of the loaded drugs and contribute to specific targeted therapy. Nanomedicine platforms that integrate molecular imaging and therapy into one nanosystem are being explored as a means to meet many current challenges in human disease detection and therapy. The ability to link drug molecules to Cd-free QDs provides new possibilities for advanced diagnosis and treatment of human diseases. In the following paragraphs, we discuss recent progress toward using Cd-free QDs as drug carriers.

Ag_2S QDs functionalized with cyclic RGD peptide (cRGD) and doxorubicin (DOX) were used for combined in vivo targeted imaging and drug delivery.[209] Specifically, these nanoconjugates targeted the $\alpha_v\beta_3$ integrins overexpressed by U87 tumor cells and MDA-MB-231 xenograft tumors in mice. The DOX-functionalized QDs inhibited tumor cell growth. A 16-day survival rate of 100% was reported for Ehrlich ascites carcinoma (EAC) tumor-bearing mice treated with these nanoconjugates (Figure 53). These results demonstrate the potential of Ag_2S QDs as multifunctional probes for achieving targeted imaging and therapy.

A similar study employed $AgInS_2$/ZnS QDs conjugated with methotrexate (MTX), for cancer treatment.[432] Water-dispersible $AgInS_2$/ZnS QDs were prepared by an ultrasonication method, and then MTX was covalently linked to their surface using carbodiimide chemistry. An MTT assay indicated that the $AgInS_2$/ZnS QDs coated with poly(maleic anhydride-*alt*-1-octadecene) were highly biocompatible without MTX conjugation. Confocal laser scanning microscopy showed that the

DOI: 10.1021/acs.chemrev.6b00290
Chem. Rev. 2016, 116, 12234–12327

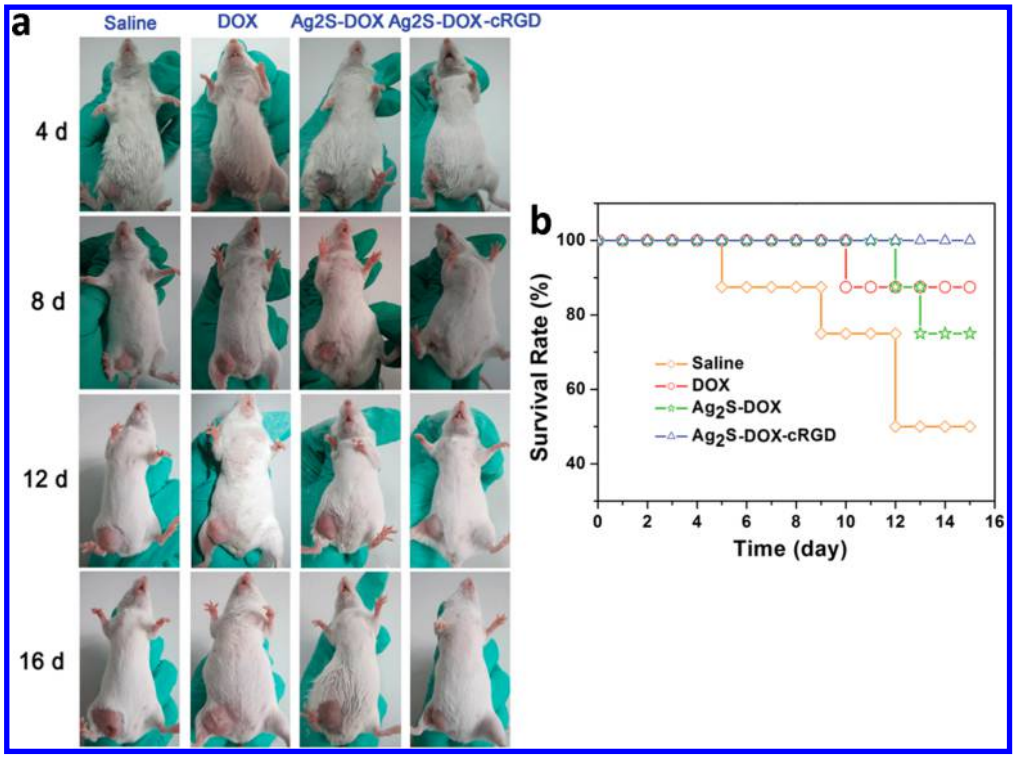

Figure 53. Evaluation of therapeutic outcomes of EAC tumor-bearing mice. (a) Photographs of tumor-bearing mice in the four groups after the indicated duration of treatment. (b) Survival rate of mice from the four groups over 16 days of treatment. Reprinted with permission from Chen et al.[209] Copyright 2014 Royal Society of Chemistry.

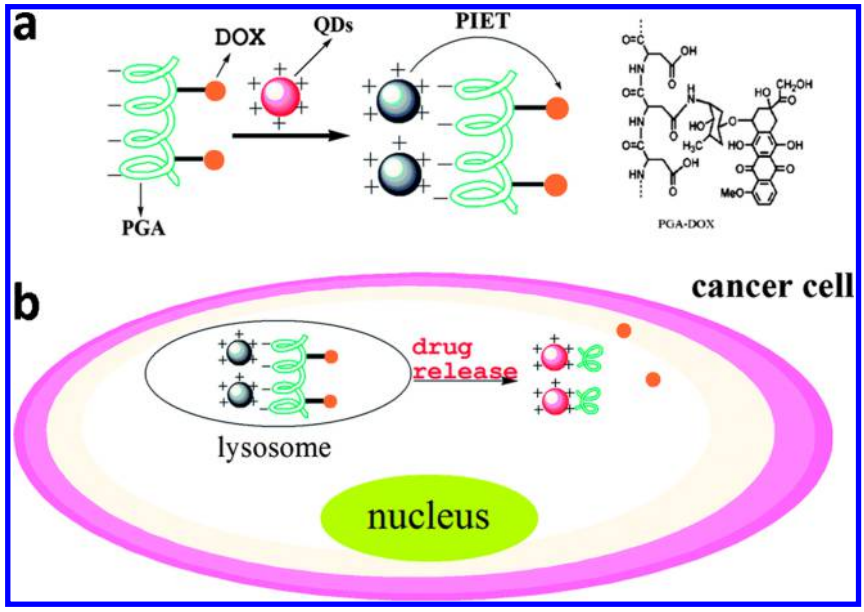

Figure 54. Schematic design of a $CuInS_2$ QD/PGA-DOX complex and its cellular delivery. (a) Construction of the nanocomplex, in which the PL of $CuInS_2$ QDs was quenched by DOX through a photoinduced electron-transfer (PIET) process. (b) The nanocomplex was taken up by cancer cells and the DOX was released by hydrolase in lysosomes, restoring $CuInS_2$ QD PL and leading to cell death. Reprinted with permission from Gao et al.[200] Copyright 2014 Royal Society of Chemistry.

MTX-conjugated $AgInS_2$/ZnS QDs were effectively taken up by HeLa cells. An MTT assay revealed a strong antiproliferative effect in HeLa cells at a dose of 300 μg/mL. This finding suggests that MTX-conjugated $AgInS_2$/ZnS QDs can be further tailored for effective cancer theranostics.

Rather than directly modifying the QD surface for drug delivery, QDs can be encapsulated in larger particles. For instance, theranostic silica (SiO_2) nanohybrids loaded with $CuInS_2$/ZnS QDs and Fe_3O_4 magnetic NPs were prepared and used as drug delivery vehicles and imaging probes for dual mode PL and MR imaging.[470] These nanohybrids were stably dispersed in water with hydrodynamic diameter below 30 nm. The nanohybrids were taken up by MCF-7 human breast cancer cells within 1 h and were located within the cytoplasm

DOI: 10.1021/acs.chemrev.6b00290
Chem. Rev. 2016, 116, 12234−12327

and near the nucleus. In MRI, the particles displayed a high spin−spin (T_2) relaxivity (r_2 = 214 mM^{-1} s^{-1}). A Pt(IV)-based anticancer drug was conjugated to the NPs, and their theranostic potential was assessed. The cytotoxicity of drug-conjugated nanohybrids was higher than that of the free drug. This indicates that the fabricated nanohybrids can be employed as multifunctional probes for simultaneous tumor imaging and chemotherapy.

Su's group reported a nanodrug delivery system created by electrostatic complexation of $CuInS_2$ QDs with poly(L-glutamic acid) (PGA) conjugated with DOX molecules.[200] They first prepared water-dispersible cysteine-capped $CuInS_2$ QDs by a hydrothermal method. DOX can quench the PL of QDs via a photoinduced electron transfer. Thus, the conjugated QDs do not exhibit PL. After the nanocomplexes were taken up by cancer cells, PGA was hydrolyzed, releasing DOX, and restoring the PL of the $CuInS_2$ QDs. The nanocomplexes delivered DOX to PC-3M cancer cells and released DOX to kill the cells (Figure 54). DOX release was monitored by recording the PL intensity from the $CuInS_2$ QDs. The multifunctional nanocomplex has potential for use in molecular imaging studies of drug distribution.

Later, the same group demonstrated the synthesis of MUC1 aptamer functionalized near-IR $CuInS_2$ QDs and loaded those QDs with daunorubicin for targeted cancer therapy.[198] More specifically, the $CuInS_2$ QDs were conjugated with MUC1 aptamer-$(CGA)_7$ which allowed daunorubicin to intercalate between the double-stranded CG sequence of the MUC1-functionalized QDs. The aptamer-functionalized QDs effectively delivered daunorubicin to the targeted prostate cancer cells. More importantly, they could be used to detect the concentration of daunorubicin by monitoring the PL intensity of $CuInS_2$ QDs, which was proportional to the drug concentration. The detection limit for daunorubicin was about 19 nM.

Using similar concepts, other research groups have prepared various types of QD/drug formulations and have examined their anticancer efficacy in comparison with free drugs. Mathew et al. prepared folic acid conjugated carboxymethyl chitosan coordinated to Mn-doped ZnS QDs and used them for targeted imaging and controlled drug delivery to cancer cells.[471] Fluorouracil drug molecules were encapsulated within the folic acid conjugated carboxymethyl chitosan NPs. The drug loaded NPs were 130−150 nm in diameter. MCF-7 breast cancer cells were used to assess imaging, targeted delivery, and cytotoxicity of the NPs. MTT assays showed a sharp reduction in cell viability with increasing NP dose. The stable luminescence of the Mn-doped ZnS QDs could be employed for imaging the drug carrier in cancer cells, without causing any adverse effects to the metabolic activity or morphology of the examined cells.

Our group engineered multifunctional InP/ZnS QDs for multimodal cancer imaging and therapy.[412] We coencapsulated luminescent InP/ZnS QDs and DOX within PEGylated micelles, and then covalently attached DOTA-chelated Gd^{3+} to the micelle surface to provide MRI contrast. Cell viability assays were performed to evaluate the therapeutic efficiency of the nanoprobes. The viability of cells treated with the DOX−QD micelle NPs decreased to less than 20% at a concentration of 80 μg/mL, confirming the cytotoxicity of the QD theranostic nanoprobes. Anti-claudin-4 conjugated QD NPs were delivered to tumor sites in vivo in a mouse model, providing high contrast tumor imaging.

Xu et al. showed that glycopolypeptide can be used to encapsulate Mn-doped ZnS QDs to make the QDs suitable for biological applications.[433] They studied the loading capacity and release of the anti-inflammatory drug ibuprofen on the glycopolypeptide coated QDs, demonstrating high loading efficiency and controllable release (Figure 55). Compared with the drug-loaded QDs or with the free drug, the QDs alone had lower cytotoxicity when cocultured with HEK293T cells.

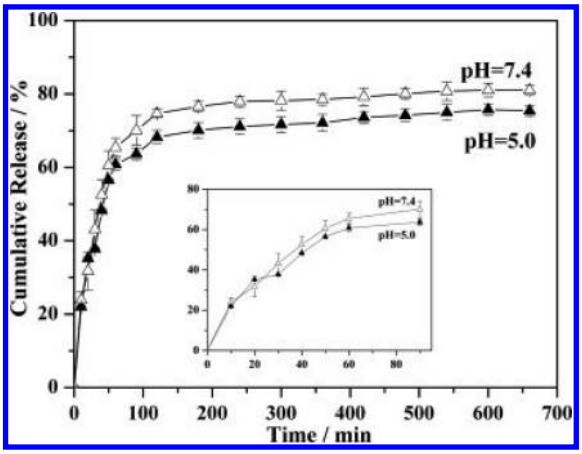

Figure 55. Release profiles of ibuprofen from glycopolypeptide-coated Mn-doped ZnS QDs in PBS solutions of different pHs at 37 °C (mean ± SD, n = 3). Reprinted with permission from Xu et al.[433] Copyright 2011 Elsevier.

Silicon QDs have recently garnered tremendous attention for biological applications ranging from imaging to drug delivery. Si has very low elemental toxicity, and is potentially biodegradable. Moreover, the Si QD surface can be modified by covalent attachment of organic molecules. Although significant efforts have been made to promote the targeting of NPs, many injected NPs are inevitably captured and cleared by mononuclear phagocytes leading to accumulation in the RES organs. This increases the risks of acute or chronic toxicity of the NPs. To date, few studies report self-destruction of NPs into nontoxic and excretable byproducts. A good example was demonstrated by Park et al. They demonstrated the preparation of luminescent porous silicon NPs with near-IR PL, which could be loaded with drug molecules for cancer therapy and imaging.[472] The biodistribution and degradation of the particles was monitored based on the location and intensity of PL from NPs. The luminescent porous Si NPs were able to self-degrade in vivo, and their byproducts were renally cleared over a relatively short period of time. For drug loading, positively charged DOX was electrostatically attached to the negatively charged porous Si NPs. DOX was released slowly at physiological pH and temperature, reaching a plateau within 8 h. Free silicic acid was detected in solution, demonstrating the degradation of the NPs, and its appearance correlated well with the DOX release profile. This study was among the first to demonstrate biodegradable inorganic NPs with drug loading ability for in vivo applications such as targeted therapy and sensing of circulating tumor cells.

Another interesting study was reported by Xu et al. They synthesized silicon/polymer core/shell water-dispersible NPs as carriers for DOX.[473] The size of the nanoprobes ranged from 40 to 110 nm. Their drug loading efficiency was estimated to be 6.1−7.4 wt % for NPs, and the drug release profile depended

DOI: 10.1021/acs.chemrev.6b00290
Chem. Rev. 2016, 116, 12234−12327

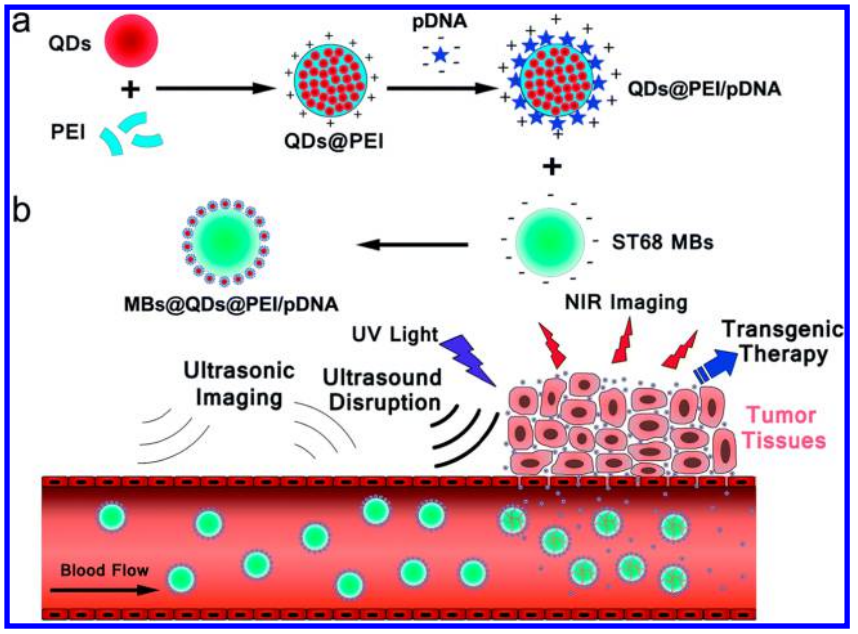

Figure 56. Schematic illustration of gene delivery based on QDs: (a) formation of MBs@QDs@PEI/pDNA complex; (b) NIR PL/ultrasonic bimodal imaging and targeted delivery of pDNA through ultrasound-targeted microbubble destruction. Reprinted with permission from Yang et al.[413] Copyright 2015 Royal Society of Chemistry.

upon the pH of the environment. Cytotoxicity studies showed that DOX-loaded Si QDs exhibited strong anticancer activity against HeLa cells. The authors also performed a hemolysis study in this work and determined the hemolysis percentages of polymer-coated Si QDs were less than 2%, which was within the range of safe values. These nanocarriers were also used as an optical tracker for PL imaging at the cellular level. Hanada et al. prepared water-dispersible alminoprofen-conjugated Si QDs for drug delivery.[474] Alminoprofen is an anti-inflammatory drug that is commonly used as an analgesic for rheumatism. The authors demonstrated that these nanoconjugates are less toxic than unconjugated Si QDs or the free-standing drug. Nonetheless, the nanoconjugates preserved the medicinal effect of the free drug.

In addition to direct attachment of drug molecules to the Si QD surface, one can also coencapsulate drugs and Si QDs in polymeric NPs to produce multifunctional probes. Si QDs and a hydrophobic anticancer drug, quercetin, were coencapsulated within poly(ethylene glycol)-*block*-polylactide (PEG−PLA) NPs for cell staining and to promote the solubility of quercetin in biological buffers.[225] The NPs were prepared by a double emulsion method, and their cytotoxicity toward HepG2 cells was studied. The drug-loaded NPs suppressed hepatoma HepG2 cells more effectively than free quercetin. Moreover, the nanoformulation was effective in inhibiting DNA damage induced by hydrogen peroxide in cells. These findings demonstrated that the coencapsulation of quercetin and QDs into one nanosystem could improve aqueous availability of the drug, and enhance biocompatibility of the overall NP formulation while providing the ability to monitor drug delivery and uptake.

Targeted cancer therapy has long been a major focus in the clinical research community, aiming to improve the effectiveness of therapy while reducing systemic exposure of normal tissues to toxic chemotherapeutic agents. Bioconjugated polymeric NPs are often used to carry QDs and drugs for in vivo applications because they provide tunable particle size and controllable drug release behavior. Deepagan et al. prepared multifunctional NPs composed of Mn-doped ZnS QDs and camptothecin in a poly(lactic-*co*-glycolic acid) matrix. The NPs, 180−200 nm in diameter, targeted EGF receptors, overexpressed on 30% of cancer cells, using the cetuximab antibody.[475] Drug release measurements demonstrated a slow release profile in PBS at pH 7.4. The authors observed high camptothecin activity and uptake of particles in A549 and KB cell lines, which overexpress the EGF receptor. These results indicate that anti-EGF antibody-conjugated NPs embedded with QDs and camptothecin can be used as a theranostic probe to locate and kill tumor cells.

6.2. Gene Delivery

Nanoparticle-based gene delivery is a major research area in nanomedicine.[84,476] Gene therapy can address healthcare issues ranging from genetically inherited or acquired diseases, to cancer at a fundamental (genetic) level, to drug or alcohol addiction. The two principal types of gene therapy with a direct action on genetic activity are (1) gene augmentation therapy, enhancing expression of a specific missing/malfunctioning gene by the delivery of an appropriate plasmid DNA, and (2) gene silencing by RNA interference using a double-stranded RNA, short interfering RNA (siRNA), aimed at targeting and impairing the post-transcriptional expression of undesirable genes. Another type of gene therapy that is receiving increasing attention is an indirect approach, again involving RNA interference, for (a) genetically induced triggering of the "neurogenesis" pathway for combating various neurodegenerative diseases and (b) genetically triggered boosting of innate immune response. Detailed discussion of these modalities of gene therapy are provided by Prasad,[3] and recent advances in clinical trials of gene therapy were reviewed by Naldini.[477]

Early work on gene therapy mainly used engineered viruses (viral vectors) as very efficient gene delivery vectors. However, their translation for human applications involved many risks associated with the mutagenicity and immunogenicity of viruses. As a result, nanoparticles emerged as a class of

DOI: 10.1021/acs.chemrev.6b00290
Chem. Rev. 2016, 116, 12234−12327

"nonviral" gene carriers. In general, nonviral vector-mediated methods have lower transfection efficiency compared to viral methods. However, recent advances have made nonviral vectors relatively easy to prepare, they are less immunogenic and oncogenic than viral vectors, and they do not have recombination potential. Integrating genetic substances, such as plasmid DNA, RNA, and small interfering RNA (siRNA) into nanocomplexes for targeted gene delivery to tissues and cells is a growing pharmacotherapy research area.[151,478] We describe here nonviral vector-mediated gene delivery using functionalized Cd-free QDs.

Yang et al. prepared $CuInS_2$/ZnS QDs and used them for multimodal imaging and gene delivery in vitro.[413] The QDs were functionalized with polyethyleneimine (PEI) to allow them to form complexes with plasmid DNA (pDNA). These nanocomplexes were then attached to the surface of microbubbles and delivered to the tumor site (Figure 56). The microbubble formulation provided contrast in both ultrasound and PL imaging. In vitro cell experiments demonstrated that pDNA was released from the microbubbles after they were taken up by HeLa cells. High transfection efficiency was achieved by using ultrasound to destroy the microbubbles. Cytotoxicity, immunotoxicity, and histological analysis suggested that the formulation is suitable for translational medical research. Similarly, chitosan-coated Mn-doped ZnS QDs were proposed for gene delivery.[434] Nanocomplexes were prepared by binding pDNA containing the bifunctional cytosine deaminase−uracil phosphoribosyl transferase (pCD-UPRT) gene to the chitosan-stabilized QDs.

Klein et al. employed luminescent Si QDs as a traceable transfection tool for silencing the ABCB1 gene in Caco-2 cells by RNA interference (RNAi).[435] The QDs were 2−3 nm in diameter, with green PL. They were capped with 2-vinylpyridine to enable electrostatic binding of siRNA. Real-time PCR analysis showed a substantial decrease in ABCB1 mRNA level, confirming release of siRNA from QDs to the cytosol. In situ fluorescence spectroscopy was used to monitor the Pgp efflux dynamics of transfected Caco-2 cells. Reduced transport efficiency for Rhodamine 123 further demonstrated the successful transfection.

Using a similar approach, Chinnathambi et al. modified Si QDs with allylamine and then electrostatically bound cytosine-phosphate-guanine oligodeoxynucleotides (CpG ODN) to them.[479] The binding mode affected the bifurcation of cytokine induction. The authors also compared the simultaneous induction of IFN-a and IL-6 using CpG ODN2006x3-PD as free molecules, electrostatically bound to Si QDs, or covalently linked to the Si QDs.

6.3. Protein and Peptide Delivery

QDs have also been studied as nanocarriers for therapeutic proteins and peptides with varying degrees of effectiveness.[219,480−483] In the following paragraphs, we discuss the recent trend of using QDs as a loading platform for protein and peptide delivery applications. Cell-penetrating peptides (CPPs) are small peptides that are able to penetrate cell membranes and deliver cargo into cells. A recent study used CPPs to deliver QDs into cells with minimal toxic effect. Liu et al. prepared carboxyl-terminated InP/ZnS QDs decorated with poly(ethylene glycol) lipids for peptide delivery in vitro.[41] CPPs were noncovalently bound to the functionalized QDs to form stable nanocomplexes, which were used for delivery of QDs into human A549 cells.

For protein delivery and sensing applications, Liu et al. prepared water-dispersible $CuInS_2$ QDs and functionalized them with bovine serum albumin.[436] The QD PL was quenched by 1,4-dihydronicotinamide adenine dinucleotide (NADH), but not by 1,4-nicotinamide adenine dinucleotide (NAD^+). The QDs were used to track the lactate dehydrogenase catalyzed reaction of pyruvate by sensing the presence of NADH through QD PL quenching. The protein-coated QDs were employed for detecting pyruvate molecules, with a detection limit of 25 nM.

Tu et al. prepared porous silicon NP probes by electrochemical etching.[437] The luminescent Si QDs within the porous silicon were functionalized with carboxyl-terminated ligands. Their PL QY reached 50%. The Si QDs were conjugated with goat antihuman IgG antibody which was modified with horseradish peroxidase (HRP). Although the authors did not perform biological studies with the porous silicon NPs, the development of antibody-conjugated silicon-based QDs paves the way for future in vivo delivery and sensing experiments.

Chatterjee et al. studied the interaction of bovine serum albumin and allylamine capped Si QDs, using fluorescence intensity, quenching, and lifetime measurements, circular dichroism spectroscopy, and FTIR spectroscopy to monitor changes in the secondary structure of BSA adsorbed on the Si QDs.[484] BSA fluorescence was quenched by Si QDs, due to ground-state complex formation. The association process was driven by a favorable negative enthalpy change and an unfavorable negative entropy change. This result was explained by considering the specific hydrogen bond between amine groups on the NPs and carboxylate groups of glutamate and aspartate residues of BSA.

6.4. Cancer Nanotechnology

Cancer nanotechnology is a multidisciplinary research area that employs nanotechnology solutions to solve challenges faced by the cancer research community. Broadly speaking, this field covers research themes ranging from molecular imaging to targeted therapy. When QDs are linked to antibodies, proteins, peptides, or other small biomolecules, they can be used to target tumor antigens, receptors overexpressed on cancer cells, or tumor angiogenesis with high specificity.[73,485−487] More importantly, multimodal diagnostic (e.g., optical, photoacoustic, or magnetic) and therapeutic (e.g., photothermal, photodynamic, or chemoradiotherapeutic) agents can be integrated with QDs for advanced theranostic applications. Recent reports have shown that these QD bioprobes can be used for cellular labeling and targeted drug delivery for cancer therapy and can be incorporated into nanoscale or microscale devices for early cancer sensing and screening of biological samples.[488−490] The application of QDs in cancer nanotechnology provides new opportunities for personalized medicine in which biomarkers are attached to the QDs and used for diagnosing and treating cancer based on the individual patient's genetic profile.

Tan et al. demonstrated intracellular synthesis of near-IR (NIR) luminescent Ag_2S QDs in HepG2 cancer cells.[491] Treating cultured hepatoma carcinoma cells (HepG2 cells) with silver and sulfur precursors led them to produce Ag_2S with reasonable emission efficiency in the presence of glutathione in the cells. These intracellularly prepared Ag_2S QDs were administrated into nude mice by subcutaneous injection, and the mice were imaged under 758 nm laser excitation. PL of the Ag_2S QDs was clearly detected from the treated animals. This in situ preparation of Ag_2S QDs in HepG2 cells was a unique method of making QDs that coud potentially be extended for in

DOI: 10.1021/acs.chemrev.6b00290
Chem. Rev. 2016, 116, 12234−12327

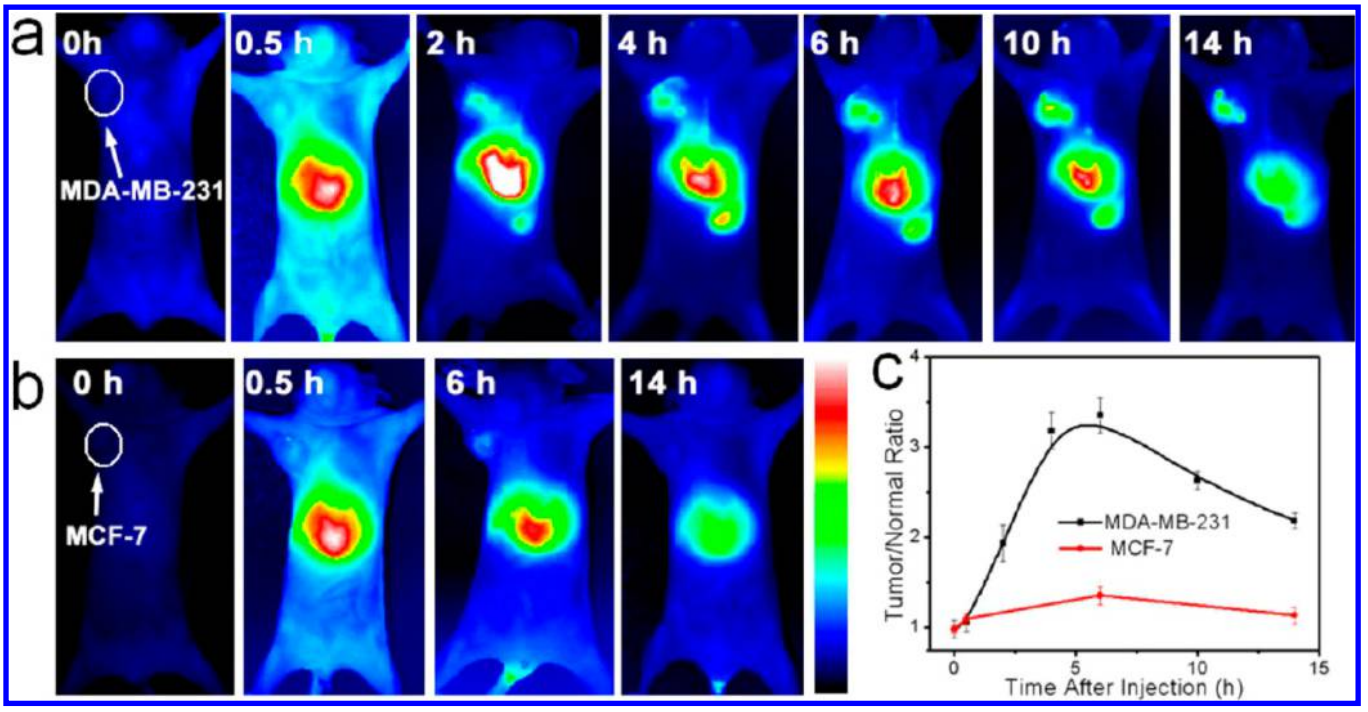

Figure 57. Biodistribution of NIR QD-loaded RGD-SOC micelles in nude mice bearing (a) MDA-MB-231 tumor or (b) MCF-7 tumor. (c) Corresponding temporal evolution curves of tumor-to-normal tissue PL ratios in the two groups. Reprinted from Deng et al.[137] Copyright 2012 American Chemical Society.

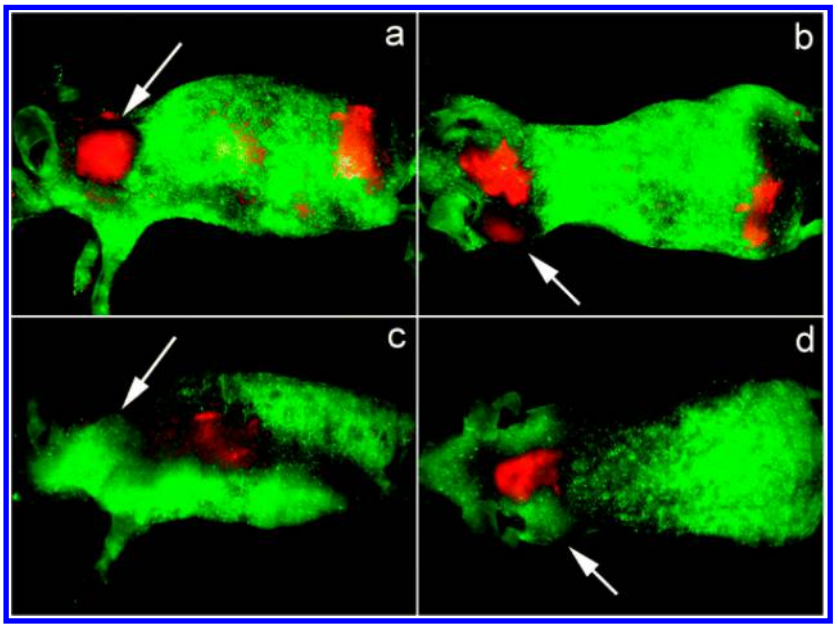

Figure 58. In vivo luminescence imaging of Panc-1 tumor-bearing mice (arrows, tumor) injected with folic acid conjugated QDs (a and b) and nonbioconjugated QDs (c and d). The fluorescence from QDs was coded red, and the autofluoresence was coded green. Reprinted with permission from Yong et al.[281] Copyright 2010 Royal Society of Chemistry.

situ formation of QDs in tumors in vivo, which would reduce the need for making, characterizing, and delivering water-dispersible QDs.

Deng et al. used a one-pot synthesis method to produce hydrophobic luminescent Zn−Ag−In−Se QDs[137] and tuned their PL from 660 to 800 nm by tailoring the Ag/Zn ratio. After optimizing the synthesis, the PL QY reached 50% in some cases. RGD peptide (arginine-glycine-aspartic acid)-modified *N*-succinyl-*N*′-octyl chitosan (RGD-SOC) was used to make the QDs water-dispersible. For in vitro optical imaging, $\alpha_v\beta_3$ integrin receptor positive MDA-MB-231 cells and $\alpha_v\beta_3$ integrin receptor negative MCF-7 cells were treated with QD-loaded RGD-SOC NPs. PL imaging showed that a large fraction of QD-loaded RGD-SOC NPs entered the cytoplasm via phagocytosis in MDA-MB-231 cells. On the other hand, minimal PL was observed from the $\alpha_v\beta_3$-negative MCF-7 cells. Subsequently, these QDs were used for tumor imaging in vivo and much greater accumulation of QD-loaded RGD-SOC

DOI: 10.1021/acs.chemrev.6b00290
Chem. Rev. 2016, 116, 12234−12327

micelles was found in MDA-MB-231 tumors than in MCF-7 tumors (Figure 57).

Recently, our group has demonstrated the use of $CuInS_2$ QDs for targeted multicolor optical imaging in vivo.[281] The $CuInS_2$/ZnS QDs were made water dispersible by encapsulating them in functional phospholipid micelles, and folic acid was conjugated to the micelle surface for targeted delivery. For in vivo tumor imaging, the NPs were intravenously injected into tumor-bearing mice. Thirty minutes after injection, intense PL was detected from the tumor site. However, very weak QD PL was observed from the tumor site in mice treated with unconjugated QDs (Figure 58). More importantly, in vivo two-photon imaging of tumors was also demonstrated. Helle et al. used $CuInS_2$/ZnS QDs to visualize lymph nodes in vivo, showing that QD PL was maintained for as long as 8 h.[391] They used immunohistology and molecular techniques to evaluate the metastatic status of sentinel lymph nodes. Overall, the authors highlighted that these near-IR emitting Cd-free QDs were excellent sentinel lymph node tracing markers.

Multimodal NP platforms are desirable for cancer diagnosis and therapy. Mathew et al.[471] prepared folic acid conjugated carboxymethyl chitosan coordinated to Mn-doped zinc sulfide QDs (FA-CMC-ZnS:Mn) and loaded with 5-fluorouracil (5-FU), an anticancer drug that inhibits growth of breast cancer.[471] The NP functions included cancer targeting, controllable drug delivery, and tumor imaging. In vitro drug release studies showed that the 5-FU was released in a sustained manner through slow degradation of CMC. An MTT assay was performed to compare the cytotoxicities of FA-CMC-ZnS:Mn alone and loaded with 5-FU. The results demonstrated that the FA-CMC-ZnS:Mn alone was nontoxic to L929 cells, but increased MCF-7 cell death was observed when 5-FU was encapsulated in FA-CMC-ZnS:Mn. In vitro imaging proved that such nanoparticles could be used for tracking the path of drug delivery and for targeted imaging of cancer cells.

Silicon, an inherently nontoxic element, has been widely used in food processing and cosmetic applications. By employing Si QDs in cancer nanotechnology, we can create nontoxic nanoprobes that are useful for targeting and visualizing tumor cells. Erogbogbo et al. demonstrated preparation of folic acid conjugated Si QDs for targeted imaging of pancreatic cancer cells.[492] The attachment of folic acid onto the polymer micelles in which the Si QDs were encapsulated enhanced the specificity of the optical probes and decreased nonspecific uptake of the particles. In a separate study, they also reported bioconjugated Si QDs covalently linked to lysine, antimesothelin, and transferrin for bioimaging.[492] Folate- and antimesothelin-conjugated QDs were able to target Panc-1 cells.

Creating a single nanosystem incorporating both plasmonic and PL features can advance applications in photothermal therapy and drug delivery monitoring in vivo. Erogbogbo et al. prepared multimodal NPs by encapsulating Si QDs in polymer micelles and then depositing gold onto the micelle surface to create gold nanoshells.[493] The gold nanoshells displayed plasmonic light scattering that was used for dark field imaging, while the Si QDs were employed for PL imaging. Imaging of pancreatic cancer cells using the multimodal NPs illustrated the overlap of luminescence and light scattering from the QDs and gold nanoshells, respectively.

Recently, Shiohara et al. described size-controlled fabrication of Si QDs by a microemulsion technique. The Si QDs were coated with allylamine and employed for imaging of cancer cells.[302] The authors found that the amine terminated Si QDs mostly accumulated in lysosomes, but not in the nuclei. Such QDs may be used as two-photon optical tracers to monitor the activity of cancer cells over long time scales. Also, Wang et al. reported a facile microwave-assisted hydrosilylation process for fabricating Si QDs.[494] Capping agents with various terminal functional groups, such as alcohol, alkyl, and carboxylic acid groups, were attached onto the QD surface. The Si QDs are biocompatible and useful for long-term intracellular PL imaging. Separately, Cheng et al. described another method for preparing colloidal Si QDs for imaging of cancer cells,[179] by reduction of halogenated silane precursors in a microemulsion synthesis environment. 1,8-Nonadiyne molecules were grafted onto the hydrogen-terminated Si QDs. Subsequently, different azide molecules were conjugated to the nonadiyne-functionalized QDs, rendering them dispersible in biological buffers. These Si QDs were used for cell labeling and imaging via passive uptake.

Overall, the current trend of using QDs for cancer nanotechnology relies heavily on conjugating the QDs with specific biomolecules for targeted delivery and imaging. For in vitro applications, the NPs reported above will be useful tools for understanding and investigating the transport or interaction mechanisms between biomolecules and the tumor cells. However, if the NPs are intended to be translated for in vivo applications, many aspects must be further considered. For example, attaching biomolecules on the surface of QDs will likely increase the overall hydrodynamic size of the QDs promoting uptake by the RES system rather than renal clearance. This can lead to accumulation of QDs in the body, which may cause harmful side effects or be a cause of concern about long-term impacts, even when the QDs do not contain Cd, Pb, or similar heavy metals.

6.5. Imaging Guided Surgery

Surgery remains one of the most common modes of cancer treatment.[495−497] Intraoperative assessment of surgical margins currently depends heavily on surgeons' experience in subjectively determining the appearance and palpation of the tumor. Tumor recurrence is likely if the tumor surgical margins are not properly determined, but unnecessarily large margins cause additional pain and complications for the patient. To improve outcomes, surgeons need enhanced visualization of the tumor to maximize tumor resection and minimize damage or injury to normal tissues. Advances in optical imaging are allowing its use for real-time tumor monitoring and imaging-guided surgery.[488−490,498] Dyes such as indocyanine green are generally employed for imaging guided surgery, but have drawbacks including aggregation, limited solubility, nonspecific in vivo uptake, and lack of specific tissue targeting. Thus, the clinical research community has shown strong interest in development of QDs for surgical imaging applications.[498−500] In the past few years, QDs have increasingly been studied for surgical use, especially for tumor detection, tumor resection, and sentinel lymph node (SLN) mapping. Many research articles have argued that QDs will be a useful tool for in vivo intraoperative imaging.[501,502] In the next few paragraphs, we discuss and highlight recent developments in QDs for possible use during surgery.

Zimmer et al. produced water-dispersible InAs/ZnSe core/shell QDs that emit in the near-IR, and used these QDs as contrast agents for multiple sequential lymph node mapping.[503] Specifically, the InAs/ZnSe QDs were transferred into water using dihydrolipoic acid (DHLA) or DHLA linked to a short

DOI: 10.1021/acs.chemrev.6b00290
Chem. Rev. 2016, 116, 12234−12327

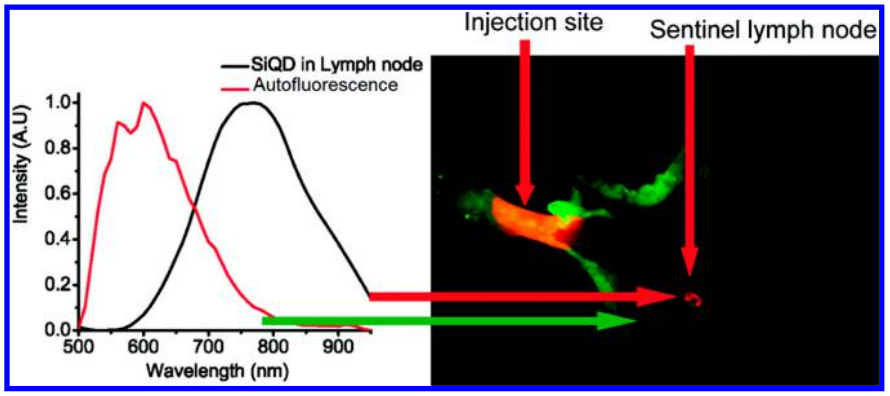

Figure 59. Sentinel lymph node PL imaging using micelle-encapsulated silicon QDs. Autofluorescence was coded green, and the unmixed SiQD signal was coded red. Reprinted from Erogbogbo et al.[38] Copyright 2011 American Chemical Society.

poly(ethylene glycol) chain through carbodiimide coupling chemistry. Using DHLA alone, the hydrodynamic size of the QDs in PBS buffer was 5.3 nm, but in fetal bovine serum it increased to 13.8 nm. DHLA-PEG functionalized QDs had an 8.7 nm hydrodynamic diameter. When the QDs were injected into the paw of a mouse, the QDs traveled throughout the body and could be detected in the SLN. In addition, the authors reported that they observed PL from QDs in interstitial fluid after intravenous injection. They deduced that such QDs were able to extravasate from blood vessels into the interstitial fluid. This shows promise for use of QDs as efficient and specific intravenously administered tracers, since the first barrier to tissue penetration is extravasation.

Improving tissue penetration depth and spatial resolution of imaging probes is essential for enhanced surgical imaging. However, scattering and absorbance of tissues in vivo present substantial barriers to these improvements. Li et al. demonstrated that Ag_2S QDs can be used as NIR luminescent probes for in vivo monitoring of lymphatic and vascular networks with deep penetration.[174] They reported that Ag_2S QDs can provide spatial resolution of 40 μm during in vivo PL imaging, and this allowed them to monitor the angiogenesis process. The authors suggest that Ag_2S QDs will be useful for dissection of sentinel lymph nodes and evaluation of blood supply in organs.

Dong et al. reported the synthesis of luminescent Ag_2Se QDs with emission at 1300 nm for in vivo surgical use.[139] After surface modification with C18-PMH-PEG, the Ag_2Se QDs displayed bright PL, high colloidal stability and enhanced biocompatibility. Subsequently, these NPs were used for deep imaging of organs and vascular structures with high spatial resolution. Such QDs will certainly create new opportunities for imaging-guided surgery applications. Ding et al. demonstrated the preparation of $CuInS_2$@ZnS:Mn QDs as multimodal imaging probes for PL and MR imaging of tumors in mice.[81] For in vivo imaging experiments, water-dispersible $CuInS_2$@ZnS:Mn QDs were prepared by functionalizing the QDs with dihydrolipoic acid−poly(ethylene glycol) ligand. In vivo PL and MR imaging experiments showed that the $CuInS_2$@ZnS:Mn QDs were able to target both subcutaneous and intraperitoneal tumors in mice.

In another study, core/shell/shell $InAs_xP_{1-x}$ QDs were synthesized with emission wavelengths from 750 to 850 nm.[439] The $InAs_xP_{1-x}$ core had a graded composition in which the arsenic concentration increased from the center to the periphery of the QDs. The QDs displayed tunable NIR emission, and growth of an InP shell on the core resulted in a red shift and increased QY. Deposition of an additional ZnSe shell further improved the stability of the NPs for biomedical imaging. These NIR-emitting core/shell/shell QDs were employed for sentinel lymph node imaging and mapping in vivo. The hydrodynamic diameter of the QDs is critical for precision SLN mapping, because NPs of 5−10 nm diameter can bypass the SLN and travel to other nodes in the chain. At the other extreme, if the NP diameter is greater than 280 nm, they can hardly move from the injection site. Thus, the NP formulation must have the right size for effective delivery to the SLN. In this study, alloyed core/shell/shell QDs coated with oligomeric phosphines displayed a hydrodynamic size of 12 nm. The authors employed an intraoperative video imaging system that superimposes the PL signals on a visible-light image of the underlying anatomy. When the QD formulation was injected into the paw of a mouse, the PL image showed the lymphatic flow of QDs from the injection site to the SLN. The authors reported that the introduced QDs traveled to the lymphatics and moved to the sentinel node within 1 min.

Erogbogbo et al. demonstrated that micelle-encapsulated Si QDs can be employed for tumor vasculature imaging and sentinel lymph node (SLN) mapping in live mice.[38] Their nanoformulation possessed stable luminescence and long tumor accumulation time in vivo (>40 h). This study used Si QDs with hydrodynamic size of 20 nm for SLN imaging. When the QDs were injected subcutaneously into the paw of a mouse, the QDs migrated through the lymphatics and moved to an axillary location. The accumulation spot of QDs showed the position of the SLN (Figure 59). Recently, $CuInS_2$ QDs have been employed for SLN imaging; however, these QDs still contain Cu and In metals that may cause some concerns from a clinical perspective.

In summary, the QD community has started to develop various Cd-free QDs, with emission peaks ranging from visible to near-IR, for in vivo surgical applications. There are two important factors to be considered for using QDs in surgery: (i) the overall hydrodynamic size of QDs will determine the transport and biodistribution of QDs; (ii) the type of surface passivation, along with size, will determine the lifespan of the QDs in vivo. By carefully controlling and tailoring these two factors, one can engineer specific QD formulations for advanced in vivo surgical applications.

6.6. In Vitro Diagnostics

QDs can be employed in clinical laboratory diagnostics that are used to ascertain disease information at the genetic or even

DOI: 10.1021/acs.chemrev.6b00290
Chem. Rev. 2016, 116, 12234−12327

protein level.[247,504] Depending on the constructed QD bioconjugates, these NPs can display functional properties such as sensing of chemicals and biomolecules. These QDs can be incorporated into devices for advanced healthcare applications. In this section, we discuss available and emerging QD-related diagnostic methods and devices integrated with QDs that take advantage of the electronic and optical properties of QDs for detection of biochemical molecules.

Zhang et al. used biocompatible Ag_2S QDs to detect photoelectrochemically active species such as glucose and cancer cells.[211] Ag_2S and Ag_2Se QDs were synthesized and assembled on SnO_2 modified ITO electrodes. The Ag_2S/SnO_2/ITO electrode showed 10 times higher photocurrent compared to Ag_2Se/SnO_2/ITO. Then the Ag_2S/SnO_2/ITO electrode was functionalized with glucose oxidase (GOx) for glucose detection or modified with 3-aminophenylboronic acid (3-APBA) for MCF-7 cancer cell detection. When the GOx modified electrode was exposed to a glucose solution, the conversion of glucose into gluconic acid and hydrogen peroxide consumed dissolved oxygen, which caused a photocurrent decrease. When the 3-APBA modified electrode was exposed to MCF-7 cells that overexpress sialic acid (SA), the strong binding of 3-APBA with SA also resulted in decreased photocurrent. A specificity test further confirmed that the photocurrent decrease was a result of the specific recognition between 3-APBA ligands and cellular surface SA. The detection limit was 3.2×10^{-5} M for glucose and 98 cells/mL for MCF-7 cells.

The long-lived room-temperature phosphorescence (RTP) of Mn-doped ZnS QDs is easily distinguished from autofluoresence and scattered light, which facilitates its use for detecting analytes in complex matrixes. Ertas and Kara used L-cysteine capped Mn-doped ZnS QDs with the anticancer drug idarubicin (IDA) to detect the interaction between double stranded DNA and IDA.[258] The RTP emission of the Mn-doped ZnS QDs was quickly quenched upon addition of IDA, which serves as an electron acceptor. The addition of dsDNA caused formation of a DNA/IDA complex, removing IDA from the QD surface and restoring the RTP signal of the QDs. The linear detection range of this method was 1.2−6.0 μM.

Recently, a simple method for the detection of thrombin using $CuInS_2$ QDs and fibrinogen (Fib) was presented.[440] Water-dispersible near-IR $CuInS_2$ QDs were prepared by a hydrothermal method and capped with mercaptopropionic acid. The introduction of fibrinogen to the $CuInS_2$ QD dispersion produced a Fib−$CuInS_2$QD complex through electrostatic binding and hydrogen bonding. This binding was accompanied by enhancement of PL intensity and a red shift of the PL peak. Addition of thrombin to the Fib−$CuInS_2$ QD system promoted polymerization of conjugated and free fibrinogen to produce fibrillar fibrin−QD aggregates. Upon centrifuging the sample, the PL intensity from the supernatant decreased with increasing thrombin concentration. In this manner, Fib−QD nanoprobes can be used to detect thrombin at concentrations from 6.7×10^{-11} to 3.9×10^{-7} mol L^{-1} with a limit of detection of 8.7×10^{-12} mol L^{-1}. Thrombin detection was also demonstrated using human serum samples directly. Compared with methods using other NPs and aptamer-based sensing approaches, this method gave a much lower detection limit for thrombin.

Shen et al. developed a lateral flow immunoassay (LFIA) system for sensing of C-reactive protein using $CuInZn_xS_{1+x}$/ZnS QDs as PL labels and a nitrocellulose filter as the substrate.[505] For this purpose, they fabricated the $CuInZn_xS_{1+x}$/ZnS core/shell QDs and transferred them into water using an amphiphilic oligomer (polymaleic acid *n*-hexadecanol ester). Then the water-dispersible QDs were conjugated to the mouse anti-C-reactive protein (anti-CRP) monoclonal antibody. Another anti-CRP monoclonal antibody was attached to the nitrocellulose membrane of the test line. The C-reactive protein in the analyte facilitated binding of the antibody on the nitrocellulose membrane with the functionalized QDs, leading to fluorescence enhancement at the test line in the LFIA system (Figure 60). The detection limit was 1 ng mL^{-1}, 100 times more sensitive than a commercial kit.

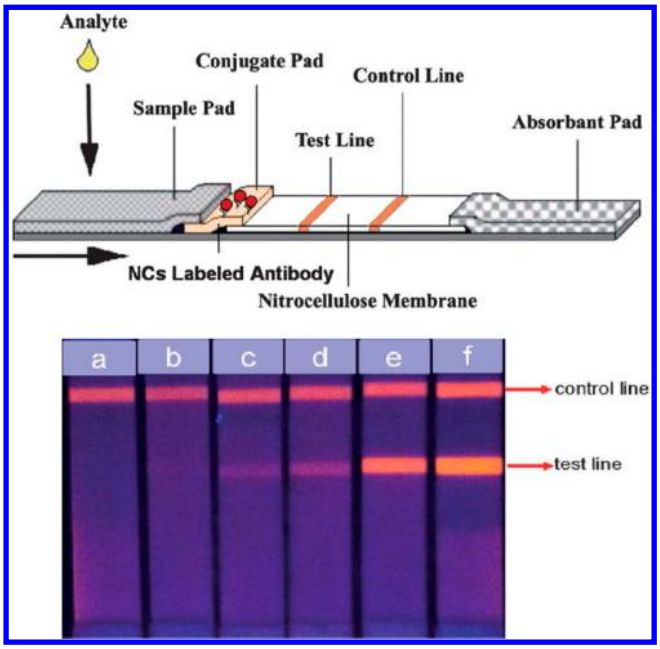

Figure 60. (upper) Schematic representation of the lateral flow immunoassay (LFIA) strip and (lower) images of LFIA strips at different concentrations of C-reactive protein. Reprinted with permission from Shen et al.[505] Copyright 2012 Royal Society of Chemistry.

Interleukin 6 (IL-6), a proinflammatory and anti-inflammatory cytokine, is often used as a biomarker for cancer or other diseases. Xiong et al. reported a facile microwave-assisted method of making water-dispersible $CuInS_2$/ZnS QDs with glutathione as the capping agent for IL-6 detection.[166] Their $CuInS_2$/ZnS QDs had an average size of 3.3 nm, long PL lifetime, and emission wavelengths tunable from the visible to the near-IR by manipulating the initial precursor ratio. The fabricated $CuInS_2$/ZnS QDs were conjugated with a secondary antibody of IL-6 and applied as optical labels in a fluoroimmunoassay. The primary antibody of IL-6 was immobilized on the object slide chip, which was treated with IL-6 samples and then incubated with the functionalized QDs. Sandwiched antibody−antigen−antibody complexes formed in the presence of IL-6 and generated fluorescence on the chip. The results suggested that these QDs can be used as point-of-care diagnostic tools for detecting biomarkers of cancer and other diseases.

Su's research group has been very active in using $CuInS_2$ QDs for various biosensing applications. For example, Liu et al. demonstrated the use of a sensitive fluorescence turn-on assay for detecting biothiols, histidine, and threonine.[506] Water-

DOI: 10.1021/acs.chemrev.6b00290
Chem. Rev. 2016, 116, 12234−12327

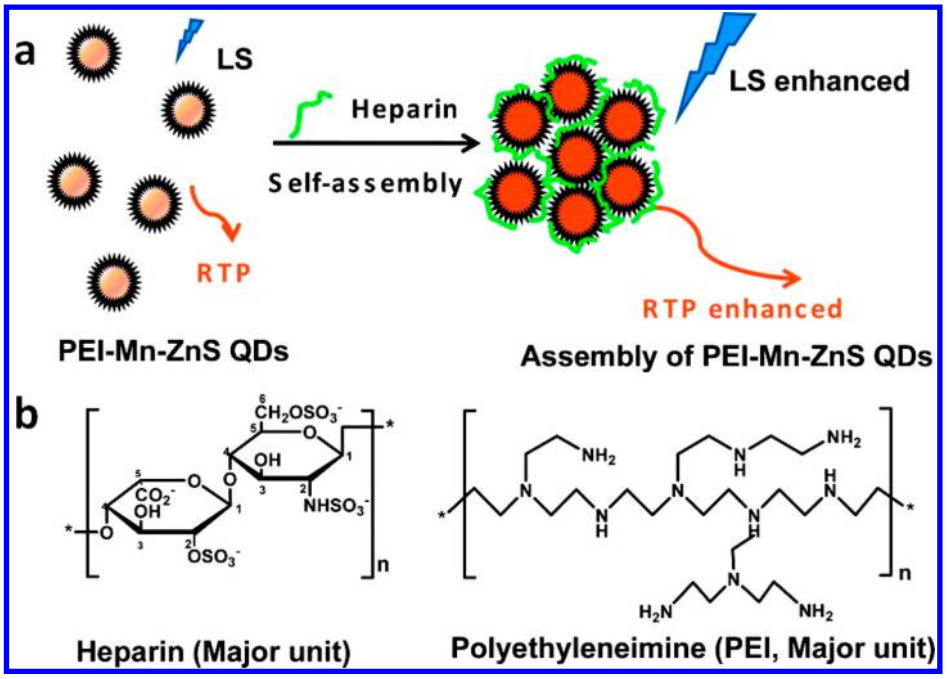

Figure 61. (a) Schematic of phosphorescence turn-on assay. (b) Chemical structures of heparin and PEI. Reprinted from Yan et al.[509] Copyright 2011 American Chemical Society.

dispersible $CuInS_2$ QDs functionalized with mercaptopropionic acid were modified with tyrosine. The PL of tyrosine−$CuInS_2$ QDs was found to decrease in the presence of Cu^{2+} ions due to the coordination effect of phenolic hydroxyls of the tyrosine molecules. Afterward, the addition of glutathione, L-cysteine, histidine, or threonine molecules was found to switch on the PL of the T−$CuInS_2$ QD−Cu^{2+} system, because these molecules possessed strong affinity toward Cu^{2+} ions. The proposed method was used for sensing L-cysteine, glutathione, threonine, and histidine in human serum samples with high sensitivity.

Correlating protein levels with disease states is important for disease detection and diagnosis. Tan et al. created phosphorescent molecularly imprinted polymers for sensing target proteins.[507] They employed an aqueous surface graft imprinting process using methacrylic acid and acrylamide as functional monomers, vinyl-modified Mn-doped ZnS QDs as supports, and bovine hemoglobin as the template. The QDs provided signal amplification and an optical readout. The molecularly imprinted polymer shell provided analyte selectivity and protected the QDs from nontarget molecules, thereby minimizing false signals. The dopant-related emission gradually decreased with increasing concentration of bovine hemoglobin. The authors demonstrated a good linear relationship for detection of bovine hemoglobin over a concentration range from 1.0×10^{-7} to 5.0×10^{-6} mol L^{-1} with recoveries of 96.7−103.8% and 92.6−94.2% for urine and serum samples, respectively. The long phosphorescence lifetime of the molecularly imprinted polymer−QDs prevents interference due to scattering and autofluorescence of the biomatrix. Subsequently, the same group reported a method for generating hybrid organic−inorganic imprinted Mn-doped ZnS QDs for sensing of bovine hemoglobin.[508] Using molecularly imprinted polymer−QD composites as a PL sensing material, the authors were able to detect relatively low concentrations of bovine hemoglobin with excellent selectivity by tracking the emission intensity changes of QDs implanted in the imprinted polymers.

Mn-doped ZnS QDs exhibited enhanced light scattering signals and phosphorescence upon aggregation. Based on this phenomenon, Yan and Wang developed a phosphorescence turn-on assay for heparin using target-induced aggregation of PEI-functionalized Mn-doped ZnS QDs.[509] The functionalized QDs possessed highly positive surface charge due to the abundant amino groups on PEI. Aggregation of the PEI-capped QDs upon addition of negatively charged heparin increased their phosphorescence intensity (Figure 61). Varying the PEI loading provided linear detection over different concentration ranges relevant to postoperative care, long-term therapy, and cardiovascular surgery. This method can also be used to determine the concentration of heparin in a diluted blood serum sample.

Manganese-doped ZnS QDs have also been applied for probing the overexpression of epidermal growth factor receptor (EGFR) in clinical tumor tissues.[442] The cysteine-capped QDs were bioconjugated to streptavidin and then attached to biotinylated EGFR antibodies using the streptavidin−biotin interaction. They were used for specific staining of EGF receptors on EGFR(+ve) A431 cells in a coculture with EGFR(−ve) NIH3T3 cells. In addition, the antibody conjugated QD formulation was used to identify EGFR overexpressing cells from clinical tumor tissues with a specificity of 86% and an accuracy of 88%, compared to immunohistochemistry techniques. Tissues stained with EGFR-modified ZnS:Mn nanocrystals displayed good luminescence even after 15 months of storage, suggesting their usefulness for long-term immunofluorescent labeling and sensing of antigens on ex vivo samples.

6.7. Infectious Diseases

Despite enormous improvements in sanitation, vaccines, antibiotics, and antiviral drugs, infectious diseases remain a major source of illness and death worldwide. A large fraction of

DOI: 10.1021/acs.chemrev.6b00290
Chem. Rev. 2016, 116, 12234−12327

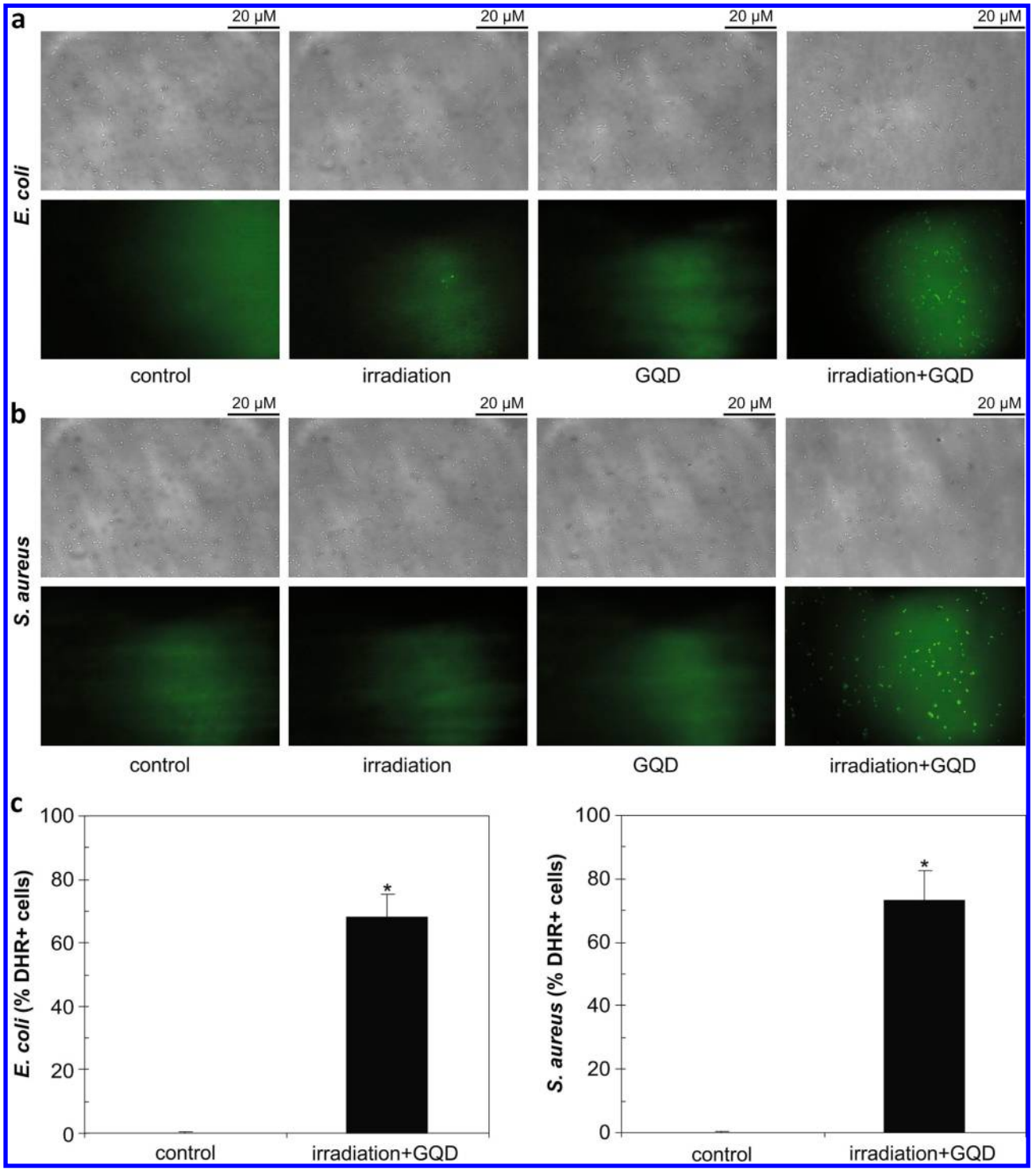

Figure 62. Photoexcited GQDs induce oxidative stress in bacterial cells. Suspensions of *E. coli* (a) and *S. aureus* (b) were treated under various conditions. After staining with dihydrorhodamine 123, bacterial cells were visualized. (c) Counts of ROS-producing bacterial cells are shown as mean ± SD values (∗, $p < 0.05$). Reprinted with permission from Ristic et al.[445] Copyright 2014 Elsevier.

infection-related mortalities occurs in developing countries, often due to poor hygiene conditions, inadequate healthcare facilities, drug costs, and comorbidities that can impair the immune system, due to malnutrition and/or immune-deficiency-causing infections such as HIV, MERS, and Ebola. The list of pathogens and the diseases caused by them is diverse and provides the basis for an entire subdiscipline of microbiology. It is also a growing list due to the evolution of new strains of pathogens. QD technology is poised to play a role in the detection, prevention, and multidrug treatment of infectious diseases,[510,511] as described in this section.

Influenza is a contagious respiratory disease that causes significant morbidity and mortality. A crucial tool for fighting influenza pandemics is timely and speedy diagnosis. Krejcova et al. reported QD−oligonucleotide complexes using influenza-derived oligonucleotides.[443] Electrochemical methods can detect the target oligonucleotide as well as metallic components of the QDs. The authors studied the electrochemical behavior

DOI: 10.1021/acs.chemrev.6b00290
Chem. Rev. 2016, 116, 12234−12327

of Zn(II), Pb(II), Cu(II), and Cd(II) ions by differential pulse anodic stripping voltammetry, and they compared the results to the behavior of ZnS, PbS, CuS, and CdS QDs. The authors analyzed the complexes between oligonucleotides (ODNs) derived from influenza and the fabricated QDs by differential pulse anodic stripping voltammetry and square wave voltammetry to detect peaks of nucleic bases. The authors showed that voltammetry could be used to discriminate QD−oligonucleotide complexes. Later, Fialova et al. developed an effective method for sensing influenza protein hemagglutinin (HA) by labeling them with CuS, PbS or CdS QDs.[512] The influenza protein was identified by analyzing the concentration of Cu(II), Pb(II), or Cd(II) ions contained in the QDs. The streptavidin-coated particles were surface-modified with biotinylated glycan for sensing influenza proteins. The functionalized QDs served as electrochemical signal amplification tags for detection of the influenza virus at concentrations of the H5N1 proteins as low as 0.0444 $\mu g/\mu L$. Although CdS QDs showed the best sensing results due to a strong interaction between the cadmium ions and protein molecules, the toxicity concern associated with these QDs still limits their potential for the clinical applications. The cadmium-free QDs could, after proper surface functionalization and size optimization, be alternative candidates for the next generation of electrochemical nanotags.

Antibacterial agents are important for microbiology due to emerging antibiotic resistance. Ristic et al. reported the use of graphene QDs prepared by an electrochemical method to generate reactive oxygen species (ROS) under photoexcitation (470 nm, 1 W) and kill two strains of pathogenic bacteria, *Escherichia coli* and methicillin-resistant *Staphylococcus aureus*.[445] Bacterial killing was observed through the reduction in number of bacterial colonies in a standard plate count method. In addition, increased propidium iodide uptake indicated cell membrane damage, and morphological defects were detected using atomic force microscopy. The induction of oxidative stress in bacteria treated with photoexcited QDs was confirmed by staining with redox-sensitive fluorochrome dihydrorhodamine 123 (Figure 62). Exposure to QDs or light alone did not generate ROS or decrease the viability of bacteria.

Pathogenic *E. coli* infections account for thousands of hospitalizations in the United States every year. Early detection of *E. coli* infections could reduce their impact. Baruah et al. used chitosan-functionalized Mn-doped ZnS QDs[446] with PL emission at 590 nm for fluorescent labeling and long-term imaging of *E. coli* cells through a fluorescence in situ hybridization (FISH) method. The positively charged chitosan allows the QDs to bind to the carboxyl and phosphoryl groups on the *E. coli* cell walls via electrostatic interaction. Translocation studies of the cells incubated with QDs showed that the QDs entered the cells. The fluorescence of the QDs was maintained well at the translocation temperature of 65 °C. The QDs were found to be biocompatible, and no harmful effects on the stained cells were observed.

The immune system safeguards an organism by discriminating and removing foreign substances from the body. Gu et al. reported the preparation of NPs for triggering the immune system and thereby improving the intended activation of antigen presenting cells.[447] Luminescent porous silicon NPs, each functionalized with multiple copies of an agonistic antibody (FGK45) to the APC receptor CD40, significantly promoted the activation of B cells. The cellular responses to the silicon NP-based stimulators were 30−40-fold higher than that of free FGK45. The PL signals of silicon NPs were used to track the biodistribution of NPs in the antigen presenting cells.

The highly pathogenic H5N1 avian influenza virus has caused outbreaks in birds in more than 60 countries since its discovery in China in 1996. The main challenge in treating H5N1 is to create effective antiviral drugs. Krejcova et al. engineered a magnetic electrochemical bar code array for detecting single point mutations (mismatches in up to four nucleotides) in the H5N1 neuraminidase gene, which aids in overcoming the drug resistance induced by point mutations.[444] Paramagnetic Dynabeads coated with oligo(dT)25 were used to isolate complementary H5N1 chains. Followed by the magnetic isolation, oligonucleotide chains of 12 (+5 adenine) or 28 (+5 adenine) bp were linked to ZnS or PbS QDs for electrochemical detection of the target gene. Cd-free QDs served as signal amplification tags. No signals were collected for the oligonucleotides without QD labeling. Each probe was hybridized for targeting a specific molecule, with more than 60% efficiency. The measured signals mapped out the mutations present in the sequence. The biosensor could detect subnanogram quantities of the target nucleic acids, demonstrating potential for future development of an influenza nanosensor based on Cd-free QDs.

7. PHARMACOKINETICS AND BIODISTRIBUTION OF CADMIUM-FREE QUANTUM DOTS

Pharmacokinetics addresses the time-dependent biodistribution of drugs or other entities from the vascular space into tissues and organs, and their clearance through metabolism and excretion.[3] In general, mathematical models are used to describe the time course of drug absorption into the plasma after systemic delivery, drug distribution, and drug elimination from the body by metabolism and excretion.[3,513,514] Thus, pharmacokinetics addresses the relationship between (i) the drug input defined by dosage form, dose, frequency, and administration route and (ii) the drug concentration in the plasma and other body tissues over time.

Serial collection and analysis of blood samples over time is required for pharmacokinetics studies. Radioactive labeling has often been used to provide sensitive detection of drugs in blood.[515] Some drugs, such as photosensitizers for photodynamic therapy, are fluorescent and can be detected optically without additional labeling.[516,517] Labeling with QDs can allow PL-based detection of nonfluorescent drugs, especially when the PL is in the near-IR window of biological optical transparency. The use of NPs for drug delivery can dramatically influence drug fate, often resulting in highly favorable pharmacokinetics. The size and surface characteristics of NPs have a major influence on the performance of NPs as drug carriers. Encapsulation of hydrophobic drugs in a NP formulation can provide improved absorption and systemic availability. In addition, liver metabolism is significantly reduced, thus leading to prolonged circulation and increased half-life. Functionalization of QDs with poly(ethylene glycol) (PEG) also prolongs circulation of NPs by reducing hydrophobic and electrostatic interactions with proteins and cells.[518,519] Other uncharged hydrophilic molecules can provide a similar effect, but PEG is by far the most popular. The surface charge of NPs plays an important role in avoiding RES uptake, minimizing opsonization, and prolonging circulation time.[520]

Biodegradation and excretion are key considerations for the in vivo use of any nanomaterial. The maximum size for renal clearance is around 5.5 nm.[521,522] Thus, NPs greater than ~5.5

DOI: 10.1021/acs.chemrev.6b00290
Chem. Rev. 2016, 116, 12234−12327

Table 4. Pharmacokinetics and Biodistribution of Cd-Free QDs

QD type	TEM size (nm)	functional groups	targeting molecules	injection	methods	model	major accumulation	postinjection	ref
Ag_2S	5.4	DHLA and 6PEG	–	tail-vein injection	PL imaging, ICP-MS	BALB/c mouse bearing 4T1 tumor	tumor, liver, spleen	72 h	21
Ag_2S	5.4	DHLA and 6PEG	–	tail-vein injection	PL imaging, ICP-MS	BALB/c mouse	liver, spleen	7 days	21
Ag_2S	5.4	6PEG and COOH	–	tail-vein injection	blood biochemistry, hematological analysis, and histological examinations	BALB/c mouse	liver, spleen	60 days	289
Ag_2Se	21.5 (HD)	C18-PMH-PEG		tail-vein injection	PL imaging	nude mouse	vasculature	a few min	139
$CuInS_2/ZnS$	~20	PEG2000-COOH and PEG2000 lipid micelles	–	subcutaneous injection	PL imaging, ICP-MS, RT-QPCR	BALB/c OlaAnN mouse bearing murine metastatic breast tumor	lymph nodes, liver, spleen	3 months	391
$CuInS_2/ZnS$	~7	dihydrolipoic acids	–	tail-vein injection	PL reflectance imaging	nude mouse	lung, spleen, liver	24 h	163
Cu–In–Se/ZnS	2–5	DHLA-sulfobetaine	–	subcutaneous injection	PL imaging, ICP-MS	BALB/c OlaHsd mouse	lymph nodes	4 h	136
Zn–Cu–In–S/ZnS	5.6	MPH and PEG-400	–	tail-vein injection	PL imaging	nude mouse	liver	6 h	284
InAs/ZnS	3.2	DHLA and DHLA-PEGn	–	intravenous injection	PL imaging	Sprague–Dawley rat	depending on no. of PEG	4 h	530
Si	15.1 (HD)	detran and attached to macrocyclic ligand–$^{64}Cu^{2+}$ complex	–	tail-vein injection	PET imaging and gamma counting	C57BL/6 mouse	liver	48 h	96
Ag_2S	2.1	BSA	antiVEGF	tail-vein injection	PL imaging, ICP-MS	nude mouse bearing U87MG tumor	tumor	24 h	291
Zn–Ag–In–Se	~5	SOC micelle	RGD-SOC	subcutaneous injection	PL imaging	nude mouse bearing MDA-MB-231 tumor or MCF-7 tumor	MDA-MB-231 tumor, liver	4 h	137
Zn–Ag–In–Se	~200 (HD)	DHLA-PEG	FA-SOC	tail-vein injection	PL imaging	nude mouse bearing Bel-7402 tumor	Bel-7402 tumor, liver	8 h	531
$CuInS_2/ZnS$	~4	SOC micelle	FA	tail-vein injection	NIR PL imaging	nude mouse bearing Bel-7402 tumor or 549 tumor	Bel-7402 tumors, liver	4 h	36
$CuInS_2/ZnS$	3–4	PEG	FA	tail-vein injection	PL imaging	nude mouse bearing Panc-1 tumor	spleen, liver	60 min	532
$CuInSe_xS_{2-x}/ZnS$	1.1–3.1	PLGA	invasin or D911A	oral gavage	PL imaging	BALB/c mouse	intestine	48 h	392
InAs/InP/ZnSe	15.9 (HD)	PEG	RGD or RAD	tail-vein injection	PL imaging	nude mice bearing U87MG tumor	tumor, liver, spleen, lung	4 h	387
InP/ZnS	5	dendron	RGD_2	tail-vein injection	PL imaging, ICP-MS	nude mouse bearing SKOV3 tumor, BALB/c mouse	tumor, liver	28 h	389

DOI: 10.1021/acs.chemrev.6b00290
Chem. Rev. 2016, 116, 12234–12327

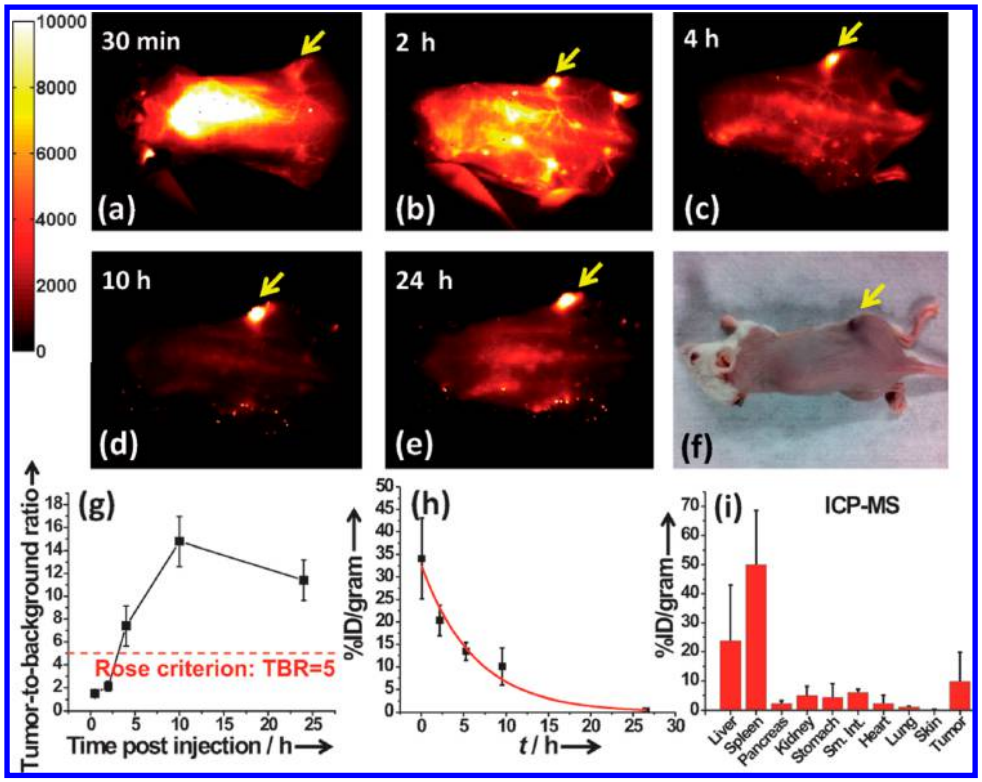

Figure 63. PL images of a 4T1 tumor-bearing mouse injected with 6PEG-Ag_2S QDs. (a–e) Time-lapse images of the mouse. (f) White-light optical image of the mouse at 24 h. (g) Tumor-to-background ratio plotted as a function of injection time. (h) Representative plot of % ID/g 6PEG-Ag_2S QDs in blood versus time after injection. (i) Quantitative biodistribution of 6PEG-Ag_2S QDs in various organs and tumor 72 h after injection, based on ICP-MS analysis. Reprinted with permission from Hong et al.[21] Copyright 2012 John Wiley and Sons.

nm in hydrodynamic diameter show dramatically reduced renal excretion rates. While this extends their circulation times, it also usually leads to capture of NPs by the RES. Thus, nanostructures that break down into components small enough to be cleared renally are often desirable. Real-time in vivo monitoring of QD PL allows detailed investigation of their biodistribution, degradation, and excretion. For example, our group has optically tracked near-IR emitting QDs delivered through the tail vein of a mouse.[523]

Biodistribution studies aim to measure the presence of NPs in tissues throughout the body. They provide very useful information on localization of a drug or NP at a targeted disease site as well as in other organs and tissues. Various factors affect NP biodistribution including plasma protein binding, hydrophobicity, and intentional functionalization of a nanoformulation to influence cellular uptake and efflux.[524,525] A detailed study of the biodistribution of a NP formulation can allow one to determine its potential for success in a targeted therapy strategy. Biodistribution profiles are most often obtained using a radioactively or fluorescently labeled nanoformulation that is injected into a small animal model (e.g., mouse, rat, or rabbit).[526,527] The treated animal is then sacrificed and the organs are removed and analyzed. Nanoparticle-based delivery can produce favorable biodistribution profiles through both active and passive targeting approaches. Nanoparticles that act as contrast agents for multimodal imaging can allow one to monitor biodistribution in live animals, reducing the number of animals required and improving the data by reducing animal-to-animal variation between time points.[528,529] This section describes recent studies of pharmacokinetics and biodistribution of Cd-free QDs (Table 4) and discusses how functionalized QDs provide benefits in targeted delivery and therapeutic efficiency of payloads, while minimizing adverse side effects.

7.1. Biodistribution of Nontargeted Cadmium-Free Quantum Dots

Ag_2S QDs are promising NIR-II (1000–1400 nm) emitters for in vivo imaging. Hong et al. prepared six-arm branched PEG-functionalized Ag_2S QDs (~5.4 nm diameter) with 1200 nm PL for in vivo imaging[21] and studied their biodistribution. NIR-II emission was monitored to analyze the biodistribution of the QDs over 24 h postinjection (Figure 63a–e). From 30 min to 24 h, PL intensity steadily increased at the tumor site and decreased in the skin and other organs, due to the EPR effect. As a result, the tumor-to-background (TBR) ratio gradually increased to a value above the Rose criterion (TBR > 5, Figure 63g). The organs were harvested 72 h after injection and inductively coupled plasma mass spectrometry (ICP-MS) was used to quantify QD content in organs (Figure 63i). The QDs mainly accumulated in the spleen and liver. Tumor uptake of PEG modified Ag_2S QDs formulation was 10% injected dose (ID)/g, which resulted from the long circulation half-life of 4 h. Excretion of the QDs was mainly through biliary transport and not through renal clearance.

The long-term biodistribution of PEG-functionalized Ag_2S QDs in mice was also investigated recently.[289] Randomly selected mice were sacrificed at fixed time points over a period of 60 days postinjection, and the retention of Ag_2S in organs and tissues was analyzed by ICP-MS. After 1 day, QDs were widely distributed among many organs and tissues. During the first week, the concentrations of the QDs gradually decreased in most organs and tissues but increased in RES organs. Over a

DOI: 10.1021/acs.chemrev.6b00290
Chem. Rev. 2016, 116, 12234–12327

period of 2 months, QDs were slowly removed from the body. The main clearance pathway was found to be fecal excretion. After 60 days, most of the QDs were cleared from the body and the rest of the QDs mainly remained in the liver, spleen, bone, and intestine.

In another study, the biodistribution of $CuInS_2$/ZnS QDs was investigated in mice bearing a metastatic breast cancer model.[391] The mice were subcutaneously injected with QDs in the right anterior paw. QD PL was detected in the sentinel lymph node a few minutes after injection and reached a maximum in intensity after 8 h. Indium content of organs and tissues was quantified using ICP-MS. The right lymph nodes and injection site had similar In concentrations 1 h after injection (40 mg of In/g of tissue), while In was not detected in the liver and spleen. After 4 h, the In concentration decreased at the injection site (14.16 mg of In/g of tissue), while the In concentration in the right lymph nodes considerably increased, and In was present in both the liver (2.46 mg of In/g of tissue) and spleen (3.36 mg of In/g of tissue). The clearance of QDs was determined by measuring In content of collected urine and feces for 4 days postinjection. The authors found that 3.5% of the injected In was excreted in feces and only a trace quantity was detected in the urine within the first 4 days. In this study, the QD PL and ICP-MS measurements complement one another, with the PL imaging allowing real-time biodistribution studies in the live animal, while the ex vivo ICP-MS measurements provide more precise quantification and allow detection of any In released by QD degradation, in addition to the In present in intact QDs.

Migration of photoluminescent Cu−In−Se/ZnS core/shell QDs from the regional lymph nodes has also been studied recently.[136] Aqueous Cu−In−Se/ZnS QDs were prepared by using hydrophilic ligands with a dithiol anchor group and a compact sulfobetaine zwitterionic group. QDs with 800 nm emission were subcutaneously injected into the right anterior paw of mice. Their near-IR PL was detected in the regional lymph node a few minutes after injection and persisted for several hours after injection (Figure 64). The QD accumulation in the right axillary lymph node after 4 h corresponded to 1.42% of the injected dose, as measured by ICP-MS analysis.

Guo et al. recently characterized the biodistribution of Zn−Cu−In−S/ZnS (ZCIS/ZnS) QDs with PL emission at 690 nm in 6-week-old female nude mice.[284] The QDs were intravenously injected into mice that were then monitored for 6 h.

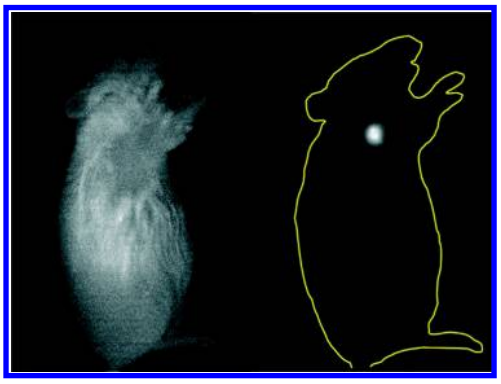

Figure 64. In vivo PL imaging of a mouse before (left) and 4 h after (right) subcutaneous injection of QDs. The injection point is hidden to improve the visualization of the lymph node. Reprinted from Cassette et al.[136] Copyright 2010 American Chemical Society.

The PL of the QDs was observed in the liver and lung. At 6 h postinjection, major organs were harvested to evaluate the QD biodistribution. Strong PL was observed in the liver, indicating accumulation of the QDs in the RES. The authors suggest that the first-pass hepatic removal was due to the size of the QDs (~49 nm). The QDs were slowly removed from the liver through hepatobiliary processing, as shown by the gradual decrease of PL signal from the liver.

A 2009 study observed organ- and tissue-selective distribution and excretion routes of NIR InAs/ZnS QDs based upon the overall size of functionalized QDs with a fixed inorganic core size.[530] The QDs were not functionalized with any targeting ligands. The QD cores were ~3.2 nm in diameter. Dihydrolipoic acid (DHLA) and DHLA-PEG_n (where n = 2, 3, 4, 8, 14, or 22) were used as surface coating agents to prepare water-dispersible NIR QDs of varied size. The QDs dispersed in PBS at pH 7.4 had hydrodynamic diameters ranging from 4.5 to 16 nm as the number of PEG repeating units increased from 0 to 22. The QDs were intravenously injected into Sprague−Dawley rats, and their distribution and excretion were analyzed (Figure 65). The QDs coated with DHLA PEG2 were located mainly in the liver. Those coated with DHLA-PEG3 accumulated in the kidneys and bladder. QDs coated with DHLA-PEG4 were more rapidly excreted through the liver and kidneys. QDs coated with DHLA-PEG8 were observed in the pancreas. QDs coated with DHLA-PEG14 were removed quickly through the liver to the intestine. QDs with DHLA PEG22 were found mainly in the vasculature at 4 h postinjection. To verify that the QDs were indeed removed through renal clearance, the kidney was harvested at 4 h postinjection, and cross-sectional images were taken and analyzed. QDs with DHLA-PEG4, with a diameter of 5.6 nm, could pass through the glomerular filters, and PL of QDs could be found in the medulla and cortex. QDs coated with DHLA-PEG2 were not found in the kidney, but mainly accumulated in the liver.

Dextran-coated Si QDs with a hydrodynamic diameter of 15.1 nm were attached to a macrocyclic ligand−$^{64}Cu^{2+}$ complex for multimodal imaging of clearance and distribution patterns.[96] The QD biodistribution in mice was determined by in vivo positron emission tomography (PET) and ex vivo gamma counting. A short burst of fast clearance was followed by a long slow clearance of QDs from the blood. Two minutes after tail-vein injection, 95.7% ID/g QDs had been removed from the blood. After 10 min, only 2.5% ID/g remained in the blood. Then, the clearance slowed and 1.5% ID/g remained in the blood after 120 min. The fast clearance of Si QDs was similar to that of PEG-coated CdSe QDs (12 or 21 nm). Five minutes and 1 h postinjection, the QDs mainly accumulated in the urinary bladder and the liver. After 4, 24, and 48 h, the QDs were mainly in the liver. A weak PL signal was still detected in the bladder 4 h postinjection. Based on ex vivo gamma counting analysis of major organs, the liver took up about 12.4% ID/g, and the kidneys took up 3.0−4.0% ID/g QDs. Other organs, such as heart, intestine, spleen, and lung, also displayed accumulation of QDs. A small amount of QDs was located in the bladder and brain. The authors explained that when the QDs were dispersed into the blood, they were rapidly opsonized, which accelerated the phagocytosis process. Ultrasmall NPs with size less than 7 nm were rapidly removed through renal filtration, and larger particles were captured by the RES system.

DOI: 10.1021/acs.chemrev.6b00290
Chem. Rev. 2016, 116, 12234−12327

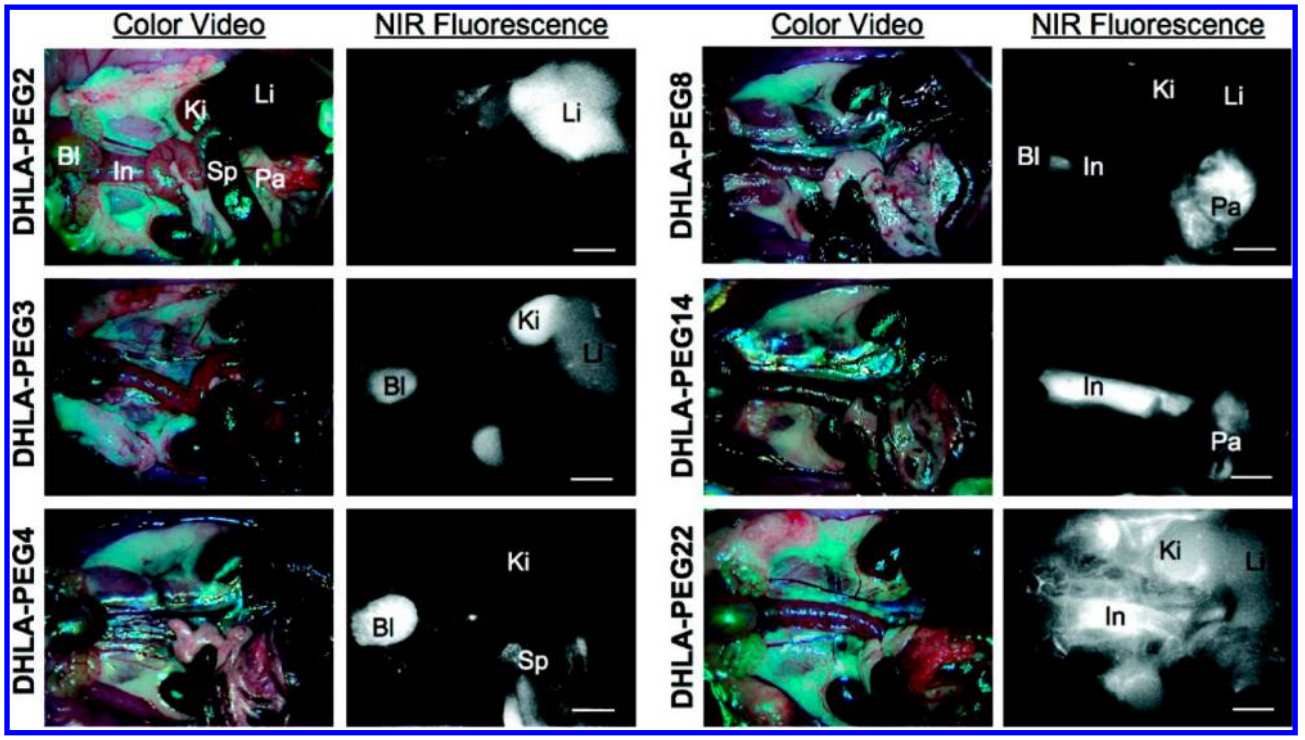

Figure 65. PL imaging of InAs(ZnS) QDs in Sprague−Dawley rats 4 h postinjection. The QDs were coated with DHLA-PEG2, DHLA-PEG3, DHLA-PEG4, DHLA-PEG8, DHLA-PEG14, and DHLA-PEG22. Ki, kidneys; Bl, bladder; Li, liver; Pa, pancreas; Sp, spleen; and In, intestine. Scale bar = 500 μm. Reprinted from Choi et al.[530] Copyright 2009 American Chemical Society.

Li et al. studied the biodistribution of $CuInS_2$/ZnS QDs in healthy nude mice.[163] The core/shell QDs had PL tunable from 550 to 815 nm with a maximum PL QY of 60%. These QDs' PL lifetimes of hundreds of nanoseconds allowed use of time-resolved imaging to remove background autofluorescence. The QDs were transferred to the aqueous phase using DHLA. The QDs were intravenously injected into nude mice and the distribution of the QDs was monitored for 24 h using a fluorescence reflectance imaging system (Figure 66). Fifteen minutes postinjection, the QDs accumulated in the spleen, liver, and lung. The liver and spleen are RES organs and known for removing foreign particles from the body, especially when the particles are covered with circulating plasma opsonins. The results suggest that the negatively charged DHLA-coated QDs favored opsonin binding and aggregation in vivo, promoting RES uptake.

7.2. Biodistribution of Targeted Cadmium-Free Quantum Dots

Ag_2S QDs bioconjugated with antiVEGF were employed for in vivo cancer targeted imaging.[291] In this study, 0.02 mmol of the bioconjugated QDs in PBS was intravenously injected into U87MG tumor-bearing mice with a volume of 500 μL per mouse. PL from antiVEGF-Ag_2S QDs was detected in the tumors 0.5 h after injection and remained detectable 24 h after injection. In contrast, the antiVEGF-Ag_2S QDs were mostly cleared from the body of normal mice 12 h after injection, and PL signals disappeared completely after 24 h. Thus, the excretion rate of antiVEGF-Ag_2S QDs in the tumor-bearing mice was much slower than in healthy mice. This may be due to the high affinity of the antiVEGF to tumors, which led to retention of the antiVEGF-Ag_2S QDs at the tumor site.

The pharmacokinetics and biodistribution of hydrophobic luminescent Zn−Ag−In−Se (ZAISe) QDs discussed in section 6.4 were also analyzed in Deng's work.[137] Nude mice bearing MDA-MB-231 or MCF-7 tumors were treated with NIR QD-loaded RGD-SOC NPs. Four hours after treatment, strong PL was detected at the tumor site for MDA-MB-231 tumor bearing mice but not for MCF-7 tumor bearing mice. Unfortunately, no further biodistribution analysis was reported. Later, the same group employed quaternary Zn−Ag−In−Se QDs loaded into folate-modified *N*-succinyl-*N*′-octyl chitosan NPs for imaging tumors in vivo.[531] Strong PL was observed from the tumors of folic acid receptor positive Bel-7402 tumor-bearing mice, indicating that a significant fraction of the QDs were located in the tumor matrix. This group has also reported another method to produce water-dispersible quaternary Zn−Ag−In−S QDs modified with DHLA-PEG-based ligands.[296] The QDs were further conjugated with targeting ligands such as folate and RGD peptide for imaging of tumor cells such as MDA-MB-231 cells and Bel-7402 cells.

The biodistribution of $CuInS_2$/ZnS QDs in tumors and major organs has also been studied over a period of a few hours.[36] The QDs, with PL from 550 to 800 nm and QY up to 80%, were packaged within folate-modified *N*-succinyl-*N*′-octyl chitosan (FA-SOC) micelles for targeted delivery and imaging. They were intravenously injected into Bel-7402 tumor-bearing nude mice (FA receptor positive model) and A549 tumor-bearing nude mice (FA receptor negative model). At 4 h postinjection, PL was detected in the liver and the tumor area in the Bel-7402 tumor-bearing nude mice, but no QD PL was detected at the tumor site for the nude mice bearing A549 tumors. This result demonstrated specific uptake of FA-conjugated nanomicelles to FA receptor positive tumors.

Recently, our group used $CuInS_2$/ZnS QDs for targeted in vivo tumor imaging.[281] The $CuInS_2$/ZnS QDs were encapsulated in phospholipid micelles, which were further conjugated with folic acid (FA). Thirty minutes after intravenous injection,

DOI: 10.1021/acs.chemrev.6b00290
Chem. Rev. 2016, 116, 12234−12327

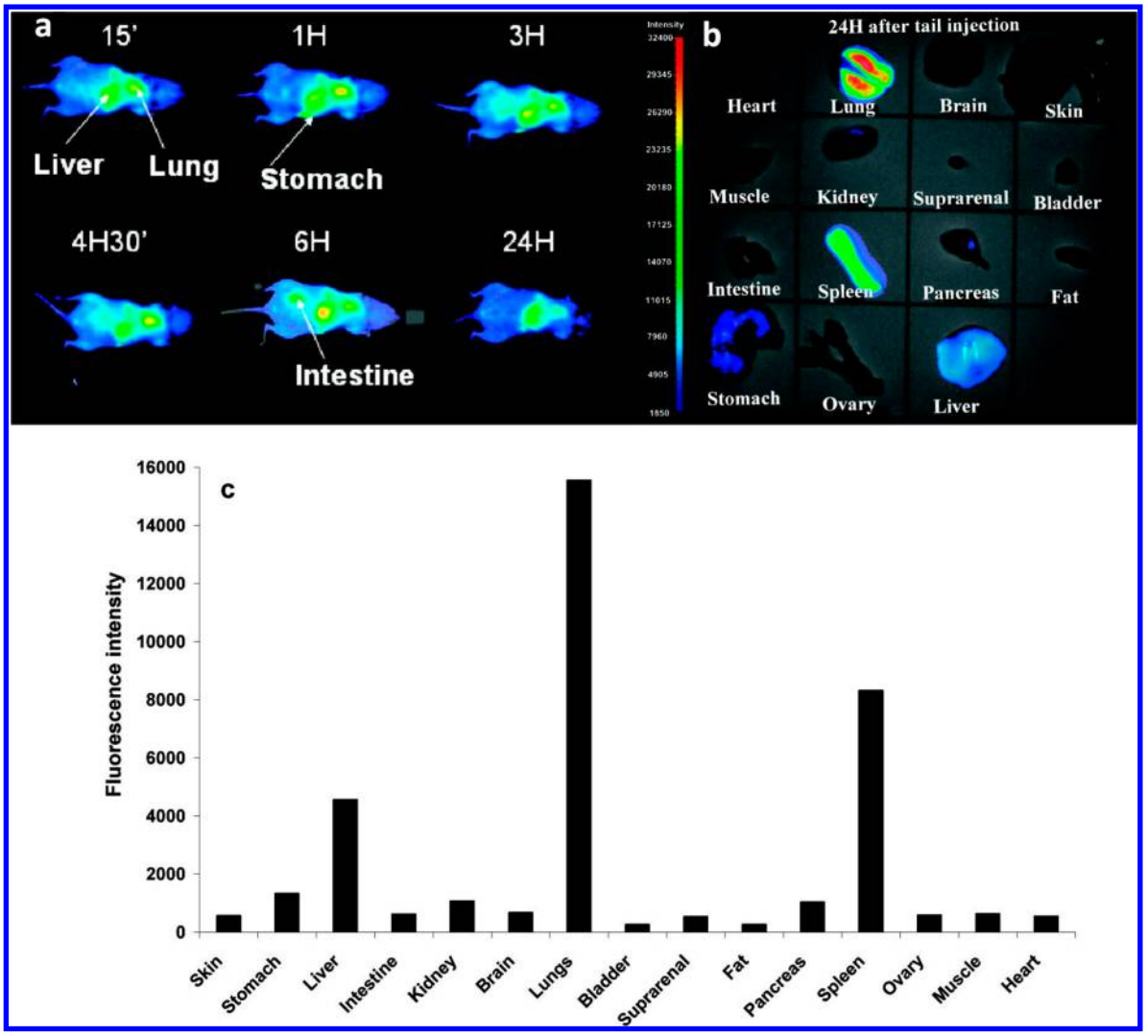

Figure 66. Biodistribution of $CuInS_2$/ZnS QDs in healthy nude mice. (a) PL images showing the temporal evolution of the biodistribution of QDs injected into the tail of a healthy nude mouse. (b) PL images of the different parts of the mouse after dissection. (c) Biodistribution and tissue PL of the QDs, 24 h after tail-vein administration. Reprinted from Li et al.[163] Copyright 2009 American Chemical Society.

QD PL was detected from the tumor sites of mice treated with the FA-conjugated QDs, but not from the tumors of mice treated with nonbioconjugated QDs, demonstrating the specificity of folic acid conjugation for tumor targeting. After 60 min, the mice were sacrificed and analyzed with a small animal luminescence imaging system. QDs had mainly accumulated in the spleen and the liver, indicating clearance by the RES. QD PL was detected in the lung and kidneys, but the signals were much weaker than those from the liver and the spleen.

$CuInSe_xS_{2-x}$/ZnS QDs have also been used as a contrast agent for tracking a microparticle-based oral vaccine in mice.[392] The $CuInSe_xSe_{2-x}$/ZnS QDs were encapsulated with poly(lactic-*co*-glycolic acid) (PLGA) to form microparticles that were then conjugated with invasin or D911A. The invasin-functionalized PLGA microparticles (15 mg) encapsulating the $CuInSe_xSe_{2-x}$ QDs were orally introduced into mice and tracked. The mice were imaged at 15 min, 18 h, and 2 days after treatment. At 15 min, QD PL was primarily found in the stomach. At 18 and 45 h, most ingested microparticles had been excreted, and QD PL was restricted to the colon and the cecum.

Tumor uptake and the biodistribution of peptide-conjugated, PEG-passivated, near-IR InAs/InP/ZnSe QDs were studied in vivo.[387] The hydrodynamic diameter of QDs was 15.9 nm, and their circulation half-life was about 29 min. After conjugating the QDs with RGD or RAD peptides, the authors administered them to tumor-bearing nude mice. Tumor uptake of QD-RGD conjugates was much higher than that of QD-PEG and QD-RAD conjugates. Semiquantitative analysis of tumor uptake was performed using an IVIS Imaging System and Living Imaging software. The results showed a tumor uptake of 10.7% ID/g in mice treated with QD-RGD. At 4 h postinjection, the mice were sacrificed and their organs were harvested to study the biodistribution of all the QD formulations (Figure 67). The QD PL of the liver was highest among the harvested organs, followed by the spleen and lung. Detectable but small PL signal was observed from the kidney, intestine, and bone.

The pharmacokinetics and distribution of dendron-coated InP/ZnS QDs were also examined in a tumor-bearing nude mouse model and healthy mice.[389] The dendron-coated QDs were functionalized with arginine-glycine-aspartic acid peptide dimers (RGD_2) for tumor targeting and labeling, and then injected intravenously into SKOV3 tumor-bearing nude mice.

DOI: 10.1021/acs.chemrev.6b00290
Chem. Rev. 2016, 116, 12234−12327

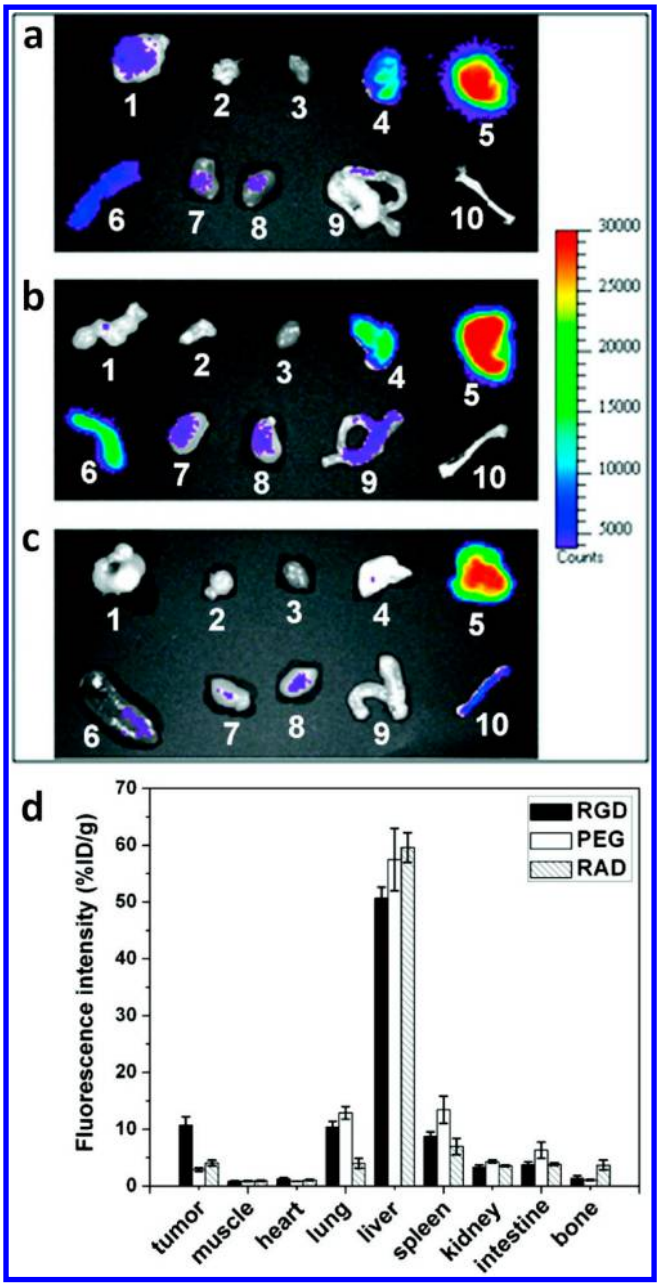

Figure 67. PL imaging of major organs of mice injected with (a) QD800-RGD, (b) QD800-PEG, and (c) QD800-RAD and sacrificed after 4 h. 1, U87MG tumor; 2, muscle; 3, heart; 4, lung; 5, liver; 6, spleen; 7, kidney (left); 8, kidney (right); 9, intestine; and 10, bone. (d) ROI analysis of major organs in ex vivo PL imaging. Reprinted from Gao et al.[387] Copyright 2010 American Chemical Society.

The PL from both QD-dendron-RGD_2 and QD-dendron were detected in tumors at 1 h postinjection, and stained tumors were easily distinguishable from tissues 4 h postinjection. In mice treated with QD-dendron-RGD_2, the QDs remained in the tumor even after 24 h, but PL was not detected at this time point for mice treated with the QD-dendron formulation. This demonstrated the specific targeting ability of the QD-dendron-RGD_2 to integrin $\alpha_v\beta_3$-positive SKOV3 tumors. To further quantify the biodistribution of the QD-dendron, ICP-MS analysis was performed in BALB/c mice. One nanomole of QD-dendron dispersion was injected intravenously into the mice, and the blood and organs were analyzed. Twenty-four hours after injection, ~60% of the QD-dendron was removed from the body. Some QDs accumulated in the liver, spleen, and kidney. QD-dendron NPs accumulated in all organs, were excreted within 1 week, and were almost completely cleared at 10 weeks postinjection. The authors also investigated whether the QD-dendron could be removed through the renal system (Figure 68). QD PL was observed from the urinary bladder 30 min postinjection, and PL was also detected in the collected urine 90 min postinjection. The authors highlighted that QDs with larger hydrodynamic sizes (e.g., 20 nm) were generally located in the RES system where they may induce higher risk for long-term toxicity. Smaller QDs were more likely to be cleared through renal filtration, thereby reducing their potential toxicity.

8. IN VITRO AND IN VIVO TOXICITY OF CADMIUM-FREE QUANTUM DOTS

The toxicity of QDs must be addressed if they are to achieve their potential to positively impact healthcare. Substantial concern about the possible toxicity of QDs has been voiced by the press, biomedical researchers, bioengineers, and practicing physicians.[533,534] Detailed risk−benefit analyses of the use of engineered QDs for nanomedicine are crucial for their translation into specific diagnostic and therapeutic applications. The toxicity of QDs depends upon those physicochemical properties that determine QD behavior in vitro and in vivo,[3,31] as well as the elemental composition of the QDs themselves. Studies of QD toxicology aim to understand how QDs might interact with biological systems to produce toxic effects. Risk factors associated with unintentional environmental exposure to QDs are also of great interest. Such unintentional exposure could result from handling of QDs or commercial products containing QDs, including inhalation of airborne QDs.[535−538] In general, the toxic effects generated by intentional and unintentional exposures to QDs are of the same types, but the exposure routes and doses can be very different. The chemical components, physical characteristics (e.g., size, shape, and stability), and surface properties (e.g., surface charge, surface coating) of the QDs play major roles in determining their toxicity.[277,539,540] Because of the high surface-to-volume ratio of QDs, surface-initiated processes are particularly important. Thus, the size and shape of QDs clearly have an important role to play in determining overall toxicity. A key source of QD toxicity can be the release of heavy metal ions. For example, the release of highly toxic Cd^{2+}, Pb^{2+}, or Hg^{2+} ions from CdSe, CdTe, PbSe, PbS, or HgTe QDs has been of great concern to the biomedical community, and has prompted the development of the Cd-free QDs discussed in this review.[56,541−543] Clearly, the toxicity of QDs is dependent on a wide range of their physicochemical properties. This makes consistent, reproducible toxicological studies of QDs that produce generalizable results very challenging compared to toxicology studies of standard chemicals, i.e. well-defined molecules. As a result, many contradicting toxicological results on the same type of QDs have been reported. These discrepancies often originate from subtle differences in the QD's physicochemical characteristics.[31] This demonstrates the urgent need for the QD research community to create a set of characterization protocols to standardize important tests and assays for accurate assessment of QD toxicity in vitro and in vivo, accompanied by standardized means of characterizing the QD's physicochemical properties. This section describes recent findings on in vitro and in vivo toxicity of Cd-free QDs and discusses how these

DOI: 10.1021/acs.chemrev.6b00290
Chem. Rev. 2016, 116, 12234−12327

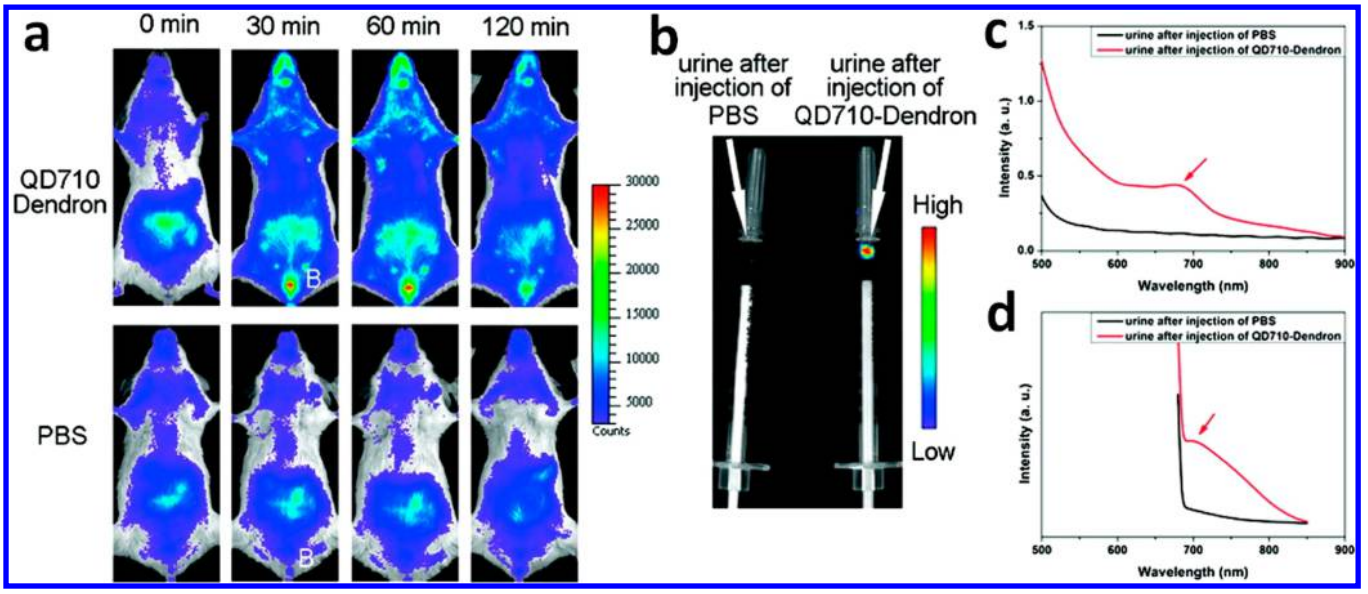

Figure 68. Renal clearance of QD710-dendron. (a) PL imaging of BALB/c mice before and after tail-vein injection of QD710-dendron or PBS. The PL signal originating from QD710-dendron in the bladder (labeled as "B") was clearly visible. (b) PL imaging of urine samples collected 90 min postinjection of QD710-dendron or PBS. (c) UV−vis absorbance and (d) PL emission spectra of the urine samples collected 90 min postinjection of QD710-dendron or PBS show absorbance and emission from QD710-dendron. Reprinted from Gao et al.[389] Copyright 2012 American Chemical Society.

functionalized QDs may interact with biological systems to generate adverse responses. The studies of QD toxicity discussed in this section are summarized in Table 5.

8.1. In Vitro Toxicity

The biocompatibility of polymer-coated Ag_2Se QDs (C18-PMH-PEG-Ag_2Se QDs) was evaluated using standard MTT and apoptosis/necrosis assays.[139] Human mesenchymal stem cells (hMSCs) and mouse fibroblast L929 cells were used for the cytotoxicity evaluation. The authors used both normal cells and stem cells to examine the cytotoxicity of Ag_2Se QDs more holistically, based on the fact that hMSCs are very sensitive to their environment. The two cell lines were exposed to Ag_2Se QDs at concentrations ranging from 0 to 100 μg/mL for 24 h. Cell viability determined by MTT assay demonstrated that the L929 cells and hMSCs maintained their viability even at 100 μg/mL. Flow cytometry was used to analyze apoptosis/necrosis events of L929 cells and hMSCs treated with polymer-coated Ag_2Se QDs for 24 h. For both cell lines, when exposed to Ag_2Se QDs at 50 and 100 μg/mL, the population of cells that underwent apoptosis and necrosis was the same as in control experiments without exposure to Ag_2Se QDs.

Cytotoxicity studies have also been carried out to assess the biocompatibility of Pluronic F127 micelle-encapsulated $CuInS_2$/ZnS and $AgInS_2$/ZnS QDs.[355] For the cell viability study, human macrophages were treated with varying concentrations (0−300 μg/mL) of QDs for 48 h. Cell viability remained above 85% throughout this concentration range, indicating that the cytotoxicity of the QDs was minimal. Recently, hybrid $CuInS_2$ QD@SiO_2 nanobeads and anti-PSCA conjugated $CuInS_2$ QD@SiO_2 nanobeads were evaluated using the MTT assay for their toxicity to PC-3M cells.[317] Both were nontoxic at concentrations up to 150 μg/mL. Similarly, the MTT assay and morphological analysis were used to evaluate the cytotoxicity of ZnS−$AgInS_2$ (ZAIS)/ZnS QDs and CdTe/CdS QDs toward HepG2 cells.[222] The MTT assay was carried out after 24 h incubation; the metabolic activity of cells was similar to that of the control group (Figure 69). No morphological changes were observed in the cells treated with ZAIS/ZnS QDs, further demonstrating that these QDs were nontoxic over the concentration range of 5−50 μg/mL. In contrast, exposure to CdTe/CdS QDs decreased metabolic activity of the cells significantly.

Our group reported cytotoxicity evaluation of PEGylated phospholipid micelle-encapsulated $CuInS_2$/ZnS QDs using the MTT assay.[281] Cells maintained 80% viability when treated with 195 μg/mL micelle-encapsulated QDs for 24 h, suggesting the QDs have minimal cytotoxicity. Cysteine-capped CdTe QDs were also studied, for comparison. The concentration corresponding to 50% cell viability (IC_{50}) was estimated to be 100 μg/mL for CdTe QDs and 300 μg/mL for $CuInS_2$/ZnS QDs in Panc-1 cells. This indicates that the $CuInS_2$/ZnS QDs can be loaded into cells at a higher dosage for bioimaging studies. The difference in toxicity between Cd-containing and Cd-free QDs is, in this case, notable, but the Cd-free QDs still exhibit significant toxicity at high doses. In another study, Wang et al. performed cytotoxicity assays of $CuInS_2$/ZnS QDs modified with the cationic surfactant (1-tetradecyl)-trimethylammonium bromide (TTAB).[544] The Cell Counting Kit-8 assay study showed that CIS−ZnS−TTAB QDs had little impact on the cell viability of the MCF-7 cells treated with QDs; 80% of the cells survived the QD treatment. The cytotoxicity test for hydrophilic Zn−Cu−In−S/ZnS (ZCIS/ZnS) QDs[284] was also performed on NIH/3T3 cells for 24 h and showed no significant signs of toxicity at doses up to 1 mM Cu ions. The in vitro cytotoxicity of InAs/InP/ZnSe core/shell/shell QDs with near-IR PL was also studied.[299] The MTT assay showed that InAs/InP/ZnSe core/shell/shell QDs at 10 nmol/L are significantly less cytotoxic compared to CdTe/ZnS core/shell QDs.

In a more recent study, the cytotoxicity of zwitterion-like $CuInS_2$/ZnS QDs (ZWL-QDs) toward human primary glioblastoma (U-87 MG) cells and human embryonic kidney 293 (HEK-293) cells was assessed.[545] The cell viability was

DOI: 10.1021/acs.chemrev.6b00290
Chem. Rev. 2016, 116, 12234−12327

Table 5. Toxicity of Cd-Free QDs

QD type	surface modification	dose	time	assay methods	model	toxic effects	ref
Ag_2Se	C18-PMH-PEG	0−100 μg/mL	24 h	MTT, apoptosis, and necrosis assay	hMSCs and L929 cells	>50 μg/mL, apoptosis and necrosis	139
$CuInS_2$ and $AgInS_2$	F127	0−300 mg/mL	48 h	cell viability study	human macrophages	cell viability >85% at 300 mg/mL	355
ZnS−$AgInS_2$/ZnS	sugar chain	5−50 μg/mL	24 h	MTT	HepG2 cells	nontoxic	222
$CuInS_2$@SiO_2	amine functionalized	0−150 mg/mL	24 h	MTT	PC-3M cells	nontoxic	317
$CuInS_2$/ZnS	PEG	100−950 μg/mL	24 h	MTT	Panc-1 cells	cell viability >80% at 195 μg/mL	281
$CuInS_2$/ZnS	TTAB	0−500 μM	6 h	Cell Counting Kit-8, Hoechst 33258	MCF-7, HeLa, HepG2 cells	cell viability >80% at 500 μM	544
Zn−Cu−In−S/ZnS	MPH, PEG-400	0−1 μM Cu^+	24 h	MTT	NIH/3T3 cell	nontoxic	284
InAs/InP/ZnSe	MPA	10−100 nmol/L	48 h	MTT	RAW 264.7 cells	less toxic than CdTe/ZnTe	299
zwitterion-like $CuInS_2$/ZnS	PMAO-DMAPA	0−100 nmol/L	72 h	MTT, FDA/PI staining	U87MG, HEK-293 cells	minimally toxic	545
$CuInS_2$/ZnS	PEI, pDNA, ST68MBs	0−1 mM	48 h	MTT	HeLa, HUVEC cells	cell viability >90% even at 1 mM	413
$CuInS_2$/ZnS	PEI, pDNA, ST68MBs	0−0.5 mM	24 h	calcein AM/PI staining	BMDC, T cells	nontoxic at 0.5 mM	413
graphene QDs	grafting alkylamines, reduced by $NaBH_4$	0−400 μg/mL	24 h	MTT	MC3T3 cells	cell viability >80% at 400 μg/mL GQDs, cell viability <60% at 400 μg/mL mGQDs	310
InGaP/ZnS	PEG	4−1000 nM	48 h	MTT, TEM, Caspase 3 activity assay, reduced glutathione assay etc.	LLC-PK1 cells	less toxic than CdSe	546
InP/ZnS	1 or 2 shell layer	0−500 nM, with or without light	24 h	MTT, ROS assay	PC12, KB, MDA-231-MB, NIH3T3, and B16 cells	depends on number of shells, concentration, and cell type	547
InP/ZnS	MPA	0−100 nM	24 h	MTT, qRT-PCR	zebrafish liver cells	altered gene expression	548
Ag_2S	PEG	0, 15, 30 mg/kg	60 days	blood biochemistry, hematology, pathology analysis	BALB/c mouse	no appreciable toxicity at test dose	289
$AgInS_2$	F127	3 mg/mouse	15 min to ∼24 h	time-dependent imaging, histological analysis	nude mouse	no tissue injury	331
$CuInS_2$/ZnS	DHLA-PEG1000, DPPE-PEG2000	20, 100 pmol/mouse	7 days	histological analysis	mouse	no inflammation at 20 pmol dose, inflammation occurring at 10 times higher dose for $CuInS_2$/ZnS QDs than for CdTeSe/CdZnS QDs	390

DOI: 10.1021/acs.chemrev.6b00290
Chem. Rev. 2016, 116, 12234−12327

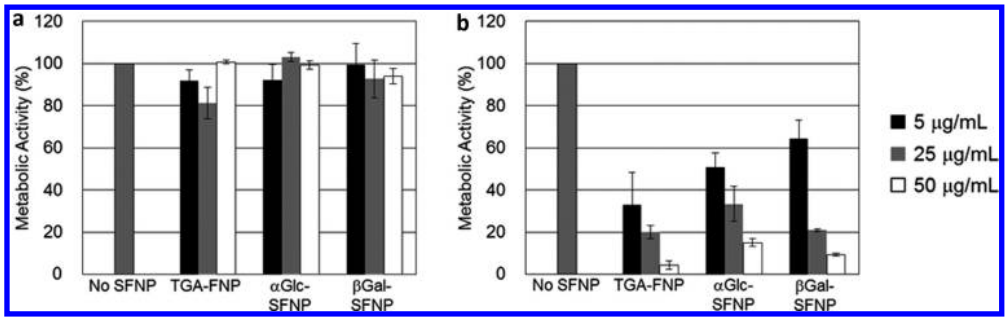

Figure 69. MTT assay comparison for HepG2 cells treated with ZAIS/ZnS QDs (a) or CdTe/CdS QDs (b) for 24 h. Reprinted from Shinchi et al.[222] Copyright 2014 American Chemical Society.

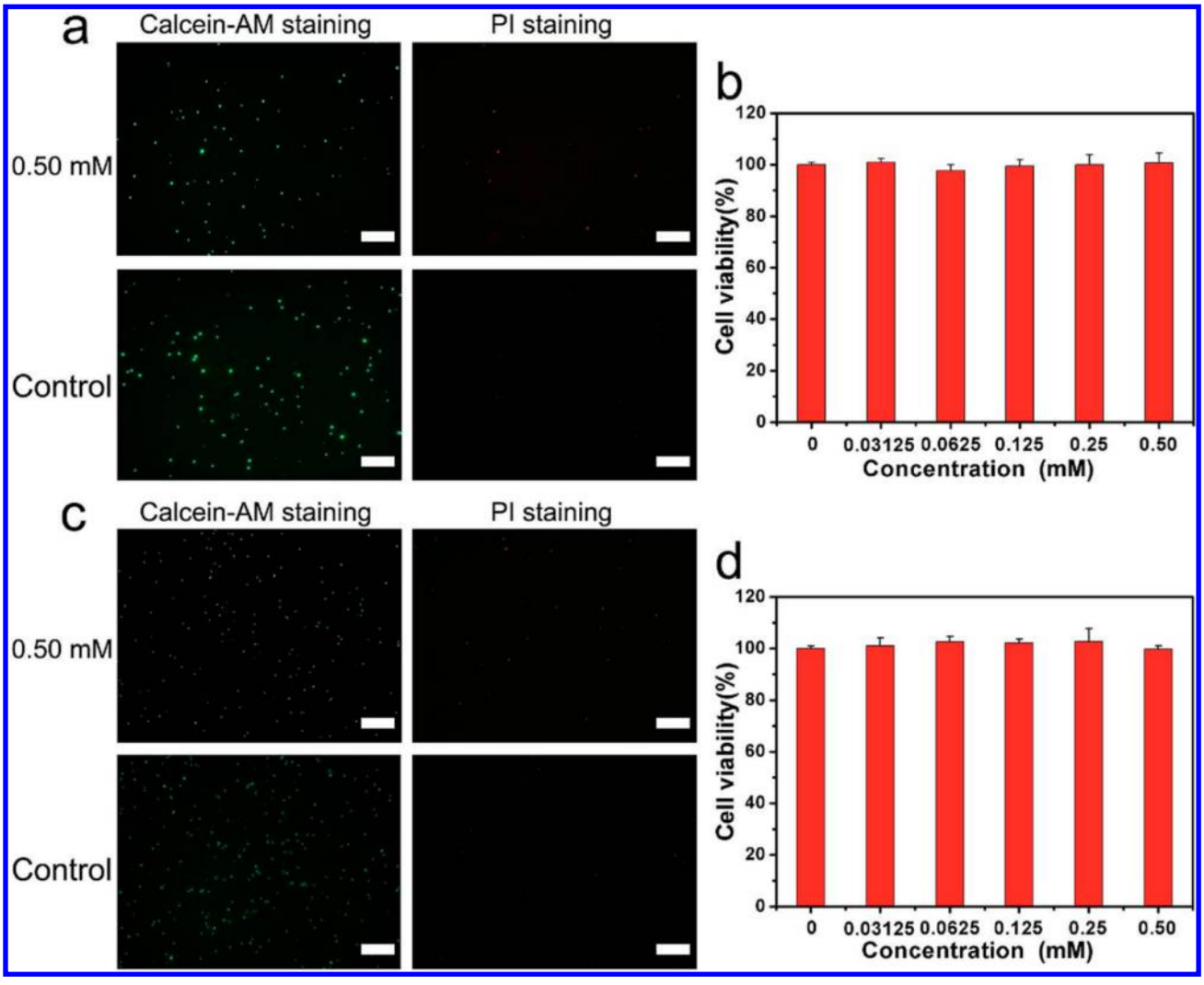

Figure 70. Fluorescence microscopy images of BMDC cells (a) and T cells (c) treated with MB@QD@PEI/pDNA and live/dead staining with calcein AM and PI. Scale bars are 500 μm. The cell viability of BMDC cells (b) and T cells (d) treated with MB@QD@PEI/pDNA for 24 h. Reprinted with permission from Yang et al.[413] Copyright 2015 Royal Society of Chemistry.

determined by staining the cells with FDA/PI to differentiate between live and dead cells. Both U-87MG and HEK-293 cells were treated with 20 nM ZWL-QDs, and untreated cells were used as controls. The toxicity of the ZWL-QDs was insignificant compared to the controls. Relative cell viability for both cells after 72 h of incubation with different ZWL-QD concentrations was determined. The onset of ZWL-QD toxicity was at ~100 nM.

The potential toxicity of a $CuInS_2$/ZnS alloy QD-based multifunctional contrast agent was also investigated using the MTT assay.[413] Specifically, the QDs were passivated with polyethylenimine (PEI), allowing them to complex with plasmid DNA (pDNA). The DNA conjugated QDs adsorbed onto the surface of microbubbles (MBs) formed in a mixed surfactant system containing Tween 80 and Span 60, creating MB@QD@PEI/pDNA complexes. The biocompatibility of these nanocomplexes was evaluated in HeLa cells and human

DOI: 10.1021/acs.chemrev.6b00290
Chem. Rev. 2016, 116, 12234−12327

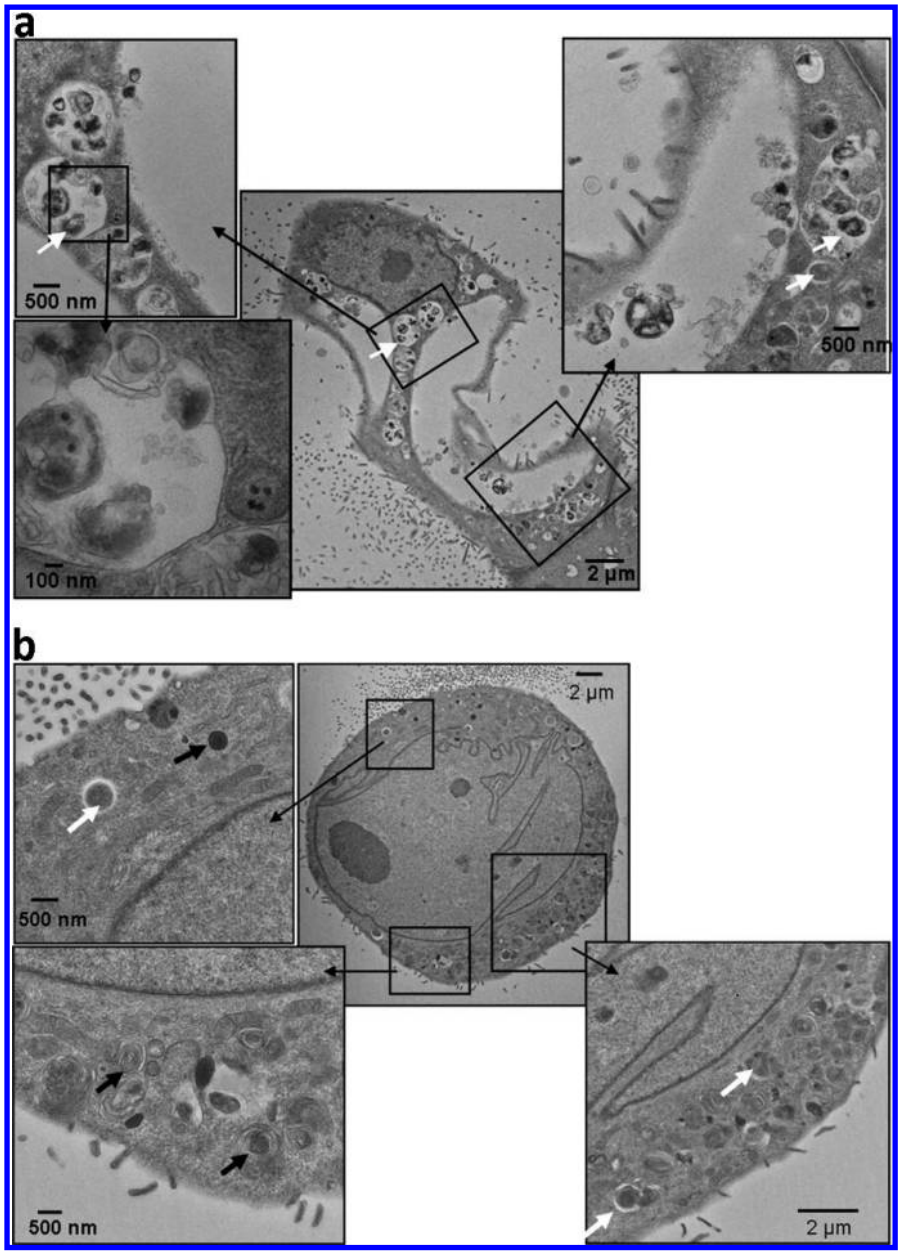

Figure 71. TEM ultrastructures of LLC-PK1 cells treated for 24 h with 10 nM CdSe QD (a) or 100 nM InGaP QD (b). White arrows, autophagic vacuoles; black arrows, lysosomal remnants. Reprinted with permission from Stern et al.[546] Copyright 2008 Oxford University Press.

umbilical vein endothelial (HUVEC) cells. Both cell types were treated with varying doses of the MB@QD@PEI/pDNA formulation for 48 h, and the viability of the treated cells was evaluated by an MTT assay. The viability of HeLa and HUVEC cells remained above 90% up to a concentration equivalent to 1 mM PEI. To further evaluate the biocompatibility of the nanocomplex formulation, bone marrow dendritic cells (BMDC) and T cells were treated with the formulation for 24 h. The viable cells were stained green using calcein acetoxymethyl ester, and the dead cells were stained red using propidium iodide (PI). Fluorescence microscopy of the live/dead stained cells revealed no adverse effects to either BMDC or T cells after treatment with the MB@QD@PEI/pDNA formulation (Figure 70).

The in vitro cytotoxicity of different graphene QDs was tested using the MTT assay,[310] demonstrating that graphene QDs and r-graphene QDs (graphene QDs reduced with $NaBH_4$) had low toxicity toward MC3T3 cells. The cell viability remained near 80% in the presence of 400 μg/mL graphene QDs or r-graphene QDs. On the other hand, m-graphene QDs (alkylamine modified graphene QDs) showed a clear dose-dependent impact on cell viability. The cell viability dropped below 60% in the presence of 400 μg/mL m-graphene QDs. The authors attributed the cytotoxicity to the presence of alkylamines, in which both alkyl chains and nitrogen adversely impacted the cells.

Stern et al. investigated cytotoxicity mechanisms of lipid-coated and PEGylated CdSe/ZnS and InGaP/ZnS QDs with core sizes of 5.1 and 3.7 nm.[546] Based on MTT assay results, the CdSe/ZnS QDs ($IC_{50} \sim 10$ nM) were determined to be 10-fold more toxic to porcine renal proximal tubule (LLC-PK1) cells compared to the InGaP/ZnS QDs ($IC_{50} \sim 100$ nM). Using reduced glutathione content and lipid peroxide analysis, the authors found that neither type of QDs induced oxidative

DOI: 10.1021/acs.chemrev.6b00290
Chem. Rev. 2016, 116, 12234−12327

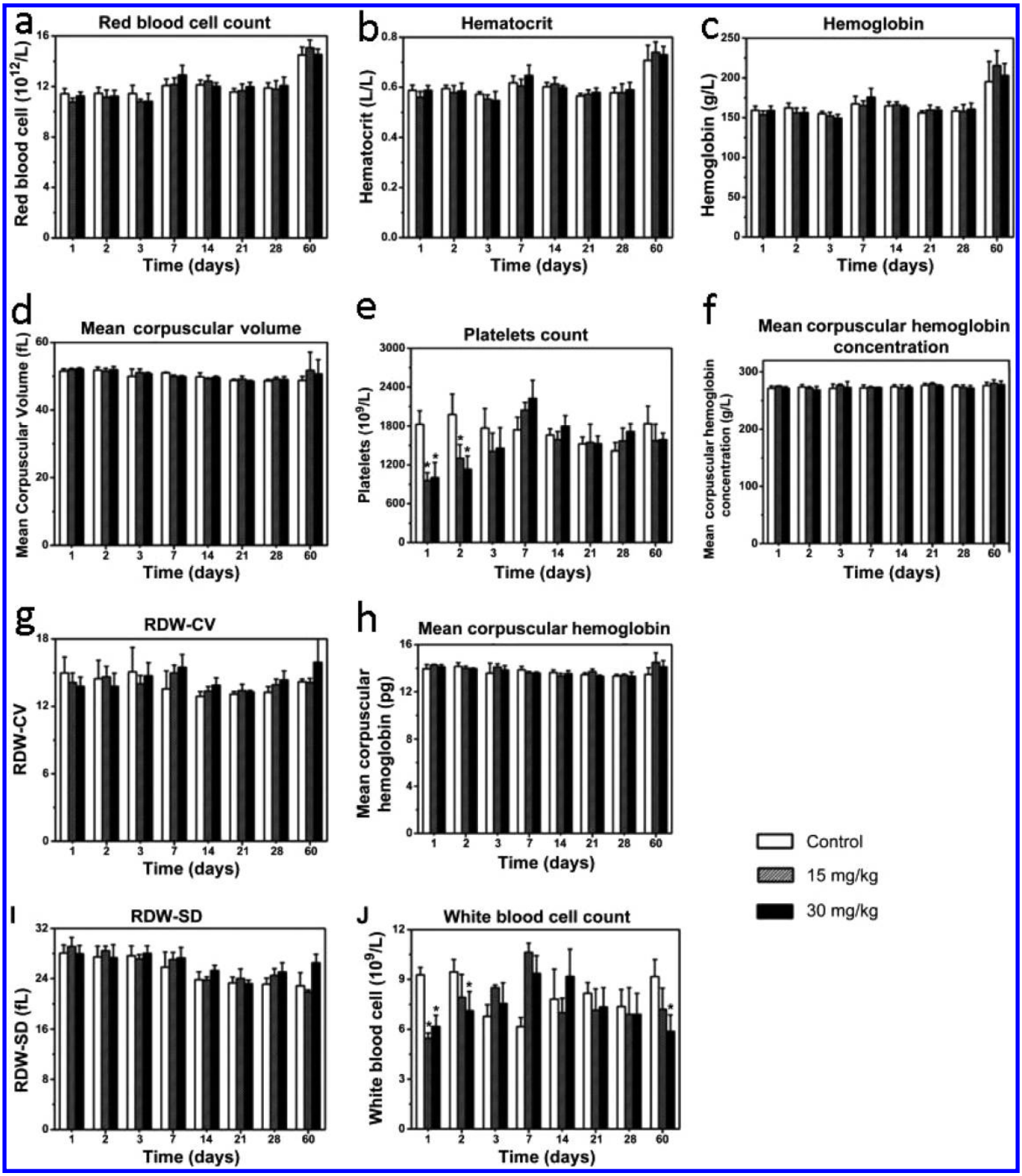

Figure 72. Hematology data on female BALB/c mice treated with PEGylated-Ag_2S QDs at 0, 15, and 30 mg/kg at 1, 2, 3, 7, 14, 28, and 60 days postinjection. ∗, $P < 0.05$. Reprinted with permission from Zhang et al.[289] Copyright 2013 Elsevier.

stress, suggesting that the toxicity was not associated with the QD metals. The cells treated with CdSe QDs were not linked with any changes in Cd-related caspase-3 enzyme activation or metallothionein-IA gene expression. On the other hand, treating LLC-PK1 cells with InGaP QDs caused a significant increase in MT-IA expression during the first 24 h posttreatment. More importantly, the authors found the evidence of extensive autophagy for QD-treated cells. This was determined by analyzing Lysotracker dye uptake, cell morphology from TEM images (Figure 71), and LC3 immunoblotting. Autophagy is a process involving recycling and degrading of long-lived proteins and organelles by lysosomes. It is also

DOI: 10.1021/acs.chemrev.6b00290
Chem. Rev. 2016, 116, 12234−12327

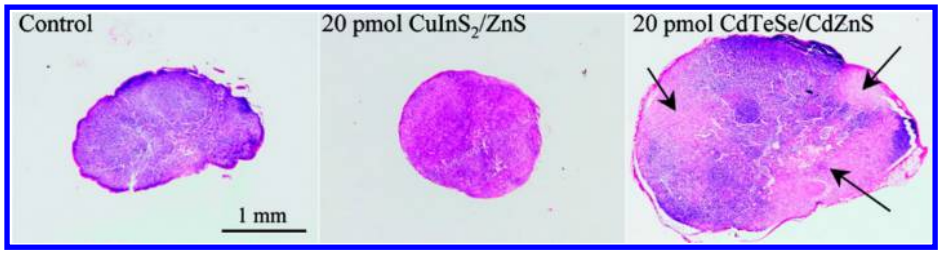

Figure 73. Histological sections of RALNs resected 7 days postinjection for mice injected with a saline buffer solution (control), $CuInS_2$/ZnS QDs, and CdTeSe/CdZnS QDs. Black arrows, inflammation sites. Reprinted from Pons et al.[390] Copyright 2010 American Chemical Society.

viewed as a general pathway of programmed cell death which has a similar homeostatic function as apoptosis.

8.2. In Vivo Toxicity

Some detailed studies of in vivo toxicity of Cd-free quantum dots have also been reported. The toxicology of NIR Ag_2S QDs was studied in mice.[289] The effect of PEGylated-Ag_2S QDs on the body weight of mice was examined by comparing treated and untreated mice for 2 months after injection. The control group and experimental groups receiving injected doses of 15 and 30 mg/kg showed similar weight gain. In addition, blood biochemistry analysis was carried out, evaluating the ratio of albumin to globulin, glucose, globulin, total protein, total cholesterin, aspartate aminotransferase, alkaline phosphatase, alanine aminotransferase, blood urea nitrogen, and albumin. Mice were sacrificed for blood sample collection at intervals during the 60 days following treatment. All biochemistry parameters remained in the normal range compared to the control group of mice, for both 15 and 30 mg/kg doses. Hematological toxicity was assessed by white blood cell count, red blood cell count, mean corpuscular volume, mean corpuscular hemoglobin, mean corpuscular hemoglobin concentration, hematocrit, hemoglobin, platelet count, and red blood cell volume distribution width (Figure 72). Except for platelet and white blood cell counts, all these hematological indicators were in the normal range. The platelet and white blood cell levels in the experimental groups dropped significantly during the first few days after the injection of the NPs. The authors speculated that this drop was caused by macrophage inhibition and platelet damage associated with the acute immune response to the injected Ag_2S QDs. For mice receiving 30 mg/kg QDs, necropsies were performed on animals sacrificed at 3, 7, 14, 21, 28, and 60 days postinjection. Tissue sections from the liver, spleen, and kidney were analyzed by H&E staining, and no obvious lesions or signs of hydropic damage were found.

Liu et al. employed histological imaging to determine the toxicity of micelle-encapsulated $AgInS_2$ QDs in mice.[331] After completing MTT assays using Panc-1 cells, the authors carried out histological studies of acute toxicity induced by QDs on the lung, liver, spleen, kidney, heart, and brain of mice. Small animals treated with Pluronic micelle-encapsulated $AgInS_2$ QDs did not show any tissue injury in any of these organs. No drastic differences in body weight were observed between treated and control mice for more than a week. Together, these results support the lack of acute toxicity of the Pluronic micelle-encapsulated $AgInS_2$ formulations in small animals.

The inflammatory response of the axillary lymph node (LN) was examined in mice treated with CdTeSe/CdZnS and $CuInS_2$/ZnS QDs.[390] QD dispersions were subcutaneously injected in the right anterior paw of mice. The two types of QDs displayed similar performance in LN imaging, because the QDs possessed similar extinction coefficients, QYs, and hydrodynamic sizes. The weights of the right axillary LN (RALN) and right lateral thoracic LN (RLTLN) dissected at 7 days postinjection were analyzed. The percentage of the total injected dose taken up by the RALN at 7 days postinjection was larger for $CuInS_2$/ZnS QDs (4%) compared to CdTeSe/CdZnS (1.5%) (Figure 73). The authors mentioned that, for both QD formulations, there is a clear dose-dependent increase in weight of the RALNs and this indicates the increasing toxicity of the QDs. Also, they found a distinct difference in the toxicity between the two types of QDs. Inflammation was observed in mice treated with 10 pmol of CdTeSe/CdZnS QDs, and the mass of the RALN was drastically increased. Similar inflammation was detected for the injection of 100 pmol of $CuInS_2$/ZnS. Histological analysis was also performed on sections of the RALNs at 7 days postinjection. The RALN of mice treated with 20 pmol of $CuInS_2$/ZnS displayed no signs of inflammation, whereas the same dose of CdTeSe/CdZnS QDs induced inflammation in the RALN of the treated mice. Signs of inflammation observed from the histological samples include polynuclear cells, histiocytes, and vacuoles of digestion in the examined regions of interest. The inflammatory response of the axillary LN induced by $CuInS_2$/ZnS QDs was much lower than that induced by CdTeSe/CdZnS QDs, and the minimum dose of $CuInS_2$/ZnS QDs used for RALN detection was 50 times lower than the minimum dose that induced RALN inflammation. This comparison between Cd-based and Cd-free QDs shows that the window of operation between the dose needed for imaging and that which causes an inflammatory response was much wider for the $CuInS_2$/ZnS QDs, illustrating their clear advantage in this application.

8.3. Mechanisms of Toxicity

A primary mechanism of nanotoxicity associated with QDs is oxidative stress due to generation of reactive oxygen species (ROS), particularly under light exposure.[3] Chibli et al. investigated the role of ROS generation in the cytotoxicity of InP/ZnS QDs.[547] When QDs are excited by illumination, they may generate various ROS species such as singlet oxygen, hydrogen peroxide, and hydroxyl radicals due to the transfer of their electrons/holes to oxygen molecules or other acceptors/donors in cells. These reductive and oxidative processes have been reported when using CdSe QDs and are also expected to occur with InP QDs based on the similar energy levels of their band edge and defect states. EPR and ROS assays showed that InP and InP/ZnS QDs generated considerable superoxide and a small amount of hydroxyl radicals, but no singlet oxygen. In a sulforhodamine B (SRB) cytotoxicity assay, no toxicity was observed in PC12 cells treated with QDs at concentrations up to 500 nM, with or without light exposure. For KB cells treated with 500 nM InP/ZnS QDs with one shell layer of ZnS, a dramatic reduction in cell growth was observed. On the other

DOI: 10.1021/acs.chemrev.6b00290
Chem. Rev. 2016, 116, 12234−12327

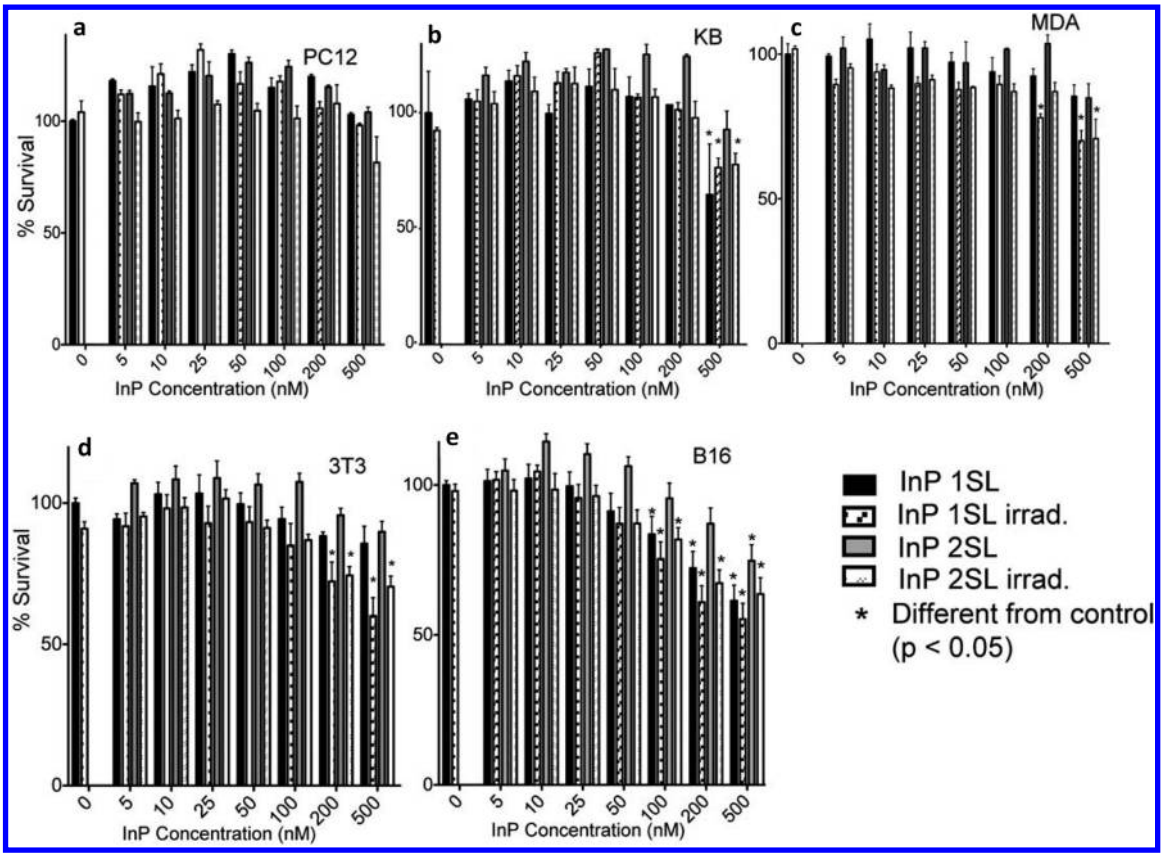

Figure 74. Cell viability after treatment with InP/ZnS with one ZnS shell layer (1SL) or two ZnS shell layers (2SL) and either kept in the dark or irradiated ("irrad"). The cell lines included (a) PC12, (b) KB, (c) MDA-231-MB, (d) NIH3T3, and (e) B16. Reprinted with permission from Chibli et al.[547] Copyright 2011 Royal Society of Chemistry.

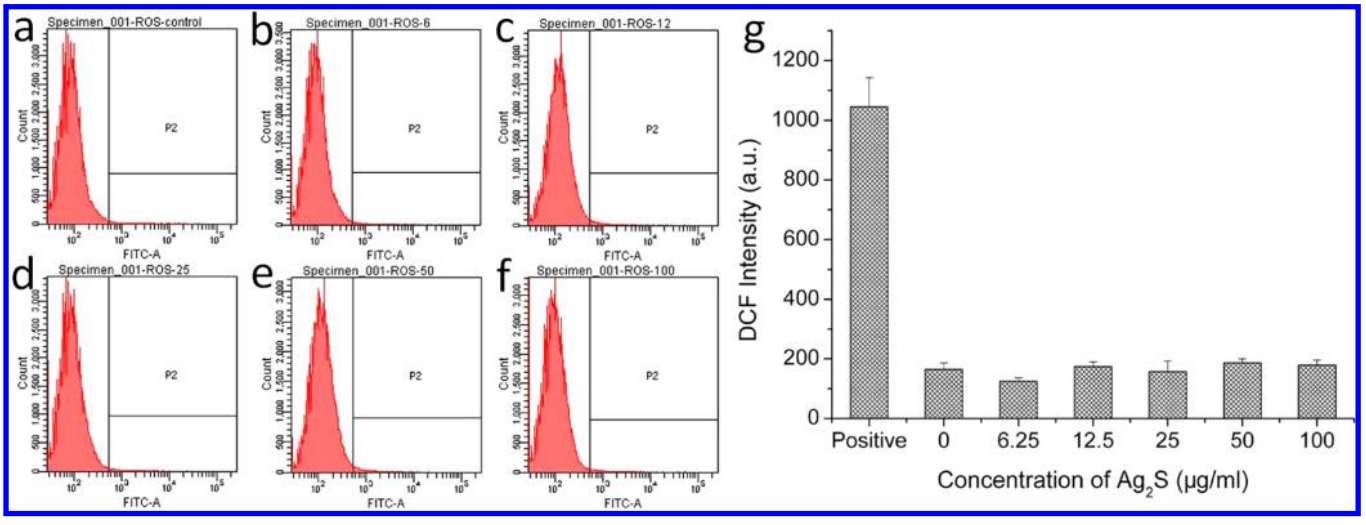

Figure 75. ROS induced by DHLA-Ag_2S QDs after 72 h treatment. FACS plots with Ag_2S QD concentrations of 0 (a), 6.25 (b), 12.5 (c), 25 (d), 50 (e), and 100 μg/mL (f). (g) Quantitative flow cytometry results. Reprinted from Zhang et al.[290] Copyright 2012 American Chemical Society.

hand, InP/ZnS QDs with two shell layers of ZnS displayed a significant adverse impact only in the presence of light. MDA and 3T3 cells treated with QDs and subsequently illuminated showed significant signs of toxicity at 200 nM dosage. The one-shell-layer InP/ZnS QDs were highly toxic to the mouse melanoma cell line B16 at 100 nM, in the presence and absence of light, while two-shell-layer InP/ZnS QDs displayed toxicity at 200 nM only with light exposure (Figure 74). The distinct toxicity reduction and good electron transfer efficiency for double-shell InP/ZnS QDs in the above-mentioned five cell lines compared to those observed for CdTe or CdSe/ZnS QDs demonstrates the promise of these Cd-free QDs as alternatives to Cd-based QDs for photosensitization applications.

The cytotoxicities of Cd salt, Zn salt, Cd-based QDs, and Zn-based QDs were investigated using zebrafish liver cells (ZFL).[548] The IC_{50} values at 24 h of CdSe/ZnS and InP/ZnS QDs were much larger than that of CdTe QDs, suggesting that ZnS-capped QDs were more biocompatible than CdTe

DOI: 10.1021/acs.chemrev.6b00290
Chem. Rev. 2016, 116, 12234−12327

core QDs alone. Isolated mRNA from these QD exposures were employed to determine the expression of metal response genes such as metallothionein (MT), divalent metal transporter (DMT-1), zrt and irt like protein (ZIP-1), metal response element-binding transcription factor (MTF-1), and the zinc transporter (ZnT-1). The expression of metal homeostasis genes was altered by CdSe/ZnS and InP/ZnS QDs in a manner that is different from the Cd salt, Zn salt, or CdTe QDs. The authors suggest that the coating of ZnS shell on QDs reduces the QD toxicity that is associated with the release of heavy metal ions, but the coating does not eliminate the toxic effects associated with the overall NP formulation itself.

The cytotoxicity of Ag_2S QDs, including their influence on ROS generation, cell proliferation and apoptosis/necrosis, and DNA damage were considered by Zhang et al.[290] Mouse fibroblast L929 cells were used for the cytotoxicity assay. After exposing the L929 cells to Ag_2S QDs at five different concentrations (6.25, 12.5, 25, 50, and 100 μg/mL) for 72 h, the cell proliferation was quantified and determined to be dose-independent. Using Hoechst and EdU as staining agents for cell counting, the researchers found no statistically significant differences in the total number of L929 cells or the number of cells with newly synthesized DNA, suggesting that Ag_2S QDs did not impact cell proliferation. To investigate apoptosis and necrosis, flow cytometry with Annexin V-FITC staining and propidium iodide (PI) staining was conducted. The flow cytometry data showed very low cytotoxicity in terms of generating apoptosis and necrosis events in the cells after 72 h of treatment. ROS produced by the Ag_2S QDs was determined by measuring the fluorescence intensity of 2′,7′-dichlorofluorescein (DCF). This ROS assay involves the use of the cell-permeable probe 2′,7′-dichlorodihydrofluorescein diacetate (DCFH-DA), which diffuses into the cells and is hydrolyzed into nonfluorescent DCFH by cellular esterase. When ROS are present, the DCFH will be oxidized to DCF and show strong fluorescence. Flow cytometry measurements showed that cells treated with 100 μg/mL QDs for 72 h generated very low amounts of ROS, with no statistically significant difference from the negative control (Figure 75).

Brunetti et al. conducted a detailed in vitro and in vivo toxicity study of an InP/ZnS QD formulation.[276] Toxicity of CdSe/ZnS QDs is largely associated with the release of Cd^{2+} ions from the QD surface. Approximately the same amount of In^{3+} ions was released from the InP/ZnS QDs surface. However, the toxicity of In^{3+} is much lower than that of Cd^{2+}. In this work, human lung carcinoma A549 cells, an epithelial cell line, and human neuroblastoma SH SY5Y cells, a neuronal cell line, were used to investigate cytotoxicity of CdSe/ZnS and InP/ZnS QDs over a concentration range of 1 pM−5 nM. Cell viability was determined using the WST-8 assay at 24 and 48 h of incubation. CdSe/ZnS QDs caused stronger adverse impact to the cell viability than InP/ZnS QDs. At 24 h incubation, the toxic effect of CdSe/ZnS QDs was detectable at a concentration of 1 nM. After 48 h incubation, cell viability loss was detected for CdSe/ZnS QDs even at 10 pM. The highest toxicity was observed for the neuronal cell line with 27 and 46% viability losses after 24 and 48 h of incubation with 5 nM CdSe/ZnS QDs. The A549 cells were less sensitive to the QDs. A 33% reduction in cell viability was detected after 48 h of incubation with 5 nM CdSe/ZnS QDs. On the other hand, incubation of the same cell line with 5 nM InP/ZnS QDs did not cause any significant reduction in cell viability. To further probe the molecular mechanism underlying the reduction in cell viability, the authors carried out a series of different assays. The lactate dehydrogenase (LDH) leakage assay was employed to evaluate cell membrane damage. The assay revealed that the presence of 1 pM CdSe/ZnS QDs produced significant membrane damage in the cell types mentioned above. In contrast, no change in LDH was detected upon exposing the cells to InP/ZnS QDs. Oxidative stress within the QD-treated cells was also analyzed. A positive DCF-DA (dichlorofluorescein diacetate) assay showed that cell cultures treated with 1 pM Cd-containing QDs for 24 h generated intracellular reactive oxygen species (ROS). To further confirm the generation of ROS caused by oxidative stress, real-time qPCR was used to determine the expression levels of CAT, Gpx, SOD1, and SOD2 genes coding for antioxidant and detoxifying enzymes. The expression profiles determined without photoactivation of QDs revealed that the treated cells experienced oxidative stress when they were exposed with CdSe/ZnS QDs. The same concentration of InP/ZnS QDs did not cause any detectable overexpression of genes correlated with oxidative stress. The results revealed that epithelial cell line A549 was less susceptible to QD-induced damage than the neuronal cell line SH SY5Y. The authors also studied the toxicity of CdSe/ZnS and InP/ZnS QDs in fruit flies by feeding them QD-supplemented food. The authors used real-time qPCR to investigate the mechanisms of QD toxicity. For instance, they investigated variations in expression levels of genes associated with DNA damage and stress response. *Drosophila* flies were fed with food containing CdSe/ZnS or InP/ZnS QDs, or with standard food as a control. Gene expression was observed in the fruit flies fed with food containing 100 and 500 pM CdSe/ZnS QDs, revealing systemic toxicity involving increased ROS production, the generation of abnormal proteins, and the presence of genomic perturbation. Gene expression in fruit flies treated with the InP/ZnS QDs was much closer to that of the control group (Figure 76).

9. CONCLUDING REMARKS AND PERSPECTIVES

This review summarized recent developments in Cd-free QDs for biophotonics and nanomedicine applications. Thanks to tremendous efforts invested in the synthesis and functionalization of these QDs, the past decade has witnessed a substantial

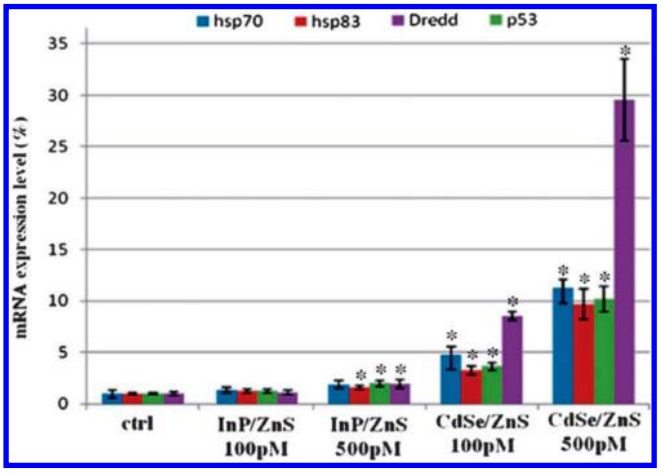

Figure 76. mRNA expression levels of *Drosophila* flies treated with InP/ZnS or CdSe/ZnS QDs. *, $P < 0.05$ compared with control ($n = 8$). Reprinted with permission from Brunetti et al.[276] Copyright 2013 Royal Society of Chemistry.

DOI: 10.1021/acs.chemrev.6b00290
Chem. Rev. 2016, 116, 12234−12327

improvement in their optical properties, stability, and biocompatibility. Although the first Cd-free QDs exhibited low QY and/or poor optical or colloidal stability, recent studies of InP, $CuInS_2$, and $AgInS_2$ QDs have reported much improved QY, in many cases over 50%, with broad wavelength tunability. The use of Ag_2S and Ag_2Se QDs extends the accessible emission wavelengths to the NIR-II window, which was not possible using conventional Cd-based QDs. Meanwhile, Si QDs and emerging graphene QDs provide advantages in terms of biocompatibility, the abundance of their component elements, and the ability to form covalent bonds with organic ligands. The best-quality Cd-free QDs have achieved optical performance matching that of Cd-based QDs in several applications. The low toxicity of their components has relieved some of the concerns associated with their use in vivo and has improved their prospects for future clinical applications. Moreover, these Cd-free QDs exhibit diverse and unique optical properties such as long PL lifetime, large multiphoton absorbance cross section, considerable near-IR absorbance, and upconverted emission. These distinguishing features can expand their use to novel applications including time-gated imaging, multiphoton imaging, photoacoustic imaging, and upconversion imaging. Nonetheless, many opportunities remain to improve the engineering of Cd-free QDs to achieve better physicochemical properties and to further enrich their surface chemistry. Further investigations of their fate and toxicological impact in different biological models are urgently needed. New techniques and instrumentation that fully exploit the advantages of these materials must be further developed, standardized, and commercialized. Based on this comprehensive survey of the Cd-free QD literature, here we summarize the current status, trends, and emerging directions in the synthesis and biomedical applications of Cd-free QDs.

9.1. Quantum Dot Synthesis and Functionalization

(a) Mature and reproducible synthesis methods are needed for consistent production of monodispersed Cd-free QDs with high PL intensity, narrow PL spectral width, and broad wavelength tunability. The optimization of synthesis is a case-by-case challenge depending on the specific type of Cd-free QD. Also, strategies to avoid or to deliberately introduce defects must be investigated based on PL mechanism (e.g., band-edge emission or internal/surface defect-related emission) of the Cd-free QDs. For $CuInS_2$, $AgInS_2$, and ZnO QDs, high QY has been reported in recent studies, but their emission spectra remain broad, primarily due to polydispersity, and this can limit their use in multiplexed imaging and other advanced applications. Improved synthesis methods, with better control of size, stoichiometry, and surface passivation, along with improved fundamental understanding of all sources of emission broadening, are needed to expand the range of applications of these QDs. Although InP QDs exhibit high QY with narrower emission spectra, they are typically prepared from expensive and pyrophoric precursors that discourage larger-scale production and application. For Ag_2S and Ag_2Se QDs, improving the PL QY in the near-IR range remains an important goal. Si QDs remain relatively less understood, with dramatically different results obtained from QDs produced by solution-phase and high-temperature gas-phase synthesis. Although high QYs have been reported, such materials can be produced by very few laboratories, limiting their broader application. Controlled synthesis of graphene QDs is less mature than the other materials discussed here. Improving the wavelength tunability of these QDs and using inexpensive and environmentally friendly starting materials are important research directions. In contrast to the best developed Cd-based QDs, particularly CdSe/ZnS QDs, which are available commercially as relatively standardized products and whose synthesis has been widely replicated, most of the Cd-free QDs are not commercially available and cannot readily be produced by research groups without prior QD synthesis experience. Interlaboratory reproducibility and consistency remains a major challenge for many of these materials. Standardized, reproducible protocols are essential for clinical translation of these materials.

(b) The preparation of Cd-free QDs that retain their bright PL and exhibit long-term colloidal stability in water and biological media remains an important need. Two general routes to producing high-performance Cd-free QDs in aqueous media are possible: (1) direct synthesis of hydrophilic QDs in water or hydrophilic solvents and (2) phase transfer of hydrophobic QDs into the aqueous phase. The former method requires identification of appropriate ligands and reaction conditions for nanocrystal growth. For example, several studies on aqueous synthesis of $CuInS_2$ QDs selected ligands based on the hard−soft acid−base theory to balance the reactivity of the different cations. The optimal ligands and reaction conditions are material-specific, which limits the ability to adapt existing protocols to new QD materials. For phase transfer of Cd-free QDs, researchers can build upon strategies used for modifying Cd-based QDs and other nanocrystals. However, differences in both QD composition and surface ligands used during synthesis require unique surface chemistry, such that methods used for other materials cannot always be directly applied to Cd-free QDs. For example, exchange of organothiol ligands on Cd-free QDs for hydrophilic thiol ligands may result in unsuccessful/incomplete ligand exchange or PL quenching. Encapsulation using polymers or silica shells solves these problems but is usually accompanied by a substantial size increase. Improved material-specific phase transfer approaches are still needed for most of the Cd-free QDs.

(c) The biofunctionalization of Cd-free QDs is in a relatively early stage of development, and advances are expected to further increase targeting specificity, biomolecule sensitivity, and gene/drug loading efficiency for a diverse array of applications. The potential of unfunctionalized Cd-free QDs of appropriate size and surface passivation for tumor imaging based on passive targeting has been demonstrated for several types of Cd-free QDs. Molecules including folic acid and antiVEGF have also been widely used to functionalize Cd-free QDs for targeting general classes of tumors. In the coming years, we can expect that ligands for targeting specific tumor markers, multivalent ligands, and mixed ligands that only target cells expressing specific combinations of biomarkers will further increase the targeting specificity of Cd-free QDs. For drug/gene delivery, maximizing loading capacity may lead to compromised optical properties and/or reduced biocompatibility. For example, increasing the positive surface charge of Cd-free QDs could result in more adsorption of negatively charged drugs/genes, but the toxicity induced by the highly positively charged nanocomplexes raises new concerns. In such trade-off situations, a balance must be found to optimize overall performance in specific delivery applications. Cd-free QDs will continue to develop in two roles for delivery applications: (1) those in which QDs are directly conjugated with the drug or gene and (2) those in which they are encapsulated together

DOI: 10.1021/acs.chemrev.6b00290
Chem. Rev. 2016, 116, 12234−12327

with the therapeutic cargo in a larger carrier to serve as optical probes.

(d) The integration of Cd-free QDs with other contrast agents (e.g., radioactive labels, gold NPs, magnetic ions or NPs, and Raman tags) for multimodal and multispectral imaging provides a cross-evaluation approach for acquiring comprehensive information to understand the complex nature of tumors and other disease states. The advantages of optical imaging, including high spatial resolution, low cost, and high scanning speed, make it complementary to CT, MRI, PET, and SPECT imaging techniques. Initial attempts to integrate multiple imaging methods have included coencapsulation of multiple contrast agents in polymer assemblies or cosynthesis of different types of labels in one reaction system. Both the design of new multimodal probes and development of integrated imaging systems required to fully exploit the possibilities enabled by these new probes will remain fruitful research areas in the coming years.

9.2. Understanding of Quantum Dot Behavior in Living Systems

Biodistribution and toxicity profiles of Cd-free QDs must be more fully understood and mechanistically related to their size, shape, surface properties, administration method, and the applied animal models. Circulation and retention times, which are crucial for long-term imaging, have been shown to vary substantially for Cd-free QDs of different sizes, with and without targeting ligands. The most common fates of the Cd-free QDs were (1) accumulation in the RES organs and (2) excretion. The dominant pathway is mainly determined by hydrodynamic size, in the actual state of aggregation in which they are present in vivo, but is also influenced by the QD type and surface properties. Toxicity evaluation of Cd-free QDs requires comparative studies between different types of QDs and more systematic studies on various cell lines and animal models. Although Cd-free QDs such as InP, $CuInS_2$, doped ZnSe, and Ag_2Se QDs do not contain Cd or other highly toxic elements, their components (e.g., In, Se) are not completely benign in biological systems. The release profile of these elements and biological responses to them must be more fully characterized. For graphene QDs and Si QDs, which are based on nontoxic elements, attention should be drawn to toxicity induced by phenomena including immune response and generation of ROS as well as to their long-term fate. To date, although some studies have reported reduced toxicity from Cd-free QDs compared to Cd-based QDs at the same concentration, this information must be carefully evaluated according to their ability to also achieve the same performance at the same concentration in applications. Moreover, the diversity of methods used for evaluation of in vivo and in vitro toxicity profiles make intercomparison of results challenging or impossible. Going forward, more uniform standards for toxicology studies of QDs, and greater involvement of the traditional toxicology research community, are needed to move Cd-free QDs closer to clinical application.

9.3. New Applications and Technologies

(a) Magnetic manipulation combined with optical imaging using combined or coupled superparamagnetic and photoluminescent QDs or superparamagnetic and plasmonic NPs opens up possibilities for highly multiplexed analysis. Such structures enable the use of external magnetic fields to separate targets by magnetic mobility. Pairing these with hyperspectral imaging allows multiplexing by emission or absorbance color. Together, this enables two-dimensional multiplexing for analysis of very complex mixtures of biomolecules. The same materials can be used for simultaneous cell labeling and magnetic sorting. Combining magnetic sorting with optical labeling in this way can enhance sensitivity and specificity of biomarker detection. Such structures can also be used for magnetically enhanced targeted delivery of drugs and genes. Magnetic−plasmonic QDs can serve as magnetically guided probes for dark field imaging, photoacoustic tomography in the IR, photothermal imaging, and photothermal therapy.

(b) Another new direction is multivariate near-IR flow cytometry which will allow the use of this cell-sorting technique with little or no sample preparation.[99,549,550] With near-IR labels, even whole blood samples can be analyzed, as blood has minimal absorbance in the near-IR region.[132] The Cd-free QDs discussed here are more stable than near-IR organic dyes and also have narrower emission bands and broad excitation spectra, which facilitate multiplexed detection. This QD technology can also be coupled to microbead capture technology for enhanced detection and analysis of the expression of specific soluble proteins and of exosomes, which are signatures of specific diseases.

(c) Newly emerging applications that exploit unique optical properties of Cd-free QDs, including those mentioned above, will benefit from the development and commercialization of corresponding imaging systems. For near-IR imaging, multiphoton imaging, and time-gated imaging, a specific QD formulation may require excitation with a nonstandard wavelength, pulse duration, and/or pulse frequency. The QDs may exhibit PL at nonstandard wavelengths or with PL lifetimes much different from conventional dyes. Fully exploiting these new probes thus requires specialized optical setups that provide the excitation and collect the PL in a spatially and temporarily constrained way, which present a challenge for biological and medical researchers. The availability of standard configurations of the imaging tools for these methods can increase the signal-to-noise ratio and allow these imaging techniques to go beyond the current stage of proof-of-concept studies to widespread practical use. This also extends to multimodal imaging setups that, for example, combine ultrasound, photoacoustic, and PL imaging in ways that fully exploit the possibilities opened up by new multimodal imaging probes.

AUTHOR INFORMATION

Corresponding Authors

*E-mail: swihart@buffalo.edu (M.T.S.).
*E-mail: ktyong@ntu.edu.sg (K.-T.Y.).
*E-mail: pnprasad@buffalo.edu (P.N.P.).

Author Contributions

[∇]G.X. and S.Z.: These authors equally share the first authorship.

Notes

The authors declare no competing financial interest.

Biographies

Gaixia Xu is a professor in the College of Optoelectronic Engineering at Shenzhen University. She received her Ph.D. in biomedical engineering from Zhejiang University in 2005. Following that, she completed her postdoctoral research at Shenzhen University from 2005 to 2007 and at the University at Buffalo, The State University of New York, from 2007 to 2008. Her interests include optical tracking/

DOI: 10.1021/acs.chemrev.6b00290
Chem. Rev. 2016, 116, 12234−12327

drug delivery/cancer theranostics by using nanoparticles, and the biomedical applications of multimodal microscopy and nanoscopy.

Shuwen Zeng received her Ph.D. from the School of Electrical and Electronic Engineering at Nanyang Technological University. She is currently working as a postdoctoral research fellow at CNRS-International-NTU-THALES Research Alliance (CINTRA)/UMI 3288, Singapore. Her main research interests focus on nanomaterials preparation and their sensing applications.

Butian Zhang is a Ph.D. student under the guidance of Prof. Ken Tye Yong in the School of Electrical and Electronic Engineering at Nanyang Technological University in Singapore. She received her B.S. degree in engineering from Shandong University in China in 2012. Her research interests include synthesis and surface functionalization of quantum dots for biomedical applications.

Mark T. Swihart is a UB Distinguished Professor of Chemical and Biological Engineering and Executive Director of the New York State Center of Excellence in Materials Informatics at the University at Buffalo, The State University of New York. He earned his Ph.D. in chemical engineering from the University of Minnesota in 1997, followed by one year of postdoctoral research in mechanical engineering at the University of Minnesota. His research interests are in the synthesis and processing of inorganic nanomaterials for applications ranging from energy harvesting and conversion to nanomedicine. He has received awards for his research from the American Chemical Society, the Electrochemical Society, and the American Association for Aerosol Research, and is a fellow of the American Association for the Advancement of Science.

Ken-Tye Yong is an associate professor in the School of Electrical and Electronic Engineering at Nanyang Technological University. He received his Ph.D. in chemical and biological engineering from The University at Buffalo, The State University of New York, in 2006. Following completion of his graduate studies, he did his postdoct at the Institute for Lasers, Photonics and Biophotonics in SUNY at Buffalo from 2006 to 2009, where his research focus is in the area of biophotonics and nanomedicine. Currently, his research group interests include engineering nanomaterials for biophotonic and nanomedicine applications, fabricating miniaturized devices for drug delivery, developing nanosensors for biodetection, and creating devices for nanophotonics studies.

Paras N. Prasad is a SUNY Distinguished Professor of Chemistry, Physics, Electrical Engineering and Medicine; the Samuel P. Capen Chair of Chemistry; and the Executive Director of the Institute for Lasers, Photonics, and Biophotonics, University at Buffalo, State University of New York. He was named among the top 50 science and technology leaders in the world by *Scientific American* in 2005, and was recognized as a highly cited researcher in both chemistry and materials science fields by Thomas Reuters in 2014. He has published over 750 scientific and technical papers, four monographs (*Introduction to Nanomedicine and Nanobioengineering*, *Nanophotonics*, *Introduction to Biophotonics*, *Introduction to Nonlinear Optical Effects in Molecules and Polymers*), and eight edited books. He has received many scientific awards and honors (Morley Medal; Schoellkopf Medal; Guggenheim Fellowship; SPIE President's Gold Medal; Honorary Doctorates from KTH, Sweden, and from the Aix Marseille Université, France; Fellow of the APS, OSA, and SPIE, etc.). His interests include biophotonics, nanophotonics, nanomedicine, metamaterials, and solar cells.

ACKNOWLEDGMENTS

This review was prepared with support from the National Basic Research Program of China (2012CB85802 and 2015CB352005), National Natural Science Foundation of China (31671491, 61235012, 61335001, 81301318, and 81501213), Guangdong Natural Science Foundation (2014A030312008), Basic Research Foundation of Shenzhen (JCYJ20140418095735543, JCYJ20140418091413563, and JCYJ20140418182819164), China Scholarship Council (CSC), Singapore Ministry of Education (Grants Tier 2 MOE2010-T2-2-010 (M4020020.040 ARC2/11) and Tier 1 M4010360.040 RG29/10), NTU−NHG Innovation Collaboration Grant (M4061202.040), NTU−A*STAR Silicon Technologies, Centre of Excellence, under the program grant No. 11235100003, and School of Electrical and Electronic Engineering at NTU. The work in Buffalo was supported by The New York State Center of Excellence in Materials Informatics and by a grant from the Research Foundation of SUNY.

REFERENCES

(1) Prasad, P. N. *Nanophotonics*; Wiley: Hoboken, NJ, 2004.
(2) Prasad, P. N. *Introduction to Biophotonics*; Wiley-Interscience: Hoboken, NJ, 2003.
(3) Prasad, P. N. *Introduction to Nanomedicine and Nanobioengineering*; John Wiley & Sons: Hoboken, NJ, 2012.
(4) Liu, J.; Lau, S. K.; Varma, V. A.; Moffitt, R. A.; Caldwell, M.; Liu, T.; Young, A. N.; Petros, J. A.; Osunkoya, A. O.; Krogstad, T.; et al. Molecular Mapping of Tumor Heterogeneity on Clinical Tissue Specimens with Multiplexed Quantum Dots. *ACS Nano* **2010**, *4*, 2755−2765.
(5) Montalti, M.; Cantelli, A.; Battistelli, G. Nanodiamonds and Silicon Quantum Dots: Ultrastable and Biocompatible Luminescent Nanoprobes for Long-Term Bioimaging. *Chem. Soc. Rev.* **2015**, *44*, 4853−4921.
(6) Liu, Q.; Guo, B.; Rao, Z.; Zhang, B.; Gong, J. R. Strong Two-Photon-Induced Fluorescence from Photostable, Biocompatible Nitrogen-Doped Graphene Quantum Dots for Cellular and Deep-Tissue Imaging. *Nano Lett.* **2013**, *13*, 2436−2441.
(7) Koneswaran, M.; Narayanaswamy, R. Ultrasensitive Detection of Vitamin B6 Using Functionalised CdS/ZnS Core−Shell Quantum Dots. *Sens. Actuators, B* **2015**, *210*, 811−816.
(8) Jiang, P.; Zhu, C.-N.; Zhang, Z.-L.; Tian, Z.-Q.; Pang, D.-W. Water-Soluble Ag_2S Quantum Dots for Near-Infrared Fluorescence Imaging *in vivo*. *Biomaterials* **2012**, *33*, 5130−5135.
(9) Zhang, B.; Wang, Y.; Yang, C.; Hu, S.; Gao, Y.; Zhang, Y.; Wang, Y.; Demir, H. V.; Liu, L.; Yong, K.-T. The Composition Effect on the Optical Properties of Aqueous Synthesized Cu−In−S and Zn−Cu−In−S Quantum Dot Nanocrystals. *Phys. Chem. Chem. Phys.* **2015**, *17*, 25133−25141.
(10) Cho, E.; Jang, H.; Lee, J.; Jang, E. Modeling on the Size Dependent Properties of InP Quantum Dots: A Hybrid Functional Study. *Nanotechnology* **2013**, *24*, 215201−215201.
(11) Vanmaekelbergh, D. l.; Van Vugt, L. K.; Bakker, H. E.; Rabouw, F. T.; Nijs, B. d.; van Dijk-Moes, R. J.; van Huis, M. A.; Baesjou, P. J.; van Blaaderen, A. Shape-Dependent Multiexciton Emission and Whispering Gallery Modes in Supraparticles of CdSe/Multishell Quantum Dots. *ACS Nano* **2015**, *9*, 3942−3950.
(12) Zhang, B.; Hu, R.; Wang, Y.; Yang, C.; Liu, X.; Yong, K.-T. Revisiting the principles of preparing aqueous quantum dots for biological applications: the effects of surface ligands on the physicochemical properties of quantum dots. *RSC Adv.* **2014**, *4*, 13805−13816.
(13) Galloway, J. F.; Winter, A.; Lee, K. H.; Park, J. H.; Dvoracek, C. M.; Devreotes, P.; Searson, P. C. Quantitative Characterization of the Lipid Encapsulation of Quantum Dots for Biomedical Applications. *Nanomedicine* **2012**, *8*, 1190−1199.
(14) Ren, M.; Xu, H.; Huang, X.; Kuang, M.; Xiong, Y.; Xu, H.; Xu, Y.; Chen, H.; Wang, A. Immunochromatographic Assay for Ultrasensitive Detection of Aflatoxin B1 in Maize by Highly Luminescent

DOI: 10.1021/acs.chemrev.6b00290
Chem. Rev. 2016, 116, 12234−12327

Quantum Dot Beads. *ACS Appl. Mater. Interfaces* **2014**, *6*, 14215−14222.
(15) Zhan, N.; Palui, G.; Mattoussi, H. Preparation of Compact Biocompatible Quantum Dots Using Multicoordinating Molecular-Scale Ligands based on a Zwitterionic Hydrophilic Motif and Lipoic Acid Anchors. *Nat. Protoc.* **2015**, *10*, 859−874.
(16) Liu, H.; Xu, S.; He, Z.; Deng, A.; Zhu, J.-J. Supersandwich Cytosensor for Selective and Ultrasensitive Detection of Cancer Cells Using Aptamer-DNA Concatamer-Quantum Dots Probes. *Anal. Chem.* **2013**, *85*, 3385−3392.
(17) Li, M.; Wang, Q.; Shi, X.; Hornak, L. A.; Wu, N. Detection of Mercury (II) by Quantum Dot/DNA/Gold Nanoparticle Ensemble based Nanosensor via Nanometal Surface Energy Transfer. *Anal. Chem.* **2011**, *83*, 7061−7065.
(18) Wegner, K. D.; Lindén, S.; Jin, Z.; Jennings, T. L.; Khoulati, R. e.; van Bergen en Henegouwen, P. M.; Hildebrandt, N. Nanobodies and Nanocrystals: Highly Sensitive Quantum Dot-Based Homogeneous FRET Immunoassay for Serum-Based EGFR Detection. *Small* **2014**, *10*, 734−740.
(19) Cassette, E.; Helle, M.; Bezdetnaya, L.; Marchal, F.; Dubertret, B.; Pons, T. Design of New Quantum Dot Materials for Deep Tissue Infrared Imaging. *Adv. Drug Delivery Rev.* **2013**, *65*, 719−731.
(20) Sasaki, A.; Tsukasaki, Y.; Komatsuzaki, A.; Sakata, T.; Yasuda, H.; Jin, T. Recombinant Protein (EGFP-Protein G)-Coated PbS Quantum Dots for *in vitro* and *in vivo* Dual Fluorescence (Visible and Second-NIR) Imaging of Breast Tumor. *Nanoscale* **2015**, *7*, 5115−5119.
(21) Hong, G.; Robinson, J. T.; Zhang, Y.; Diao, S.; Antaris, A. L.; Wang, Q.; Dai, H. *In vivo* Fluorescence Imaging with Ag_2S Quantum Dots in the Second Near-Infrared Region. *Angew. Chem., Int. Ed.* **2012**, *51*, 9818−9821.
(22) Tan, L.; Wan, A.; Zhao, T.; Huang, R.; Li, H. Aqueous Synthesis of Multidentate-Polymer-Capping Ag_2Se Quantum Dots with Bright Photoluminescence Tunable in a Second Near-Infrared Biological Window. *ACS Appl. Mater. Interfaces* **2014**, *6*, 6217−6222.
(23) Zrazhevskiy, P.; True, L. D.; Gao, X. Multicolor Multicycle Molecular Profiling with Quantum Dots for Single-Cell Analysis. *Nat. Protoc.* **2013**, *8*, 1852−1869.
(24) Probst, C. E.; Zrazhevskiy, P.; Bagalkot, V.; Gao, X. Quantum Dots As a Platform for Nanoparticle Drug Delivery Vehicle Design. *Adv. Drug Delivery Rev.* **2013**, *65*, 703−718.
(25) Zheng, F.; Zhang, P.; Xi, Y.; Chen, J.; Li, L.; Zhu, J.-J. Aptamer/Graphene Quantum Dots Nanocomposite Capped Fluorescent Mesoporous Silica Nanoparticles for Intracellular Drug Delivery and Real-time Monitoring of Drug Release. *Anal. Chem.* **2015**, *87*, 11739−11745.
(26) Torchilin, V. P. Multifunctional, Stimuli-Sensitive Nanoparticulate Systems for Drug Delivery. *Nat. Rev. Drug Discovery* **2014**, *13*, 813−827.
(27) Bruneau, A.; Fortier, M.; Gagne, F.; Gagnon, C.; Turcotte, P.; Tayabali, A.; Davis, T. A.; Auffret, M.; Fournier, M. *In vitro* Immunotoxicology of Quantum Dots and Comparison with Dissolved Cadmium and Tellurium. *Environ. Toxicol.* **2015**, *30*, 9−25.
(28) Pichaandi, J.; van Veggel, F. C. Near-Infrared Emitting Quantum Dots: Recent Progress on Their Synthesis and Characterization. *Coord. Chem. Rev.* **2014**, *263*−*264*, 138−150.
(29) Corazzari, I.; Gilardino, A.; Dalmazzo, S.; Fubini, B.; Lovisolo, D. Localization of CdSe/ZnS Quantum Dots in the Lysosomal Acidic Compartment of Cultured Neurons and Its Impact on Viability: Potential Role of Ion Release. *Toxicol. In Vitro* **2013**, *27*, 752−759.
(30) Li, K.; Chen, J.; Bai, S.; Wen, X.; Song, S.; Yu, Q.; Li, J.; Wang, Y. Intracellular Oxidative Stress and Cadmium Ions Release Induce Cytotoxicity of Unmodified Cadmium Sulfide Quantum Dots. *Toxicol. In Vitro* **2009**, *23*, 1007−1013.
(31) Yong, K.-T.; Law, W.-C.; Hu, R.; Ye, L.; Liu, L.; Swihart, M. T.; Prasad, P. N. Nanotoxicity Assessment of Quantum Dots: From Cellular to Primate Studies. *Chem. Soc. Rev.* **2013**, *42*, 1236−1250.
(32) Tsoi, K. M.; Dai, Q.; Alman, B. A.; Chan, W. C. Are Quantum Dots Toxic? Exploring the Discrepancy between Cell Culture and Animal Studies. *Acc. Chem. Res.* **2013**, *46*, 662−671.
(33) Tan, S. J.; Jana, N. R.; Gao, S.; Patra, P. K.; Ying, J. Y. Surface-Ligand-Dependent Cellular Interaction, Subcellular Localization, and Cytotoxicity of Polymer-Coated Quantum Dots. *Chem. Mater.* **2010**, *22*, 2239−2247.
(34) Johnson, C. M.; Pate, K. M.; Shen, Y.; Viswanath, A.; Tan, R.; Benicewicz, B. C.; Moss, M. A.; Greytak, A. B. A Methacrylate-based Polymeric Imidazole Ligand Yields Quantum Dots with Low Cytotoxicity and Low Nonspecific Binding. *J. Colloid Interface Sci.* **2015**, *458*, 310−314.
(35) Liu, L.; Yong, K.-T.; Roy, I.; Law, W.-C.; Ye, L.; Liu, J.; Liu, J.; Kumar, R.; Zhang, X.; Prasad, P. N. Bioconjugated Pluronic Triblock-Copolymer Micelle-Encapsulated Quantum Dots for Targeted Imaging of Cancer: *in vitro* and *in vivo* Studies. *Theranostics* **2012**, *2*, 705−713.
(36) Deng, D.; Chen, Y.; Cao, J.; Tian, J.; Qian, Z.; Achilefu, S.; Gu, Y. High-Quality $CuInS_2$/ZnS Quantum Dots for *in vitro* and *in vivo* Bioimaging. *Chem. Mater.* **2012**, *24*, 3029−3037.
(37) Hussain, S.; Won, N.; Nam, J.; Bang, J.; Chung, H.; Kim, S. One-Pot Fabrication of High-Quality InP/ZnS (Core/Shell) Quantum Dots and Their Application to Cellular Imaging. *ChemPhysChem* **2009**, *10*, 1466−1470.
(38) Erogbogbo, F.; Yong, K. T.; Roy, I.; Hu, R.; Law, W. C.; Zhao, W. W.; Ding, H.; Wu, F.; Kumar, R.; Swihart, M. T.; et al. *In vivo* Targeted Cancer Imaging, Sentinel Lymph Node Mapping and Multi-Channel Imaging with Biocompatible Silicon Nanocrystals. *ACS Nano* **2011**, *5*, 413−423.
(39) Gary, D. C.; Glassy, B. A.; Cossairt, B. M. Investigation of Indium Phosphide Quantum Dot Nucleation and Growth Utilizing Triarylsilylphosphine Precursors. *Chem. Mater.* **2014**, *26*, 1734−1744.
(40) Zan, F.; Ren, J. Gas-Liquid Phase Synthesis of Highly Luminescent InP/ZnS Core/Shell Quantum Dots Using Zinc Phosphide As a New Phosphorus Source. *J. Mater. Chem.* **2012**, *22*, 1794−1799.
(41) Liu, B. R.; Winiarz, J. G.; Moon, J.-S.; Lo, S.-Y.; Huang, Y.-W.; Aronstam, R. S.; Lee, H.-J. Synthesis, Characterization and Applications of Carboxylated and Polyethylene-Glycolated Bifunctionalized InP/ZnS Quantum Dots in Cellular Internalization Mediated by Cell-Penetrating Peptides. *Colloids Surf., B* **2013**, *111*, 162−170.
(42) Yong, K.-T.; Ding, H.; Roy, I.; Law, W.-C.; Bergey, E. J.; Maitra, A.; Prasad, P. N. Imaging Pancreatic Cancer Using Bioconjugated InP Quantum Dots. *ACS Nano* **2009**, *3* (3), 502−510.
(43) van der Stam, W.; Berends, A. C.; Rabouw, F. T.; Willhammar, T.; Ke, X.; Meeldijk, J. D.; Bals, S.; de Mello Donega, C. Luminescent $CuInS_2$ Quantum Dots by Partial Cation Exchange in $Cu_{2-x}S$ Nanocrystals. *Chem. Mater.* **2015**, *27*, 621−628.
(44) Speranskaya, E. S.; Beloglazova, N. V.; Abé, S.; Aubert, T.; Smet, P. F.; Poelman, D.; Goryacheva, I. Y.; De Saeger, S.; Hens, Z. Hydrophilic, Bright $CuInS_2$ Quantum Dots as Cd-free Fluorescent Labels in Quantitative Immunoassay. *Langmuir* **2014**, *30*, 7567−7575.
(45) Kang, X.; Huang, L.; Yang, Y.; Pan, D. Scaling up the Aqueous Synthesis of Visible Light Emitting Multinary AgInS2/ZnS Core/Shell Quantum Dots. *J. Phys. Chem. C* **2015**, *119*, 7933−7940.
(46) Chang, J.-Y.; Wang, G.-Q.; Cheng, C.-Y.; Lin, W.-X.; Hsu, J.-C. Strategies for Photoluminescence Enhancement of $AgInS_2$ Quantum Dots and Their Application as Bioimaging Probes. *J. Mater. Chem.* **2012**, *22*, 10609−10618.
(47) Chen, G.; Tian, F.; Zhang, Y.; Zhang, Y.; Li, C.; Wang, Q. Tracking of Transplanted Human Mesenchymal Stem Cells in Living Mice using Near-Infrared Ag_2S Quantum Dots. *Adv. Funct. Mater.* **2014**, *24*, 2481−2488.
(48) Geszke-Moritz, M.; Clavier, G.; Lulek, J.; Schneider, R. Copper- or Manganese-Doped ZnS Quantum Dots as Fluorescent Probes for Detecting Folic Acid in Aqueous Media. *J. Lumin.* **2012**, *132*, 987−991.

DOI: 10.1021/acs.chemrev.6b00290
Chem. Rev. 2016, 116, 12234−12327

(49) Rajesh, C.; Phadnis, C. V.; Sonawane, K. G.; Mahamuni, S. Synthesis and Optical Properties of Copper-Doped ZnSe Quantum Dots. *Phys. Scr.* **2015**, *90*, 015803−015803.
(50) Bacon, M.; Bradley, S. J.; Nann, T. Graphene Quantum Dots. *Part. Part. Syst. Charact.* **2014**, *31*, 415−428.
(51) Zhu, S.; Zhang, J.; Qiao, C.; Tang, S.; Li, Y.; Yuan, W.; Li, B.; Tian, L.; Liu, F.; Hu, R.; et al. Strongly Green-Photoluminescent Graphene Quantum Dots for Bioimaging Applications. *Chem. Commun.* **2011**, *47*, 6858−6860.
(52) Dey, S.; Govindaraj, A.; Biswas, K.; Rao, C. Luminescence Properties of Boron and Nitrogen Doped Graphene Quantum Dots Prepared from Arc-Discharge-Generated Doped Graphene Samples. *Chem. Phys. Lett.* **2014**, *595*−*596*, 203−208.
(53) Cheng, X.; Lowe, S. B.; Reece, P. J.; Gooding, J. J. Colloidal Silicon Quantum Dots: From Preparation to the Modification of Self-Assembled Monolayers (SAMs) for Bio-applications. *Chem. Soc. Rev.* **2014**, *43*, 2680−2700.
(54) He, Y.; Zhong, Y.; Peng, F.; Wei, X.; Su, Y.; Lu, Y.; Su, S.; Gu, W.; Liao, L.; Lee, S.-T. One-Pot Microwave Synthesis of Water-Dispersible, Ultraphoto-and pH-Stable, and Highly Fluorescent Silicon Quantum Dots. *J. Am. Chem. Soc.* **2011**, *133*, 14192−14195.
(55) Pisanic, T., II; Zhang, Y.; Wang, T. Quantum Dots in Diagnostics and Detection: Principles and Paradigms. *Analyst* **2014**, *139*, 2968−2981.
(56) Wang, Y.; Hu, R.; Lin, G.; Roy, I.; Yong, K.-T. Functionalized Quantum Dots for Biosensing and Bioimaging and Concerns on Toxicity. *ACS Appl. Mater. Interfaces* **2013**, *5*, 2786−2799.
(57) Wegner, K. D.; Hildebrandt, N. Quantum Dots: Bright and Versatile *in vitro* and *in vivo* Fluorescence Imaging Biosensors. *Chem. Soc. Rev.* **2015**, *44*, 4792−4834.
(58) Cunha-Reis, C.; El Haj, A. J.; Yang, X.; Yang, Y. Fluorescent Labeling of Chitosan for Use in Non-Invasive Monitoring of Degradation in Tissue Engineering. *J. Tissue Eng. Regener. Med.* **2013**, *7*, 39−50.
(59) Chen, G.; Ågren, H.; Ohulchanskyy, T. Y.; Prasad, P. N. Light Upconverting Core−Shell Nanostructures: Nanophotonic Control for Emerging Applications. *Chem. Soc. Rev.* **2015**, *44*, 1680−1713.
(60) Mattoussi, H.; Palui, G.; Na, H. B. Luminescent Quantum Dots as Platforms for Probing *in vitro* and *in vivo* Biological Processes. *Adv. Drug Delivery Rev.* **2012**, *64*, 138−166.
(61) Acharya, A. Luminescent Magnetic Quantum Dots for *in vitro*/*in vivo* Imaging and Applications in Therapeutics. *J. Nanosci. Nanotechnol.* **2013**, *13*, 3753−3768.
(62) Abdullah-Al-Nahain; In, I.; Lee, H.; Lee, K. D.; Jeong, J. H.; Park, S. Y.; Lee, J.-E. Target Delivery and Cell Imaging Using Hyaluronic Acid-Functionalized Graphene Quantum Dots. *Mol. Pharmaceutics* **2013**, *10*, 3736−3744.
(63) Minami, S. S.; Sun, B.; Popat, K.; Kauppinen, T.; Pleiss, M.; Zhou, Y.; Ward, M. E.; Floreancig, P.; Mucke, L.; Desai, T.; et al. Selective Targeting of Microglia by Quantum Dots. *J. Neuroinflammation* **2012**, *9*, 22−35.
(64) Li, J.; Liu, F.; Shao, Q.; Min, Y.; Costa, M.; Yeow, E. K.; Xing, B. Enzyme-Responsive Cell-Penetrating Peptide Conjugated Mesoporous Silica Quantum Dot Nanocarriers for Controlled Release of Nucleus-Targeted Drug Molecules and Real-Time Intracellular Fluorescence Imaging of Tumor Cells. *Adv. Healthcare Mater.* **2014**, *3*, 1230−1239.
(65) Erogbogbo, F.; Yong, K. T.; Roy, I.; Xu, G.; Prasad, P. N.; Swihart, M. T. Biocompatible Luminescent Silicon Quantum Dots for Imaging of Cancer Cells. *ACS Nano* **2008**, *2*, 873−878.
(66) Liu, J.-H.; Cao, L.; LeCroy, G. E.; Wang, P.; Meziani, M. J.; Dong, Y.; Liu, Y.; Luo, P. G.; Sun, Y.-P. Carbon "Quantum" Dots for Fluorescence Labeling of Cells. *ACS Appl. Mater. Interfaces* **2015**, *7*, 19439−19445.
(67) Aswathy, R. G.; Yoshida, Y.; Maekawa, T.; Kumar, D. S. Near-Infrared Quantum Dots for Deep Tissue Imaging. *Anal. Bioanal. Chem.* **2010**, *397*, 1417−1435.
(68) Wang, L.-W.; Peng, C.-W.; Chen, C.; Li, Y. Quantum Dots-based Tissue and *in vivo* Imaging in Breast Cancer Researches: Current Status and Future Perspectives. *Breast Cancer Res. Treat.* **2015**, *151*, 7−17.
(69) Markovic, Z. M.; Ristic, B. Z.; Arsikin, K. M.; Klisic, D. G.; Harhaji-Trajkovic, L. M.; Todorovic-Markovic, B. M.; Kepic, D. P.; Kravic-Stevovic, T. K.; Jovanovic, S. P.; Milenkovic, M. M.; et al. Graphene Quantum Dots as Autophagy-Inducing Photodynamic Agents. *Biomaterials* **2012**, *33*, 7084−7092.
(70) Ge, J.; Lan, M.; Zhou, B.; Liu, W.; Guo, L.; Wang, H.; Jia, Q.; Niu, G.; Huang, X.; Zhou, H.; et al. A Graphene Quantum Dot Photodynamic Therapy Agent with High Singlet Oxygen Generation. *Nat. Commun.* **2014**, *5*, 4596−4604.
(71) He, Y.; Wang, X.; Sun, J.; Jiao, S.; Chen, H.; Gao, F.; Wang, L. Fluorescent Blood Glucose Monitor by Hemin-Functionalized Graphene Quantum Dots based Sensing System. *Anal. Chim. Acta* **2014**, *810*, 71−78.
(72) Nigam, P.; Waghmode, S.; Louis, M.; Wangnoo, S.; Chavan, P.; Sarkar, D. Graphene Quantum Dots Conjugated Albumin Nanoparticles for Targeted Drug Delivery and Imaging of Pancreatic Cancer. *J. Mater. Chem. B* **2014**, *2*, 3190−3195.
(73) Carbary-Ganz, J. L.; Welge, W. A.; Barton, J. K.; Utzinger, U. *In vivo* Molecular Imaging of Colorectal Cancer Using Quantum Dots Targeted to Vascular Endothelial Growth Factor Receptor 2 and Optical Coherence Tomography/Laser-Induced Fluorescence Dual-Modality Imaging. *J. Biomed. Opt.* **2015**, *20*, 096015−096015.
(74) Hafian, H.; Sukhanova, A.; Turini, M.; Chames, P.; Baty, D.; Pluot, M.; Cohen, J. H.; Nabiev, I.; Millot, J.-M. Multiphoton Imaging of Tumor Biomarkers with Conjugates of Single-Domain Antibodies and Quantum Dots. *Nanomedicine* **2014**, *10*, 1701−1709.
(75) van Manen, H.-J.; Otto, C. Hybrid Confocal Raman Fluorescence Microscopy on Single Cells Using Semiconductor Quantum Dots. *Nano Lett.* **2007**, *7*, 1631−1636.
(76) Bharali, D. J.; Lucey, D. W.; Jayakumar, H.; Pudavar, H. E.; Prasad, P. N. Folate-Receptor-Mediated Delivery of InP Quantum Dots for Bioimaging Using Confocal and Two-Photon Microscopy. *J. Am. Chem. Soc.* **2005**, *127*, 11364−11371.
(77) Soenen, S. J.; Manshian, B. B.; Aubert, T.; Himmelreich, U.; Demeester, J.; De Smedt, S. C.; Hens, Z.; Braeckmans, K. Cytotoxicity of Cadmium-Free Quantum Dots and Their Use in Cell Bioimaging. *Chem. Res. Toxicol.* **2014**, *27*, 1050−1059.
(78) Qin, Y.; Zhou, Z.-W.; Pan, S.-T.; He, Z.-X.; Zhang, X.; Qiu, J.-X.; Duan, W.; Yang, T.; Zhou, S.-F. Graphene Quantum Dots Induce Apoptosis, Autophagy, and Inflammatory Response via p38 Mitogen-Activated Protein Kinase and Nuclear Factor-κB Mediated Signaling Pathways in Activated THP-1 Macrophages. *Toxicology* **2015**, *327*, 62−76.
(79) Kara, A.; Ünak, P.; Selçuki, C.; Akça, Ö.; Medine, E. İ.; Sakarya, S. PHA-L Lectin and Carbohydrate Relationship: Conjugation with CdSe/CdS Nanoparticles, Radiolabeling and *in vitro* Affinities on MCF-7 cells. *J. Radioanal. Nucl. Chem.* **2014**, *299*, 807−813.
(80) Lee, D.-E.; Koo, H.; Sun, I.-C.; Ryu, J. H.; Kim, K.; Kwon, I. C. Multifunctional Nanoparticles for Multimodal Imaging and Theragnosis. *Chem. Soc. Rev.* **2012**, *41*, 2656−2672.
(81) Ding, X.; Liow, C. H.; Zhang, M.; Huang, R.; Li, C.; Shen, H.; Liu, M.; Zou, Y.; Gao, N.; Zhang, Z.; et al. Surface Plasmon Resonance Enhanced Light Absorption and Photothermal Therapy in the Second Near-Infrared Window. *J. Am. Chem. Soc.* **2014**, *136*, 15684−15693.
(82) Wu, Q.; Chen, L.; Huang, L.; Wang, J.; Liu, J.; Hu, C.; Han, H. Quantum Dots Decorated Gold Nanorod as Fluorescent-Plasmonic Dual-Modal Contrasts Agent for Cancer Imaging. *Biosens. Bioelectron.* **2015**, *74*, 16−23.
(83) Shi, Y.; Pan, Y.; Zhong, J.; Yang, J.; Zheng, J.; Cheng, J.; Song, R.; Yi, C. Facile Synthesis of Gadolinium (III) Chelates Functionalized Carbon Quantum Dots for Fluorescence and Magnetic Resonance Dual-Modal Bioimaging. *Carbon* **2015**, *93*, 742−750.
(84) Chen, G.; Roy, I.; Yang, C.; Prasad, P. N. Nanochemistry and Nanomedicine for Nanoparticle-based Diagnostics and Therapy. *Chem. Rev.* **2016**, *116*, 2826−2885.

DOI: 10.1021/acs.chemrev.6b00290
Chem. Rev. 2016, 116, 12234−12327

(85) Farokhzad, O. C.; Langer, R. Nanomedicine: Developing Smarter Therapeutic and Diagnostic Modalities. *Adv. Drug Delivery Rev.* **2006**, *58*, 1456−1459.
(86) Rizzo, L. Y.; Theek, B.; Storm, G.; Kiessling, F.; Lammers, T. Recent Progress in Nanomedicine: Therapeutic, Diagnostic and Theranostic Applications. *Curr. Opin. Biotechnol.* **2013**, *24*, 1159−1166.
(87) Caruso, F.; Hyeon, T.; Rotello, V. M. Nanomedicine. *Chem. Soc. Rev.* **2012**, *41*, 2537−2538.
(88) Boisseau, P.; Loubaton, B. Nanomedicine, Nanotechnology in Medicine. *C. R. Phys.* **2011**, *12*, 620−636.
(89) Singh, S.; Sharma, A.; Robertson, G. P. Realizing the Clinical Potential of Cancer Nanotechnology by Minimizing Toxicologic and Targeted Delivery Concerns. *Cancer Res.* **2012**, *72*, 5663−5668.
(90) Bakalova, R.; Lazarova, D.; Nikolova, B.; Atanasova, S.; Zlateva, G.; Zhelev, Z.; Aoki, I. Delivery of Size-Controlled Long-Circulating Polymersomes in Solid Tumours, Visualized by Quantum Dots and Optical Imaging *in vivo*. *Biotechnol. Biotechnol. Equip.* **2015**, *29*, 175−180.
(91) Guo, W.; Chen, N.; Tu, Y.; Dong, C.; Zhang, B.; Hu, C.; Chang, J. Synthesis of Zn-Cu-In-S/ZnS Core/Shell Quantum Dots with Inhibited Blue-Shift Photoluminescence and Applications for Tumor Targeted Bioimaging. *Theranostics* **2013**, *3*, 99−108.
(92) Zhang, M.-Z.; Yu, R.-N.; Chen, J.; Ma, Z.-Y.; Zhao, Y.-D. Targeted Quantum Dots Fluorescence Probes Functionalized with Aptamer and Peptide for Transferrin Receptor on Tumor Cells. *Nanotechnology* **2012**, *23*, 485104−485104.
(93) Erogbogbo, F.; Chang, C.-W.; May, J. L.; Liu, L.; Kumar, R.; Law, W.-C.; Ding, H.; Yong, K. T.; Roy, I.; Sheshadri, M.; et al. Bioconjugation of Luminescent Silicon Quantum Dots to Gadolinium Ions for Bioimaging Applications. *Nanoscale* **2012**, *4*, 5483−5489.
(94) Liu, Y.; Ai, K.; Yuan, Q.; Lu, L. Fluorescence-Enhanced Gadolinium-Doped Zinc Oxide Quantum Dots for Magnetic Resonance and Fluorescence Imaging. *Biomaterials* **2011**, *32*, 1185−1192.
(95) Guo, W.; Sun, X.; Jacobson, O.; Yan, X.; Min, K.; Srivatsan, A.; Niu, G.; Kiesewetter, D. O.; Chang, J.; Chen, X. Intrinsically Radioactive ^{64}Cu CuInS/ZnS Quantum Dots for PET and Optical Imaging: Improved Radiochemical Stability and Controllable Cerenkov Luminescence. *ACS Nano* **2015**, *9*, 488−495.
(96) Tu, C.; Ma, X.; House, A.; Kauzlarich, S. M.; Louie, A. Y. PET Imaging and Biodistribution of Silicon Quantum Dots in Mice. *ACS Med. Chem. Lett.* **2011**, *2*, 285−288.
(97) Singh, S. P. Multifunctional Magnetic Quantum Dots for Cancer Theranostics. *J. Biomed. Nanotechnol.* **2011**, *7*, 95−97.
(98) Xia, H.-X.; Yang, X.-Q.; Song, J.-T.; Chen, J.; Zhang, M.-Z.; Yan, D.-M.; Zhang, L.; Qin, M.-Y.; Bai, L.-Y.; Zhao, Y.-D.; et al. Folic Acid-Conjugated Silica-Coated Gold Nanorods and Quantum Dots for Dual-Modality CT and Fluorescence Imaging and Photothermal Therapy. *J. Mater. Chem. B* **2014**, *2*, 1945−1953.
(99) Huang, C.-L.; Huang, C.-C.; Mai, F.-D.; Yen, C.-L.; Tzing, S.-H.; Hsieh, H.-T.; Ling, Y.-C.; Chang, J.-Y. Application of Paramagnetic Graphene Quantum Dots as a Platform for Simultaneous Dual-Modality Bioimaging and Tumor-Targeted Drug Delivery. *J. Mater. Chem. B* **2015**, *3*, 651−664.
(100) Chen, T.; Zhao, T.; Wei, D.; Wei, Y.; Li, Y.; Zhang, H. Core−Shell Nanocarriers with ZnO Quantum Dots-Conjugated Au Nanoparticle for Tumor-Targeted Drug Delivery. *Carbohydr. Polym.* **2013**, *92*, 1124−1132.
(101) Chang, Y.-M.; Shieh, J.; Chu, P.-Y.; Lee, H.-Y.; Lin, C.-M.; Juang, J.-Y. Enhanced Free Exciton and Direct Band-Edge Emissions at Room Temperature in Ultrathin ZnO Films Grown on Si Nanopillars by Atomic Layer Deposition. *ACS Appl. Mater. Interfaces* **2011**, *3*, 4415−4419.
(102) Gurinovich, L.; Gurin, V.; Ivanov, V.; Bodnar, I.; Molochko, A.; Solovej, N. Crystal Structure and Optical Properties of $CuInS_2$ Nanocrystals in a Glass Matrix. *Phys. Status Solidi B* **1998**, *208*, 533−540.
(103) Zhao, N.; Qi, L. Low-Temperature Synthesis of Star-Shaped PbS Nanocrystals in Aqueous Solutions of Mixed Cationic/Anionic Surfactants. *Adv. Mater.* **2006**, *18*, 359−362.
(104) Lipovskii, A.; Kolobkova, E.; Petrikov, V.; Kang, I.; Olkhovets, A.; Krauss, T.; Thomas, M.; Silcox, J.; Wise, F.; Shen, Q.; et al. Synthesis and Characterization of PbSe Quantum Dots in Phosphate Glass. *Appl. Phys. Lett.* **1997**, *71*, 3406−3408.
(105) Kayanuma, Y. Quantum-Size Effects of Interacting Electrons and Holes in Semiconductor Microcrystals with Spherical Shape. *Phys. Rev. B: Condens. Matter Mater. Phys.* **1988**, *38*, 9797−9805.
(106) Bellessa, J.; Voliotis, V.; Grousson, R.; Wang, X.; Ogura, M.; Matsuhata, H. Quantum-Size Effects on Radiative Lifetimes and Relaxation of Excitons in Semiconductor Nanostructures. *Phys. Rev. B: Condens. Matter Mater. Phys.* **1998**, *58*, 9933−9940.
(107) Norris, D.; Bawendi, M. Measurement and Assignment of the Size-Dependent Optical Spectrum in CdSe Quantum Dots. *Phys. Rev. B: Condens. Matter Mater. Phys.* **1996**, *53*, 16338−16346.
(108) Wise, F. W. Lead Salt Quantum Dots: The Limit of Strong Quantum Confinement. *Acc. Chem. Res.* **2000**, *33*, 773−780.
(109) Brus, L. E. Electron-Electron and Electron-Hole Interactions in Small Semiconductor Crystallites: The Size Dependence of the Lowest Excited Electronic State. *J. Chem. Phys.* **1984**, *80*, 4403−4409.
(110) Bawendi, M. G.; Steigerwald, M. L.; Brus, L. E. The Quantum Mechanics of Larger Semiconductor Clusters ("Quantum Dots"). *Annu. Rev. Phys. Chem.* **1990**, *41*, 477−496.
(111) Mirzaei, J.; Reznikov, M.; Hegmann, T. Quantum Dots as Liquid Crystal Dopants. *J. Mater. Chem.* **2012**, *22*, 22350−22365.
(112) Ediger, M.; Bester, G.; Gerardot, B.; Badolato, A.; Petroff, P.; Karrai, K.; Zunger, A.; Warburton, R. Fine Structure of Negatively and Positively Charged Excitons in Semiconductor Quantum Dots: Electron-Hole Asymmetry. *Phys. Rev. Lett.* **2007**, *98*, 036808.
(113) Ribeiro, F.; Latge, A.; Pacheco, M.; Barticevic, Z. Quantum Dots under Electric and Magnetic Fields: Impurity-Related Electronic Properties. *J. Appl. Phys.* **1997**, *82*, 270−274.
(114) Karabulut, I.; Baskoutas, S. Linear and Nonlinear Optical Absorption Coefficients and Refractive Index Changes in Spherical Quantum Dots: Effects of Impurities, Electric Field, Size, and Optical Intensity. *J. Appl. Phys.* **2008**, *103*, 073512−073512.
(115) Gan, C.; Zhang, Y.; Battaglia, D.; Peng, X.; Xiao, M. Fluorescence Lifetime of Mn-Doped ZnSe Quantum Dots with Size Dependence. *Appl. Phys. Lett.* **2008**, *92*, 241111−241111.
(116) Komarala, V. K.; Xie, C.; Wang, Y.; Xu, J.; Xiao, M. Time-Resolved Photoluminescence Properties of $CuInS_2$/ZnS Nanocrystals: Influence of Intrinsic Defects and External Impurities. *J. Appl. Phys.* **2012**, *111*, 124314−124314.
(117) Wen, X.; Yu, P.; Toh, Y.-R.; Ma, X.; Tang, J. On the Upconversion Fluorescence in Carbon Nanodots and Graphene Quantum Dots. *Chem. Commun.* **2014**, *50*, 4703−4706.
(118) Tu, C.; Ma, X.; Pantazis, P.; Kauzlarich, S. M.; Louie, A. Y. Paramagnetic, Silicon Quantum Dots for Magnetic Resonance and Two-Photon Imaging of Macrophages. *J. Am. Chem. Soc.* **2010**, *132*, 2016−2023.
(119) Geszke, M.; Murias, M.; Balan, L.; Medjahdi, G.; Korczynski, J.; Moritz, M.; Lulek, J.; Schneider, R. Folic Acid-Conjugated Core/Shell ZnS:Mn/ZnS Quantum Dots as Targeted Probes for Two Photon Fluorescence Imaging of Cancer Cells. *Acta Biomater.* **2011**, *7*, 1327−1338.
(120) Deutsch, Z.; Avidan, A.; Pinkas, I.; Oron, D. Energetics and Dynamics of Exciton-Exciton Interactions in Compound Colloidal Semiconductor Quantum Dots. *Phys. Chem. Chem. Phys.* **2011**, *13*, 3210−3219.
(121) Acharya, K. P.; Nguyen, H. M.; Paulite, M.; Piryatinski, A.; Zhang, J.; Casson, J. L.; Xu, H.; Htoon, H.; Hollingsworth, J. A. Elucidation of Two Giants: Challenges to Thick-Shell Synthesis in CdSe/ZnSe and ZnSe/CdS Core/Shell Quantum Dots. *J. Am. Chem. Soc.* **2015**, *137*, 3755−3758.
(122) Chen, C.-W.; Wu, D.-Y.; Chan, Y.-C.; Lin, C. C.; Chung, P.-H.; Hsiao, M.; Liu, R.-S. Evaluations of the Chemical Stability and

DOI: 10.1021/acs.chemrev.6b00290
Chem. Rev. 2016, 116, 12234−12327

Cytotoxicity of $CuInS_2$ and $CuInS_2$/ZnS Core/Shell Quantum Dots. *J. Phys. Chem. C* **2015**, *119*, 2852−2860.
(123) Kim, S.; Fisher, B.; Eisler, H.-J.; Bawendi, M. Type-II Quantum Dots: CdTe/CdSe (Core/Shell) and CdSe/ZnTe (Core/Shell) Heterostructures. *J. Am. Chem. Soc.* **2003**, *125*, 11466−11467.
(124) Bang, J.; Park, J.; Lee, J. H.; Won, N.; Nam, J.; Lim, J.; Chang, B. Y.; Lee, H. J.; Chon, B.; Shin, J.; et al. ZnTe/ZnSe (Core/Shell) Type-II Quantum Dots: Their Optical and Photovoltaic Properties. *Chem. Mater.* **2010**, *22*, 233−240.
(125) Song, Y.; Li, Y.; Wang, X.; Su, X.; Ma, Q. Novel Aqueous Synthesis Methods for ZnTe/ZnSe and Mn^{2+}-Doped ZnTe/ZnSe Type-II Core/Shell Quantum Dots. *RSC Adv.* **2015**, *5*, 6271−6278.
(126) Tyrakowski, C. M.; Shamirian, A.; Rowland, C. E.; Shen, H.; Das, A.; Schaller, R. D.; Snee, P. T. Bright Type II Quantum Dots. *Chem. Mater.* **2015**, *27*, 7276−7281.
(127) Soni, U.; Pal, A.; Singh, S.; Mittal, M.; Yadav, S.; Elangovan, R.; Sapra, S. Simultaneous Type-I/Type-II Emission from CdSe/CdS/ZnSe Nano-Heterostructures. *ACS Nano* **2014**, *8*, 113−123.
(128) Smith, A. M.; Mohs, A. M.; Nie, S. Tuning the Optical and Electronic Properties of Colloidal Nanocrystals by Lattice Strain. *Nat. Nanotechnol.* **2009**, *4*, 56−63.
(129) Liu, C.; Mu, L.; Jia, J.; Zhou, X.; Lin, Y. Boosting the Cell Efficiency of CdSe Quantum Dot Sensitized Solar Cell Via a Modified ZnS Post-Treatment. *Electrochim. Acta* **2013**, *111*, 179−184.
(130) Reiss, P.; Protiere, M.; Li, L. Core/Shell Semiconductor Nanocrystals. *Small* **2009**, *5*, 154−168.
(131) Ippen, C.; Greco, T.; Wedel, A. InP/ZnSe/ZnS: A Novel Multishell System for InP Quantum Dots for Improved Luminescence Efficiency and Its application in a Light-Emitting Device. *J. Inf. Disp.* **2012**, *13*, 91−95.
(132) Smith, A. M.; Mancini, M. C.; Nie, S. Bioimaging: Second Window for *in vivo* Imaging. *Nat. Nanotechnol.* **2009**, *4*, 710−711.
(133) Dai, M.; Ogawa, S.; Kameyama, T.; Okazaki, K.-i.; Kudo, A.; Kuwabata, S.; Tsuboi, Y.; Torimoto, T. Tunable Photoluminescence From the Visible to Near-Infrared Wavelength Region of Non-Stoichiometric $AgInS_2$ Nanoparticles. *J. Mater. Chem.* **2012**, *22*, 12851−12858.
(134) Chen, B.; Zhong, H.; Zhang, W.; Tan, Z. a.; Li, Y.; Yu, C.; Zhai, T.; Bando, Y.; Yang, S.; Zou, B. Highly Emissive and Color-Tunable $CuInS_2$-Based Colloidal Semiconductor Nanocrystals: Off-Stoichiometry Effects and Improved Electroluminescence Performance. *Adv. Funct. Mater.* **2012**, *22*, 2081−2088.
(135) Li, L.; Pandey, A.; Werder, D. J.; Khanal, B. P.; Pietryga, J. M.; Klimov, V. I. Efficient Synthesis of Highly Luminescent Copper Indium Sulfide-based Core/Shell Nanocrystals with Surprisingly Long-Lived Emission. *J. Am. Chem. Soc.* **2011**, *133*, 1176−1179.
(136) Cassette, E.; Pons, T.; Bouet, C.; Helle, M.; Bezdetnaya, L.; Marchal, F.; Dubertret, B. Synthesis and Characterization of Near-Infrared Cu−In−Se/ZnS Core/Shell Quantum Dots for *in vivo* Imaging. *Chem. Mater.* **2010**, *22*, 6117−6124.
(137) Deng, D.; Qu, L.; Zhang, J.; Ma, Y.; Gu, Y. Quaternary Zn−Ag−In−Se Quantum Dots for Biomedical Optical Imaging of RGD-Modified Micelles. *ACS Appl. Mater. Interfaces* **2013**, *5*, 10858−10865.
(138) Jiang, P.; Tian, Z.-Q.; Zhu, C.-N.; Zhang, Z.-L.; Pang, D.-W. Emission-Tunable Near-Infrared Ag_2S Quantum Dots. *Chem. Mater.* **2012**, *24*, 3−5.
(139) Dong, B.; Li, C.; Chen, G.; Zhang, Y.; Zhang, Y.; Deng, M.; Wang, Q. Facile Synthesis of Highly Photoluminescent Ag_2Se Quantum Dots as a New Fluorescent Probe in the Second Near-Infrared Window for *in vivo* Imaging. *Chem. Mater.* **2013**, *25*, 2503−2509.
(140) Luther, J. M.; Jain, P. K.; Ewers, T.; Alivisatos, A. P. Localized Surface Plasmon Resonances Arising From Free Carriers in Doped Quantum Dots. *Nat. Mater.* **2011**, *10*, 361−366.
(141) Faucheaux, J. A.; Stanton, A. L. D.; Jain, P. K. Plasmon Resonances of Semiconductor Nanocrystals: Physical Principles and New Opportunities. *J. Phys. Chem. Lett.* **2014**, *5*, 976−985.
(142) Kriegel, I.; Jiang, C. Y.; Rodriguez-Fernandez, J.; Schaller, R. D.; Talapin, D. V.; da Como, E.; Feldmann, J. Tuning the Excitonic and Plasmonic Properties of Copper Chalcogenide Nanocrystals. *J. Am. Chem. Soc.* **2012**, *134*, 1583−1590.
(143) Cooper, J. K.; Gul, S.; Lindley, S. A.; Yano, J.; Zhang, J. Z. Tunable Photoluminescent Core/Shell Cu^+-Doped ZnSe/ZnS Quantum Dots Codoped with Al^{3+}, Ga^{3+}, or In^{3+}. *ACS Appl. Mater. Interfaces* **2015**, *7*, 10055−10066.
(144) Zeng, R.; Shen, R.; Zhao, Y.; Sun, Z.; Li, X.; Zheng, J.; Cao, S.; Zou, B. Water-Soluble, Highly Emissive, Color-Tunable, and Stable Cu-Doped ZnSeS/ZnS Core/Shell Nanocrystals. *CrystEngComm* **2014**, *16*, 3414−3423.
(145) Tarantino, U.; Fanucci, E.; Iundusi, R.; Celi, M.; Altobelli, S.; Gasbarra, E.; Simonetti, G.; Manenti, G. Lumbar Spine MRI in Upright Position for Diagnosing Acute and Chronic Low Back Pain: Statistical Analysis of Morphological Changes. *J. Orthop. Traumatol.* **2013**, *14*, 15−22.
(146) Li, H.; Hosseini, A.; Li, J.-S.; Gill, T. J., IV; Li, G. Quantitative Magnetic Resonance Imaging (MRI) Morphological Analysis of Knee Cartilage in Healthy and Anterior Cruciate Ligament-Injured Knees. *Knee Surg. Sports Traumatol. Arthrosc.* **2012**, *20*, 1496−1502.
(147) Hart, H., Jr; Bottomley, P.; Edelstein, W.; Karr, S.; Leue, W.; Mueller, O.; Redington, R.; Schenck, J.; Smith, L.; Vatis, D. Nuclear Magnetic Resonance Imaging: Contrast-To-Noise Ratio as a Function of Strength of Magnetic Field. *AJR, Am. J. Roentgenol.* **1983**, *141*, 1195−1201.
(148) Hashemi, R. H.; Bradley, W. G.; Lisanti, C. J. *MRI: The Basics*; Lippincott Williams & Wilkins: Philadelphia, 2012.
(149) Ogawa, M.; Regino, C. A.; Marcelino, B.; Williams, M.; Kosaka, N.; Bryant, L. H., Jr; Choyke, P. L.; Kobayashi, H. New Nanosized Biocompatible MR Contrast Agents based on Lysine-Dendri-Graft Macromolecules. *Bioconjugate Chem.* **2010**, *21*, 955−960.
(150) Rohrer, M.; Bauer, H.; Mintorovitch, J.; Requardt, M.; Weinmann, H.-J. Comparison of Magnetic Properties of MRI Contrast Media Solutions at Different Magnetic Field Strengths. *Invest. Radiol.* **2005**, *40*, 715−724.
(151) Wang, Y.; Yang, C.; Hu, R.; Toh, H. T.; Liu, X.; Lin, G.; Yin, F.; Yoon, H. S.; Yong, K.-T. Assembling Mn:ZnSe Quantum Dots-siRNA Nanoplexes for Gene Silencing in Tumor Cells. *Biomater. Sci.* **2015**, *3*, 192−202.
(152) Zhang, X.; Brynda, M.; Britt, R. D.; Carroll, E. C.; Larsen, D. S.; Louie, A. Y.; Kauzlarich, S. M. Synthesis and Characterization of Manganese-Doped Silicon Nanoparticles: Bifunctional Paramagnetic-Optical Nanomaterial. *J. Am. Chem. Soc.* **2007**, *129*, 10668−10669.
(153) Wang, Y.; Wu, B.; Yang, C.; Liu, M.; Sum, T. C.; Yong, K. T. Synthesis and Characterization of Mn: ZnSe/ZnS/ZnMnS Sandwiched QDs for Multimodal Imaging and Theranostic Applications. *Small* **2016**, *12*, 534−546.
(154) Jahanbin, T.; Gaceur, M.; Gros-Dagnac, H.; Benderbous, S.; Merah, S. A. High Potential of Mn-Doped ZnS Nanoparticles with Different Dopant Concentrations as Novel MRI Contrast Agents: Synthesis and *in vitro* Relaxivity Studies. *J. Nanopart. Res.* **2015**, *17*, 258.
(155) Lin, B.; Yao, X.; Zhu, Y.; Shen, J.; Yang, X.; Jiang, H.; Zhang, X. Multifunctional Manganese-Doped Core−Shell Quantum Dots for Magnetic Resonance and Fluorescence Imaging of Cancer Cells. *New J. Chem.* **2013**, *37*, 3076−3083.
(156) Ding, K.; Jing, L.; Liu, C.; Hou, Y.; Gao, M. Magnetically Engineered Cd-free Quantum Dots as Dual-Modality Probes for Fluorescence/Magnetic Resonance Imaging of Tumors. *Biomaterials* **2014**, *35*, 1608−1617.
(157) Yang, W.; Guo, W.; Gong, X.; Zhang, B.; Wang, S.; Chen, N.; Yang, W.; Tu, Y.; Fang, X.; Chang, J. Facile Synthesis of Gd−Cu−In−S/ZnS Bimodal Quantum Dots with Optimized Properties for Tumor Targeted Fluorescence/MR *In vivo* Imaging. *ACS Appl. Mater. Interfaces* **2015**, *7*, 18759−18768.
(158) Zheng, Y.; Zou, Y.; Jiang, J. Synthesis of Gd-Doped $CuInS_2$ Quantum Dots Exhibiting Photoluminescence and High Longitudinal Relaxivity. *Mater. Lett.* **2016**, *168*, 86−89.
(159) Sitbon, G.; Bouccara, S.; Tasso, M.; Francois, A.; Bezdetnaya, L.; Marchal, F.; Beaumont, M.; Pons, T. Multimodal Mn-Doped I−

DOI: 10.1021/acs.chemrev.6b00290
Chem. Rev. 2016, 116, 12234−12327

III−VI Quantum Dots for Near Infrared Fluorescence and Magnetic Resonance Imaging: From Synthesis to *in vivo* Application. *Nanoscale* **2014**, *6*, 9264−9272.
(160) Xu, S.; Ziegler, J.; Nann, T. Rapid Synthesis of Highly Luminescent InP and InP/ZnS Nanocrystals. *J. Mater. Chem.* **2008**, *18*, 2653−2656.
(161) Tessier, M. D.; Dupont, D.; De Nolf, K.; De Roo, J.; Hens, Z. Economic and Size-Tunable Synthesis of InP/ZnE (E = S, Se) Colloidal Quantum Dots. *Chem. Mater.* **2015**, *27*, 4893−4898.
(162) Liu, S.; Zhang, H.; Qiao, Y.; Su, X. One-Pot Synthesis of Ternary $CuInS_2$ Quantum Dots with Near-Infrared Fluorescence in Aqueous Solution. *RSC Adv.* **2012**, *2*, 819−825.
(163) Li, L.; Daou, T. J.; Texier, I.; Kim Chi, T. T.; Liem, N. Q.; Reiss, P. Highly Luminescent $CuInS_2$/ZnS Core/Shell Nanocrystals: Cadmium-Free Quantum Dots for *In vivo* Imaging. *Chem. Mater.* **2009**, *21*, 2422−2429.
(164) Li, S.; Chen, Y.; Huang, L.; Pan, D. Simple Continuous-Flow Synthesis of Cu-In-Zn-S/ZnS and Ag-In-Zn-S/ZnS Core/Shell Quantum Dots. *Nanotechnology* **2013**, *24*, 395705−395705.
(165) Chen, Y.; Li, S.; Huang, L.; Pan, D. Green and Facile Synthesis of Water-Soluble Cu−In−S/ZnS Core/Shell Quantum Dots. *Inorg. Chem.* **2013**, *52*, 7819−7921.
(166) Xiong, W. W.; Yang, G. H.; Wu, X. C.; Zhu, J. J. Aqueous Synthesis of Color-Tunable $CuInS_2$/ZnS Nanocrystals for the Detection of Human Interleukin 6. *ACS Appl. Mater. Interfaces* **2013**, *5*, 8210−8216.
(167) Ogawa, T.; Kuzuya, T.; Hamanaka, Y.; Sumiyama, K. Synthesis of Ag−In Binary Sulfide Nanoparticles—Structural Tuning and Their Photoluminescence Properties. *J. Mater. Chem.* **2010**, *20*, 2226−2231.
(168) Hamanaka, Y.; Ozawa, K.; Kuzuya, T. Enhancement of Donor-Acceptor Pair Emissions in Colloidal $AgInS_2$ Quantum Dots with High Concentrations of Defects. *J. Phys. Chem. C* **2014**, *118*, 14562−14568.
(169) Mao, B.; Chuang, C.-H.; McCleese, C.; Zhu, J.; Burda, C. Near-Infrared Emitting $AgInS_2$/ZnS Nanocrystals. *J. Phys. Chem. C* **2014**, *118*, 13883−13889.
(170) Torimoto, T.; Adachi, T.; Okazaki, K.-i.; Sakuraoka, M.; Shibayama, T.; Ohtani, B.; Kudo, A.; Kuwabata, S. Facile Synthesis of ZnS−$AgInS_2$ Solid Solution Nanoparticles for a Color-Adjustable Luminophore. *J. Am. Chem. Soc.* **2007**, *129*, 12388−12389.
(171) Subramaniam, P.; Lee, S. J.; Shah, S.; Patel, S.; Starovoytov, V.; Lee, K. B. Generation of a Library of Non-Toxic Quantum Dots for Cellular Imaging and siRNA Delivery. *Adv. Mater.* **2012**, *24*, 4014−4019.
(172) Zhao, Y.; Pan, H.; Lou, Y.; Qiu, X.; Zhu, J.; Burda, C. Plasmonic $Cu_{2-x}S$ Nanocrystals: Optical and Structural Properties of Copper-Deficient Copper(I) Sulfides. *J. Am. Chem. Soc.* **2009**, *131*, 4253−4261.
(173) Allen, P. M.; Bawendi, M. G. Ternary I−III−VI Quantum Dots Luminescent in the Red to Near-Infrared. *J. Am. Chem. Soc.* **2008**, *130*, 9240−9241.
(174) Li, C.; Zhang, Y.; Wang, M.; Zhang, Y.; Chen, G.; Li, L.; Wu, D.; Wang, Q. *In vivo* Real-Time Visualization of Tissue Blood Flow and Angiogenesis Using Ag_2S Quantum Dots in the NIR-II Window. *Biomaterials* **2014**, *35*, 393−400.
(175) Wang, C.; Gao, X.; Ma, Q.; Su, X. Aqueous Synthesis of Mercaptopropionic Acid Capped Mn^{2+}-Doped ZnSe Quantum Dots. *J. Mater. Chem.* **2009**, *19*, 7016−7022.
(176) Srivastava, B. B.; Jana, S.; Karan, N. S.; Paria, S.; Jana, N. R.; Sarma, D.; Pradhan, N. Highly Luminescent Mn-Doped ZnS Nanocrystals: Gram-Scale Synthesis. *J. Phys. Chem. Lett.* **2010**, *1*, 1454−1458.
(177) Kim, S.; Park, J.; Kim, T.; Jang, E.; Jun, S.; Jang, H.; Kim, B.; Kim, S.-W. Reverse Type-I ZnSe/InP/ZnS Core/Shell/Shell Nanocrystals: Cadmium-Free Quantum Dots for Visible Luminescence. *Small* **2011**, *7*, 70−73.
(178) Intartaglia, R.; Barchanski, A.; Bagga, K.; Genovese, A.; Das, G.; Wagener, P.; Di Fabrizio, E.; Diaspro, A.; Brandi, F.; Barcikowski, S. Bioconjugated Silicon Quantum Dots From One-Step Green Synthesis. *Nanoscale* **2012**, *4*, 1271−1274.
(179) Cheng, X.; Lowe, S. B.; Ciampi, S.; Magenau, A.; Gaus, K.; Reece, P. J.; Gooding, J. J. Versatile "Click Chemistry" Approach to Functionalizing Silicon Quantum Dots: Applications toward Fluorescent Cellular Imaging. *Langmuir* **2014**, *30*, 5209−5216.
(180) Sugimoto, H.; Fujii, M.; Fukuda, Y.; Imakita, K.; Akamatsu, K. All-Inorganic Water-Dispersible Silicon Quantum Dots: Highly Efficient Near-Infrared Luminescence in a Wide pH Range. *Nanoscale* **2014**, *6*, 122−126.
(181) Asok, A.; Gandhi, M. N.; Kulkarni, A. R. Enhanced Visible Photoluminescence in ZnO Quantum Dots by Promotion of Oxygen Vacancy Formation. *Nanoscale* **2012**, *4*, 4943−4946.
(182) Xiong, H.-M.; Xu, Y.; Ren, Q.-G.; Xia, Y.-Y. Stable Aqueous ZnO@Polymer Core−Shell Nanoparticles with Tunable Photoluminescence and Their Application in Cell Imaging. *J. Am. Chem. Soc.* **2008**, *130*, 7522−7523.
(183) Lin, L.; Xu, Y.; Zhang, S.; Ross, I. M.; Ong, A. C. M.; Allwood, D. A. Fabrication of Luminescent Monolayered Tungsten Dichalcogenides Quantum Dots with Giant Spin-Valley Coupling. *ACS Nano* **2013**, *7*, 8214−8223.
(184) Shen, J. H.; Zhu, Y. H.; Yang, X. L.; Zong, J.; Zhang, J. M.; Li, C. Z. One-Pot Hydrothermal Synthesis of Graphene Quantum Dots Surface-Passivated by Polyethylene Glycol and Their Photoelectric Conversion Under Near-Infrared Light. *New J. Chem.* **2012**, *36*, 97−101.
(185) Wu, X.; Tian, F.; Wang, W.; Chen, J.; Wu, M.; Zhao, J. X. Fabrication of Highly Fluorescent Graphene Quantum Dots Using L-Glutamic Acid for *in vitro*/*in vivo* Imaging and Sensing. *J. Mater. Chem. C* **2013**, *1*, 4676−4684.
(186) Mićić, O. I.; Sprague, J.; Lu, Z.; Nozik, A. J. Highly Efficient Band-Edge Emission From InP Quantum Dots. *Appl. Phys. Lett.* **1996**, *68*, 3150−3152.
(187) Fu, H.; Zunger, A. InP Quantum Dots: Electronic Structure, Surface Effects, and the Redshifted Emission. *Phys. Rev. B: Condens. Matter Mater. Phys.* **1997**, *56*, 1496−1508.
(188) Mićić, O. I.; Ahrenkiel, S. P.; Nozik, A. J. Synthesis of Extremely Small InP Quantum Dots and Electronic Coupling in Their Disordered Solid Films. *Appl. Phys. Lett.* **2001**, *78*, 4022−4024.
(189) Allen, P. M.; Walker, B. J.; Bawendi, M. G. Mechanistic Insights into the Formation of InP Quantum Dots. *Angew. Chem., Int. Ed.* **2010**, *49*, 760−762.
(190) Fan, G.; Wang, C.; Fang, J. Solution-based Synthesis of III−V Quantum Dots and Their Applications in Gas Sensing and Bio-Imaging. *Nano Today* **2014**, *9*, 69−84.
(191) Mićić, O. I.; Cheong, H. M.; Fu, H.; Zunger, A.; Sprague, J. R.; Mascarenhas, A.; Nozik, A. J. Size-Dependent Spectroscopy of InP Quantum Dots. *J. Phys. Chem. B* **1997**, *101*, 4904−4912.
(192) Biju, V.; Mundayoor, S.; Omkumar, R. V.; Anas, A.; Ishikawa, M. Bioconjugated Quantum Dots for Cancer Research: Present Status, Prospects and Remaining Issues. *Biotechnol. Adv.* **2010**, *28*, 199−213.
(193) Stasiuk, G. J.; Tamang, S.; Imbert, D.; Poillot, C.; Giardiello, M.; Tisseyre, C.; Barbier, E. L.; Fries, P. H.; de Waard, M.; Reiss, P.; et al. Cell-Permeable Ln(III) Chelate-Functionalized InP Quantum Dots As Multimodal Imaging Agents. *ACS Nano* **2011**, *5*, 8193−8201.
(194) Bain, L. E.; Ivanisevic, A. Engineering the Cell−Semiconductor Interface: A Materials Modification Approach using II-VI and III-V Semiconductor Materials. *Small* **2015**, *11*, 768−780.
(195) Narayanaswamy, A.; Feiner, L. F.; van der Zaag, P. J. Temperature Dependence of the Photoluminescence of InP/ZnS Quantum Dots. *J. Phys. Chem. C* **2008**, *112*, 6775−6780.
(196) Zhang, Z.; Liu, D.; Li, D.; Huang, K.; Zhang, Y.; Shi, Z.; Xie, R.; Han, M.-Y.; Wang, Y.; Yang, W. Dual Emissive Cu:InP/ZnS/InP/ZnS Nanocrystals: Single-Source "Greener" Emitters with Flexibly Tunable Emission from Visible to Near-Infrared and Their Application in White Light-Emitting Diodes. *Chem. Mater.* **2015**, *27*, 1405−1411.
(197) Thomas, A.; Nair, P. V.; George Thomas, K. InP Quantum Dots: An Environmentally Friendly Material with Resonance Energy Transfer Requisites. *J. Phys. Chem. C* **2014**, *118*, 3838−3845.
(198) Lin, Z.; Ma, Q.; Fei, X.; Zhang, H.; Su, X. A Novel Aptamer Functionalized $CuInS_2$ Quantum Dots Probe for Daunorubicin

DOI: 10.1021/acs.chemrev.6b00290
Chem. Rev. 2016, 116, 12234−12327

Sensing and Near Infrared Imaging of Prostate Cancer Cells. *Anal. Chim. Acta* **2014**, *818*, 54−60.
(199) Foda, M. F.; Huang, L.; Shao, F.; Han, H.-Y. Biocompatible and Highly Luminescent Near-Infrared $CuInS_2$/ZnS Quantum Dots Embedded Silica Beads for Cancer Cell Imaging. *ACS Appl. Mater. Interfaces* **2014**, *6*, 2011−2017.
(200) Gao, X.; Liu, Z.; Lin, Z.; Su, X. $CuInS_2$ Quantum Dots/Poly(L-Glutamic Acid)-Drug Conjugates for Drug Delivery and Cell Imaging. *Analyst* **2014**, *139*, 831−836.
(201) Cheng, C.-Y.; Ou, K.-L.; Huang, W.-T.; Chen, J.-K.; Chang, J.-Y.; Yang, C.-H. Gadolinium-Based $CuInS_2$/ZnS Nanoprobe for Dual-Modality Magnetic Resonance/Optical Imaging. *ACS Appl. Mater. Interfaces* **2013**, *5*, 4389−4400.
(202) Kolny-Olesiak, J.; Weller, H. Synthesis and Application of Colloidal $CuInS_2$ Semiconductor Nanocrystals. *ACS Appl. Mater. Interfaces* **2013**, *5*, 12221−12237.
(203) Lin, Z.; Fei, X.; Ma, Q.; Gao, X.; Su, X. $CuInS_2$ Quantum Dots@Silica Near-Infrared Fluorescent Nanoprobe for Cell Imaging. *New J. Chem.* **2014**, *38*, 90−96.
(204) Rao, P.; Yao, W.; Li, Z.; Kong, L.; Zhang, W.; Li, L. Highly Stable $CuInS_2$@ZnS:Al Core@Shell Quantum Dots: The Role of Aluminium Self-Passivation. *Chem. Commun.* **2015**, *51*, 8757−8760.
(205) Zhang, W.; Lou, Q.; Ji, W.; Zhao, J.; Zhong, X. Color-Tunable Highly Bright Photoluminescence of Cadmium-Free Cu-Doped Zn−In−S Nanocrystals and Electroluminescence. *Chem. Mater.* **2014**, *26*, 1204−1212.
(206) Jiang, T.; Song, J.; Wang, H.; Ye, X.; Wang, H.; Zhang, W.; Yang, M.; Xia, R.; Zhu, L.; Xu, X. Aqueous Synthesis of Color Tunable Cu Doped Zn-In-S/ZnS Nanoparticles in the Whole Visible Region for Cellular Imaging. *J. Mater. Chem. B* **2015**, *3*, 2402−2410.
(207) Li, J.; Kempken, B.; Dzhagan, V.; Zahn, D. R. T.; Grzelak, J.; Mackowski, S.; Parisi, J.; Kolny-Olesiak, J. Alloyed $CuInS_2$-ZnS Nanorods: Synthesis, Structure and Optical Properties. *CrystEngComm* **2015**, *17*, 5634−5643.
(208) Hu, S.; Zeng, S.; Zhang, B.; Yang, C.; Song, P.; Hang Danny, T. J.; Lin, G.; Wang, Y.; Anderson, T.; Coquet, P.; et al. Preparation of Biofunctionalized Quantum Dots Using Microfluidic Chips for Bioimaging. *Analyst* **2014**, *139*, 4681−4690.
(209) Chen, H.; Li, B.; Zhang, M.; Sun, K.; Wang, Y.; Peng, K.; Ao, M.; Guo, Y.; Gu, Y. Characterization of Tumor-Targeting Ag_2S Quantum Dots for Cancer Imaging and Therapy *in vivo*. *Nanoscale* **2014**, *6*, 12580−12590.
(210) Langevin, M.-A.; Lachance-Quirion, D.; Ritcey, A. M.; Allen, C. N. Size-Dependent Extinction Coefficients and Transition Energies of Near-Infrared beta-Ag_2Se Colloidal Quantum Dots. *J. Phys. Chem. C* **2013**, *117*, 5424−5428.
(211) Zhang, X.; Liu, M.; Liu, H.; Zhang, S. Low-Toxic Ag_2S Quantum Dots for Photoelectrochemical Detection Glucose and Cancer Cells. *Biosens. Bioelectron.* **2014**, *56*, 307−312.
(212) Ji, C.; Zhang, Y.; Zhang, T.; Liu, W.; Zhang, X.; Shen, H.; Wang, Y.; Gao, W.; Wang, Y.; Zhao, J.; et al. Temperature-Dependent Photoluminescence of Ag_2Se Quantum Dots. *J. Phys. Chem. C* **2015**, *119*, 13841−13846.
(213) Wang, C.; Xu, S.; Zhao, Z.; Wang, Z.; Cui, Y. Aqueous Synthesis of Nontoxic Ag_2Se/ZnSe Quantum Dots Designing as Fluorescence Sensors for Detection of Ag(I) and Cu(II) Ions. *J. Fluoresc.* **2015**, *25*, 41−48.
(214) Duman, F. D.; Hocaoglu, I.; Ozturk, D. G.; Gozuacik, D.; Kiraz, A.; Acar, H. Y. Highly Luminescent and Cytocompatible Cationic Ag_2S NIR-Emitting Quantum Dots for Optical Imaging and Gene Transfection. *Nanoscale* **2015**, *7*, 11352−11362.
(215) Jiang, P.; Wang, R.; Chen, Z. Thiol-based Non-Injection Synthesis of Near-Infrared Ag_2S/ZnS Core/Shell Quantum Dots. *RSC Adv.* **2015**, *5*, 56789−56793.
(216) Zhang, X.; Liu, J.; Johansson, E. M. J. Efficient Charge-Carrier Extraction From Ag_2S Quantum Dots Prepared by the SILAR Method for Utilization of Multiple Exciton Generation. *Nanoscale* **2015**, *7*, 1454−1462.
(217) Zhang, Y.; Liu, Y.; Li, C.; Chen, X.; Wang, Q. Controlled Synthesis of Ag_2S Quantum Dots and Experimental Determination of the Exciton Bohr Radius. *J. Phys. Chem. C* **2014**, *118*, 4918−4923.
(218) Sun, J.; Yu, W.; Usman, A.; Isimjan, T. T.; Dgobbo, S.; Alarousu, E.; Takanabe, K.; Mohammed, O. F. Generation of Multiple Excitons in Ag_2S Quantum Dots: Single High-Energy versus Multiple-Photon Excitation. *J. Phys. Chem. Lett.* **2014**, *5*, 659−665.
(219) Gui, R.; Wan, A.; Liu, X.; Yuan, W.; Jin, H. Water-Soluble Multidentate Polymers Compactly Coating Ag_2S Quantum Dots with Minimized Hydrodynamic Size and Bright Emission Tunable From Red to Second Near-Infrared Region. *Nanoscale* **2014**, *6*, 5467−5473.
(220) Zhu, C.-N.; Jiang, P.; Zhang, Z.-L.; Zhu, D.-L.; Tian, Z.-Q.; Pang, D.-W. Ag_2Se Quantum Dots with Tunable Emission in the Second Near-Infrared Window. *ACS Appl. Mater. Interfaces* **2013**, *5*, 1186−1189.
(221) Park, Y. J.; Oh, J. H.; Han, N. S.; Yoon, H. C.; Park, S. M.; Do, Y. R.; Song, J. K. Photoluminescence of Band Gap States in $AgInS_2$ Nanoparticles. *J. Phys. Chem. C* **2014**, *118*, 25677−25683.
(222) Shinchi, H.; Wakao, M.; Nagata, N.; Sakamoto, M.; Mochizuki, E.; Uematsu, T.; Kuwabata, S.; Suda, Y. Cadmium-Free Sugar-Chain-Immobilized Fluorescent Nanoparticles Containing Low-Toxicity ZnS-$AgInS_2$ Cores for Probing Lectin and Cells. *Bioconjugate Chem.* **2014**, *25*, 286−295.
(223) Tan, L.; Liu, S.; Li, X.; Chronakis, I. S.; Shen, Y. A New Strategy for Synthesizing $AgInS_2$ Quantum Dots Emitting Brightly in Near-Infrared Window for *in vivo* Imaging. *Colloids Surf., B* **2015**, *125*, 222−229.
(224) Regulacio, M. D.; Win, K. Y.; Lo, S. L.; Zhang, S.-Y.; Zhang, X.; Wang, S.; Han, M.-Y.; Zheng, Y. Aqueous Synthesis of Highly Luminescent $AgInS_2$-ZnS Quantum Dots and Their Biological Applications. *Nanoscale* **2013**, *5*, 2322−2327.
(225) Wang, Q.; Bao, Y.; Ahire, J.; Chao, Y. Co-encapsulation of Biodegradable Nanoparticles with Silicon Quantum Dots and Quercetin for Monitored Delivery. *Adv. Healthcare Mater.* **2013**, *2*, 459−466.
(226) Chinnathambi, S.; Chen, S.; Ganesan, S.; Hanagata, N. Silicon Quantum Dots for Biological Applications. *Adv. Healthcare Mater.* **2014**, *3*, 10−29.
(227) Dohnalova, K.; Gregorkiewicz, T.; Kusova, K. Silicon Quantum dots: Surface Matters. *J. Phys.: Condens. Matter* **2014**, *26*, 173201−173228.
(228) Ban, R.; Zheng, F.; Zhang, J. A Highly Sensitive Fluorescence Assay for 2,4,6-Trinitrotoluene using Amine-Capped Silicon Quantum Dots as a Probe. *Anal. Methods* **2015**, *7*, 1732−1737.
(229) Ohta, S.; Yamura, K.; Inasawa, S.; Yamaguchi, Y. Aggregates of Silicon Quantum Dots as a Drug Carrier: Selective Intracellular Drug Release based on pH-Responsive Aggregation/Dispersion. *Chem. Commun.* **2015**, *51*, 6422−6425.
(230) Wang, L.; Li, Q.; Wang, H.-Y.; Huang, J.-C.; Zhang, R.; Chen, Q.-D.; Xu, H.-L.; Han, W.; Shao, Z.-Z.; Sun, H.-B. Ultrafast Optical Spectroscopy of Surface-Modified Silicon Quantum Dots: Unraveling the Underlying Mechanism of the Ultrabright and Color-Tunable Photoluminescence. *Light: Sci. Appl.* **2015**, *4*, e245−e253.
(231) Hua, F.; Swihart, M. T.; Ruckenstein, E. Efficient Surface Grafting of Luminescent Silicon Quantum Dots by Photoinitiated Hydrosilylation. *Langmuir* **2005**, *21*, 6054−6062.
(232) Li, X.; He, Y.; Swihart, M. T. Surface Functionalization of Silicon Nanoparticles Produced by Laser-Driven Pyrolysis of Silane Followed by HF-HNO_3 Etching. *Langmuir* **2004**, *20*, 4720−4727.
(233) Li, X.; He, Y.; Talukdar, S. S.; Swihart, M. T. Process for Preparing Macroscopic Quantities of Brightly Photoluminescent Silicon Nanoparticles with Emission Spanning the Visible Spectrum. *Langmuir* **2003**, *19*, 8490−8496.
(234) Sato, S.; Swihart, M. T. Propionic-Acid-Terminated Silicon Nanoparticles: Synthesis and Optical Characterization. *Chem. Mater.* **2006**, *18*, 4083−4088.
(235) Mangolini, L.; Thimsen, E.; Kortshagen, U. High-Yield Plasma Synthesis of Luminescent Silicon Nanocrystals. *Nano Lett.* **2005**, *5*, 655−659.

DOI: 10.1021/acs.chemrev.6b00290
Chem. Rev. 2016, 116, 12234−12327

(236) Jurbergs, D.; Rogojina, E.; Mangolini, L.; Kortshagen, U. Silicon Nanocrystals with Ensemble Quantum Yields Exceeding 60%. *Appl. Phys. Lett.* **2006**, *88*, 233116.
(237) Veinot, J. G. Synthesis, Surface Functionalization, and Properties of Freestanding Silicon Nanocrystals. *Chem. Commun.* **2006**, 4160−4168.
(238) Gupta, A.; Swihart, M. T.; Wiggers, H. Luminescent Colloidal Dispersion of Silicon Quantum Dots from Microwave Plasma Synthesis: Exploring the Photoluminescence Behavior Across the Visible Spectrum. *Adv. Funct. Mater.* **2009**, *19*, 696−703.
(239) He, G. S.; Zheng, Q. D.; Yong, K. T.; Erogbogbo, F.; Swihart, M. T.; Prasad, P. N. Two- and Three-Photon Absorption and Frequency Upconverted Emission of Silicon Quantum Dots. *Nano Lett.* **2008**, *8*, 2688−2692.
(240) Dasog, M.; Yang, Z.; Regli, S.; Atkins, T. M.; Faramus, A.; Singh, M. P.; Muthuswamy, E.; Kauzlarich, S. M.; Tilley, R. D.; Veinot, J. G. Chemical Insight into the Origin of Red and Blue Photoluminescence Arising From Freestanding Silicon Nanocrystals. *ACS Nano* **2013**, *7*, 2676−2685.
(241) Hua, F.; Erogbogbo, F.; Swihart, M. T.; Ruckenstein, E. Organically Capped Silicon Nanoparticles with Blue Photoluminescence Prepared by Hydrosilylation Followed by Oxidation. *Langmuir* **2006**, *22*, 4363−4370.
(242) Liu, J.; Erogbogbo, F.; Yong, K.-T.; Ye, L.; Liu, J.; Hu, R.; Chen, H.; Hu, Y.; Yang, Y.; Yang, J.; et al. Assessing Clinical Prospects of Silicon Quantum Dots: Studies in Mice and Monkeys. *ACS Nano* **2013**, *7*, 7303−7310.
(243) Zhou, T.; Anderson, R. T.; Li, H.; Bell, J.; Yang, Y.; Gorman, B. P.; Pylypenko, S.; Lusk, M. T.; Sellinger, A. Bandgap Tuning of Silicon Quantum Dots by Surface Functionalization with Conjugated Organic Groups. *Nano Lett.* **2015**, *15*, 3657−3663.
(244) Swihart, M. T. In *Nanotechnology in Biology and Medicine: Methods, Devices, and Applications*; Vo-Dinh, T., Ed.; CRC Press: Boca Raton, FL, 2007; Vol. *4*.
(245) Zhu, S.; Song, Y.; Zhao, X.; Shao, J.; Zhang, J.; Yang, B. The Photoluminescence Mechanism in Carbon Dots (Graphene Quantum Dots, Carbon Nanodots, and Polymer Dots): Current State and Future Perspective. *Nano Res.* **2015**, *8*, 355−381.
(246) Ju, J.; Chen, W. In Situ Growth of Surfactant-Free Gold Nanoparticles on Nitrogen-Doped Graphene Quantum Dots for Electrochemical Detection of Hydrogen Peroxide in Biological Environments. *Anal. Chem.* **2015**, *87*, 1903−1910.
(247) Sk, M. A.; Ananthanarayanan, A.; Huang, L.; Lim, K. H.; Chen, P. Revealing the Tunable Photoluminescence Properties of Graphene Quantum Dots. *J. Mater. Chem. C* **2014**, *2*, 6954−6960.
(248) Sandeep Kumar, G.; Roy, R.; Sen, D.; Ghorai, U. K.; Thapa, R.; Mazumder, N.; Saha, S.; Chattopadhyay, K. K. Amino-Functionalized Graphene Quantum dots: Origin of Tunable Heterogeneous Photoluminescence. *Nanoscale* **2014**, *6*, 3384−3391.
(249) Lin, L.; Rong, M.; Luo, F.; Chen, D.; Wang, Y.; Chen, X. Luminescent Graphene Quantum Dots as New Fluorescent Materials for Environmental and Biological Applications. *TrAC, Trends Anal. Chem.* **2014**, *54*, 83−102.
(250) Sun, J.; Yang, S.; Wang, Z.; Shen, H.; Xu, T.; Sun, L.; Li, H.; Chen, W.; Jiang, X.; Ding, G.; et al. Ultra-High Quantum Yield of Graphene Quantum Dots: Aromatic-Nitrogen Doping and Photoluminescence Mechanism. *Part. Part. Syst. Charact.* **2015**, *32*, 434−440.
(251) Yang, H.; Holloway, P. H.; Ratna, B. B. Photoluminescent and Electroluminescent Properties of Mn-Doped ZnS Nanocrystals. *J. Appl. Phys.* **2003**, *93*, 586−592.
(252) Erwin, S. C.; Zu, L.; Haftel, M. I.; Efros, A. L.; Kennedy, T. A.; Norris, D. J. Doping Semiconductor Nanocrystals. *Nature* **2005**, *436*, 91−94.
(253) Wu, P.; Yan, X.-P. Doped Quantum Dots for Chemo/Biosensing and Bioimaging. *Chem. Soc. Rev.* **2013**, *42*, 5489−5521.
(254) Wu, P.; Zhang, J.; Wang, S.; Zhu, A.; Hou, X. Sensing during In Situ Growth of Mn-Doped ZnS QDs: A Phosphorescent Sensor for Detection of H_2S in Biological Samples. *Chem. - Eur. J.* **2014**, *20*, 952−956.
(255) Sapra, S.; Prakash, A.; Ghangrekar, A.; Periasamy, N.; Sarma, D. D. Emission Properties of Manganese-Doped ZnS Nanocrystals. *J. Phys. Chem. B* **2005**, *109*, 1663−1668.
(256) Geszke-Moritz, M.; Piotrowska, H.; Murias, M.; Balan, L.; Moritz, M.; Lulek, J.; Schneider, R. Thioglycerol-Capped Mn-Doped ZnS Quantum Dot Bioconjugates as Efficient Two-Photon Fluorescent Nano-Probes for Bioimaging. *J. Mater. Chem. B* **2013**, *1*, 698−706.
(257) Yu, J. H.; Kwon, S.-H.; Petrasek, Z.; Park, O. K.; Jun, S. W.; Shin, K.; Choi, M.; Park, Y. I.; Park, K.; Na, H. B.; et al. High-Resolution Three-Photon Biomedical Imaging Using Doped ZnS Nanocrystals. *Nat. Mater.* **2013**, *12*, 359−366.
(258) Ertas, N.; Kara, H. E. S. L-Cysteine Capped Mn-Doped ZnS Quantum Dots as a Room Temperature Phosphorescence Sensor for in-vitro Binding Assay of Idarubicin and DNA. *Biosens. Bioelectron.* **2015**, *70*, 345−350.
(259) Gul, S.; Cooper, J. K.; Glans, P.-A.; Guo, J.; Yachandra, V. K.; Yano, J.; Zhang, J. Z. Effect of Al^{3+} Co-doping on the Dopant Local Structure, Optical Properties, and Exciton Dynamics in Cu^{+}-Doped ZnSe Nanocrystals. *ACS Nano* **2013**, *7*, 8680−8692.
(260) Jain, P. K. Plasmon-in-a-Box: On the Physical Nature of Few-Carrier Plasmon Resonances. *J. Phys. Chem. Lett.* **2014**, *5*, 3112−3119.
(261) Liu, X.; Swihart, M. T. Heavily-Doped Colloidal Semiconductor and Metal Oxide Nanocrystals: An Emerging New Class of Plasmonic Nanomaterials. *Chem. Soc. Rev.* **2014**, *43*, 3908−3920.
(262) Zeng, S.; Yong, K.-T.; Roy, I.; Dinh, X.-Q.; Yu, X.; Luan, F. A Review on Functionalized Gold Nanoparticles for Biosensing Applications. *Plasmonics* **2011**, *6*, 491−506.
(263) Zeng, S.; Baillargeat, D.; Ho, H.-P.; Yong, K.-T. Nanomaterials enhanced Surface Plasmon Resonance for Biological and Chemical Sensing Applications. *Chem. Soc. Rev.* **2014**, *43*, 3426−3452.
(264) Zeng, S.; Sreekanth, K. V.; Shang, J.; Yu, T.; Chen, C.-K.; Yin, F.; Baillargeat, D.; Coquet, P.; Ho, H.-P.; Kabashin, A. V.; et al. Graphene-Gold Metasurface Architectures for Ultrasensitive Plasmonic Biosensing. *Adv. Mater.* **2015**, *27*, 6163−6169.
(265) Niezgoda, J. S.; Harrison, M. A.; McBride, J. R.; Rosenthal, S. J. Novel Synthesis of Chalcopyrite $Cu_xIn_yS_2$ Quantum Dots with Tunable Localized Surface Plasmon Resonances. *Chem. Mater.* **2012**, *24*, 3294−3297.
(266) Niezgoda, J. S.; Yap, E.; Keene, J. D.; McBride, J. R.; Rosenthal, S. J. Plasmonic $Cu_xIn_yS_2$ Quantum Dots Make Better Photovoltaics Than Their Nonplasmonic Counterparts. *Nano Lett.* **2014**, *14*, 3262−3269.
(267) Wang, X.; Swihart, M. T. Controlling the Size, Shape, Phase, Band Gap, and Localized Surface Plasmon Resonance of $Cu_{2-x}S$ and Cu_xIn_yS Nanocrystals. *Chem. Mater.* **2015**, *27*, 1786−1791.
(268) Liu, X.; Wang, X.; Zhou, B.; Law, W. C.; Cartwright, A. N.; Swihart, M. T. Size-Controlled Synthesis of $Cu_{2-x}E$ (E= S, Se) Nanocrystals with Strong Tunable Near-Infrared Localized Surface Plasmon Resonance and High Conductivity in Thin Films. *Adv. Funct. Mater.* **2013**, *23*, 1256−1264.
(269) Wang, F.; Li, Q.; Lin, L.; Peng, H.; Liu, Z.; Xu, D. Monodisperse Copper Chalcogenide Nanocrystals: Controllable Synthesis and the Pinning of Plasmonic Resonance Absorption. *J. Am. Chem. Soc.* **2015**, *137*, 12006−12012.
(270) Liu, X.; Wang, X.; Swihart, M. T. $Cu_{2-x}S_{1-y}Se_y$ Alloy Nanocrystals with Broadly Tunable Near-Infrared Localized Surface Plasmon Resonance. *Chem. Mater.* **2013**, *25*, 4402−4408.
(271) Liu, Z.; Liu, X.; Du, Y.; Ren, J.; Qu, X. Using Plasmonic Copper Sulfide Nanocrystals as Smart Light-Driven Sterilants. *ACS Nano* **2015**, *9*, 10335−10346.
(272) Liu, X.; Wang, X.; Swihart, M. T. Composition-Dependent Crystal Phase, Optical Properties, and Self-Assembly of Cu−Sn−S Colloidal Nanocrystals. *Chem. Mater.* **2015**, *27*, 1342−1348.
(273) Liu, M.; Xue, X.; Ghosh, C.; Liu, X.; Liu, Y.; Furlani, E. P.; Swihart, M. T.; Prasad, P. N. Room-Temperature Synthesis of Covellite Nanoplatelets with Broadly Tunable Localized Surface Plasmon Resonance. *Chem. Mater.* **2015**, *27*, 2584−2590.

DOI: 10.1021/acs.chemrev.6b00290
Chem. Rev. 2016, 116, 12234−12327

(274) Lee, K. S.; El-Sayed, M. A. Gold and Silver Nanoparticles in Sensing and Imaging: Sensitivity of Plasmon Response to Size, Shape, and Metal Composition. *J. Phys. Chem. B* **2006**, *110*, 19220−19225.
(275) Gary, D. C.; Terban, M. W.; Billinge, S. J. L.; Cossairt, B. M. Two-Step Nucleation and Growth of InP Quantum Dots via Magic-Sized Cluster Intermediates. *Chem. Mater.* **2015**, *27*, 1432−1441.
(276) Brunetti, V.; Chibli, H.; Fiammengo, R.; Galeone, A.; Malvindi, M. A.; Vecchio, G.; Cingolani, R.; Nadeau, J. L.; Pompa, P. P. InP/ZnS as a Safer Alternative to CdSe/ZnS Core/Shell Quantum Dots: *in vitro* and *in vivo* Toxicity Assessment. *Nanoscale* **2013**, *5*, 307−317.
(277) Lin, G.; Ouyang, Q.; Hu, R.; Ding, Z.; Tian, J.; Yin, F.; Xu, G.; Chen, Q.; Wang, X.; Yong, K.-T. *In vivo* Toxicity Assessment of Non-Cadmium Quantum Dots in BALB/c Mice. *Nanomedicine* **2015**, *11*, 341−350.
(278) Micic, O. I.; Curtis, C. J.; Jones, K. M.; Sprague, J. R.; Nozik, A. J. Synthesis and Characterization of InP Quantum Dots. *J. Phys. Chem.* **1994**, *98*, 4966−4969.
(279) Battaglia, D.; Peng, X. Formation of High Quality InP and InAs Nanocrystals in a Noncoordinating Solvent. *Nano Lett.* **2002**, *2*, 1027−1030.
(280) Choi, H. S.; Kim, Y.; Park, J. C.; Oh, M. H.; Jeon, D. Y.; Nam, Y. S. Highly Luminescent, Off-Stoichiometric $Cu_xIn_yS_2$/ZnS Quantum Dots for Near-Infrared Fluorescence Bio-Imaging. *RSC Adv.* **2015**, *5*, 43449−43455.
(281) Yong, K.-T.; Roy, I.; Hu, R.; Ding, H.; Cai, H.; Zhu, J.; Zhang, X.; Bergey, E. J.; Prasad, P. N. Synthesis of Ternary $CuInS_2$/ZnS Quantum Dot Bioconjugates and Their Applications for Targeted Cancer Bioimaging. *Integr. Biol.* **2010**, *2*, 121−129.
(282) Xie, R.; Rutherford, M.; Peng, X. Formation of High-Quality I−III−VI Semiconductor Nanocrystals by Tuning Relative Reactivity of Cationic Precursors. *J. Am. Chem. Soc.* **2009**, *131*, 5691−5697.
(283) Nam, D.-E.; Song, W.-S.; Yang, H. Facile, Air-Insensitive Solvothermal Synthesis of Emission-Tunable $CuInS_2$/ZnS Quantum Dots with High Quantum Yields. *J. Mater. Chem.* **2011**, *21*, 18220−18226.
(284) Guo, W.; Chen, N.; Dong, C.; Tu, Y.; Chang, J.; Zhang, B. One-Pot Synthesis of Hydrophilic ZnCuInS/ZnS Quantum Dots for *in vivo* Imaging. *RSC Adv.* **2013**, *3*, 9470−9475.
(285) Tang, R.; Xue, J.; Xu, B.; Shen, D.; Sudlow, G. P.; Achilefu, S. Tunable Ultrasmall Visible-to-Extended Near-Infrared Emitting Silver Sulfide Quantum Dots for Integrin-Targeted Cancer Imaging. *ACS Nano* **2015**, *9*, 220−230.
(286) Gui, R.; Jin, H.; Wang, Z.; Tan, L. Recent Advances in Synthetic Methods and Applications of Colloidal Silver Chalcogenide Quantum Dots. *Coord. Chem. Rev.* **2015**, *296*, 91−124.
(287) Du, Y.; Xu, B.; Fu, T.; Cai, M.; Li, F.; Zhang, Y.; Wang, Q. Near-Infrared Photoluminescent Ag_2S Quantum Dots from a Single Source Precursor. *J. Am. Chem. Soc.* **2010**, *132*, 1470−1471.
(288) Hocaoglu, I.; Cizmeciyan, M. N.; Erdem, R.; Ozen, C.; Kurt, A.; Sennaroglu, A.; Acar, H. Y. Development of Highly Luminescent and Cytocompatible Near-IR-Emitting Aqueous Ag_2S Quantum Dots. *J. Mater. Chem.* **2012**, *22*, 14674−14681.
(289) Zhang, Y.; Zhang, Y.; Hong, G.; He, W.; Zhou, K.; Yang, K.; Li, F.; Chen, G.; Liu, Z.; Dai, H.; et al. Biodistribution, Pharmacokinetics and Toxicology of Ag_2S Near-Infrared Quantum Dots in Mice. *Biomaterials* **2013**, *34*, 3639−3646.
(290) Zhang, Y.; Hong, G.; Zhang, Y.; Chen, G.; Li, F.; Dai, H.; Wang, Q. Ag_2S Quantum Dot: A Bright and Biocompatible Fluorescent Nanoprobe in the Second Near-Infrared Window. *ACS Nano* **2012**, *6*, 3695−3702.
(291) Wang, Y.; Yan, X.-P. Fabrication of Vascular Endothelial Growth Factor Antibody Bioconjugated Ultrasmall Near-Infrared Fluorescent Ag_2S Quantum Dots for Targeted Cancer Imaging *in vivo*. *Chem. Commun.* **2013**, *49*, 3324−3326.
(292) Shen, S.; Zhang, Y.; Peng, L.; Du, Y.; Wang, Q. Matchstick-Shaped Ag_2S−ZnS Heteronanostructures Preserving both UV/Blue and Near-Infrared Photoluminescence. *Angew. Chem., Int. Ed.* **2011**, *50*, 7115−7118.
(293) Shen, S.; Zhang, Y.; Liu, Y.; Peng, L.; Chen, X.; Wang, Q. Manganese-Doped Ag_2S-ZnS Heteronanostructures. *Chem. Mater.* **2012**, *24*, 2407−2413.
(294) Gu, Y.-P.; Cui, R.; Zhang, Z.-L.; Xie, Z.-X.; Pang, D.-W. Ultrasmall Near-Infrared Ag_2Se Quantum Dots with Tunable Fluorescence for *in vivo* Imaging. *J. Am. Chem. Soc.* **2012**, *134*, 79−82.
(295) Song, J.; Jiang, T.; Guo, T.; Liu, L.; Wang, H.; Xia, T.; Zhang, W.; Ye, X.; Yang, M.; Zhu, L.; et al. Facile Synthesis of Water-Soluble Zn-Doped $AgIn_5S_8$/ZnS Core/Shell Fluorescent Nanocrystals and Their Biological Application. *Inorg. Chem.* **2015**, *54*, 1627−1633.
(296) Deng, D.; Cao, J.; Qu, L.; Achilefu, S.; Gu, Y. Highly Luminescent Water-Soluble Quaternary Zn-Ag-In-S Quantum Dots for Tumor Cell-Targeted Imaging. *Phys. Chem. Chem. Phys.* **2013**, *15*, 5078−5083.
(297) Gao, J.; Chen, K.; Xie, R.; Xie, J.; Lee, S.; Cheng, Z.; Peng, X.; Chen, X. Ultrasmall Near-Infrared Non-Cadmium Quantum Dots for *in vivo* Tumor Imaging. *Small* **2010**, *6*, 256−261.
(298) Xie, R.; Peng, X. Synthetic Scheme for High-Quality InAs Nanocrystals Based on Self-Focusing and One-Pot Synthesis of InAs-Based Core-Shell Nanocrystals. *Angew. Chem., Int. Ed.* **2008**, *47*, 7677−7680.
(299) Xie, R.; Chen, K.; Chen, X.; Peng, X. InAs/InP/ZnSe Core/Shell/Shell Quantum Dots as Near-Infrared Emitters: Bright, Narrow-Band, Non-Cadmium Containing, and Biocompatible. *Nano Res.* **2008**, *1*, 457−464.
(300) Fan, J.-W.; Vankayala, R.; Chang, C.-L.; Chang, C.-H.; Chiang, C.-S.; Hwang, K. C. Preparation, Cytotoxicity and *in vivo* Bioimaging of Highly Luminescent Water-Soluble Silicon Quantum Dots. *Nanotechnology* **2015**, *26*, 215703−215703.
(301) Shen, P.; Ohta, S.; Inasawa, S.; Yamaguchi, Y. Selective Labeling of the Endoplasmic Reticulum in Live Cells with Silicon Quantum Dots. *Chem. Commun.* **2011**, *47*, 8409−8411.
(302) Shiohara, A.; Prabakar, S.; Faramus, A.; Hsu, C.-Y.; Lai, P.-S.; Northcote, P. T.; Tilley, R. D. Sized Controlled Synthesis, Purification, and Cell Studies with Silicon Quantum Dots. *Nanoscale* **2011**, *3*, 3364−3370.
(303) Xu, S.; Li, D.; Wu, P. One-Pot, Facile, and Versatile Synthesis of Monolayer MoS_2/WS_2 Quantum Dots as Bioimaging Probes and Efficient Electrocatalysts for Hydrogen Evolution Reaction. *Adv. Funct. Mater.* **2015**, *25*, 1127−1136.
(304) Zeng, S.; Hu, S.; Xia, J.; Anderson, T.; Dinh, X.-Q.; Meng, X.-M.; Coquet, P.; Yong, K.-T. Graphene−MoS_2 Hybrid Nanostructures Enhanced Surface Plasmon Resonance Biosensors. *Sens. Actuators, B* **2015**, *207*, 801−810.
(305) Zheng, X. T.; Ananthanarayanan, A.; Luo, K. Q.; Chen, P. Glowing Graphene Quantum Dots and Carbon Dots: Properties, Syntheses, and Biological Applications. *Small* **2015**, *11*, 1620−1636.
(306) Pan, D. Y.; Zhang, J. C.; Li, Z.; Wu, M. H. Hydrothermal Route for Cutting Graphene Sheets into Blue-Luminescent Graphene Quantum Dots. *Adv. Mater.* **2010**, *22*, 734−738.
(307) Peng, J.; Gao, W.; Gupta, B. K.; Liu, Z.; Romero-Aburto, R.; Ge, L.; Song, L.; Alemany, L. B.; Zhan, X.; Gao, G.; et al. Graphene Quantum Dots Derived from Carbon Fibers. *Nano Lett.* **2012**, *12*, 844−849.
(308) Dong, Y.; Chen, C.; Zheng, X.; Gao, L.; Cui, Z.; Yang, H.; Guo, C.; Chi, Y.; Li, C. M. One-Step and High Yield Simultaneous Preparation of Single- and Multi-Layer Graphene Quantum Dots from CX-72 Carbon Black. *J. Mater. Chem.* **2012**, *22*, 8764−8766.
(309) Zhao, H.; Chang, Y.; Liu, M.; Gao, S.; Yu, H.; Quan, X. A Universal Immunosensing Strategy Based on Regulation of the Interaction between Graphene and Graphene Quantum Dots. *Chem. Commun.* **2013**, *49*, 234−236.
(310) Zhu, S.; Zhang, J.; Tang, S.; Qiao, C.; Wang, L.; Wang, H.; Liu, X.; Li, B.; Li, Y.; Yu, W.; et al. Surface Chemistry Routes to Modulate the Photoluminescence of Graphene Quantum Dots: From Fluorescence Mechanism to Up-Conversion Bioimaging Applications. *Adv. Funct. Mater.* **2012**, *22*, 4732−4740.
(311) Zhang, J.; Zhu, A.; Zhao, T.; Wu, L.; Wu, P.; Hou, X. Glucose Oxidase-directed, Instant Synthesis of Mn-Doped ZnS Quantum Dots

DOI: 10.1021/acs.chemrev.6b00290
Chem. Rev. 2016, 116, 12234−12327

in Neutral Media with Retained Enzymatic Activity: Mechanistic Study and Biosensing Application. *J. Mater. Chem. B* **2015**, *3*, 5942−5950.
(312) Song, Y.; Li, Y.; Liu, Y.; Su, X.; Ma, Q. Highly Sensitive and Selective Detection of Phosphate Using Novel Highly Photoluminescent Water-Soluble Mn-Doped ZnTe/ZnSe Quantum Dots. *Talanta* **2015**, *144*, 680−685.
(313) Cao, S.; Zhao, J.; yang, w.; Li, C.; Zheng, J. Mn^{2+}-Doped Zn-In-S Quantum Dots with Tunable Bandgaps and High Photoluminescence Properties. *J. Mater. Chem. C* **2015**, *3*, 8844−8851.
(314) Manzoor, K.; Johny, S.; Thomas, D.; Setua, S.; Menon, D.; Nair, S. Bio-Conjugated Luminescent Quantum Dots of Doped ZnS: a Cyto-Friendly System for Targeted Cancer Imaging. *Nanotechnology* **2009**, *20*, 065102−065102.
(315) Wu, P.; He, Y.; Wang, H.-F.; Yan, X.-P. Conjugation of Glucose Oxidase onto Mn-Doped ZnS Quantum Dots for Phosphorescent Sensing of Glucose in Biological Fluids. *Anal. Chem.* **2010**, *82*, 1427−1433.
(316) Wu, P.; Miao, L.-N.; Wang, H.-F.; Shao, X.-G.; Yan, X.-P. A Multidimensional Sensing Device for the Discrimination of Proteins Based on Manganese-Doped ZnS Quantum Dots. *Angew. Chem., Int. Ed.* **2011**, *50*, 8118−8121.
(317) Zhou, R.; Li, M.; Wang, S.; Wu, P.; Wu, L.; Hou, X. Low-Toxic Mn-Doped ZnSe/ZnS Quantum Dots Conjugated with Nano-Hydroxyapatite for Cell Imaging. *Nanoscale* **2014**, *6*, 14319−14325.
(318) Yang, H.-J.; Chen, C.-Y.; Yuan, F.-W.; Tuan, H.-Y. Designed Synthesis of Solid and Hollow $Cu_{2-x}Te$ Nanocrystals with Tunable Near-Infrared Localized Surface Plasmon Resonance. *J. Phys. Chem. C* **2013**, *117*, 21955−21964.
(319) Vu, T. Q.; Lam, W. Y.; Hatch, E. W.; Lidke, D. S. Quantum Dots for Quantitative Imaging: from Single Molecules to Tissue. *Cell Tissue Res.* **2015**, *360*, 71−86.
(320) Hu, T.; Liu, X.; Liu, S.; Wang, Z.; Tang, Z. Toward Understanding of Transfer Mechanism between Electrochemiluminescent Dyes and Luminescent Quantum Dots. *Anal. Chem.* **2014**, *86*, 3939−3946.
(321) Guo, W.; Yang, W.; Wang, Y.; Sun, X.; Liu, Z.; Zhang, B.; Chang, J.; Chen, X. Color-Tunable Gd-Zn-Cu-In-S/ZnS Quantum Dots for Dual Modality Magnetic Resonance and Fluorescence Imaging. *Nano Res.* **2014**, *7*, 1581−1591.
(322) Chen, H.; Zhang, M.; Li, B.; Chen, D.; Dong, X.; Wang, Y.; Gu, Y. Versatile Antimicrobial Peptide-Based ZnO Quantum Dots for *in vivo* Bacteria Diagnosis and Treatment with High Specificity. *Biomaterials* **2015**, *53*, 532−544.
(323) Johari-Ahar, M.; Barar, J.; Alizadeh, A. M.; Davaran, S.; Omidi, Y.; Rashidi, M.-R. Methotrexate-Conjugated Quantum Dots: Synthesis, Characterisation and Cytotoxicity in Drug Resistant Cancer Cells. *J. Drug Target* **2016**, *24*, 120−133.
(324) Zeng, W.-J.; Peng, C.-W.; Yuan, J.-P.; Cui, R.; Li, Y. Quantum Dot-Based Multiplexed Imaging in Malignant Ascites: A New Model for Malignant Ascites Classification. *Int. J. Nanomed.* **2015**, *10*, 1759−1768.
(325) Chen, Y.-Y.; Cheng, B.-R.; He, Z.-B.; Wang, S.-Y.; Wang, Z.-M.; Sun, M.; Song, H.-B.; Fang, Y.; Chen, F.-F.; Xiong, B. Capture and Identification of Heterogeneous Circulating Tumor Cells Using Transparent Nanomaterials and Quantum Dots-Based Multiplexed Imaging. *J. Cancer* **2016**, *7*, 69−79.
(326) Benítez-Martínez, S.; Valcárcel, M. Graphene Quantum Dots in Analytical Science. *TrAC, Trends Anal. Chem.* **2015**, *72*, 93−113.
(327) Liu, H.; Fan, Y.; Wang, J.; Song, Z.; Shi, H.; Han, R.; Sha, Y.; Jiang, Y. Intracellular Temperature Sensing: An Ultra-bright Luminescent Nanothermometer with Non-Sensitivity to pH and Ionic Strength. *Sci. Rep.* **2015**, *5*, 14879−14879.
(328) Wang, F.; Gu, Z.; Lei, W.; Wang, W.; Xia, X.; Hao, Q. Graphene Quantum Dots as a Fluorescent Sensing Platform for Highly Efficient Detection of Copper (II) ions. *Sens. Actuators, B* **2014**, *190*, 516−522.
(329) Liang, R.-P.; Qiu, W.-B.; Zhao, H.-F.; Xiang, C.-Y.; Qiu, J.-D. Electrochemiluminescence Resonance Energy Transfer between Graphene Quantum Dots and Graphene Oxide for Sensitive Protein Kinase Activity and Inhibitor Sensing. *Anal. Chim. Acta* **2016**, *904*, 58−64.
(330) Choi, A. O.; Neibert, K. D.; Maysinger, D. In *Quantum Dots: Applications in Biology*; Fontes, A., Santos, B. S., Eds.; Springer: New York, 2014; pp 191−206.
(331) Liu, L.; Hu, R.; Roy, I.; Lin, G.; Ye, L.; Reynolds, J. L.; Liu, J.; Liu, J.; Schwartz, S. A.; Zhang, X.; et al. Synthesis of Luminescent Near-Infrared $AgInS_2$ Nanocrystals as Optical Probes for *in vivo* Applications. *Theranostics* **2013**, *3*, 109−115.
(332) Deng, D.; Qu, L.; Gu, Y. Near-Infrared Broadly Emissive $AgInSe_2$/ZnS Quantum Dots for Biomedical Optical Imaging. *J. Mater. Chem. C* **2014**, *2*, 7077−7085.
(333) Dong, C.; Liu, Z.; Zhang, L.; Guo, W.; Li, X.; Liu, J.; Wang, H.; Chang, J. pH-Induced Charge-Reversible NIR Fluorescence Nanoprobe for Tumor-Specific Imaging. *ACS Appl. Mater. Interfaces* **2015**, *7*, 7566−7575.
(334) Nurunnabi, M.; Khatun, Z.; Nafiujjaman, M.; Lee, D. G.; Lee, Y. K. Surface Coating of Graphene Quantum Dots Using Mussel-Inspired Polydopamine for Biomedical Optical Imaging. *ACS Appl. Mater. Interfaces* **2013**, *5*, 8246−8253.
(335) Zhong, Y.; Sun, X.; Wang, S.; Peng, F.; Bao, F.; Su, Y.; Li, Y.; Lee, S.-T.; He, Y. Facile, Large-Quantity Synthesis of Stable, Tunable-Color Silicon Nanoparticles and Their Application for Long-Term Cellular Imaging. *ACS Nano* **2015**, *9*, 5958−5967.
(336) Gao, X.; Zhang, H.; Li, Y.; Su, X. Mn-Doped ZnSe D-Dots-Based Alpha-Methylacyl-CoA Racemase Probe for Human Prostate Cancer Cell Imaging. *Anal. Bioanal. Chem.* **2012**, *402*, 1871−1877.
(337) Yu, Z.; Ma, X.; Yu, B.; Pan, Y.; Liu, Z. Synthesis and Characterization of ZnS:Mn/ZnS Core/Shell Nanoparticles for Tumor Targeting and Imaging *in vivo*. *J. Biomater. Appl.* **2013**, *28*, 232−240.
(338) Mandal, G.; Darragh, M.; Wang, Y. A.; Heyes, C. D. Cadmium-Free Quantum Dots as Time-Gated Bioimaging Probes in Highly-Autofluorescent Human Breast Cancer Cells. *Chem. Commun.* **2013**, *49*, 624−626.
(339) Zhu, S.; Zhou, N.; Hao, Z.; Maharjan, S.; Zhao, X.; Song, Y.; Sun, B.; Zhang, K.; Zhang, J.; Sun, H.; et al. Photoluminescent Graphene Quantum Dots for *in vitro* and *in vivo* Bioimaging Using Long Wavelength Emission. *RSC Adv.* **2015**, *5*, 39399−39403.
(340) Liu, X.; Law, W.-C.; Jeon, M.; Wang, X.; Liu, M.; Kim, C.; Prasad, P. N.; Swihart, M. T. $Cu_{2-x}Se$ Nanocrystals with Localized Surface Plasmon Resonance as Sensitive Contrast Agents for *in vivo* Photoacoustic Imaging: Demonstration of Sentinel Lymph Node Mapping. *Adv. Healthcare Mater.* **2013**, *2*, 952−957.
(341) Ku, G.; Zhou, M.; Song, S.; Huang, Q.; Hazle, J.; Li, C. Copper Sulfide Nanoparticles As a New Class of Photoacoustic Contrast Agent for Deep Tissue Imaging at 1064 nm. *ACS Nano* **2012**, *6*, 7489−7496.
(342) Srinivasan, K.; Thiruppathiraja, C.; Subramanian, K.; Dinakaran, K. Sensitive Detection of C. Parvum Using Near-Infrared Emitting Ag_2S-Silica Core-Shell Nanospheres. *RSC Adv.* **2014**, *4*, 62399−62403.
(343) Cui, R.; Gu, Y.-P.; Bao, L.; Zhao, J.-Y.; Qi, B.-P.; Zhang, Z.-L.; Xie, Z.-X.; Pang, D.-W. Near-Infrared Electrogenerated Chemiluminescence of Ultrasmall Ag_2Se Quantum Dots for the Detection of Dopamine. *Anal. Chem.* **2012**, *84*, 8932−8935.
(344) Yan, S.; Zhang, L.; Tang, Y.; Lv, Y. Synthesis of Water-Soluble Ag_2Se QDs as a Novel Resonance Rayleigh Scattering Sensor for Highly Sensitive and Selective ConA Detection. *Analyst* **2014**, *139*, 4210−4215.
(345) Liu, S.; Shi, F.; Zhao, X.; Chen, L.; Su, X. 3-Aminophenyl Boronic Acid-Functionalized $CuInS_2$ Quantum Dots as a Near-Infrared Fluorescence Probe for the Determination of Dopamine. *Biosens. Bioelectron.* **2013**, *47*, 379−384.
(346) Qian, Z. S.; Shan, X. Y.; Chai, L. J.; Ma, J. J.; Chen, J. R.; Feng, H. DNA Nanosensor Based on Biocompatible Graphene Quantum Dots and Carbon Nanotubes. *Biosens. Bioelectron.* **2014**, *60*, 64−70.
(347) Cao, J.; Zhu, H.; Deng, D.; Xue, B.; Tang, L.; Mahounga, D.; Qian, Z.; Gu, Y. *In vivo* NIR Imaging with PbS Quantum Dots

DOI: 10.1021/acs.chemrev.6b00290
Chem. Rev. 2016, 116, 12234−12327

Entrapped in Biodegradable Micelles. *J. Biomed. Mater. Res., Part A* **2012**, *100A*, 958−968.
(348) Hessel, C. M.; Pattani, V. P.; Rasch, M.; Panthani, M. G.; Koo, B.; Tunnell, J. W.; Korgel, B. A. Copper Selenide Nanocrystals for Photothermal Therapy. *Nano Lett.* **2011**, *11*, 2560−2566.
(349) Liu, X.; Li, B.; Fu, F.; Xu, K.; Zou, R.; Wang, Q.; Zhang, B.; Chen, Z.; Hu, J. Facile Synthesis of Biocompatible Cysteine-Coated CuS Nanoparticles with High Photothermal Conversion Efficiency for Cancer Therapy. *Dalton T.* **2014**, *43*, 11709−11715.
(350) Fahmi, M. Z.; Ou, K.-L.; Chen, J.-K.; Ho, M.-H.; Tzing, S.-H.; Chang, J.-Y. Development of Bovine Serum Albumin-Modified Hybrid Nanoclusters for Magnetofluorescence Imaging and Drug Delivery. *RSC Adv.* **2014**, *4*, 32762−32772.
(351) Zhao, C.; Bai, Z.; Liu, X.; Zhang, Y.; Zou, B.; Zhong, H. Small GSH-Capped CuInS2 Quantum Dots: MPA-Assisted Aqueous Phase Transfer and Bioimaging Applications. *ACS Appl. Mater. Interfaces* **2015**, *7*, 17623−17629.
(352) Zhou, J.; Yang, Y.; Zhang, C.-Y. Toward Biocompatible Semiconductor Quantum Dots: From Biosynthesis and Bioconjugation to Biomedical Application. *Chem. Rev.* **2015**, *115*, 11669−11717.
(353) Chen, G.; Tian, F.; Li, C.; Zhang, Y.; Weng, Z.; Zhang, Y.; Peng, R.; Wang, Q. *In vivo* Real-Time Visualization of Mesenchymal Stem cells Tropism for Cutaneous Regeneration Using NIR-II Fluorescence Imaging. *Biomaterials* **2015**, *53*, 265−273.
(354) Hu, F.; Li, C.; Zhang, Y.; Wang, M.; Wu, D.; Wang, Q. Real-time *in vivo* Visualization of Tumor Therapy by a Near-Infrared-II Ag_2S Quantum Dot-Based Theranostic Nanoplatform. *Nano Res.* **2015**, *8*, 1637−1647.
(355) Liu, L.; Hu, R.; Law, W. C.; Roy, I.; Zhu, J.; Ye, L.; Hu, S.; Zhang, X.; Yong, K. T. Optimizing the Synthesis of Red- and Near-Infrared $CuInS_2$ and $AgInS_2$ Semiconductor Nanocrystals for Bioimaging. *Analyst* **2013**, *138*, 6144−6153.
(356) Yu, K.; Ng, P.; Ouyang, J.; Zaman, M. B.; Abulrob, A.; Baral, T. N.; Fatehi, D.; Jakubek, Z. J.; Kingston, D.; Wu, X.; et al. Low-Temperature Approach to Highly Emissive Copper Indium Sulfide Colloidal Nanocrystals and Their Bioimaging Applications. *ACS Appl. Mater. Interfaces* **2013**, *5*, 2870−2880.
(357) Fahmi, M. Z.; Chang, J. Y. Forming Double Layer-Encapsulated Quantum Dots for Bio-imaging and Cell Targeting. *Nanoscale* **2013**, *5*, 1517−1528.
(358) Bouccara, S.; Fragola, A.; Giovanelli, E.; Sitbon, G.; Lequeux, N.; Pons, T.; Loriette, V. Time-Gated Cell Imaging Using Long Lifetime Near-Infrared-Emitting Quantum Dots for Autofluorescence Rejection. *J. Biomed. Opt.* **2014**, *19*, 051208−051208.
(359) Soenen, S. J.; Rivera-Gil, P.; Montenegro, J.-M.; Parak, W. J.; De Smedt, S. C.; Braeckmans, K. Cellular Toxicity of Inorganic Nanoparticles: Common Aspects and Guidelines for Improved Nanotoxicity Evaluation. *Nano Today* **2011**, *6*, 446−465.
(360) Peng, F.; Su, Y.; Zhong, Y.; Fan, C.; Lee, S.-T.; He, Y. Silicon Nanomaterials Platform for Bioimaging, Biosensing, and Cancer Therapy. *Acc. Chem. Res.* **2014**, *47*, 612−623.
(361) Cheng, X.; Hinde, E.; Owen, D. M.; Lowe, S. B.; Reece, P. J.; Gaus, K.; Gooding, J. J. Enhancing Quantum Dots for Bioimaging Using Advanced Surface Chemistry and Advanced Optical Microscopy: Application to Silicon Quantum Dots (SiQDs). *Adv. Mater.* **2015**, *27*, 6144−6150.
(362) Lee, C.; Kim, J.; Zhang, Y.; Jeon, M.; Liu, C.; Song, L.; Lovell, J. F.; Kim, C. Dual-Color Photoacoustic Lymph Node Imaging Using Nanoformulated Naphthalocyanines. *Biomaterials* **2015**, *73*, 142−148.
(363) Chen, P.-J.; Kang, Y.-D.; Lin, C.-H.; Chen, S.-Y.; Hsieh, C.-H.; Chen, Y.-Y.; Chiang, C.-W.; Lee, W.; Hsu, C.-Y.; Liao, L.-D.; et al. Multitheragnostic Multi-GNRs Crystal-Seeded Magnetic Nano-seaurchin for Enhanced *in vivo* Mesenchymal-Stem-Cell Homing, Multimodal Imaging, and Stroke Therapy. *Adv. Mater.* **2015**, *27*, 6488−6495.
(364) Ripoll, J.; Koberstein-Schwarz, B.; Ntziachristos, V. Unleashing Optics and Optoacoustics for Developmental Biology. *Trends Biotechnol.* **2015**, *33*, 679−691.
(365) Garcia-Uribe, A.; Erpelding, T. N.; Krumholz, A.; Ke, H.; Maslov, K.; Appleton, C.; Margenthaler, J. A.; Wang, L. V. Dual-Modality Photoacoustic and Ultrasound Imaging System for Non-invasive Sentinel Lymph Node Detection in Patients with Breast Cancer. *Sci. Rep.* **2015**, *5*, 15748−15748.
(366) Mou, J.; Li, P.; Liu, C.; Xu, H.; Song, L.; Wang, J.; Zhang, K.; Chen, Y.; Shi, J.; Chen, H. Ultrasmall $Cu_{2-x}S$ Nanodots for Highly Efficient Photoacoustic Imaging-Guided Photothermal Therapy. *Small* **2015**, *11*, 2275−2283.
(367) Wang, H.-Y.; Hua, X.-W.; Wu, F.-G.; Li, B.; Liu, P.; Gu, N.; Wang, Z.; Chen, Z. Synthesis of Ultrastable Copper Sulfide Nanoclusters via Trapping the Reaction Intermediate: Potential Anticancer and Antibacterial Applications. *ACS Appl. Mater. Interfaces* **2015**, *7*, 7082−7092.
(368) Gao, D.; Zhang, P.; Liu, C.; Chen, C.; Gao, G.; Wu, Y.; Sheng, Z.; Song, L.; Cai, L. Compact Chelator-Free Ni-Integrated CuS Nanoparticles with Tunable Near-Infrared Absorption and Enhanced Relaxivity for *in vivo* Dual-Modal Photoacoustic/MR Imaging. *Nanoscale* **2015**, *7*, 17631−17636.
(369) Liu, X.; Lee, C.; Law, W. C.; Zhu, D.; Liu, M.; Jeon, M.; Kim, J.; Prasad, P. N.; Kim, C.; Swihart, M. T. Au-$Cu_{2-x}Se$ Heterodimer Nanoparticles with Broad Localized Surface Plasmon Resonance as Contrast Agents for Deep Tissue Imaging. *Nano Lett.* **2013**, *13*, 4333−4339.
(370) Ding, K.; Zeng, J.; Jing, L.; Qiao, R.; Liu, C.; Jiao, M.; Li, Z.; Gao, M. Aqueous Synthesis of PEGylated Copper Sulfide Nanoparticles for Photoacoustic Imaging of Tumors. *Nanoscale* **2015**, *7*, 11075−11081.
(371) Yang, K.; Zhu, L.; Nie, L.; Sun, X.; Cheng, L.; Wu, C.; Niu, G.; Chen, X.; Liu, Z. Visualization of Protease Activity *in vivo* Using an Activatable Photo-Acoustic Imaging Probe Based on CuS Nanoparticles. *Theranostics* **2014**, *4*, 134−141.
(372) Zha, Z.; Zhang, S.; Deng, Z.; Li, Y.; Li, C.; Dai, Z. Enzyme-Responsive Copper Sulphide Nanoparticles for Combined Photoacoustic Imaging, Tumor-Selective Chemotherapy and Photothermal Therapy. *Chem. Commun.* **2013**, *49*, 3455−3457.
(373) Liu, R.; Jing, L.; Peng, D.; Li, Y.; Tian, J.; Dai, Z. Manganese (II) Chelate Functionalized Copper Sulfide Nanoparticles for Efficient Magnetic Resonance/Photoacoustic Dual-Modal Imaging Guided Photothermal Therapy. *Theranostics* **2015**, *5*, 1144−1153.
(374) Song, J.; Yang, X.; Jacobson, O.; Lin, L.; Huang, P.; Niu, G.; Ma, Q.; Chen, X. Sequential Drug Release and Enhanced Photothermal and Photoacoustic Effect of Hybrid Reduced Graphene Oxide-Loaded Ultrasmall Gold Nanorod Vesicles for Cancer Therapy. *ACS Nano* **2015**, *9*, 9199−9209.
(375) Lin, Z.; Pan, D.; Hu, T.; Liu, Z.; Su, X. A Near-Infrared Fluorescent Bioassay for Thrombin Using Aptamer-Modified $CuInS_2$ Quantum Dots. *Microchim. Acta* **2015**, *182*, 1933−1939.
(376) Liu, S.; Shi, F.; Chen, L.; Su, X. Dopamine Functionalized $CuInS_2$ Quantum Dots as a Fluorescence Probe for Urea. *Sens. Actuators, B* **2014**, *191*, 246−251.
(377) Xiong, W.-W.; Yang, G.-H.; Wu, X.-C.; Zhu, J.-J. Microwave-Assisted Synthesis of Highly Luminescent $AgInS_2$/ZnS Nanocrystals for Dynamic Intracellular Cu(II) Detection. *J. Mater. Chem. B* **2013**, *1*, 4160−4165.
(378) Liu, S.; Na, W.; Pang, S.; Shi, F.; Su, X. A Label-Free Fluorescence Detection Strategy for Lysozyme Assay Using $CuInS_2$ Quantum Dots. *Analyst* **2014**, *139*, 3048−3054.
(379) Liu, S.; Pang, S.; Huang, H.; Su, X. 3-Aminophenylboronic Acid-Functionalized CuInS 2 Quantum Dots as a Near-Infrared Fluorescence Probe for the Detection of Dicyandiamide. *Analyst* **2014**, *139*, 5852−5857.
(380) Wu, P.; Zhao, T.; Tian, Y.; Wu, L.; Hou, X. Protein-Directed Synthesis of Mn-Doped ZnS Quantum Dots: A Dual-Channel Biosensor for Two Proteins. *Chem. - Eur. J.* **2013**, *19*, 7473−7479.
(381) Ren, H.-B.; Wu, B.-Y.; Chen, J.-T.; Yan, X.-P. Silica-Coated S2-Enriched Manganese-Doped ZnS Quantum Dots as a Photoluminescence Probe for Imaging Intracellular Zn^{2+} Ions. *Anal. Chem.* **2011**, *83*, 8239−8244.

DOI: 10.1021/acs.chemrev.6b00290
Chem. Rev. 2016, 116, 12234−12327

(382) Wen, L.-N.; Xie, M.-X. Competitive Binding Assay for G-Quadruplex DNA and Sanguinarine Based on Room Temperature Phosphorescence of Mn-Doped ZnS Quantum Dots. *J. Photochem. Photobiol., A* **2014**, *279*, 24−31.
(383) Zhu, D.; Chen, Y.; Jiang, L.; Geng, J.; Zhang, J.; Zhu, J.-J. Manganese-Doped ZnSe Quantum Dots as a Probe for Time-Resolved Fluorescence Detection of 5-Fluorouracil. *Anal. Chem.* **2011**, *83*, 9076−9081.
(384) Qian, Z. S.; Shan, X. Y.; Chai, L. J.; Chen, J. R.; Feng, H. Dual-Colored Graphene Quantum Dots-Labeled Nanoprobes/Graphene Oxide: Functional Carbon Materials for Respective and Simultaneous Detection of DNA and Thrombin. *Nanotechnology* **2014**, *25*, 415501.
(385) Zhang, L.; Zhang, Z. Y.; Liang, R. P.; Li, Y. H.; Qiu, J. D. Boron-Doped Graphene Quantum Dots for Selective Glucose Sensing Based on the "Abnormal" Aggregation-Induced Photoluminescence Enhancement. *Anal. Chem.* **2014**, *86*, 4423−4430.
(386) Jin, T.; Imamura, Y. Applications of Highly Bright PbS Quantum Dots to Non-Invasive Near-Infrared Fluorescence Imaging in the Second Optical Window. *ECS J. Solid State Sci. Technol.* **2016**, *5*, R3138−R3145.
(387) Gao, J.; Chen, K.; Xie, R.; Xie, J.; Yan, Y.; Cheng, Z.; Peng, X.; Chen, X. *In vivo* Tumor-Targeted Fluorescence Imaging Using Near-Infrared Non-Cadmium Quantum Dots. *Bioconjugate Chem.* **2010**, *21*, 604−609.
(388) Gao, J.; Chen, K.; Miao, Z.; Ren, G.; Chen, X.; Gambhir, S. S.; Cheng, Z. Affibody-Based Nanoprobes for HER2-Expressing Cell and Tumor Imaging. *Biomaterials* **2011**, *32*, 2141−2148.
(389) Gao, J.; Chen, K.; Luong, R.; Bouley, D. M.; Mao, H.; Qiao, T.; Gambhir, S. S.; Cheng, Z. A Novel Clinically Translatable Fluorescent Nanoparticle for Targeted Molecular Imaging of Tumors in Living Subjects. *Nano Lett.* **2012**, *12*, 281−286.
(390) Pons, T.; Pic, E.; Lequeux, N.; Cassette, E.; Bezdetnaya, L.; Guillemin, F.; Marchal, F.; Dubertret, B. Cadmium-Free $CuInS_2$/ZnS Quantum Dots for Sentinel Lymph Node Imaging with Reduced Toxicity. *ACS Nano* **2010**, *4*, 2531−2538.
(391) Helle, M.; Cassette, E.; Bezdetnaya, L.; Pons, T.; Leroux, A.; Plenat, F.; Guillemin, F.; Dubertret, B.; Marchal, F. Visualisation of Sentinel Lymph Node with Indium-Based Near Infrared Emitting Quantum Dots in a Murine Metastatic Breast Cancer Model. *PLoS One* **2012**, *7*, e44433−e44433.
(392) Panthani, M. G.; Khan, T. A.; Reid, D. K.; Hellebusch, D. J.; Rasch, M. R.; Maynard, J. A.; Korgel, B. A. *In vivo* Whole Animal Fluorescence Imaging of a Microparticle-Based Oral Vaccine Containing ($CuInSe_xS_{2-x}$)/ZnS Core/Shell Quantum Dots. *Nano Lett.* **2013**, *13*, 4294−4298.
(393) Janowski, M.; Bulte, J. W. M.; Walczak, P. Personalized Nanomedicine Advancements for Stem Cell Tracking. *Adv. Drug Delivery Rev.* **2012**, *64*, 1488−1507.
(394) Kawabori, M.; Kuroda, S.; Sugiyama, T.; Ito, M.; Shichinohe, H.; Houkin, K.; Kuge, Y.; Tamaki, N. Intracerebral, but Not Intravenous, Transplantation of Bone Marrow Stromal Cells Enhances Functional Recovery in Rat Cerebral Infarct: An Optical Imaging Study. *Neuropathology* **2012**, *32*, 217−226.
(395) Zhao, P.; Zheng, M.; Luo, Z.; Gong, P.; Gao, G.; Sheng, Z.; Zheng, C.; Ma, Y.; Cai, L. NIR-Driven Smart Theranostic Nanomedicine for On-Demand Drug Release and Synergistic Antitumour Therapy. *Sci. Rep.* **2015**, *5*, 14258−14258.
(396) Chen, Q.; Ke, H.; Dai, Z.; Liu, Z. Nanoscale Theranostics for Physical Stimulus-Responsive Cancer Therapies. *Biomaterials* **2015**, *73*, 214−230.
(397) Kang, S.; Bhang, S. H.; Hwang, S.; Yoon, J.-K.; Song, J.; Jang, H.-K.; Kim, S.; Kim, B.-S. Mesenchymal Stem Cells Aggregate and Deliver Gold Nanoparticles to Tumors for Photothermal Therapy. *ACS Nano* **2015**, *9*, 9678−9690.
(398) Dong, J.; Zink, J. I. Light or Heat? The Origin of Cargo Release from Nanoimpeller Particles Containing Upconversion Nanocrystals under IR Irradiation. *Small* **2015**, *11*, 4165−4172.
(399) Oh, M. H.; Yu, J. H.; Kim, I.; Nam, Y. S. Genetically Programmed Clusters of Gold Nanoparticles for Cancer Cell-Targeted Photothermal Therapy. *ACS Appl. Mater. Interfaces* **2015**, *7*, 22578−22586.
(400) Cao, M.; Wang, P.; Kou, Y.; Wang, J.; Liu, J.; Li, Y.; Li, J.; Wang, L.; Chen, C. Gadolinium(III)-Chelated Silica Nanospheres Integrating Chemotherapy and Photothermal Therapy for Cancer Treatment and Magnetic Resonance Imaging. *ACS Appl. Mater. Interfaces* **2015**, *7*, 25014−25023.
(401) Guo, J.; Rahme, K.; Fitzgerald, K. A.; Holmes, J. D.; O'Driscoll, C. M. Biomimetic Gold Nanocomplexes for Gene Knockdown: Will Gold Deliver Dividends for Small Interfering RNA Nanomedicines? *Nano Res.* **2015**, *8*, 3111−3140.
(402) Jiang, T.; Song, J.; Zhang, W.; Wang, H.; Li, X.; Xia, R.; Zhu, L.; Xu, X. Au-Ag@Au Hollow Nanostructure with Enhanced Chemical Stability and Improved Photothermal Transduction Efficiency for Cancer Treatment. *ACS Appl. Mater. Interfaces* **2015**, *7*, 21985−21994.
(403) Tian, Q.; Jiang, F.; Zou, R.; Liu, Q.; Chen, Z.; Zhu, M.; Yang, S.; Wang, J.; Wang, J.; Hu, J. Hydrophilic Cu_9S_5 Nanocrystals: A Photothermal Agent with a 25.7% Heat Conversion Efficiency for Photothermal Ablation of Cancer Cells *in vivo*. *ACS Nano* **2011**, *5*, 9761−9771.
(404) Chen, F.; Cai, W. Nanomedicine for Targeted Photothermal Cancer Therapy: Where Are We Now? *Nanomedicine* **2015**, *10*, 1−3.
(405) Chen, Y.; Hou, Z.; Liu, B.; Huang, S.; Li, C.; Lin, J. DOX-Cu_9S_5@$mSiO_2$-PG Composite Fibers for Orthotopic Synergistic Chemo- and Photothermal Tumor Therapy. *Dalton Trans.* **2015**, *44*, 3118−3127.
(406) Wang, S.; Riedinger, A.; Li, H.; Fu, C.; Liu, H.; Li, L.; Liu, T.; Tan, L.; Barthel, M. J.; Pugliese, G.; et al. Plasmonic Copper Sulfide Nanocrystals Exhibiting Near-Infrared Photothermal and Photodynamic Therapeutic Effects. *ACS Nano* **2015**, *9*, 1788−1800.
(407) Lu, F.; Wang, J.; Yang, L.; Zhu, J.-J. A Facile One-Pot Synthesis of Colloidal Stable, Monodisperse, Highly PEGylated CuS@$mSiO_2$ Nanocomposites for the Combination of Photothermal Therapy and Chemotherapy. *Chem. Commun.* **2015**, *51*, 9447−9450.
(408) Liu, X.; Ren, Q.; Fu, F.; Zou, R.; Wang, Q.; Xin, G.; Xiao, Z.; Huang, X.; Liu, Q.; Hu, J. CuS@$mSiO_2$-PEG Core-Shell Nanoparticles as a NIR Light Responsive Drug Delivery Nanoplatform for Efficient Chemo-Photothermal Therapy. *Dalton Trans.* **2015**, *44*, 10343−10351.
(409) Lin, B.; Yao, X.; Zhu, Y.; Shen, J.; Yang, X.; Li, C. Multifunctional Gadolinium-Labeled Silica-Coated Core/Shell Quantum Dots for Magnetic Resonance and Fluorescence Imaging of Cancer Cells. *RSC Adv.* **2014**, *4*, 20641−20648.
(410) Shen, J.; Li, Y.; Zhu, Y.; Yang, X.; Yao, X.; Li, J.; Huang, G.; Li, C. Multifunctional Gadolinium-Labeled Silica-Coated Fe_3O_4 and $CuInS_2$ Nanoparticles as a Platform for *in vivo* Tri-Modality Magnetic Resonance and Fluorescence Imaging. *J. Mater. Chem. B* **2015**, *3*, 2873−2882.
(411) Mou, J.; Liu, C.; Li, P.; Chen, Y.; Xu, H.; Wei, C.; Song, L.; Shi, J.; Chen, H. A Facile Synthesis of Versatile $Cu_{2-x}S$ Nanoprobe for Enhanced MRI and Infrared Thermal/Photoacoustic Multimodal Imaging. *Biomaterials* **2015**, *57*, 12−21.
(412) Hu, R.; Wang, Y.; Liu, X.; Lin, G.; Tan, C. H.; Law, W.-C.; Roy, I.; Yong, K.-T. Rational Design of Multimodal and Multifunctional InP Quantum Dot Nanoprobes for Cancer: *In vitro* and *in vivo* Applications. *RSC Adv.* **2013**, *3*, 8495−8503.
(413) Yang, Y.; Wang, J.; Li, X.; Lin, L.; Yue, X. A Near Infrared Fluorescent/Ultrasonic Bimodal Contrast Agent for Imaging Guided pDNA Delivery via Ultrasound Targeted Microbubble Destruction. *RSC Adv.* **2015**, *5*, 8404−8414.
(414) Yang, Y.; Wu, H.; Shi, B.; Guo, L.; Zhang, Y.; An, X.; Zhang, H.; Yang, S. Hydrophilic Cu_3BiS_3 Nanoparticles for Computed Tomography Imaging and Photothermal Therapy. *Part. Part. Syst. Char.* **2015**, *32*, 668−679.
(415) Poulose, A. C.; Veeranarayanan, S.; Mohamed, M. S.; Nagaoka, Y.; Aburto, R. R.; Mitcham, T.; Ajayan, P. M.; Bouchard, R. R.; Sakamoto, Y.; Yoshida, Y.; et al. Multi-stimuli Responsive Cu_2S Nanocrystals as Trimodal Imaging and Synergistic Chemo-Photothermal Therapy Agents. *Nanoscale* **2015**, *7*, 8378−8388.

DOI: 10.1021/acs.chemrev.6b00290
Chem. Rev. 2016, 116, 12234−12327

(416) Chen, F.; Hong, H.; Goel, S.; Graves, S. A.; Orbay, H.; Ehlerding, E. B.; Shi, S.; Theuer, C. P.; Nickles, R. J.; Cai, W. *In vivo* Tumor Vasculature Targeting of CuS@MSN Based Theranostic Nanomedicine. *ACS Nano* **2015**, *9*, 3926−3934.
(417) Song, X.-R.; Wang, X.; Yu, S.-X.; Cao, J.; Li, S.-H.; Li, J.; Liu, G.; Yang, H.-H.; Chen, X. Co_9Se_8 Nanoplates as a New Theranostic Platform for Photoacoustic/Magnetic Resonance Dual-Modal-Imaging-Guided Chemo-Photothermal Combination Therapy. *Adv. Mater.* **2015**, *27*, 3285−3291.
(418) Moghimi, S. M.; Hunter, A. C.; Murray, J. C. Nanomedicine: Current Status and Future Prospects. *FASEB J.* **2005**, *19*, 311−330.
(419) Jain, R. K.; Stylianopoulos, T. Delivering Nanomedicine to Solid Tumors. *Nat. Rev. Clin. Oncol.* **2010**, *7*, 653−664.
(420) Huang, P.; Gao, Y.; Lin, J.; Hu, H.; Liao, H.-S.; Yan, X.; Tang, Y.; Jin, A.; Song, J.; Niu, G.; et al. Tumor-Specific Formation of Enzyme-Instructed Supramolecular Self-Assemblies as Cancer Theranostics. *ACS Nano* **2015**, *9*, 9517−9527.
(421) Chen, F.; Nayak, T. R.; Goel, S.; Valdovinos, H. F.; Hong, H.; Theuer, C. P.; Barnhart, T. E.; Cai, W. *In vivo* Tumor Vasculature Targeted PET/NIRF Imaging with TRC105(Fab)-Conjugated, Dual-Labeled Mesoporous Silica Nanoparticles. *Mol. Pharmaceutics* **2014**, *11*, 4007−4014.
(422) He, Q.; Kiesewetter, D. O.; Qu, Y.; Fu, X.; Fan, J.; Huang, P.; Liu, Y.; Zhu, G.; Liu, Y.; Qian, Z.; et al. NIR-Responsive On-Demand Release of CO from Metal Carbonyl-Caged Graphene Oxide Nanomedicine. *Adv. Mater.* **2015**, *27*, 6741−6746.
(423) Landgraf, L.; Christner, C.; Storck, W.; Schick, I.; Krumbein, I.; Daehring, H.; Haedicke, K.; Heinz-Herrmann, K.; Teichgraeber, U.; Reichenbach, J. R.; et al. A Plasma Protein Corona Enhances the Biocompatibility of Au@Fe_3O_4 Janus Particles. *Biomaterials* **2015**, *68*, 77−88.
(424) Song, J.; Huang, P.; Duan, H.; Chen, X. Plasmonic Vesicles of Amphiphilic Nanocrystals: Optically Active Multifunctional Platform for Cancer Diagnosis and Therapy. *Acc. Chem. Res.* **2015**, *48*, 2506−2515.
(425) Boisselier, E.; Astruc, D. Gold Nanoparticles in Nanomedicine: Preparations, Imaging, Diagnostics, Therapies and Toxicity. *Chem. Soc. Rev.* **2009**, *38*, 1759−1782.
(426) Gao, J.; Gu, H.; Xu, B. Multifunctional Magnetic Nanoparticles: Design, Synthesis, and Biomedical Applications. *Acc. Chem. Res.* **2009**, *42*, 1097−1107.
(427) Prato, M.; Kostarelos, K.; Bianco, A. Functionalized Carbon Nanotubes in Drug Design and Discovery. *Acc. Chem. Res.* **2008**, *41*, 60−68.
(428) Shi, J.; Votruba, A. R.; Farokhzad, O. C.; Langer, R. Nanotechnology in Drug Delivery and Tissue Engineering: From Discovery to Applications. *Nano Lett.* **2010**, *10*, 3223−3230.
(429) Roy, I.; Ohulchanskyy, T. Y.; Bharali, D. J.; Pudavar, H. E.; Mistretta, R. A.; Kaur, N.; Prasad, P. N. Optical Tracking of Organically Modified Silica Nanoparticles as DNA Carriers: A Nonviral, Nanomedicine Approach for Gene Delivery. *Proc. Natl. Acad. Sci. U. S. A.* **2005**, *102*, 279−284.
(430) Huang, W.-C.; Chiang, W.-H.; Cheng, Y.-H.; Lin, W.-C.; Yu, C.-F.; Yen, C.-Y.; Yeh, C.-K.; Chern, C.-S.; Chiang, C.-S.; Chiu, H.-C. Tumortropic Monocyte-Mediated Delivery of Echogenic Polymer Bubbles and Therapeutic Vesicles for Chemotherapy of Tumor Hypoxia. *Biomaterials* **2015**, *71*, 71−83.
(431) Moon, H.; Kang, J.; Sim, C.; Kim, J.; Lee, H.; Chang, J. H.; Kim, H. Multifunctional Theranostic Contrast Agent for Photoacoustics- and Ultrasound-Based Tumor Diagnosis and Ultrasound-Stimulated Local Tumor Therapy. *J. Controlled Release* **2015**, *218*, 63−71.
(432) Wu, P.-J.; Ou, K.-L.; Chen, J.-K.; Fang, H.-P.; Tzing, S.-H.; Lin, W.-X.; Chang, J.-Y. Methotrexate-Conjugated $AgInS_2$/ZnS Quantum Dots for Optical Imaging and Drug Delivery. *Mater. Lett.* **2014**, *128*, 412−416.
(433) Xu, Z.; Li, B.; Tang, W.; Chen, T.; Zhang, H.; Wang, Q. Glycopolypeptide-Encapsulated Mn-Doped ZnS Quantum Dots for Drug Delivery: Fabrication, Characterization, and *in vitro* Assessment. *Colloids Surf., B* **2011**, *88*, 51−57.
(434) Sanpui, P.; Pandey, S. B.; Chattopadhyay, A.; Ghosh, S. S. Incorporation of Gene Therapy Vector in Chitosan Stabilized Mn^{2+}-Doped ZnS Quantum Dot. *Mater. Lett.* **2010**, *64*, 2534−2537.
(435) Klein, S.; Zolk, O.; Fromm, M. F.; Schroedl, F.; Neuhuber, W.; Kryschi, C. Functionalized Silicon Quantum Dots Tailored for Targeted siRNA Delivery. *Biochem. Biophys. Res. Commun.* **2009**, *387*, 164−168.
(436) Liu, S.; Shi, F.; Chen, L.; Su, X. Albumin Coated $CuInS_2$ Quantum Dots as a Near-Infrared Fluorescent Probe for NADH, and Their Application to an Assay for Pyruvate. *Microchim. Acta* **2014**, *181*, 339−345.
(437) Tu, C.-C.; Chou, Y.-N.; Hung, H.-C.; Wu, J.; Jiang, S.; Lin, L. Y. Fluorescent Porous Silicon Biological Probes with High Quantum Efficiency and Stability. *Opt. Express* **2014**, *22*, 29996−30003.
(438) Charron, G.; Stuchinskaya, T.; Edwards, D. R.; Russell, D. A.; Nann, T. Insights into the Mechanism of Quantum Dot-Sensitized Singlet Oxygen Production for Photodynamic Therapy. *J. Phys. Chem. C* **2012**, *116*, 9334−9342.
(439) Kim, S. W.; Zimmer, J. P.; Ohnishi, S.; Tracy, J. B.; Frangioni, J. V.; Bawendi, M. G. Engineering $InAs_xP_{1-x}$/InP/ZnSe III-V Alloyed Core/Shell Quantum Dots for the Near-Infrared. *J. Am. Chem. Soc.* **2005**, *127*, 10526−10532.
(440) Gao, X.; Liu, X.; Lin, Z.; Liu, S.; Su, X. $CuInS_2$ Quantum Dots as a Near-Infrared Fluorescent Probe for Detecting Thrombin in Human Serum. *Analyst* **2012**, *137*, 5620−5624.
(441) Liu, J.-H.; Yang, S.-T.; Chen, X.-X.; Wang, H. Fluorescent Carbon Dots and Nanodiamonds for Biological Imaging: Preparation, Application, Pharmacokinetics and Toxicity. *Curr. Drug Metab.* **2012**, *13*, 1046−1056.
(442) Aswathy, J.; Seethalekshmy, N.; Hiran, K.; Bindhu, M.; Manzoor, K.; Nair, S. V.; Menon, D. Mn-Doped Zinc Sulphide Nanocrystals for Immunofluorescent Labeling of Epidermal Growth Factor Receptors on Cells and Clinical Tumor Tissues. *Nanotechnology* **2014**, *25*, 445102.
(443) Krejcova, L.; Hynek, D.; Kopel, P.; Rodrigo, M. A. M.; Tmejova, K.; Trnkova, L.; Adam, V.; Hubalek, J.; Kizek, R. Quantum Dots for Electrochemical Labelling of Neuramidinase Genes of H5N1, H1N1 and H3N2 Influenza. *Int. J. Electrochem. Sci.* **2013**, *8*, 4457−4471.
(444) Krejcova, L.; Hynek, D.; Kopel, P.; Rodrigo, M. A. M.; Adam, V.; Hubalek, J.; Babula, P.; Trnkova, L.; Kizek, R. Development of a Magnetic Electrochemical Bar Code Array for Point Mutation Detection in the H5N1 Neuraminidase Gene. *Viruses* **2013**, *5*, 1719−1739.
(445) Ristic, B. Z.; Milenkovic, M. M.; Dakic, I. R.; Todorovic-Markovic, B. M.; Milosavljevic, M. S.; Budimir, M. D.; Paunovic, V. G.; Dramicanin, M. D.; Markovic, Z. M.; Trajkovic, V. S. Photodynamic Antibacterial Effect of Graphene Quantum Dots. *Biomaterials* **2014**, *35*, 4428−4435.
(446) Baruah, S.; Ortinero, C.; Shipin, O. V.; Dutta, J. Manganese Doped Zinc Sulfide Quantum Dots for Detection of Escherichia Coli. *J. Fluoresc.* **2012**, *22*, 403−408.
(447) Gu, L.; Ruff, L. E.; Qin, Z.; Corr, M.; Hedrick, S. M.; Sailor, M. J. Multivalent Porous Silicon Nanoparticles Enhance the Immune Activation Potency of Agonistic CD40 Antibody. *Adv. Mater.* **2012**, *24*, 3981−3987.
(448) Dhyani, H.; Ali, M. A.; Pal, S. P.; Srivastava, S.; Solanki, P. R.; Malhotra, B. D.; Sen, P. Mediator-Free Biosensor Using Chitosan Capped CdS Quantum Dots for Detection of Total Cholesterol. *RSC Adv.* **2015**, *5*, 45928−45934.
(449) Liu, S.; Na, W.; Pang, S.; Su, X. Fluorescence Detection of Pb^{2+} Based on the DNA Sequence Functionalized CdS Quantum Dots. *Biosens. Bioelectron.* **2014**, *58*, 17−21.
(450) Breger, J.; Delehanty, J. B.; Medintz, I. L. Continuing Progress Toward Controlled Intracellular Delivery of Semiconductor Quantum Dots. *Wires. Nanomed. Nanobi.* **2015**, *7*, 131−151.

DOI: 10.1021/acs.chemrev.6b00290
Chem. Rev. 2016, 116, 12234−12327

(451) Ferrari, M. Cancer Nanotechnology.: Opportunities and Challenges. *Nat. Rev. Cancer* **2005**, *5*, 161−171.
(452) Smith, A. M.; Duan, H.; Mohs, A. M.; Nie, S. Bioconjugated Quantum Dots for *in vivo* Molecular and Cellular Imaging. *Adv. Drug Delivery Rev.* **2008**, *60*, 1226−1240.
(453) Singh, R.; Lillard, J. W., Jr. Nanoparticle-Based Targeted Drug Delivery. *Exp. Mol. Pathol.* **2009**, *86*, 215−223.
(454) Zhang, Y.; Hou, Z.; Ge, Y.; Deng, K.; Liu, B.; Li, X.; Li, Q.; Cheng, Z.; Ma, P. a.; Li, C.; et al. DNA-Hybrid-Gated Photothermal Mesoporous Silica Nanoparticles for MR-Responsive and Aptamer-Targeted Drug Delivery. *ACS Appl. Mater. Interfaces* **2015**, *7*, 20696−20706.
(455) Chen, G.; Wang, L.; Cordie, T.; Vokoun, C.; Eliceiri, K. W.; Gong, S. Multi-Functional Self-Fluorescent Unimolecular Micelles for Tumor-Targeted Drug Delivery and Bioimaging. *Biomaterials* **2015**, *47*, 41−50.
(456) Win, K. Y.; Teng, C. P.; Ye, E.; Low, M.; Han, M.-Y. Evaluation of Polymeric Nanoparticle Formulations by Effective Imaging and Quantitation of Cellular Uptake for Controlled Delivery of Doxorubicin. *Small* **2015**, *11*, 1197−1204.
(457) Wang, Z.; Liu, G.; Zheng, H.; Chen, X. Rigid Nanoparticle-Based Delivery of Anti-Cancer siRNA: Challenges and Opportunities. *Biotechnol. Adv.* **2014**, *32*, 831−843.
(458) Zhang, L.; Gu, F. X.; Chan, J. M.; Wang, A. Z.; Langer, R. S.; Farokhzad, O. C. Nanoparticles in Medicine: Therapeutic Applications and Developments. *Clin. Pharmacol. Ther.* **2008**, *83*, 761−769.
(459) Arias, J. L.; Reddy, L. H.; Couvreur, P. Fe_3O_4/Chitosan Nanocomposite for Magnetic Drug Targeting to Cancer. *J. Mater. Chem.* **2012**, *22*, 7622−7632.
(460) Lin, J.; Li, Y.; Li, Y.; Wu, H.; Yu, F.; Zhou, S.; Xie, L.; Luo, F.; Lin, C.; Hou, Z. Drug/Dye-Loaded, Multifunctional PEG-Chitosan-Iron Oxide Nanocomposites for Methotraxate Synergistically Self-Targeted Cancer Therapy and Dual Model Imaging. *ACS Appl. Mater. Interfaces* **2015**, *7*, 11908−11920.
(461) Silva, A. K. A.; Luciani, N.; Gazeau, F.; Aubertin, K.; Bonneau, S.; Chauvierre, C.; Letourneur, D.; Wilhelm, C. Combining Magnetic Nanoparticles with Cell Derived Microvesicles for Drug Loading and Targeting. *Nanomedicine* **2015**, *11*, 645−655.
(462) Zrazhevskiy, P.; Sena, M.; Gao, X. Designing Multifunctional Quantum Dots for Bioimaging, Detection, and Drug Delivery. *Chem. Soc. Rev.* **2010**, *39*, 4326−4354.
(463) Chithrani, B. D.; Ghazani, A. A.; Chan, W. C. W. Determining the Size and Shape Dependence of Gold Nanoparticle Uptake into Mammalian Cells. *Nano Lett.* **2006**, *6*, 662−668.
(464) Nel, A. E.; Maedler, L.; Velegol, D.; Xia, T.; Hoek, E. M. V.; Somasundaran, P.; Klaessig, F.; Castranova, V.; Thompson, M. Understanding Biophysicochemical Interactions at the Nano-Bio Interface. *Nat. Mater.* **2009**, *8*, 543−557.
(465) Kafshgari, M. H.; Harding, F. J.; Voelcker, N. H. Insights into Cellular Uptake of Nanoparticles. *Curr. Drug Delivery* **2015**, *12*, 63−77.
(466) Xie, J.; Xu, C.; Kohler, N.; Hou, Y.; Sun, S. Controlled PEGylation of Monodisperse Fe_3O_4 Nanoparticles for Reduced Non-Specific Uptake by Macrophage Cells. *Adv. Mater.* **2007**, *19*, 3163−3166.
(467) Gao, X. L.; Tao, W. X.; Lu, W.; Zhang, Q. Z.; Zhang, Y.; Jiang, X. G.; Fu, S. K. Lectin-Conjugated PEG-PLA Nanoparticles: Preparation and Brain Delivery after Intranasal Administration. *Biomaterials* **2006**, *27*, 3482−3490.
(468) Miller-Kleinhenz, J. M.; Bozeman, E. N.; Yang, L. Targeted Nanoparticles for Image-Guided Treatment of Triple-Negative Breast Cancer: Clinical Significance and Technological Advances. *Wires. Nanomed. Nanobi.* **2015**, *7*, 797−816.
(469) Bhirde, A. A.; Patel, V.; Gavard, J.; Zhang, G.; Sousa, A. A.; Masedunskas, A.; Leapman, R. D.; Weigert, R.; Gutkind, J. S.; Rusling, J. F. Targeted Killing of Cancer Cells *in vivo* and *in vitro* with EGF-Directed Carbon Nanotube-Based Drug Delivery. *ACS Nano* **2009**, *3*, 307−316.
(470) Hsu, J.-C.; Huang, C.-C.; Ou, K.-L.; Lu, N.; Mai, F.-D.; Chen, J.-K.; Chang, J.-Y. Silica Nanohybrids Integrated with $CuInS_2$/ZnS Quantum Dots and Magnetite Nanocrystals: Multifunctional Agents for Dual-Modality Imaging and Drug Delivery. *J. Mater. Chem.* **2011**, *21*, 19257−19266.
(471) Mathew, M. E.; Mohan, J. C.; Manzoor, K.; Nair, S. V.; Tamura, H.; Jayakumar, R. Folate Conjugated Carboxymethyl Chitosan-Manganese Doped Zinc Sulphide Nanoparticles for Targeted Drug Delivery and Imaging of Cancer Cells. *Carbohydr. Polym.* **2010**, *80*, 442−448.
(472) Park, J.-H.; Gu, L.; Von Maltzahn, G.; Ruoslahti, E.; Bhatia, S. N.; Sailor, M. J. Biodegradable Luminescent Porous Silicon Nanoparticles for *in vivo* Applications. *Nat. Mater.* **2009**, *8*, 331−336.
(473) Xu, Z.; Wang, D.; Guan, M.; Liu, X.; Yang, Y.; Wei, D.; Zhao, C.; Zhang, H. Photoluminescent Silicon Nanocrystal-Based Multifunctional Carrier for pH-Regulated Drug Delivery. *ACS Appl. Mater. Interfaces* **2012**, *4*, 3424−3431.
(474) Hanada, S.; Fujioka, K.; Futamura, Y.; Manabe, N.; Hoshino, A.; Yamamoto, K. Evaluation of Anti-Inflammatory Drug-Conjugated Silicon Quantum Dots: Their Cytotoxicity and Biological Effect. *Int. J. Mol. Sci.* **2013**, *14*, 1323−1334.
(475) Deepagan, V. G.; Sarmento, B.; Menon, D.; Nascimento, A.; Jayasree, A.; Sreeranganathan, M.; Koyakutty, M.; Nair, S. V.; Rangasamy, J. *In vitro* Targeted Imaging and Delivery of Camptothecin Using Cetuximab-Conjugated Multifunctional PLGA-ZnS Nanoparticles. *Nanomedicine* **2012**, *7*, 507−519.
(476) Lin, W. J.; Chien, W. H. Peptide-Conjugated Micelles as a Targeting Nanocarrier for Gene Delivery. *J. Nanopart. Res.* **2015**, *17*, 349.
(477) Naldini, L. Gene Therapy Returns to Centre Stage. *Nature* **2015**, *526*, 351−360.
(478) Chen, G.; Zhu, J.-Y.; Zhang, Z.-L.; Zhang, W.; Ren, J.-G.; Wu, M.; Hong, Z.-Y.; Lv, C.; Pang, D.-W.; Zhao, Y.-F. Transformation of Cell-Derived Microparticles into Quantum-Dot-Labeled Nanovectors for Antitumor siRNA Delivery. *Angew. Chem., Int. Ed.* **2015**, *54*, 1036−1040.
(479) Chinnathambi, S.; Chen, S.; Ganesan, S.; Hanagata, N. Binding Mode of CpG Oligodeoxynucleotides to Nanoparticles Regulates Bifurcated Cytokine Induction via Toll-Like Receptor 9. *Sci. Rep.* **2012**, *2*, 534.
(480) Zhao, J.; Zhang, B.; Shen, S.; Chen, J.; Zhang, Q.; Jiang, X.; Pang, Z. CREKA Peptide-Conjugated Dendrimer Nanoparticles for Glioblastoma Multiforme Delivery. *J. Colloid Interface Sci.* **2015**, *450*, 396−403.
(481) Benezra, M.; Phillips, E.; Overholtzer, M.; Zanzonico, P. B.; Tuominen, E.; Wiesner, U.; Bradbury, M. S. Ultrasmall Integrin-Targeted Silica Nanoparticles Modulate Signaling Events and Cellular Processes in a Concentration-Dependent Manner. *Small* **2015**, *11*, 1721−1732.
(482) Thovhogi, N.; Sibuyi, N.; Meyer, M.; Onani, M.; Madiehe, A. Targeted Delivery Using Peptide-Functionalised Gold Nanoparticles to White Adipose Tissues of Obese Rats. *J. Nanopart. Res.* **2015**, *17*, 112.
(483) Schaeffler, M.; Sousa, F.; Wenk, A.; Sitia, L.; Hirn, S.; Schleh, C.; Haberl, N.; Violatto, M.; Canovi, M.; Andreozzi, P.; et al. Blood Protein Coating of Gold Nanoparticles as Potential Tool for Organ Targeting. *Biomaterials* **2014**, *35*, 3455−3466.
(484) Chatterjee, S.; Mukherjee, T. K. Spectroscopic Investigation of Interaction between Bovine Serum Albumin and Amine-Functionalized Silicon Quantum Dots. *Phys. Chem. Chem. Phys.* **2014**, *16*, 8400−8408.
(485) Gonda, K.; Miyashita, M.; Higuchi, H.; Tada, H.; Watanabe, T. M.; Watanabe, M.; Ishida, T.; Ohuchi, N. Predictive Diagnosis of the Risk of Breast Cancer Recurrence after Surgery by Single-Particle Quantum Dot Imaging. *Sci. Rep.* **2015**, *5*, 14322−14322.
(486) Hu, K.; Wang, H.; Tang, G.; Huang, T.; Tang, X.; Liang, X.; Yao, S.; Nie, D. *In vivo* Cancer Dual-Targeting and Dual-Modality Imaging with Functionalized Quantum Dots. *J. Nucl. Med.* **2015**, *56*, 1278−1284.

DOI: 10.1021/acs.chemrev.6b00290
Chem. Rev. 2016, 116, 12234−12327

(487) Dong, H.; Dai, W.; Ju, H.; Lu, H.; Wang, S.; Xu, L.; Zhou, S.-F.; Zhang, Y.; Zhang, X. Multifunctional Poly(L-lactide)-Polyethylene Glycol-Grafted Graphene Quantum Dots for Intracellular MicroRNA Imaging and Combined Specific-Gene-Targeting Agents Delivery for Improved Therapeutics. *ACS Appl. Mater. Interfaces* **2015**, *7*, 11015−11023.
(488) Bu, L.; Ma, X.; Tu, Y.; Shen, B.; Cheng, Z. Optical Image-Guided Cancer Therapy. *Curr. Pharm. Biotechnol.* **2013**, *14*, 723−732.
(489) Li, C.-H.; Kuo, T.-R.; Su, H.-J.; Lai, W.-Y.; Yang, P.-C.; Chen, J.-S.; Wang, D.-Y.; Wu, Y.-C.; Chen, C.-C. Fluorescence-Guided Probes of Aptamer-Targeted Gold Nanoparticles with Computed Tomography Imaging Accesses for *in vivo* Tumor Resection. *Sci. Rep.* **2015**, *5*, 15675−15675.
(490) Xi, L.; Zhou, G.; Gao, N.; Yang, L.; Gonzalo, D. A.; Hughes, S. J.; Jiang, H. Photoacoustic and Fluorescence Image-Guided Surgery Using a Multifunctional Targeted Nanoprobe. *Ann. Surg. Oncol.* **2014**, *21*, 1602−1609.
(491) Tan, L.; Wan, A.; Li, H. Synthesis of Near-Infrared Quantum Dots in Cultured Cancer Cells. *ACS Appl. Mater. Interfaces* **2014**, *6*, 18−23.
(492) Erogbogbo, F.; Tien, C. A.; Chang, C. W.; Yong, K. T.; Law, W. C.; Ding, H.; Roy, I.; Swihart, M. T.; Prasad, P. N. Bioconjugation of Luminescent Silicon Quantum Dots for Selective Uptake by Cancer Cells. *Bioconjugate Chem.* **2011**, *22*, 1081−1088.
(493) Erogbogbo, F.; Liu, X.; May, J. L.; Narain, A.; Gladding, P.; Swihart, M. T.; Prasad, P. N. Plasmonic Gold and Luminescent Silicon Nanoplatforms for Multimode Imaging of Cancer Cells. *Integr. Biol.* **2013**, *5*, 144−150.
(494) Wang, J.; Liu, Y.; Peng, F.; Chen, C.; He, Y.; Ma, H.; Cao, L.; Sun, S. A General Route to Efficient Functionalization of Silicon Quantum Dots for High-Performance Fluorescent Probes. *Small* **2012**, *8*, 2430−2435.
(495) Shah, J. P.; Gil, Z. Current Concepts in Management of Oral Cancer - Surgery. *Oral Oncol.* **2009**, *45*, 394−401.
(496) Tagliabue, M.; Elrefaey, S. H.; Peccatori, F.; Favia, G.; Navach, V.; Pignataro, L.; Capaccio, P.; Venturino, M.; Tredici, S.; Alterio, D.; et al. Tongue Cancer During Pregnancy: Surgery and More, a Multidisciplinary Challenge. *Crit. Rev. Oncol. Hemat.* **2016**, *98*, 1−11.
(497) Bozec, A.; Ceruse, P. Head and Neck Oncologic Surgery Today and Tomorrow. *Oncologie* **2015**, *17*, 220−224.
(498) Li, Y.; Li, Z.; Wang, X.; Liu, F.; Cheng, Y.; Zhang, B.; Shi, D. *In vivo* Cancer Targeting and Imaging-Guided Surgery with Near Infrared-Emitting Quantum Dot Bioconjugates. *Theranostics* **2012**, *2*, 769−776.
(499) Zhou, M.; Li, J.; Liang, S.; Sood, A. K.; Liang, D.; Li, C. CuS Nanodots with Ultrahigh Efficient Renal Clearance for Positron Emission Tomography Imaging and Image-Guided Photothermal Therapy. *ACS Nano* **2015**, *9*, 7085−7096.
(500) Ashitate, Y.; Hyun, H.; Kim, S. H.; Lee, J. H.; Henary, M.; Frangioni, J. V.; Choi, H. S. Simultaneous Mapping of Pan and Sentinel Lymph Nodes for Real-Time Image-Guided Surgery. *Theranostics* **2014**, *4*, 693−700.
(501) Rizvi, S. B.; Rouhi, S.; Taniguchi, S.; Yang, S. Y.; Green, M.; Keshtgar, M.; Seifalian, A. M. Near-Infrared Quantum Dots for HER2 Localization and Imaging of Cancer Cells. *Int. J. Nanomed.* **2014**, *9*, 1323−1337.
(502) Li, C.; Cao, L.; Zhang, Y.; Yi, P.; Wang, M.; Tan, B.; Deng, Z.; Wu, D.; Wang, Q. Preoperative Detection and Intraoperative Visualization of Brain Tumors for More Precise Surgery: A New Dual-Modality MRI and NIR Nanoprobe. *Small* **2015**, *11*, 4517−4525.
(503) Zimmer, J. P.; Kim, S. W.; Ohnishi, S.; Tanaka, E.; Frangioni, J. V.; Bawendi, M. G. Size Series of Small Indium Arsenide-Zinc Selenide Core-Shell Nanocrystals and Their Application to *in vivo* Imaging. *J. Am. Chem. Soc.* **2006**, *128*, 2526−2527.
(504) Kotagiri, N.; Li, Z.; Xu, X.; Mondal, S.; Nehorai, A.; Achilefu, S. Antibody Quantum Dot Conjugates Developed via Copper-Free Click Chemistry for Rapid Analysis of Biological Samples Using a Microfluidic Microsphere Array System. *Bioconjugate Chem.* **2014**, *25*, 1272−1281.
(505) Shen, H.; Yuan, H.; Wu, F.; Bai, X.; Zhou, C.; Wang, H.; Lu, T.; Qin, Z.; Ma, L.; Li, L. S. Facile Synthesis of High-Quality $CuInZn_xS_{2+x}$ Core/Shell Nanocrystals and Their Application for Detection of C-Reactive Protein. *J. Mater. Chem.* **2012**, *22*, 18623−18630.
(506) Liu, S.; Shi, F.; Chen, L.; Su, X. Tyrosine-functionalized $CuInS_2$ Quantum Dots as a Fluorescence Probe for the Determination of Biothiols, Histidine and Threonine. *Analyst* **2013**, *138*, 5819−5825.
(507) Tan, L.; Kang, C.; Xu, S.; Tang, Y. Selective Room Temperature Phosphorescence Sensing of Target Protein Using Mn-Doped ZnS QDs-Embedded Molecularly Imprinted Polymer. *Biosens. Bioelectron.* **2013**, *48*, 216−223.
(508) Tan, L.; Huang, C.; Peng, R.; Tang, Y.; Li, W. Development of Hybrid Organic-Inorganic Surface Imprinted Mn-Doped ZnS QDs and Their Application as a Sensing Material for Target Proteins. *Biosens. Bioelectron.* **2014**, *61*, 506−511.
(509) Yan, H.; Wang, H.-F. Turn-On Room Temperature Phosphorescence Assay of Heparin with Tunable Sensitivity and Detection Window Based on Target-Induced Self-Assembly of Polyethyleneimine Capped Mn-Doped ZnS Quantum Dots. *Anal. Chem.* **2011**, *83*, 8589−8595.
(510) Klostranec, J. M.; Xiang, Q.; Farcas, G. A.; Lee, J. A.; Rhee, A.; Lafferty, E. I.; Perrault, S. D.; Kain, K. C.; Chan, W. C. W. Convergence of Quantum Dot Barcodes with Microfluidics and Signal Processing for Multiplexed High-Throughput Infectious Disease Diagnostics. *Nano Lett.* **2007**, *7*, 2812−2818.
(511) Lin, M.; Pei, H.; Yang, F.; Fan, C.; Zuo, X. Applications of Gold Nanoparticles in the Detection and Identification of Infectious Diseases and Biothreats. *Adv. Mater.* **2013**, *25*, 3490−3496.
(512) Fialova, D.; Krejcova, L.; Janu, L.; Blazkova, I.; Krystofova, O.; Hynek, D.; Kopel, P.; Drbohlavova, J.; Konecna, M.; Vaculovicova, M. Flow Injection Electrochemical Analysis of Complexes of Influenza Proteins with CdS, PbS and CuS Quantum Dots. *Int. J. Electrochem. Sci.* **2013**, *8*, 10805−10817.
(513) Ballesta, A.; Clairambault, J. Physiologically Based Mathematical Models to Optimize Therapies against Metastatic Colorectal Cancer: A Mini-Review. *Curr. Pharm. Des.* **2014**, *20*, 37−48.
(514) Ulmschneider, M. B.; Searson, P. C. Mathematical Models of the Steps Involved in the Systemic Delivery of a Chemotherapeutic to a Solid Tumor: From Circulation to Survival. *J. Controlled Release* **2015**, *212*, 78−84.
(515) Gordi, T.; Baillie, R.; Vuong, L. T.; Abidi, S.; Dueker, S.; Vasquez, H.; Pegis, P.; Hopper, A. O.; Power, G. G.; Blood, A. B. Pharmacokinetic Analysis of 14C-Ursodiol in Newborn Infants Using Accelerator Mass Spectrometry. *J. Clin. Pharmacol.* **2014**, *54*, 1031−1037.
(516) Spring, B. Q.; Rizvi, I.; Xu, N.; Hasan, T. The Role of Photodynamic Therapy in Overcoming Cancer Drug Resistance. *Photoch. Photobio. Sci.* **2015**, *14*, 1476−1491.
(517) Shen, X.; Li, S.; Li, L.; Yao, S. Q.; Xu, Q. H. Highly Efficient, Conjugated-Polymer-Based Nano-Photosensitizers for Selectively Targeted Two-Photon Photodynamic Therapy and Imaging of Cancer Cells. *Chem. - Eur. J.* **2015**, *21*, 2214−2221.
(518) Termsarasab, U.; Yoon, I.-S.; Park, J.-H.; Moon, H. T.; Cho, H.-J.; Kim, D.-D. Polyethylene Glycol-Modified Arachidyl Chitosan-Based Nanoparticles for Prolonged Blood Circulation of Doxorubicin. *Int. J. Pharm.* **2014**, *464*, 127−134.
(519) Wang, X.; Yang, C.; Wang, C.; Guo, L.; Zhang, T.; Zhang, Z.; Yan, H.; Liu, K. Polymeric Micelles with α-Glutamyl-Terminated PEG Shells Show Low Non-Specific Protein Adsorption and a Prolonged *in vivo* Circulation Time. *Mater. Sci. Eng., C* **2016**, *59*, 766−772.
(520) García, K. P.; Zarschler, K.; Barbaro, L.; Barreto, J. A.; O'Malley, W.; Spiccia, L.; Stephan, H.; Graham, B. Zwitterionic-Coated "Stealth" Nanoparticles for Biomedical Applications: Recent Advances in Countering Biomolecular Corona Formation and Uptake by the Mononuclear Phagocyte System. *Small* **2014**, *10*, 2516−2529.
(521) Huang, H.; Hernandez, R.; Geng, J.; Sun, H.; Song, W.; Chen, F.; Graves, S. A.; Nickles, R. J.; Cheng, C.; Cai, W.; et al. A Porphyrin-

DOI: 10.1021/acs.chemrev.6b00290
Chem. Rev. 2016, 116, 12234−12327

PEG Polymer with Rapid Renal Clearance. *Biomaterials* **2016**, *76*, 25−32.
(522) Zhang, X. D.; Chen, J.; Min, Y.; Park, G. B.; Shen, X.; Song, S. S.; Sun, Y. M.; Wang, H.; Long, W.; Xie, J.; et al. Metabolizable Bi_2Se_3 Nanoplates: Biodistribution, Toxicity, and Uses for Cancer Radiation Therapy and Imaging. *Adv. Funct. Mater.* **2014**, *24*, 1718−1729.
(523) Lin, G.; Wang, X.; Yin, F.; Yong, K.-T. Passive Tumor Targeting and Imaging by Using Mercaptosuccinic Acid-Coated Near-Infrared Quantum Dots. *Int. J. Nanomed.* **2015**, *10*, 335−345.
(524) Keelan, J. A.; Leong, J. W.; Ho, D.; Iyer, K. S. Therapeutic and Safety Considerations of Nanoparticle-Mediated Drug Delivery in Pregnancy. *Nanomedicine* **2015**, *10*, 2229−2247.
(525) Docter, D.; Strieth, S.; Westmeier, D.; Hayden, O.; Gao, M.; Knauer, S. K.; Stauber, R. H. No King without a Crown-Impact of the Nanomaterial-Protein Corona on Nanobiomedicine. *Nanomedicine* **2015**, *10*, 503−519.
(526) Gaudin, A.; Lepetre-Mouelhi, S.; Mougin, J.; Parrod, M.; Pieters, G.; Garcia-Argote, S.; Loreau, O.; Goncalves, J.; Chacun, H.; Courbebaisse, Y.; et al. Pharmacokinetics, Biodistribution and Metabolism of Squalenoyl Adenosine Nanoparticles in Mice Using Dual Radio-Labeling and Radio-HPLC Analysis. *J. Controlled Release* **2015**, *212*, 50−58.
(527) Knudsen, K. B.; Northeved, H.; Gjetting, T.; Permin, A.; Andresen, T. L.; Wegener, K. M.; Lam, H. R.; Lykkesfeldt, J. Biodistribution of Rhodamine B Fluorescence-Labeled Cationic Nanoparticles in Rats. *J. Nanopart. Res.* **2014**, *16*, 2221.
(528) Muhanna, N.; MacDonald, T. D.; Chan, H.; Jin, C. S.; Burgess, L.; Cui, L.; Chen, J.; Irish, J. C.; Zheng, G. Multimodal Nanoparticle for Primary Tumor Delineation and Lymphatic Metastasis Mapping in a Head-and-Neck Cancer Rabbit Model. *Adv. Healthcare Mater.* **2015**, *4*, 2164−2169.
(529) Kim, S. H.; Lee, J. H.; Hyun, H.; Ashitate, Y.; Park, G.; Robichaud, K.; Lunsford, E.; Lee, S. J.; Khang, G.; Choi, H. S. Near-Infrared Fluorescence Imaging for Noninvasive Trafficking of Scaffold Degradation. *Sci. Rep.* **2013**, *3*, 1198.
(530) Choi, H. S.; Ipe, B. I.; Misra, P.; Lee, J. H.; Bawendi, M. G.; Frangioni, J. V. Tissue- and Organ-Selective Biodistribution of NIR Fluorescent Quantum Dots. *Nano Lett.* **2009**, *9*, 2354−2359.
(531) Deng, D.; Qu, L.; Achilefu, S.; Gu, Y. Broad Spectrum Photoluminescent Quaternary Quantum Dots for Cell and Animal Imaging. *Chem. Commun.* **2013**, *49*, 9494−9496.
(532) Xu, G.; Yong, K.-T.; Roy, I.; Kopwitthaya, A. FGF2-Labeled Semiconductor Nanocrystals as Luminescent Biolabels for Imaging Neuroblastoma Cells. *J. Biomed. Nanotechnol.* **2010**, *6*, 641−647.
(533) Massey, M.; Wu, M.; Conroy, E. M.; Algar, W. R. Mind Your P's and Q's: The Coming of Age of Semiconducting Polymer Dots and Semiconductor Quantum Dots in Biological Applications. *Curr. Opin. Biotechnol.* **2015**, *34*, 30−40.
(534) Volkov, Y. Quantum Dots in Nanomedicine: Recent Trends, Advances and Unresolved Issues. *Biochem. Biophys. Res. Commun.* **2015**, *468*, 419−427.
(535) Wu, T.; Zhang, T.; Chen, Y.; Tang, M. Research Advances on Potential Neurotoxicity of Quantum Dots. *J. Appl. Toxicol.* **2016**, *36*, 345−351.
(536) Kovalenko, M. V. Opportunities and Challenges for Quantum Dot Photovoltaics. *Nat. Nanotechnol.* **2015**, *10*, 994−997.
(537) Hougaard, K. S.; Campagnolo, L.; Chavatte-Palmer, P.; Tarrade, A.; Rousseau-Ralliard, D.; Valentino, S.; Park, M. V.; de Jong, W. H.; Wolterink, G.; Piersma, A. H.; et al. A Perspective on the Developmental Toxicity of Inhaled Nanoparticles. *Reprod. Toxicol.* **2015**, *56*, 118−140.
(538) Wu, T.; Tang, M. Toxicity of Quantum Dots on Respiratory System. *Inhalation Toxicol.* **2014**, *26*, 128−139.
(539) Kostarelos, K. In *Encyclopedia of Nanotechnology*; Bhushan, B., Ed.; Springer: Dordrecht, The Netherlands, 2012; pp 2197−2200.
(540) Xu, S.; Cui, J.; Wang, L. Recent Developments of Low-Toxicity NIR II Quantum Dots for Sensing and Bioimaging. *TrAC, Trends Anal. Chem.* **2016**, *80*, 149−155.
(541) Soenen, S. J.; Abe, S.; Manshian, B. B.; Aubert, T.; Hens, Z.; De Smedt, S. C.; Braeckmans, K. The Effect of Intracellular Degradation on Cytotoxicity and Cell Labeling Efficacy of Inorganic Ligand-Stabilized Colloidal CdSe/CdS Quantum Dots. *J. Biomed. Nanotechnol.* **2015**, *11*, 631−643.
(542) Hu, R.; Law, W.-C.; Lin, G.; Ye, L.; Liu, J.; Liu, J.; Reynolds, J. L.; Yong, K.-T. PEGylated Phospholipid Micelle-Encapsulated Near-Infrared PbS Quantum Dots for *in vitro* and *in vivo* Bioimaging. *Theranostics* **2012**, *2*, 723−733.
(543) Zhang, B.; Wang, Y.; Hu, R.; Roy, I.; Yong, K.-T. In *Handbook of Photonics for Biomedical Engineering*; Ho, A. H.-P., Kim, D., Somekh, M. G., Eds.; Springer: Dordrecht, The Netherlands, 2014.
(544) Wang, M.; Liu, X.; Cao, C.; Wang, L. Highly Luminescent $CuInS_2$−ZnS Nanocrystals: Achieving Phase Transfer and Nuclear Homing Property Simultaneously Through Simple TTAB Modification. *J. Mater. Chem.* **2012**, *22*, 21979−21986.
(545) Huang, L.; Liao, M.; Chen, S.; Demillo, V. G.; Dupre, S. A.; Zhu, X.; Publicover, N. G.; Hunter, K. W., Jr A Polymer Encapsulation Approach to Prepare Zwitterion-Like, Biocompatible Quantum Dots with Wide pH and Ionic Stability. *J. Nanopart. Res.* **2014**, *16*, 2555.
(546) Stern, S. T.; Zolnik, B. S.; McLeland, C. B.; Clogston, J.; Zheng, J.; McNeil, S. E. Induction of Autophagy in Porcine Kidney Cells by Quantum Dots: A Common Cellular Response to Nanomaterials? *Toxicol. Sci.* **2008**, *106*, 140−152.
(547) Chibli, H.; Carlini, L.; Park, S.; Dimitrijevic, N. M.; Nadeau, J. L. Cytotoxicity of InP/ZnS Quantum Dots Related to Reactive Oxygen Species Generation. *Nanoscale* **2011**, *3*, 2552−2559.
(548) Tang, S.; Allagadda, V.; Chibli, H.; Nadeau, J. L.; Mayer, G. D. Comparison of Cytotoxicity and Expression of Metal Regulatory Genes in Zebrafish (Danio rerio) Liver Cells Exposed to Cadmium Sulfate, Zinc Sulfate and Quantum Dots. *Metallomics* **2013**, *5*, 1411−1422.
(549) Ahire, J. H.; Behray, M.; Webster, C. A.; Wang, Q.; Sherwood, V.; Saengkrit, N.; Ruktanonchai, U.; Woramongkolchai, N.; Chao, Y. Synthesis of Carbohydrate Capped Silicon Nanoparticles and Their Reduced Cytotoxicity, *in vivo* Toxicity, and Cellular Uptake. *Adv. Healthcare Mater.* **2015**, *4*, 1877−1886.
(550) Wang, Q.; Bao, Y.; Zhang, X.; Coxon, P. R.; Jayasooriya, U. A.; Chao, Y. Uptake and Toxicity Studies of Poly-Acrylic Acid Functionalized Silicon Nanoparticles in Cultured Mammalian Cells. *Adv. Healthcare Mater.* **2012**, *1*, 189−198.

DOI: 10.1021/acs.chemrev.6b00290
Chem. Rev. 2016, 116, 12234−12327